RELATIONSHIP BETWEEN AC BARKHAUSEN NOISE AND LOSSES IN ELECTRICAL STEEL

BY

HARSHAD VIRJI PATEL

A thesis submitted to Cardiff University in candidature for the degree of
Doctor of Philosophy

Wolfson Centre for Magnetics
School of Engineering
Cardiff University
Wales, United Kingdom of Great Britain and Northern Ireland

March 2009

ProQuest LLC
789 East Eisenhower Parkway
P.O. Box 1346
Ann Arbor, MI 48106-1346

To my family, especially my Mother and late Father,

without whose support this study would have not been possible

ACKNOWLEDGEMENTS

The work was carried out at the Wolfson Centre for Magnetics, School of Engineering, Cardiff University, to which I am grateful for providing the resources needed to complete this project.

I am grateful to my supervisor Professor A. J. Moses for his advice, guidance, encouragement, and especially for accepting me as his student in the later stages of my project. I would like to thank Dr P. I. Williams for his contribution to this project, his advice and valuable discussions during investigations.

I would like to express a special thanks to Professor Beckley and Professor Jiles for their advice and helpful comments throughout my project.

I would also like to thank Dr. Ir. Andrzej S. Wojtas from Stresstech Oy for providing the ferrite sensors.

I am thankful to Dr C. Ragusa from Politecnico di Torino (Italy), for providing the non-oriented electrical steel samples cut at various angles.

I would like to thank Professor S. Takahashi from the NDE and Science Research Centre, Faculty of Engineering, Iwate University, Japan, for providing cold-rolled low carbon steel and thermally aged Fe 1wt%Cu alloy samples for the ancillary study.

Finally, to several colleagues who have assisted me one way or another, especially Miss Thant Phyu Phyu Phway and Dr. Stan Zurek, in challenging me with alternative views, I feel very much indebted.

SUMMARY

The magnetic Barkhausen effect, which appears as abrupt changes in magnetisation, occurs when a ferromagnetic material is subjected to an external varying magnetic field. The origin of the effect is known to be primarily due to the discontinuous domain wall motion through a material caused by imperfections in the material. The Barkhausen effect is very sensitive to the changes in the microstructure and stress. Owing to this sensitivity, Barkhausen measurements can be used for the non-destructive evaluation of a ferromagnetic material.

Previous research has been mainly based on low frequency magnetisation to generate Barkhausen noise with a typical excitation frequency less than one Hertz.

In this work, a measuring system is presented which is capable of capturing Barkhausen noise signals at a magnetisation frequency up to 100 Hz. Enwrapping coils and the ferrite cored surface sensor methods were used to measure Barkhausen noise, and although the surface sensor was oriented perpendicular to the sample, all the sensors produced very similar trends. Due to the Barkhausen noise signal being of stochastic nature, methods of analysing Barkhausen noise signals was investigated. RMS, total sum of amplitudes, power spectrum and kurtosis all showed repetitive characteristics and were used to analyse Barkhausen signals.

A relationship between Barkhausen noise and the hysteresis component of total power loss is presented. The variation of Barkhausen noise signals and the tangential component of surface field over the surface of a grain-oriented 3%SiFe electrical steel was also examined and it was found that there is a strong indication that surface Barkhausen noise activity is influenced by grain-to-grain misorientation. In addition, the results infer that the hysteresis component of loss varies spatially with grain structure.

An ancillary study was conducted on cold rolled low-carbon steel and thermally aged Fe 1wt%Cu alloy to examine the effects of Barkhausen noise due to rolling reduction.

TABLE OF CONTENTS

CHAPTERS

CHAPTER 1

AIMS OF THE INVESTIGATION

In recent years, interest has grown in the measurement of Barkhausen noise as a method for non-destructive evaluation of ferromagnetic materials for the purpose of quality control and quality assurance. Although discovered almost 90 years ago, the origin and characteristics of Barkhausen noise is still not fully understood. It is known that Barkhausen noise is sensitive to changes in the microstructure and stress state of a material but a better understanding of relationship between Barkhausen noise and material parameters is required.

The aims and objectives of the work can be summarised as follows:

- To develop a Barkhausen noise measurement system capable of measuring and analysing Barkhausen noise signals as well as simultaneously measuring the total power loss in electrical steels.
    - Investigate various methods of measuring Barkhausen noise and implement them in the measurement system.
    - Investigate various analysing techniques to maximise the information from the Barkhausen noise signal.
- To attempts to find a relationship between Barkhausen noise and power loss, particularly the hysteresis component, in electrical steels.
- To modify the measurement system in order to investigate surface Barkhausen noise of grain-oriented 3%SiFe electrical steel.
- In addition, to conduct an ancillary study on cold rolled low-carbon steel and thermally aged FeCu to investigate how ac Barkhausen noise can be used to characterise these materials.

The overall aim is to set a solid foundation on which Barkhausen noise measurements can be used as a tool for assessing the ac magnetic performance of electrical steels and similar materials.

CHAPTER 2

MAGNETISM & MAGNETIC MATERIALS

2.1. Introduction

While demonstrating the flow of an electric current in a wire, Hans Christian Oersted noticed that the current caused a nearby compass needle to move. Oersted was the first to show a connection between electricity and magnetism [2.1]. The new phenomenon was then further studied in France by Andre-Marie Ampere, who concluded that the nature of magnetism was quite different from what everyone had believed. It was basically a force between electric currents: two parallel currents in the same direction attract, however, in opposite directions they repel.

Michael Faraday later built an electromagnet and discovered both the law of electromagnetic induction, and the link between light and magnetism, the magneto-optical Faraday Effect. James Clerk Maxwell unified the sciences of electricity, magnetism and light. Four important equations, which had the laws of Ampère, Faraday, Biot and Savart, and Laplace as special cases, were formulated from Maxwell's work in vector form [2.2].

In the study of magnetism, there are two systems of units currently in use: the mks (metres-kilograms-seconds) system, which has been adopted as the S.I. units and the cgs (centimetres-grams-seconds) system, which is also known as the Gaussian system. The S.I. system is used in this study.

2.2. Magnetic material

An electron has both an electric charge and a spin, which gives rise to a tiny magnetic field. In the case of many atoms, all electrons are paired within energy levels, so that the electrons in each pair have opposite spins and their magnetic fields cancel. In some atoms, however, there are more electrons with spins in one direction than in any other, resulting in a net magnetic field for the atom as a whole. These materials can be classified into the following categorories:

Diamagnetic - when a magnetic field is applied to a material, the magnetic moments of individual atoms tend to align in the opposite direction to the applied field, and the material does not retain the magnetic properties when the external field is removed.

Paramagnetic - when a magnetic field is applied to a material, the magnetic moments of individual atoms will tend to align with the external field. The alignment will not be complete, due to the disruptive effect of thermal vibrations. Because of this, a paramagnetic substance is only weakly attracted by a magnetic field.

Ferromagnetic - in a ferromagnetic material, there are more electrons with spins in one direction than in any other. The individual magnetic moments of the atoms in a given region tend to line up in the same direction, so that they reinforce each other. These regions are called ***domains*** [2.3]. Magnetic domains are explained in detail in chapter 3. Ferromagnetic materials were studied in this investigation. Ferromagnetic materials exhibit strong magnetic effects and are the most important magnetic substances [2.4]. They have domains where the atomic magnetic moments are all aligned. Ferromagnetism occurs in iron, cobalt, nickel and their alloys.

In an unmagnetised sample, the domains have different sizes and orientations. When an external magnetic field is applied, domains whose orientations are in the same general direction as the external field will grow at the expense of domains with other orientations. When the domains in all other directions have vanished, the remaining domains are rotated so that their directions are the same as that of the external field. After this rotation is complete, no further magnetisation can take place, no matter how strong the external field; a saturation point is said to have been reached. If the external field is then reduced to zero, it is found that the sample retains some of its magnetism; this is known as ***hysteresis***. Hysteresis is explained in detail in chapter 2.4.

All ferromagnets have a critical temperature, above which their ferromagnetic properties disappears as a result of thermal agitation. This temperature is called the ***Curie temperature***.

Anti-ferromagnetic - The exchange interaction between neighbouring atoms leads to the anti-parallel alignment of the atomic magnetic moments. Therefore, the magnetisation cancels out and the material appears to behave to some extent in the same way as a paramagnetic material.

Ferrimagnetic - Ferrimagnetism is only observed in compounds and alloys, which have more complex crystal structures than pure elements. Within these materials, the exchange interactions lead to parallel alignment of magnetic moments of atoms at some of the crystal sites and anti-parallel alignment of others. Magnetic domains are created in the material, just as a ferromagnetic material and the magnetic behaviour is also very similar, although ferrimagnetic materials usually have lower saturation magnetisation than 0.8 T.

2.3. Magnetic field & magnetic flux density

When an electrical current flows in a conducting coil, it responds by producing a magnetic field, H, measured in Amperes per metre, (A/m). Another important parameter is the magnetic induction (magnetic flux density), B, measured in Tesla, (T), which is the total flux of magnetic field lines through a unit cross sectional area of the material. In the case of free space, the relationship between B and H is linear and can be calculated as:

$$B = \mu_0 \cdot H \tag{2.1}$$

where, μ_0 - the permeability of free space ($4 \times \pi \times 10^{-7}$) (H/m)

For any other medium the relative permeability, μ_r, must be taken into account.

$$B = \mu_0 \cdot \mu_r \cdot H \tag{2.2}$$

The relative permeability of a vacuum or free space is unity by definition. The relative permeability of ferromagnetic materials is generally much greater than unity and in some special alloys may be as large as 1 million [2.1]. The relative permeability of ferromagnetic materials varies over a wide range for different applied fields. Table 2.1 shows the maximum relative permeability of typical ferromagnetic materials [2.1].

Material	Maximum relative permeability, μ_r
Cold rolled steel	2 000
Iron	5 000
3% Silicon iron (grain-oriented)	40 000
Mumetal (75%Ni, 5%Cu, 2%Cr)	100 000

Table 2.1. Relative permeability of typical ferromagnetic materials

2.4. Hysteresis in magnetic materials

Ferromagnetic materials tend to stay magnetised to some extent after an external field is removed. This tendency to "remember their magnetic history" is called **Hysteresis.** The fraction of the saturation induction, which is retained when the driving field is removed, is called the remanence, B_r, and is an important factor in permanent magnets. Coercivity, Hc, is the reverse field required to bring the magnetic induction to zero.

Figure 2.1 shows a hysteresis loop for a typical ferromagnetic material. The dotted line shows the increase in induction on the application of a field to an unmagnetised sample, this is the initial magnetisation curve. In ferromagnetic materials, the initial magnetisation curve is non-linear, as the changing induction with applied field is due to the change in the magnetic domain structure. In the initial region, the induction and field are in the same direction. The induction increases initially by the growth of favourably oriented domains, which will be magnetised in easy directions of the crystal close to the field direction (crystal description in chapter 3). When the induction can increase no further by the growth of domains, the direction of magnetisation of the domains rotates away from the easy axis to align with the field. When all the domains are fully aligned with the applied field, saturation is reached and magnetisation can increase no further.

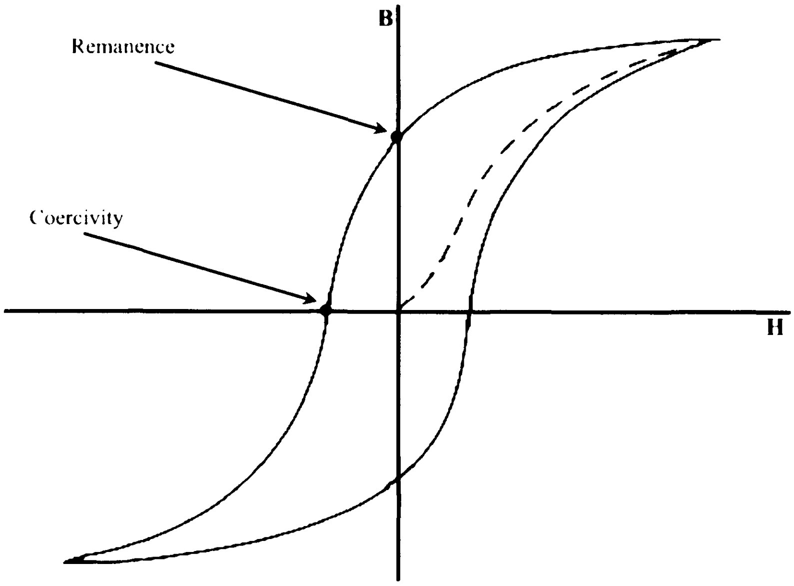

Figure 2.1. A typical hysteresis loop for a ferromagnetic material

If the field is removed, the induction does not return along the initial magnetisation curve but returns to the remanence point. The slight decrease in induction is due to the domains returning to their easy direction of magnetisation. If the direction of the applied field is reversed, the induction will lag behind the applied field and will not immediately switch direction. The induction will only reverse direction after a high enough field is applied. After applying a sufficiently high field, saturation induction is achieved in the reverse direction. If the applied field is then decreased and again applied in the opposite direction then a full hysteresis loop is traversed. If the field is repeatedly switched between alternate directions and is of sufficient magnitude then the induction and field will cycle around the hysteresis loop in an anti-clockwise direction. The area contained within the loop is proportional to the amount of energy dissipated in the material during each cycle of the field. This is discussed in chapter 2.5.

Another magnetic property that can be determined from the hysteresis loop is the *residual flux density*. Residual flux density is the magnetic flux density that remains in a material when the magnetising field is zero. The residual flux density and remanence are numerically the same after the material has been magnetised to saturation.

Magnetic materials can be classified in terms of their magnetic properties and their uses. If a material is easily magnetised and demagnetised then it is referred to as a ***soft magnetic material***, whereas if it is difficult to demagnetise then it is referred to as a ***hard*** (or permanent) ***magnetic material***. The hysteresis loop of a soft magnetic material is narrow with a small enclosed area, shown in figure 2.2a. However, the hysteresis loop of a hard magnetic material has a larger enclosed area as shown in figure 2.2b [2.4].

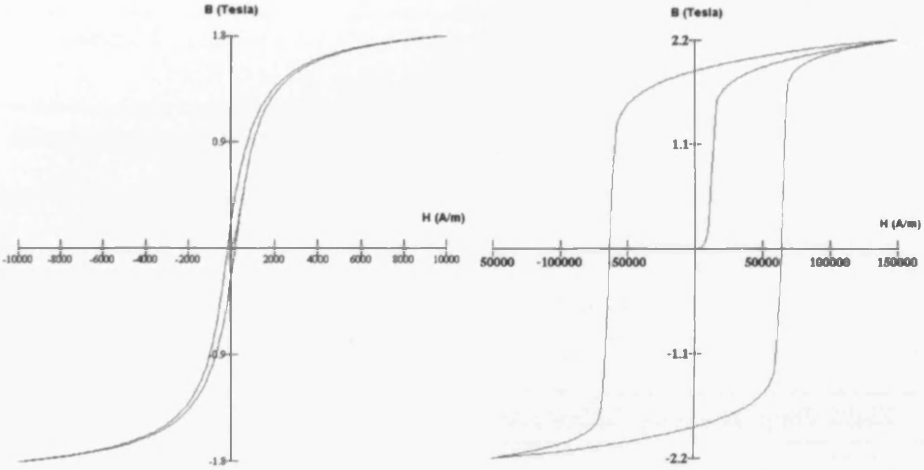

(a) Soft Material (b) Hard Material

Figure 2.2. Typical hysteresis loops for a) soft and b) hard magnetic materials

2.4.1. *Soft magnetic material*

Soft magnetic materials are easily magnetised and demagnetised, so they are used for electro-magnets. The main parameters often used as a figure of merit for soft magnetic materials, are the relative permeability, the coercivity, the saturation magnetisation and the energy loss.

Soft magnetic materials are used in ac and dc applications. In dc applications the material is magnetised in order to perform an operation and then demagnetised at the conclusion of the operation, e.g. an electromagnet on a crane will be switched on to attract scrap steel and then switched off to drop the steel. In ac applications, the material will be continuously cycled from being magnetised in one direction to the other, throughout the period of operation, e.g. as in a power supply transformer core. Typical materials and applications of soft magnetic materials are shown in table 2.2.

Material	General properties & applications
Iron with 0.2-3.2 % silicon	Small energy loss ac motors, generators and transformers
Metallic glass - combinations, of Fe, Co, Ni, B and Si	Low energy loss Used for power transformers, magnetic sensors and recording equipment
Nickel-iron alloys	High permeability applications Used for small signal communications equipment
Soft ferrite - iron, nickel and cobalt ferrite	Low electrical conductivity reduces eddy current losses Used for high frequency applications

Table 2.2. Typical materials and the application for soft magnetic materials

2.4.2. *Hard magnetic material*

Hard magnetic materials have a coercivity of greater than ~10 kA/m [2.5]. Typical hard materials and their applications are shown in table 2.3.

Material	General properties & applications
Aluminium-nickel-cobalt alloy (ALNICO), sometimes with copper and titanium	Magnets can be cast into complex shapes and perform well at higher temperatures
Rare-earth alloys (samarium-cobalt)	High magnetic strength Used in wristwatches and medical implants
Neodymium-iron-boron alloys	Very high magnetic strength Used in low weight requirement applications
Hard ferrites - barium and strontium ferrite	Low cost widespread use, including electronic applications

Table 2.3. Typical materials and the application for hard magnetic materials

2.5. Power loss

Since the coercive field must be applied to overcome the remanent magnetisation, work is done in completing the hysteresis loop and energy is lost. This energy lost is due to magnetic hysteresis and eddy currents. The energy loss, J/m^3, during a single cycle can be shown [2.1] to be equal to:

$$\int H \cdot \frac{dB}{dt} \quad dt \tag{2.3}$$

where, *dt* - is the time for one cycle; H - instantaneous value of the tangential component of the surface magnetising field; *dB/dt* - instantaneous rate of change of the spatial value of magnetic flux density

This is equal to the area enclosed by the BH loop. Power loss is specified in units of watts per kilogram of material, rather than energy lost in a single cycle. As power loss is energy lost per unit time, the core loss can be expressed as:

$$P_t = \frac{f}{D}\int\left(H \cdot \frac{dB}{dt}\right)dt \tag{2.4}$$

where, *f* - the magnetisation frequency; *D* - density of the material

The energy loss is said to originate from three sources [2.6].

1. Hysteresis loss, P_h, which is related to the work done during unpinning of Bloch walls [2.1, 2.7].

2. Classical eddy current loss, P_e, which is related to the generation of electric currents in magnetic materials and the associated resistive losses. This increases energy loss at higher frequencies of magnetisation (due to the Joule heat effect). This can be calculated using Maxwell's equations.

3. Excess loss (previously referred to as anomalous loss), P_a, which is related to the movement of domain walls within the material and acoustic vibrations.

Therefore, the total power loss, P_t, can be written as:

$$P_t = P_h + P_e + P_a \tag{2.5}$$

The breakdown of the total power loss into components based on the nature of the loss mechanism can give a better understanding and help reduce overall losses.

Hysteresis losses can be reduced by the reduction of the coercivity, with a consequent reduction in the area contained within the hysteresis loop. Eddy current losses can be reduced by increasing the resistivity of the material, increasing the resistance of the core inhibits current flow without inhibiting the flow of magnetic flux. Finally, the excess losses can be eliminated by having a completely homogeneous material, within which there will be no hindrance to the motion of domain walls, however such a pure material is impossible to produce.

The classical eddy current contribution to the power loss can be calculated providing that the characteristic of the magnetic material and its dimensions are known using equation 2.6 [2.8]. This equation is only valid if constant permeability and sinusoidal applied field are assumed. In this work, the applied magnetic flux density is kept sinusoidal however, the permeability of the material changes with flux density.

$$P_e = \frac{\pi^2 \cdot d^2 \cdot B_{peak}^2 \cdot f^2}{6 \cdot \rho \cdot D} \tag{2.6}$$

where, d - thickness (m); B_{peak} - peak flux density; ρ - resistivity (Ωm)

Transformers cores are made from thin laminations in order to reduce power loss, since P_e is inversely proportional to the thickness of the materials under magnetisation.

Hysteresis cannot be calculated because carbon impurities and stress in a material can not be predicted, however, at low magnetising frequencies (below 1 Hz) the eddy currents become negligible and only the hysteresis component is present [2.9]. Bertotti found that the loss behaviour is not far from the law [2.3]:

$$\frac{P_t}{f} = C_0 + C_1 f + C_2 \sqrt{f} \tag{2.7}$$

Where the term C_0 represents the hysteresis component of loss per cycle and C_1 the classical eddy current component per cycle and C_2 the anomalous component per cycle, that all are functions of B_{peak}. This gives a means of separating the hysteresis component of power loss (figure 2.3).

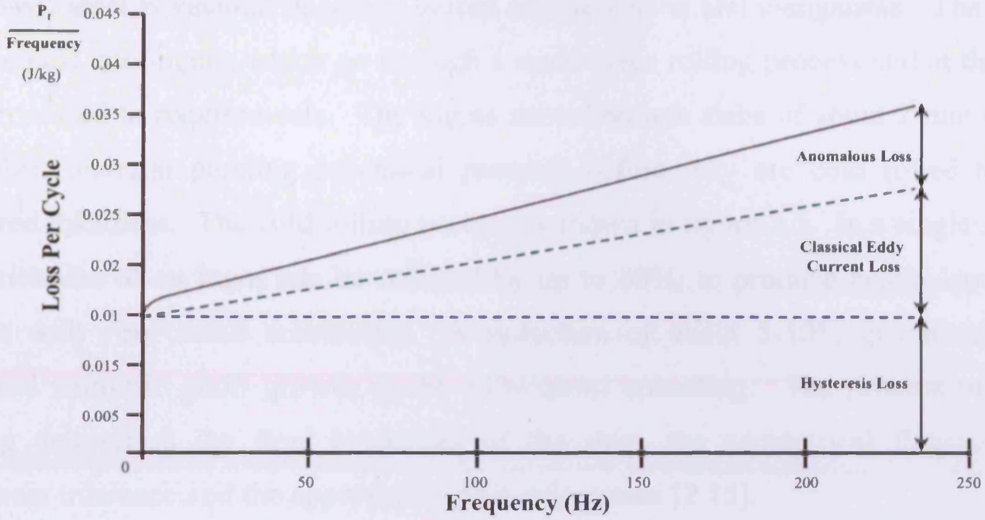

Figure 2.3. Variation of loss/cycle with frequency as implied from equation 2.7 [2.3]

2.6. Electrical steels

Iron-silicon alloys are used for transformer cores, motors, generators, and are known as ***electrical steels***. Electrical steels are soft magnetic materials used in lamination form, typically 0.1 to 0.7 mm thick. These steels are classified as three types, grain-oriented steel [2.10], non-oriented fully processed steel [2.11], and non-oriented semi-processed steel [2.12]. In the power industry, electrical voltage is usually ac and at frequencies in the range of 50-60 Hz. Alloying the iron with silicon has the effect of increasing the material's electrical resistivity, thus reducing eddy currents. Silicon also has the benefit of reducing the magnetostriction (i.e. length change on magnetisation) and the magnetocrystalline anisotropy. The addition of more than 4% silicon makes the material brittle and difficult to produce [2.6]. Typically, most electrical steels will contain between 0.2 and 3.2 % silicon [2.13].

However, a technique has been developed by JFE formally NKK cooperation to produce laminations with 6.5% silicon, 0.05 mm thick [2.14]. The magnetic permeability of the alloys increases to a maximum and iron loss decrease and the magnetostriction drops to zero in this material.

2.6.1. *Production of electrical steels*

Figure 2.4 shows an overview of one production process for electrical steel [2.15]. The basic steel is vacuum degassed before adding silicon and manganese. The alloy is then cast into ingots, which go through a multi-stage rolling process and at the end are processed to requirements. The ingots are rolled into slabs of about 2 mm thick, and then undergo pickling (chemical process) before they are cold rolled to the required thickness. The cold rolling process is shown in figure 2.5. In a single stage, the thickness of an ingot can be reduced by up to 80%, to produce nearly isotropic sheets with very small anisotropy. A reduction of about 5-10% guarantees the required isotropic grain growth in the subsequent annealing. The process of cold rolling determines the final properties of the strip, the geometrical flatness and thickness tolerance and the appropriate grain orientation [2.15].

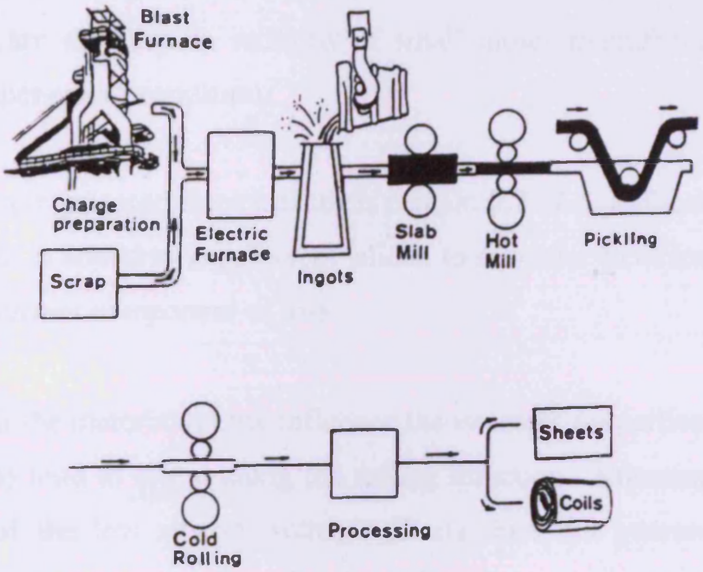

Figure 2.4. Overview of the operations in electrical steels production

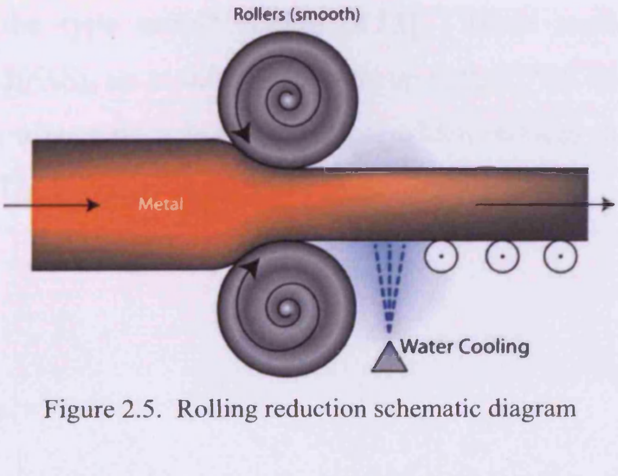

Figure 2.5. Rolling reduction schematic diagram

Strip annealing is carried out after the cold rolling process to remove stresses, to decarburise the material and to recrystallise and enlarge grains with the preferred orientation to get optimum magnetic properties.

2.6.2. Non-oriented electrical steel

Usually non-oriented electrical steel sheets are subjected to a double annealing process only, firstly after cold rolling to recrystallise and decarburise the steel and secondly to remove stresses and to obtain desired random orientation of grain growth. Non-oriented steel is very nearly isotropic making it very suitable for rotating electrical machines. Non-oriented electrical steels may be supplied fully processed, ready for punching and core fabrication, or in a semi-processed state [2.16]. Fully processed non-oriented electrical steels are used when high efficiency is required in products such as rotating motors and generators. Non-oriented semi-processed electrical steels are supplied to millions of small motor manufacturers around the world in the temper rolled condition.

Fully processed non-oriented electrical steels contain 0.2 - 6.5% silicon. Also in some steels, aluminium is added to supplement silicon to raise the electrical resistivity and lower the eddy current component of loss.

The impurities in the material do not influence the isotropic properties of the material; however, they do tend to orient along the rolling direction. Knowing the crystalline microstructure of the low silicon isotropic sheets does not guarantee a sufficient knowledge of their grain orientation due the different types of mixed texture, shown in figure 2.6. Low silicon sheets are characterised by small anisotropy of magnetic properties due to the type mixed texture [2.15]. These steels contain typically 0.025%C, up to 0.250%Si, up to 0.800%Mn and up to 0.020%S and exhibit very good magnetic properties after a decarburising anneal which reduces the carbon content to less than 0.3% [2.17].

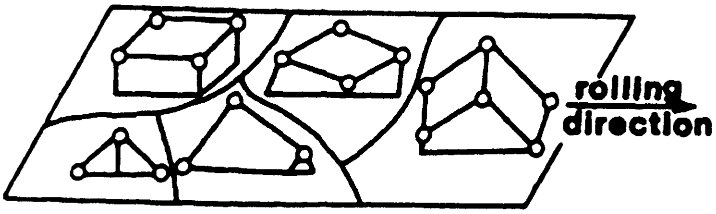

Figure 2.6. Schematic diagram for mixed type crystal orientation for non-oriented low silicon sheets

2.6.3. Grain-oriented electrical steel

Grain-oriented electrical steels were developed by Goss in 1933 [2.18]. He discovered that by a combination of hot and cold rolling, a sheet is produced with much better magnetic properties along its rolling direction than hot rolled sheet. This rolling technique gave rise to crystals in grain-oriented electrical steel that tends to be arranged with their <001> directions parallel to the rolling direction and the <110> plane parallel to the surface of the sheet (see figure 2.7, where magnetisation, *M*, is plotted against magnetic field). It is therefore easier to magnetise such a textured sheet in the rolling direction compared to a randomly textured sheet. This crystallographic structure is called the cube-on-edge or Goss texture. This improvement was due to a magnetically favourable texture produced by secondary recrystallisation during high-temperature annealing [2.18].

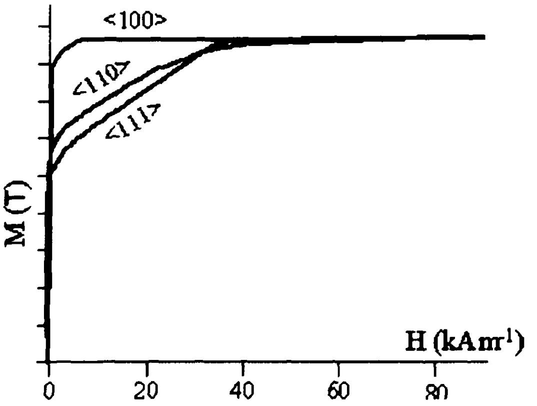

(a)

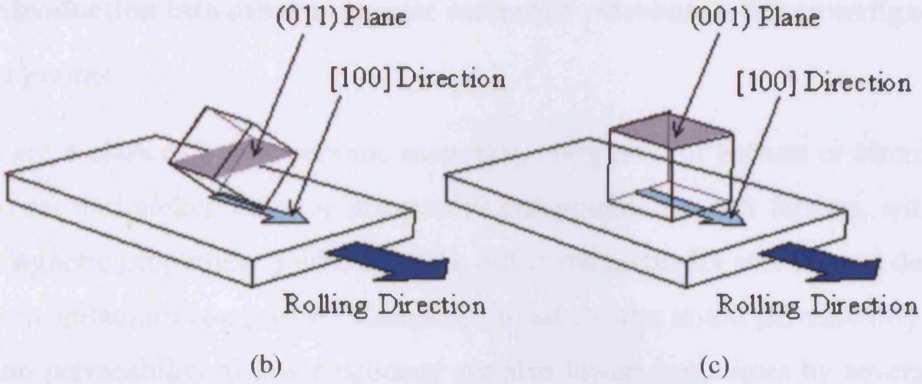

Figure 2.7. Schematic diagram of (a) the magnetocrystalline anisotropy of Fe, (b) cube-on-edge texture and (c) cube texture in grain-oriented silicon steel

Grain-oriented electrical steels are low-carbon alloys with a silicon content of approximately 3.2% with low core loss and high permeability when magnetised along the rolling direction. These steels are used primarily in transformer cores operating at moderate to high magnetic flux densities at commercial power frequencies (50 and 60 Hz).

2.6.4. *Coatings on electrical steels*

Conventional non-oriented electrical steels can be provided with three main types of insulating coatings. Firstly, an inorganic coating which has good welding and heat resistance properties with good punchability. Secondly, a semi-organic coating which has good punchability and good welding response. Thirdly, an organic coating, which has good punchability and good insulation resistance dependent on coating thickness [2.6].

In the coating process of grain-oriented electrical steels, a glass formed of magnesium silicate, which is the result of magnesium oxide reaction with silicon steel, is the basis of a surface insulation layer [2.6]. As the magnesium silicate is cooled, the Young's modulus of the glass and steel assert themselves and the steel tries to contract more than the magnesium silicate, thus leaving the steel held in tension [2.10]. This induced tension results in a lower total power loss when magnetised along the rolling direction. A supplementary phosphate coating is also applied to enhance the insulation characteristics.

2.7. Introduction into other magnetic materials relevant in this investigation

2.7.1. Ferrites

Ferrites are a class of brittle ceramic materials, composed of barium or strontium for hard ferrites and nickel, zinc, or manganese compounds for soft ferrites, with useful electromagnetic properties. Ferrites can be either magnetically soft or hard depending on their manufacture/composite. Compared to steels, the initial permeability and the maximum permeability at low frequency are also lower, sometimes by several orders of magnitude. The most distinctive characteristic of the ferrites is that they have low losses at high frequencies. The presence of ferrous ions may be avoided here by producing a slight iron deficit with respect to the theoretical value of two ions per molecule. The result is a resistivity greater by several orders than metal, making the eddy current loss completely negligible in most cases [2.7].

2.7.2. Nickel-iron alloys

The addition of nickel between 28% and 78% to iron can produce very specific properties so the applications of these alloys are often at the cutting-edge of technology [2.7]. They can have good mechanical strength, corrosion resistance and conductivity but their thermal expansion and magnetic permeability characteristics are often the vital attributes that designers seek. In some cases, the addition of a small amount of other elements such copper, chromium, or molybdenum produces a significant increase in the permeability of the material [2.7].

2.7.3. Nano-crystalline alloys

During the last 20 years, there has been much interest in nano-crystalline material, which can be produced by annealing amorphous material in the form of a tape by melt-spinning. These alloys can be single phase but are usually comprised of nano-sized grains, in the range 10-50 nm, in an amorphous matrix. They have relatively high resistivity, low anisotropy and good mechanical strength [2.7].

The alloys consist of iron, nickel and/or cobalt with one or more of the following elements: boron, carbon, copper, niobium, phosphorous and silicon. They have extremely low coercivity, an order of magnitude less than conventional grain-oriented FeSi steel, and consequently lower hysteresis losses.

References to chapter 2

[2.1] D. C. Jiles, "Introduction to magnetism and magnetic materials", Chapman & Hall, London, 1991

[2.2] J. C. Maxwell, "A dynamical theory of the electromagnetic field", Philosophical Transactions of the Royal Society of London, Vol 155, 459-512, 1865

[2.3] G. Bertotti, "Hysteresis in Magnetism: for physicists, materials scientists and engineers", Academic press, London, 1998

[2.4] J. D. Kraus, "Electromagnetics", McGraw-Hill, Fourth edition, New York, 1992

[2.5] S. Chikazumi, "Physics of Ferromagnetism", Clarendon Press, Oxford, 1997

[2.6] P. Beckley, "Electrical Steels", European Electrical Steels, Orb works, 2000

[2.7] P. Robert, "Electrical and magnetic properties of materials", Artech House, Norwood, 1998

[2.8] R. M. Bozorth, "Ferromagnetism", D. Van Nostrand company inc., USA, 1951

[2.9] G. Bertotti, "General properties of power losses in soft ferromagnetic materials", IEEE Transactions on Magnetics, Vol 24, No 1, 621-630, 1998

[2.10] Orb Electrical Steels product catalogue, "Grain oriented", Cogent Power Ltd, Newport, UK

[2.11] Orb Electrical Steels product catalogue, "Non oriented fully processed", Cogent Power Ltd, Newport, UK

[2.12] Orb Electrical Steels product catalogue, "Non oriented semi processed", Cogent Power Ltd, Newport, UK

[2.13] A. J. Moses, "Electrical Steels: past, present and future developments", IEE Proceedings, Vol 137, No 5, 233-245, 1990

[2.14] H. Haiji, K. Okada, T. Hiratani, M. Abe, M. Ninomiya, "Magnetic properties and workability of 6.5% Si steel sheet", Journal of Magnetism and Magnetic Materials, Vol 160, 109-114, 1996

[2.15] K. H. J. Buschow, "Handbook of magnetic material", Elsevier Science B.V, 327-347, 1995

[2.16] E. S. Hamdi, "Design of small electrical machine", John Wiley & Sons, New York, 1994

[2.17] A. Coombs, "Improved low loss high permeability grades, processing and properties", Journal of Physics IV France, Vol 8, 475-482, 1998

[2.18] B. D. Cullity, "Introduction to magnetic materials", Addison-Wesley, London, 1972

CHAPTER 3

MAGNETIC BARKHAUSEN NOISE

3.1. Introduction

In 1919, Prof Heinrich Georg Barkhausen (1881-1956) [3.1] discovered a magnetic effect of domain wall motion, which is known today as the **Barkhausen effect**. He proved that the magnetisation process, which is characterised by the hysteresis curve, in fact is not continuous, but is made up of small, abrupt steps caused when the magnetic domains move. When electrical pulses produced by domain movements, detected using an enwrapped search coil were added together, a noise-like signal called ***Barkhausen Noise*** is generated.

Recent research is mainly concentrated on:

- Relation between the dynamics of the magnetisation process and physical characteristics of ferromagnetic materials
- Reduction of noise level in sensors with ferromagnetic cores
- Barkhausen noise and its use in non-destructive testing (quality control)

When the Barkhausen effect was discovered, its importance for non-destructive testing (NDT) and its potential to determine material proprieties were not recognised. Quality control and condition monitoring of some industrial components require the development of new NDT techniques [3.2] and Barkhausen noise has been extensively used as an important NDT tool to investigate intrinsic properties of magnetic materials such as grain size, effectiveness of heat treatment, internal strain and mechanical hardness [3.3].

3.2. Domain magnetisation processes in bulk magnetic materials

Domains are regions of a ferromagnetic material in which the magnetic dipole moments of individual atoms are aligned parallel. Domain walls are the regions between domains where the direction of magnetisation must change; usually by either 180° or 90°, (flux closure domains have 90° walls). Figure 3.1 shows four domains in a ferromagnetic material indicating 180° and 90° walls. Neighbouring domains having magnetic moment aligned in different directions have a transition period where the magnetic moments undergo a reorientation in accordance to the neighbouring domain, figure 3.2 shows typical domain wall of δ width, with the magnetic moments going through a transition period.

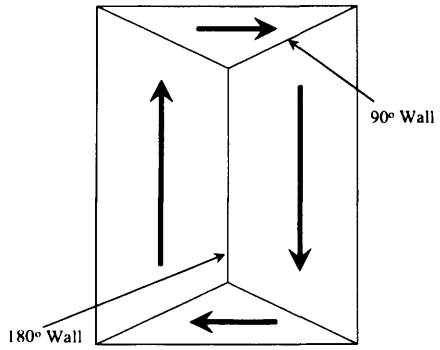

Figure 3.1. Idealised representation of four domains in a ferromagnetic material showing positions of 180° and 90° walls

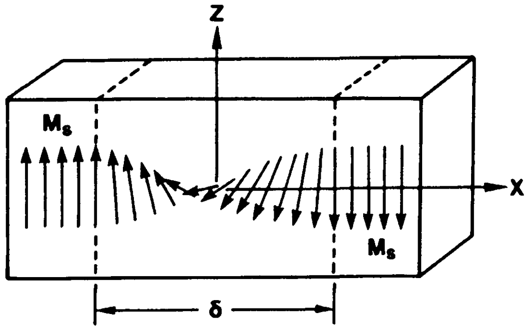

Figure 3.2. The magnetic moments of an 180° domain wall of δ width, with the magnetic moments going through a transition period

The directions of domains in unmagnetised materials vary randomly in isotropic materials. When a magnetic material is placed in an external magnetic field, all dipoles will tend to align along the direction of the applied magnetic field. Some domains are already aligned in the direction of the field. These domains tend to grow in size at the expense of neighbouring domains. The growth of a domain is merely due to a positional change in its boundaries. Dipoles in other domains will rotate into the direction of the applied field. When complete magnetic saturation is reached, each grain is composed of a unique domain that is magnetised in the direction of the applied field.

The magnetisation processes can be divided into irreversible and reversible magnetisation processes. The irreversible processes are usually associated with the dissipation of energy and with the switching of the magnetic moment from one to another equilibrium position while the reversible magnetisation is a quasistatic process. More often, both processes occur together and the material will not return to its original magnetisation, when the magnetic field is reduced or removed [3.3]. This is because the transition from reversible to irreversible processes depends on the amplitude of the magnetic field but not all processes of domain rotation and domain wall movement require the same energy level to change their state. Therefore, it happens that some irreversible processes occur at a lower energy level than some reversible processes. However, the higher the energy level (close to saturation of the material) the more irreversible processes take place.

3.3. Magnetic Barkhausen effect

The main types of noise in ferromagnetic materials are thermal noise, excess noise and Barkhausen noise but the strongest by far is said to be the Barkhausen noise [3.4]. Thermal noise is generated by the thermal energy of the conduction electrons and spin waves acting on the domain configuration in the ferromagnetic materials. Excess noise occurs during temperature changes of the sample, it is generated by the magnetisation processes caused by a changing mechanical strain inside the sample. The Barkhausen effect is a phenomenon of discontinuous changes in the flux density, B, within a ferromagnet as the magnetic field, H, is changed continuously [3.1]. Figure 3.3 shows a schematic representation of the Barkhausen effect.

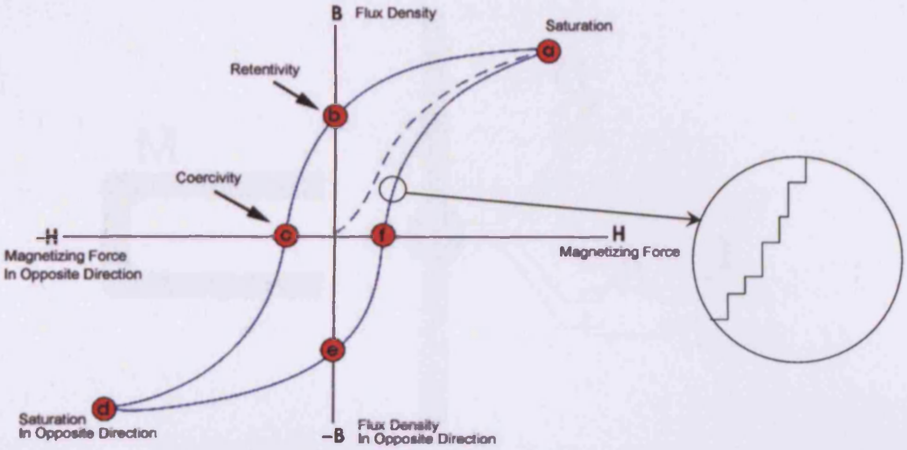

Figure 3.3. Barkhausen jumps along the BH curve

A demagnetised ferromagnetic iron rod may contain many magnetic domains with random orientation. The application of a magnetic field forces those domains that are aligned with the field to grow at the expense of those that are not. As the domains grow, so the domain walls are pinned on to impurities within the iron. Figure 3.4 shows how a planar wall is distorted as it interacts with a defect in a hypothetical case. It can be seen that increasing the magnetic field moves the domain wall (figure 3.4a), once the domain wall has reached the inclusion the domain wall gets ‘pinned’ to the inclusion, if the field is increased further the ‘pinned’ domain wall stretches (figure 3.4b), until the domain wall ‘snaps’ beyond the impurity resulting in a loss of energy (figure 3.4c). This sudden movement can be detected electronically or heard through a loud speaker as shown in figure 3.5. Barkhausen noise activities take place mostly in the area around the coercive field (H_c) when the domain wall activity is greatest (figure 3.6).

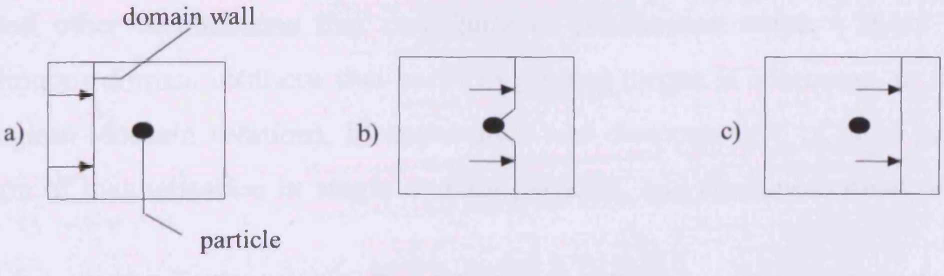

Figure 3.4. Illustration of the pinning effect a) the domain wall moving with increasing field b) the domain wall pinning to the inclusion, causing the domain wall to stretch c) and finally when the domain wall snaps away from the inclusion

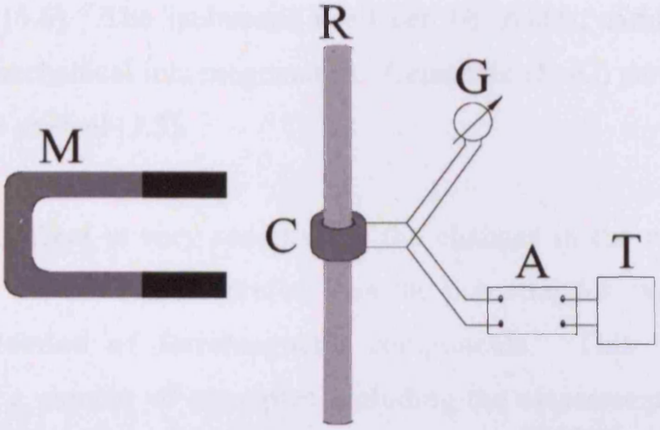

Figure 3.5. Original Barkhausen measurement system. M - magnet, R - iron rod, C - search coil, G - galvanometer, A - tube amplifier, T - telephone (loudspeaker) [3.1]

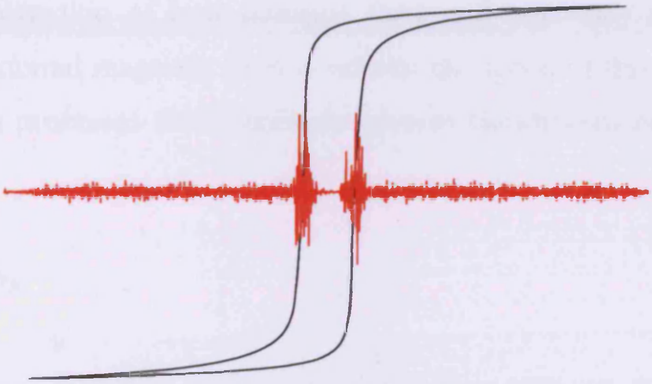

Figure 3.6. Diagram showing Barkhausen noise activity, which is greatest at the coercive field

The discontinuous jumps in magnetisation that comprise the signal are thought to be due to discontinuous domain wall displacements that occur as pinning sites are overcome, in the low field regime. This is often quoted to be the sole contributing factor to Barkhausen noise. However, Lomaev at al. [3.5] reviewed the literature and identified other mechanisms that contribute to Barkhausen noise. These are, a) discontinuous domain rotations that occur as pinning torque is overcome, in the high field regime (domain rotation), b) appearance and disappearance of Néel peaks, c) inversion of magnetisation in single domain particles, and d) displacement of Bloch walls.

A very important question is why domain walls are held at pinning sites. All physical processes try to reach a state of stability or minimum potential energy; this is also the case here. When the domain wall intersects with inclusions, the energy level of the wall is reduced [3.6]. The inclusions itself can be oxides, carbides, pores, voids, cracks or other mechanical inhomogeneities. Cementite (Fe_3C) particles are common inclusions in iron or steel [3.3].

The Barkhausen effect is very sensitive to the changes in the microstructure and stress state of a material and therefore has the potential for exploitation in non-destructive evaluation of ferromagnetic components. This has already been demonstrated in a number of examples including the assessment of the quality of heat treatment of Fe-Cr-B amorphous alloys [3.7], sub-surface stress analysis in case carburised steel [3.8], and determination of grinding effects in steel [3.9].

A qualitative explanation of how domains form and how they interact under the influence of an external magnetic field is outside the scope of this study. However, the most common processes that contribute towards Barkhausen noise are described here.

3.3.1. Bloch walls

The transition region between domains magnetised in different directions was first studied by Bloch (1932). Between two domains, a progressive rotation of the moments takes place (figure 3.2), which defines a ***Bloch wall***. The change from one direction to the other is not discontinuous but occurs over a width determined by a balance between *exchange* and m*agnetocrystalline anisotropy* energy.

The width of the domain wall varies due to the two opposing energies that create it: the magnetocrystalline anisotropy energy and the exchange energy (E_{ex}), both of which want to be as low as possible to be in a more favourable energetic state. The anisotropy energy is lowest when the individual magnetic moments are aligned with the crystal lattice axes thus reducing the width of the domain wall. Whereas the exchange energy is reduced when the magnetic moments are aligned parallel to each other and thus makes the wall thicker, due to the repulsion between them (where anti-parallel alignment would bring them closer - working to reduce the wall thickness). In the end, an equilibrium is reached between the two and the domain wall's width is set as such.

Domain wall bowing (described in chapter 3.3.2) and Bloch wall translation depends on the potential energy level of the Bloch wall and the external energy applied to that wall. When the magnetic field is strong enough, the wall will irreversibly move to a different wall energy level [3.3]. Figure 3.7 illustrates how the domain wall movement will be reversible or irreversible.

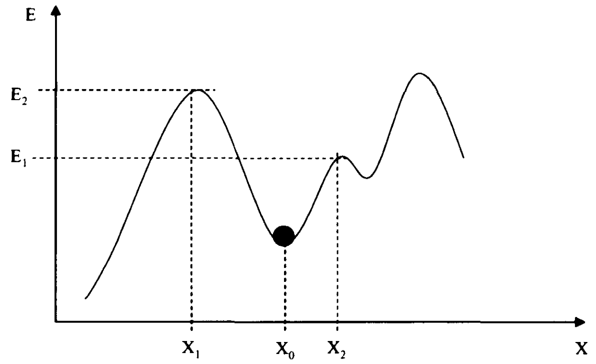

Figure 3.7. Potential energy (E) in analogy to Bloch wall energy along a distance x within the material [3.10]

The analogy of a ball on an undulating road demonstrates how a domain wall may move with an applied magnetic field. The ball represents the domain wall and the energy level, E, represents the energy applied to a domain wall to move it to the next state. The minima in the road represent the preferred energy level that a domain wall would occupy once the movement stops. The maxima in the road represent the energy level needed to move a domain wall to another preferred energy level.

The magnetic field is assumed to be along the x-axis. The magnetic field is applied, when the field energy is high enough the ball will be pushed over the next hill and enter a new energy level. The shape of the graph in figure 3.7, i.e. the occurrence of peak values, is dependent on the distribution of impurities, dislocations or mechanical stress in a material.

Irreversible domain wall displacements can be considered as the main contribution to Barkhausen noise generation.

3.3.2. *Domain wall bowing*

When a small magnetic field is applied to a magnetic material, the domain wall shows a tendency to bend. Wall bending is shown in figure 3.8. This is both reversible and irreversible under certain conditions. The domain wall can be considered as a rubber band that extends under the influence of the magnetic field and returns to its original position when the magnetic field is removed. In general, domain walls with a higher energy have a lower tendency to bend whereas domain walls with a low energy level are more flexible and bend easily.

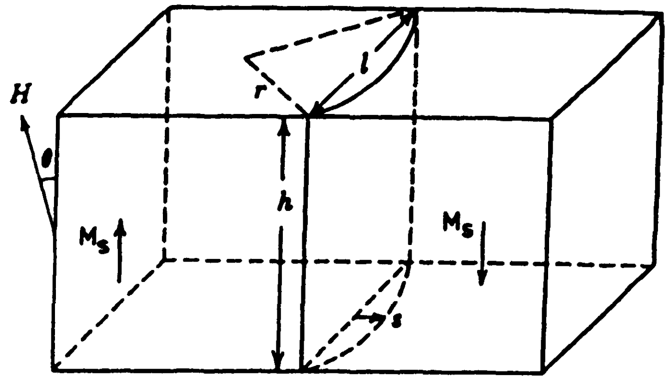

Figure 3.8. Bending of a domain wall under the action of a field. The domain wall is pinned at the boundaries and expands in the manner of an elastic membrane [3.3]. M_s - Magnetisation within the domain; h - height of the domain wall; s - distance wall is bent; r - radius of the domain wall bending; l - length of the domain wall; H - field applied to domains; θ - angle at which the field is applied to the domains

When the domain wall is sufficiently deformed such that the extension continues without further increase of the magnetic field the effect becomes irreversible. A second even more important process, which makes this effect irreversible, is when the domain wall while extending encounters a further pinning site. This pinning site prevents the wall from returning into its original position when the field is removed. The pinning effect occurs when the amplitude of the magnetic field further increases and the domain wall breaks away from its pinning sites [3.3].

3.3.3. *Domain rotation*

As a magnetic field is applied to a magnetic material, domains aligned parallel with the applied field grow at the expense of others. At larger fields, the material reaches a single domain state, which is said to be the material's technical saturation magnetisation. If the field is further increased, the magnetic moments change their direction from their original easy axis to the one that is closest to the field direction. This is ***Domain rotation***. Figure 3.9 shows the domain processes occurring as a material is magnetised to saturation. This occurs when the field overcomes the materials anisotropy energy [3.3].

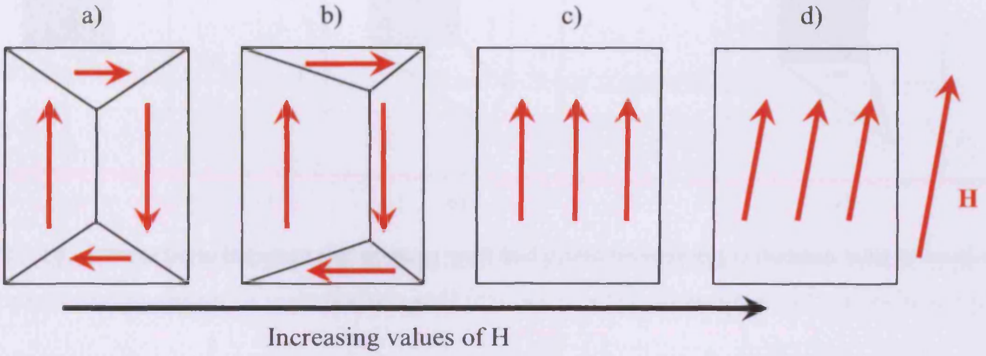

Figure 3.9. Magnetisation process - (a) the demagnetised state without any field (b) the domain wall movement with applied field (c) the single domain state (irreversible) (d) shows the final alignment after further increase of the field (reversible)

This irreversible rotation was believed to be the sole cause of Barkhausen noise. Nowadays it is known that this effect is small compared to discontinuous irreversible domain wall motion [3.3].

3.3.4. Néel peaks

Kersten [3.6] assumed that domain walls move in a planar manner through a solid and that the energy of the walls is reduced when they intersect inclusions. Néel (1944) demonstrated that energetic interactions between domain walls and inclusions also arise from internal demagnetising fields (when a piece of ferromagnetic material such as an iron rod becomes magnetised, poles form at the ends. These poles generate an internal demagnetising field, which tries to demagnetise the material). There are also magnetic free poles that are associated with the inclusion that would be an additional source of energy. Triangular 'spike' domains were predicted theoretically by Néel (1944). Figure 3.10a shows the main domain walls becoming stuck to an inclusion, and then the main domain wall moves away from the inclusion under an applied field (figure 3.10b), before becoming irreversibly detached and forming spike domains (figure 3.10c). The inclusion would never entirely be free from spike domains, until saturated.

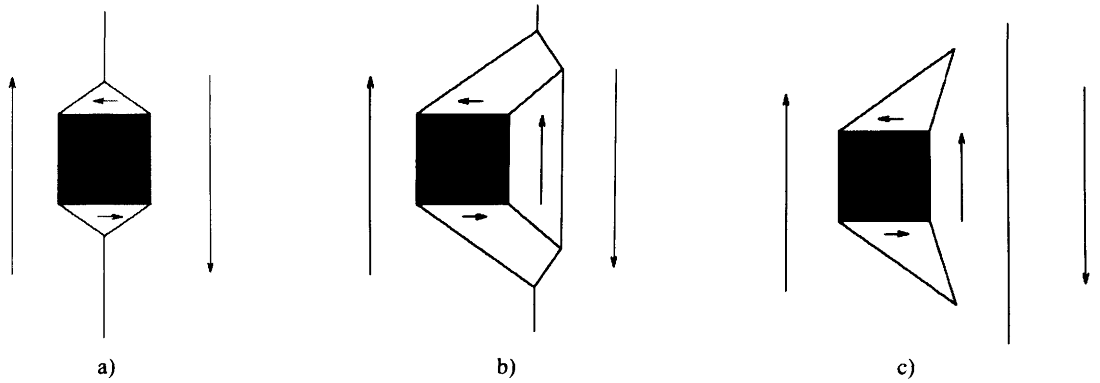

Figure 3.10. Interactions between the domain wall and cubic inclusion (a) domain wall at local energy minimum (b) movement of main domain wall (c) detachment of domain wall from inclusion [3.10]

3.4. Previous research on measurement of Barkhausen noise

Previous research on the Barkhausen effect in electrical steels has concentrated on domain studies related to Barkhausen noise, power loss relations to Barkhausen noise and Barkhausen noise measurement systems. When the effect was discovered, its potential for non-destructive testing (NDT) was not recognised. In recent years, it is often used as a magnetic NDT tool, to investigate properties such as grain size, heat treatment, strain.

Bush and Tebble [3.11] and others [3.12] investigated a method for determining the number and size distribution of Barkhausen discontinues over the whole or any part of the magnetisation curve. This work was then used by Stoner [3.13] on general problems of the analysis of magnetisation curves with a view to obtaining more complete information about the elementary processes taking place. The measurements were carried out by slowly changing the magnetisation of the specimen and the resultant Barkhausen jumps were amplified and detected as voltage pulses on an oscilloscope. Stoner concluded that Barkhausen discontinuities arise mainly from movements of 180^0 boundaries. He also concluded that to completely investigate the full magnetisation curve for a specimen it would take several months, as a very small rate of change in the field would be required to be able to count the discontinuities.

During the 1960's it was recognised that the Barkhausen noise amplitude changes when stress is applied to the specimen, but the work really gained momentum when Gardner et al [3.14] reported a relationship between Barkhausen noise and the ambient temperature of a specimen. A magnetising frequency of 0.09 Hz was used to magnetise the samples.

Extensive studies were conducted by Tiitto [3.15] on the non-destructive testing of steels analysing the statistics of Barkhausen noise. He used the amplitude of the Barkhausen noise signal as a parameter, which he compared to several microstructural steel parameters. He found that the Barkhausen noise amplitude was strongly dependent on the magnitude and direction of elastic strain. Tiitto also stated that there is a logarithmic dependence between the Barkhausen noise amplitudes and grain size, which is best to show at the beginning of the magnetisation process. He also related Barkhausen noise amplitude to carbon content and it was observed that within the range of 0.01% to 0.8% carbon content, this relationship was rather weak. However, when Barkhausen noise was plotted against mechanical hardness, reasonably good correlation of logarithmic form was observed.

Sundström and Törrönen [3.16] showed the importance of Barkhausen noise measurements and analysis for the steel industry with respect to stresses, fatigue and creep damages. They compared the traditional (destructive) ways to determine material properties with the Barkhausen noise method, and found that the disadvantages of this technique are: (*i*) sensitivity to microstnictural variations, (*ii*) limited stress range measurement and (*iii*) only a thin surface layer can be measured.

RMS analysis of Barkhausen noise was used by Karjalainen et al [3.17] to investigate the mild steel with special attention to the effect of stress below the yield strength. The results given were qualitative in nature but showed that on materials with positive magnetostriction, Barkhausen noise increases with tensile stress and decreases with compressive stress.

A pickup coil wound around the sample is the standard method of Barkhausen noise measurements. Puppin et al [3.18] used two pickup coils instead of one in their investigation of the spatial correlation of Barkhausen noise by varying the relative position of the coils. They showed that the induced signals are very similar when the coils are nearby each other, and a progressive decrease in Barkhausen noise can be seen as the coils are moved apart. The material used was amorphous FeBSiNi.

Barkhausen noise has been investigated for over 30 years for it to be used as a non-destructive testing tool and many material parameter correlations with Barkhausen noise have been observed during this period. In the 1980s with the availability of PCs and data acquisition cards research on Barkhausen noise became more feasible and increased vastly. Its capability as a tool to investigate the intrinsic features of the magnetisation process and the related hysteresis behaviour became more important. Barkhausen research got more "organised" as it became more focused on certain material parameters or industrial applications rather than doing fundamental research on the phenomenon. Hence, the following review is split into different areas.

3.4.1. Barkhausen effect studies and non-destructive testing

Jiles [3.19] measured the effect of uniaxial tensile stress of up to 85MPa on Barkhausen activity and magnetic properties of AISI4130 and AISI4140 steels. The results showed (figure 3.11) that the location of maximum Barkhausen activity was very close to the coercive point. It was observed that the Barkhausen peak height and the total number of pulses were affected by the stress. However, it was only in the AISI4140 steel that the anticipated increase of Barkhausen noise with tensile stress was observed. In AISI4130, the maximum count rate did not show a progressive trend with stress, which is presumed to be due to a broadening of the Barkhausen peak.

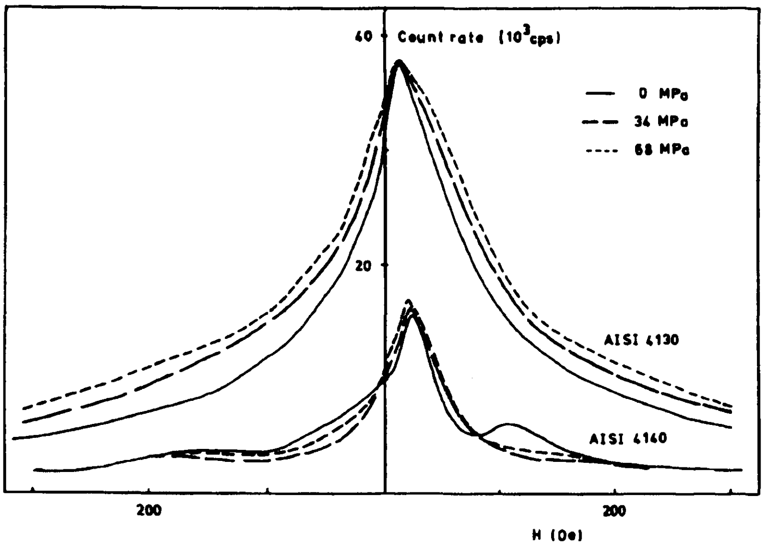

Figure 3.11. Variation of Barkhausen count rate with magnetic field for AISI4130 and4140 steels. The field was swept from -500 Oe to +500 Oe at a rate of 50 Oe per second [3.19]

In 1993, Chen et al [3.20] compared Barkhausen noise with magnetic hysteresis as a method for detecting fatigue damage. With the hysteresis method, no significant changes could be seen until the final 10-20% of the fatigue life. It was found that the Barkhausen noise method could be used to monitor fatigue damage throughout the lifetime of the material.

Jiles and Suomien [3.21] developed a model theory and calculated the effects of stress on the Barkhausen signal amplitude. Results were presented on Barkhausen measurements taken from surface modified materials and X-ray diffraction data from the same specimens. A decrease in Barkhausen signal envelope amplitude with compressive stress in the surface of the material was found.

Yasumitsu et al [3.22] studied NDT estimation of fatigue damage for mild steel by Barkhausen noise analysis. The Barkhausen noise signal was measured for each increment of tensile load during static test and for each interval of cyclic loading during fatigue test. They found that when the applied stress range is below the fatigue limit, the Barkhausen noise signal keeps nearly constant. When the applied stress range is above the fatigue limits, the ratio of Barkhausen noise peak voltage varied clearly with loading cycles. They have also proposed a procedure of residual life prediction.

A large number of investigations on Barkhausen noise are also being carried out in the Indira Gandhi Centre for Atomic Research in India [3.23, 3.24, 3.25, 3.26]. Here, the acoustic signals of Barkhausen noise measurements were found to be useful in the estimation of residual stress in carbon steel weld pads. The root mean square voltage of the acoustic Barkhausen noise signal has been used and it was reported that an increase in rms voltage of the signal corresponds to a decrease in the residual stress.

Zergoug et al [3.27] used NDT technique to characterise the region submitted to thermal processing. Steel samples were heated at temperature between 650°C and 1200°C with variable parameters (time processing, maintenance time, etc.) and Barkhausen noise was measured afterwards. It was reported that finer structure or smaller grain sizes increase the density of pinning sites available reducing the domain wall motion and therefore resulting in decreasing Barkhausen noise.

Stefanita et al [3.28] performed a study to differentiate the effects of elastic and plastic deformation on magnetic Barkhausen noise signals. Magnetic Barkhausen noise measurements were made on a number of mild steel plate samples subjected to varying degrees of uniaxial elastic and plastic deformation up to ~40% strain. Elastic strain effects on the Barkhausen noise were determined to be far more significant than plastic strain effects. This conclusion does not agree with the conclusion in [3.22] although the measurement setups were similar. The difference in the result from [3.28] and [3.22] could be due to the sample used, both measured mild steel however the composition of the material differed.

Dhar et al [3.29] made magnetic Barkhausen noise measurements on hot-rolled mild steel samples uniaxially deformed to differing magnitudes of plastic strain, to study dependence of magnetic Barkhausen noise activity on plastic strain. The results indicate an initial increase in magnetic Barkhausen noise energy with increasing plastic strain followed by a decrease at higher plastic deformations. At higher plastic deformations, they reported that the magnetic Barkhausen noise energy was found to be almost independent of plastic strain.

Anglada-Rivera et al [3.30] studied the influence of applied tensile stress and grain size on magnetic Barkhausen noise and hysteresis loops in '1005' commercial steel. They found that the peak amplitude of the Barkhausen voltage increases with applied stress, reaching a maximum value and then beginning to decrease at higher tensile stress (figure 3.12). This behaviour of increase in Barkhausen noise with applied stress was explained as the effect of domain wall dynamics i.e. the combined effect of the magnetic field and applied stress on the domain wall motion. This study also showed that the stress dependence on the magnetic Barkhausen noise voltage and on the magnetic hysteresis loop was influenced by the grain size of the samples. The maximum amplitude of magnetic Barkhausen noise voltage, B_{max} and *db/dt* decrease with grain size. They also reported that magnetic Barkhausen noise could be utilized to evaluate changes in the microstructural and mechanical properties of commercial carbon steels.

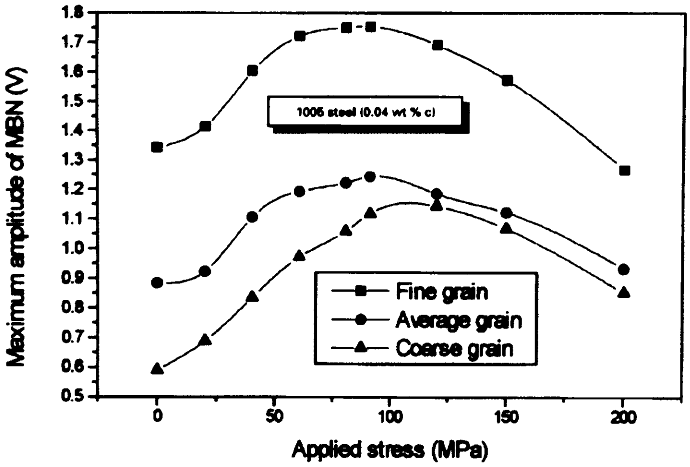

Figure 3.12. Dependence of maximum amplitude of Barkhausen noise (MBN), with applied stress for three different grain sizes (H=2.13 × 10^5 A/m) of 1005 carbon steel [3.30]

Santi et al [3.31] investigated Barkhausen noise studies of Finemet-type materials with several compositions ($Fe_{73.5}Cu_1Nb_3Si_{18.5}B_4$ (B_4), $Fe_{73.5}Cu_1Nb_3Si_{16.5}B_6$ (B_6) and $Fe_{73.5}Cu_1Nb_3Si_{13.5}B_9$ (B_9)). The samples were subjected to a series of annealing temperatures, which allowed establishing different stress levels and microstructures. It was observed that the Barkhausen noise decreased as the temperature increases up to 450°C. Above 450°C, Barkhausen noise value increased.

Kee-Ok Chang et al [3.32] used Barkhausen noise measurement techniques to measure and compare irradiation-induced changes and mechanical properties of a reactor pressure vessel of high copper weld. They confirmed that Barkhausen noise analysis is a viable magnetic parameter based technique that can be used in monitoring the changes in mechanical parameters due to neutron irradiation.

Iordache et al [3.33] investigated the effects of uniaxial tensile stresses approaching and exceeding the macroscopic elastic limit on the magnetic properties of non-oriented Fe 3.2%Si steel sheet. They reported a similar result that was already reported by Culity [3.34] for polycrystalline iron. They also concluded that the experimental results attest the role of the long-range internal stresses on the magnetic properties during strain hardening.

Perez-Benitez et al [3.35] investigated the magnetic Barkhausen noise using elemental signal parameters in '1000' commercial steel. Their results confirmed that the rms of magnetic Barkhausen noise was influenced by the applied tensile stress and grain size in '1000' commercial steel. The Barkhausen noise increased to a maximum value with applied tensile stress but it begins to decrease at higher applied stress. The peak position of the rms Barkhausen noise was shifted towards higher applied tensile stress with grain size.

Desvaux et al [3.36] used the Barkhausen noise method for estimating surface residual stress on the bearings in aeronautic engines. Their method was shown to be rapid, well suited to industrial imperatives connected to on-line measurement and easily adapted to the circular geometries of the bearings rings. In addition, they have shown the efficiency of the Barkhausen noise method for estimating the surface residual stress of bearing raceways after engine operation, in order to perform necessary bearing maintenance.

Some trends were observed where factors such as texture, microstructure, stress and temperature influence the measurement of Barkhausen noise. This can be a significant tool for analyzing physical and microstructural factors in materials but there are challenges in the interpretation of results.

3.4.2. Barkhausen effect studies and steel

Manson and Hoffmann [3.37] studied the frequency spectrum of Barkhausen noise. The frequency spectrum of Barkhausen noise was measured in iron (figure 3.13) and analysed using signal analysis techniques. Their results suggested that the mean duration of the voltage pulses caused by the domain reversals is less than 50 μs and that a domain reversal triggers other domain reversals with a time delay normally of 1 to 2 ms.

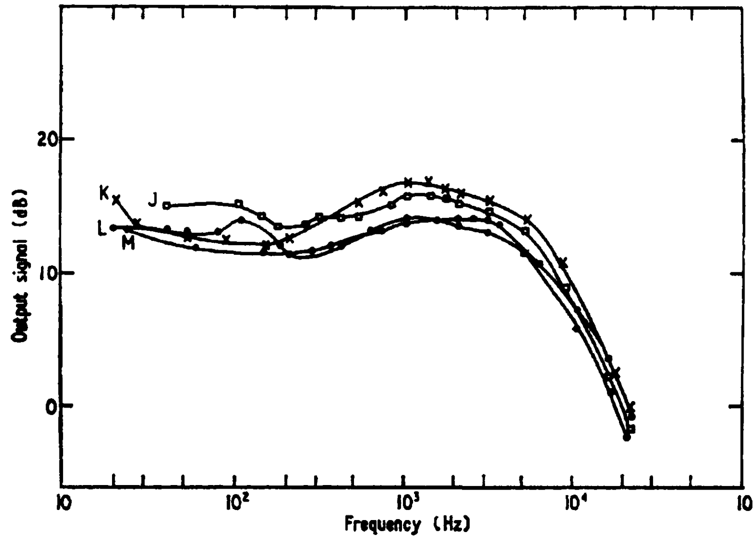

Figure 3.13. Frequency spectra of Barkhausen noise in iron; curve J, at 19 °C ambient temperature, with a peak external magnetic field of 1335 A/m modulated at 2 Hz; curve K, as curve J but with a peak field of 1780 A/m; curve L, as curve J but at 92 °C ambient temperature; curve M, at 134 °C ambient temperature, with peak external field of 1780 A/m and modulated at 3 Hz. The output signal is 0 dB at 100 μV [3.37]

In 1992, Dhar and Atherton [3.38] investigated the influence of the magnetising frequency and ac flux density on the magnetic Barkhausen noise. The measurements were performed on pipeline steel, results have been analysed using pulse-height distribution and rms value of the Barkhausen noise signal. The Barkhausen signal was detected by a coil placed on the surface of the sample with its axis normal to the plane of the sample. The samples were magnetised up to a peak flux density of 1.5 T with a magnetising frequency up to 50 Hz. It was found that with increasing flux density the Barkhausen activity initially increases but finally begins to decrease at higher magnitudes of flux density. Results also demonstrated that the Barkhausen activity increases with increasing magnetising frequency.

Ranjan and Jiles [3.39] studied the effects of grain size and carbon content on the magnetic properties of steel and the results were presented as Barkhausen effect and magnetoacoustic emission. It was shown that the addition of carbon reduces the grain size of the material. They found the rms value of Barkhausen noise increased with increasing grain size. This was because the increased grain size, which therefore reduced carbon content that allowed the domains to move further between pinning sites and thereby generating larger changes in magnetisation thus resulting in a larger Barkhausen noise activity.

Barkhausen emissions were measured to distinguish between pearlitic and bainitic microstructures in AISI4140 steel by Mitra et al [3.40]. It was found that a coarse pearlitic microstructure exhibit a larger number of domain jumps per magnetising cycle, larger rms voltage and larger peak-to-peak voltage. Bainite and spheroidized structures had lower amplitude of Barkhausen emissions due to smaller grain size and the presence of residual stresses associated with rapid cooling.

O'Sullivan et al [3.41] did a similar experiment as Mitra et al but using sample AISI4130 instead. Magnetoacoustic emission and magnetic Barkhausen noise sensing techniques were developed and employed to characterise plastically deformed and heat-treated AISI4130 ferritic stainless steel samples. The results were compared to the mechanical hardness, coercivity and residual stress of the samples. Magnetoacoustic emission and magnetic Barkhausen noise were shown to decrease with increasing permanent material deformation. They found that the inverse of magnetoacoustic emission and magnetic Barkhausen noise are linearly proportional to hardness.

Moorthy et al [3.42] used Barkhausen noise to characterise the microstructure in quenched and tempered 0.2% carbon steel. It was observed that tempering at 873K shows a single peak in Barkhausen noise behaviour after 0.5 hour and a slope change that indicates the development of two-peak behaviour after 1 hour of tempering, and 5 hours of tempering shows clear two-peak behaviour in the Barkhausen noise.

Yamaura et al [3.43] worked on the effect of grain boundary microstructures on the Barkhausen noise associated with dynamic interaction between grain boundaries and magnetic domains. The Barkhausen noise was found to be strongly dependent on the grain size in pure iron polycrystals. They also suggested a new numerical parameter related to the shape of the Barkhausen noise spectrum by taking into consideration the contribution of the grain boundary to the Barkhausen noise.

Blachnio et al studied the microstructure of chromium ferritic steel and the Barkhausen noise intensity resulting from cyclic deformation. The non-linear dependence of Barkhausen noise on the number of cycles has been shown [3.44]. The change in Barkhausen noise reflects both the multiplication and rearrangement of dislocations and the formation of vacancies and vacancy aggregates. It was found that both the cell size and dislocation structure and redistribution of vacancies considerably affect the Barkhausen noise intensity

Negley et al [3.45] investigated imaging surface conditions of ferromagnetic steel using Barkhausen technique. The material (AISI4140 CrMo steel) surface conditions such as stress, cracking, oxidation, plastic deformation and pitting produce signal changes, which were visualised through a computer-generated image of the related Barkhausen parameters. They concluded that the determination of the exact amount of fatigue and stress throughout a material using such techniques might be possible.

Many correlations have been observed between Barkhausen noise and material parameters in steels. Thus, indicating that Barkhausen noise is a powerful tool for non-destructive evaluation of magnetic materials.

3.4.3. Barkhausen effect studies and electrical steel

Komatsubara and Porteseil [3.46, 3.47] performed Barkhausen noise power measurements on several types of grain-oriented SiFe sheet. They investigated the influence of the magnetising frequency on the Barkhausen noise power in non-oriented FeSi sheets. They found that the Barkhausen noise per cycle initially decreases with frequency and then increases, seen in figure 3.14. This initial decrease in Barkhausen noise was assumed to be caused by the collapse of the space correlation in the large Barkhausen jumps.

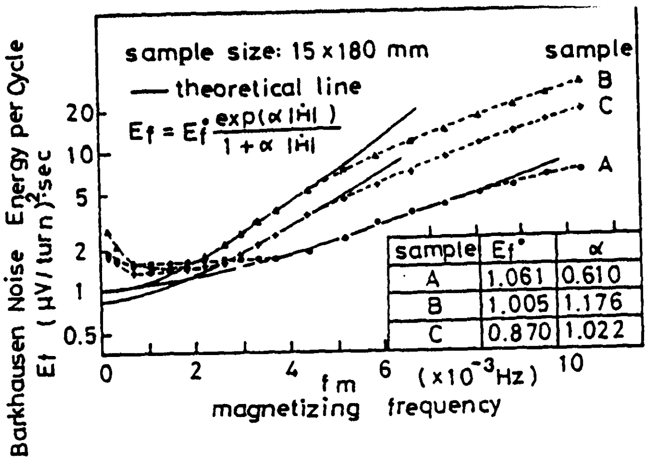

Figure 3.14. Barkhausen noise energy per cycle vs. the frequency of magnetising field; (sample A - 0.23 mm thick, grain-oriented high permeability electrical steel, sample B - 0.3 mm thick, grain-oriented high permeability electrical steel, sample C - 0.29 mm thick, conventional grain-oriented) [3.47]

Birsan and co-workers [3.48] presented results on Barkhausen power in grain-oriented 3% silicon iron samples of different quality. They found that the measurements indicated a strong correlation between the Barkhausen power and the total power losses. The magnetising frequency was 12 Hz. The Barkhausen noise was captured with a sampling rate of 500 kHz over 16 ms with a resolution of 8 bit [3.49]. The total power losses of the samples were determined by the Epstein frame method. The result showed that the Barkhausen noise power is highest for the sample with the smallest power loss.

Augustyniak et al [3.50] investigated magnetic and magnetomechanical hysteresis properties of FeSi alloys from classical and mechanical Barkhausen effects and magnetoacoustic emission. They found that the multiparameter analysis of magnetomechanical properties of grain-oriented and non-oriented FeSi revealed that the magnetoacoustic emission maxima correlated well with H strength values. At which creation and annihilation of magnetic domains is assumed to appear, this can be attributed to 90° domain wall activity. They further concluded that effects such as the Barkhausen effect, magnetoacoustic emission and magnetomechanical hysteresis with mechanical Barkhausen effect are well correlated via internal stress barriers pinning domain walls.

Lobanov et al [3.51] investigate the relation between the grain size and the intermediate stage of manufacturing electrical steel; using various techniques including the Barkhausen effect method. They concluded that when estimating parameters of grains in steels and alloys, there arise certain difficulties associated with the fact that, in addition to the grain size, many other diverse effects existing in the body of the grain itself can significantly affect the electromagnetic characteristics of the Barkhausen effect. Therefore, the reliability of determining the grain sizes by the means of the Barkhausen effect depends also on the thorough consideration of the other interfering factors.

In 2004, Gündel et al [3.52] investigated Barkhausen noise measurements on non-oriented electrical steel used in low power motors for home appliances. The rms Barkhausen noise measurement was obtained as a function of the induction. Their result showed that Barkhausen noise is present in almost all parts of the hysteresis loop, including the high induction level.

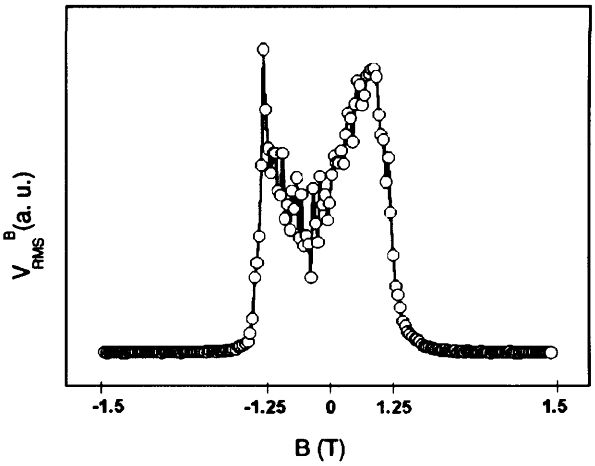

Figure 3.15. RMS Barkhausen noise voltage as a function of induction. Showing that Barkhausen noise is present in all parts of the hysteresis loop, including high induction regions [3.52]

Moses et al [3.53] investigated the correlation between angular dependence of ac Barkhausen noise and hysteresis loss in non-oriented electrical steel. Electrical steel strips cut at various angles to the rolling direction were measured. They found a correlation between Barkhausen noise and the high and low induction fraction of quasi-static hysteresis loss in non-oriented electrical steel (figure 3.16). They showed the influence of anisotropy of inter-inclusion distances on the angular dependence of loss in non-oriented steel (figure 3.17). They also noted a frequency dependence of the Barkhausen noise activity, which was probably due to the macroscopic activity that contributes to the excess loss component.

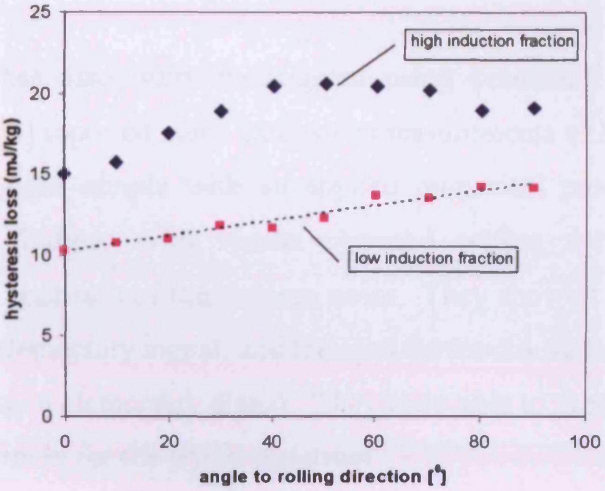

Figure 3.16. Variation high and low induction with hysteresis loss against angle to the rolling direction, with non-oriented electrical steel, at magnetising frequency of 50 Hz [3.53]

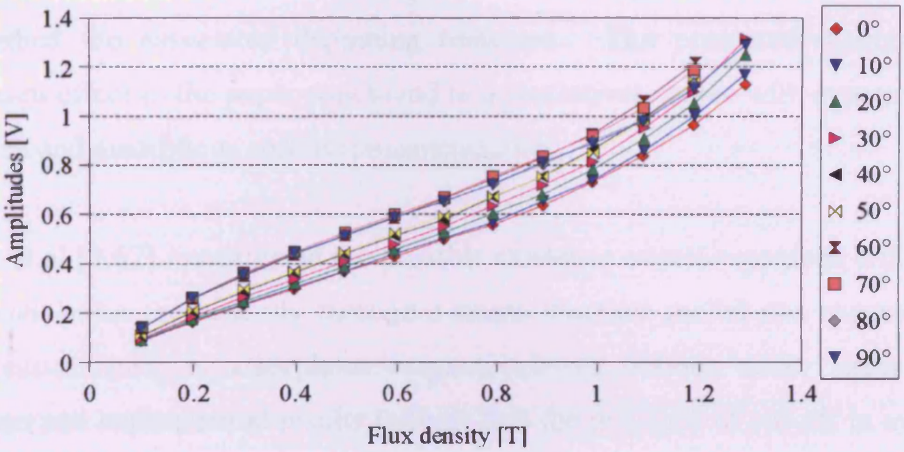

Figure 3.17. Variation of total sum of amplitudes of Barkhausen noise with peak flux density, at 50 Hz in non-oriented electrical steel cut at 0° to 90° to the rolling direction [3.53]

3.4.4. Barkhausen effect studies and domain modelling

Durin and Zapperi [3.54] conducted many studies to quantitatively understand the Barkhausen effect [3.54, 3.55, 3.56, 3.57]. Durin et al [3.55] updated their previous debate [3.54] on connection between the Barkhausen effect and non-equilibrium critical phenomena and self-organized criticality. They have again concluded that models based on the dynamics of a flexible domain wall are the most successful in explaining the experimental data. They later investigated the complex dynamics of magnetic domain walls [3.58, 3.59]. In this paper, they compared theoretical and experimental results, which point towards a deeper comprehension of the complex dynamics of magnetic domain walls (Barkhausen noise).

Barkhausen noise has also been investigated using predicted theoretical models. Spasojevic et al [3.60] reported some extensive measurements of Barkhausen noise in commercial metal glass sample with an applied numerical procedure. They then compared all the findings with results obtained within the experimental and theoretical research approach of Barkhausen noise. They showed a generic shape of a single Barkhausen elementary signal, and they put forward a mathematical expression for a single Barkhausen elementary signal. They were able to predict scaling relations and an elaborate formula for the power spectrum.

Cizeau et al [3.61] derived an equation of motion for the dynamics of ferromagnetic domain walls driven by an external magnetic field through a disordered medium, and they studied the associated depinning transition. The presented theory for the Barkhausen effect in the paper was found to quantitatively agree with experiments on crystalline and amorphous soft ferromagnetic alloys.

Babiana et al [3.62] investigated the possible existence of self-organized criticality in Barkhausen noise theoretically through a single interface model and experimentally from measurements in amorphous magnetostrictive ribbons under stress. Both simulation and experimental results indicate that the presence of cut-off in avalanche size distribution may be attributed to finite-size effects.

Many models have been developed to understand the Barkhausen effect, and many have been found to be successful in modelling Barkhausen noise. However, due to the complex nature of Barkhausen noise, and its sensitivity to the microstructure of the material it is increasingly difficult to theoretically model this behaviour.

3.4.5. Barkhausen effect studies and measurement systems

De Wulf and Melkebeek [3.63] investigated the advantages and drawbacks of using digital acquisition systems for the determination of magnetic properties of electrical steel sheet and strip. The main point that was discussed in this paper is the importance of phase accuracy and interchannel delay compensation when using LabVIEW virtual instruments. A measuring set-up based on a data acquisition card should be programmed carefully and aspects such as non-simultaneous sampling and bit resolution can have considerable consequences on the obtained result.

Zhu et al [3.2] built a computer-controlled system for making Barkhausen emission measurements on materials based on the previously developed Magneprobe system [3.50]. A block diagram of the system can be seen in figure 3.18. The system can be used to sample Barkhausen noise signals at a rate of up to 5 MHz with a voltage resolution of 1.2 mV (14 bit, 5 V full scale). The entire system is operated under computer control, which generated a triangular magnetising waveform at 2 Hz. The multifunctional system provides the capability for analysing Barkhausen emission measurements a variety of ways e.g. standard deviation, rms, fast Fourier transform (FFT), power spectral density (PSD) and pulse height distribution (PHD). The measurements can be made easily and rapidly through the use of system software. The various inspection procedures contained in the software make the system very flexible and since they are in software, new procedures can be easily added, allowing evolution of the instrument to meet new needs.

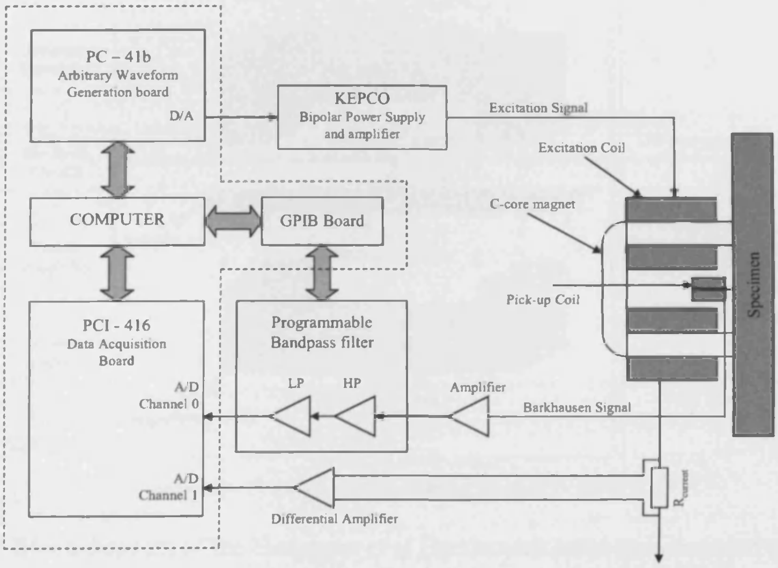

Figure 3.18. Block diagram of the Zhu et al Barkhausen noise measurement system [3.2]

Hartmann et al [3.64] designed and built a measurement system for determining ac Barkhausen noise in electrical steels. Figure 3.19 shows a block diagram of the system. This system was able to carry out Barkhausen noise investigations at magnetising frequencies up to 75 Hz. The feedback circuit ensured that the time variation of flux density was sinusoidal with a form factor better than 1.11 ±3% over the measurement range. For non-oriented electrical steel, a flux density not exceeding 1.2T was achieved. Two 80 turns search coils connected in series opposition and wound around a plastic carrier slid over the sample provided a differential signal feed to a NI 4552 AD card with a resolution of 16 bit, sample rate of 204 kHz and 95 kHz bandwidth. Having the search coils in series opposition meant that the voltage fed back to the PC mainly comprised of the Barkhausen noise component, which is partly decreased due to the separation (~1 cm) of the coils. Digital signal processing was carried out with National Instruments software package LabVIEW. This meant that the Barkhausen noise signal could be analysed in various manners e.g. rms, standard deviation, kurtosis, total sum of amplitudes, total number of points and power spectrum. In this paper, it was also found that Barkhausen noise was greater in non-oriented electrical steel than grain-oriented due to non-oriented electrical steel having smaller grain size.

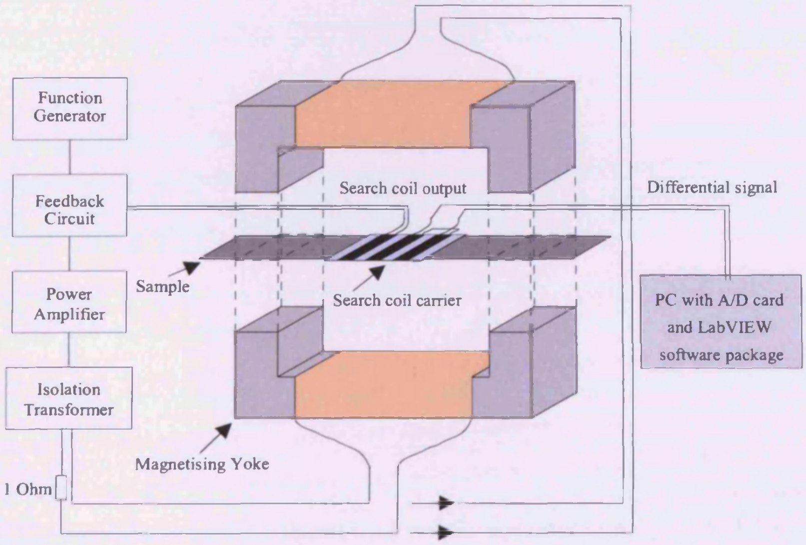

Figure 3.19. Block diagram of the Hartmann et al Barkhausen noise measurement system [3.64]

Pal'a et al [3.65] investigated the influence of magnetising frequency and construction of pick-up coil on Barkhausen noise. Different arrangements of pick-up coils were investigated on several deformed low carbon steels at several magnetising frequencies. It was concluded that when using a surface pick-up coil to measure Barkhausen noise a high initial permeability core should be used (the surface sensor is described in more detail in chapter 4). Also, the number of Barkhausen jumps per unit time increases with magnetising frequency and therefore raising the maximum value of the power spectrum.

The Zhu et al [3.2] and Hartmann et al [3.64] Barkhausen noise systems were both used as reference in designing the new Barkhausen noise measurement system in this study. Issues raised by De Wulf and Melkebeek [3.63] with digital methods were taken into account when designing the system. In addition, when designing a surface sensor a high initial permeability material was selected.

References to chapter 3

[3.1] H. Barkhausen, “Zwei mit Hilfe der neuen Verstärker entdeckte Erscheinugen”, Physik Z. 20, 401-403, 1919

[3.2] B. Zhu, M. J. Johnson, C. C. H. Lo, D. C. Jiles, “Multifunctional magnetic Barkhausen emission measurement system”, IEEE Transactions on Magnetics, Vol 37, No 3, 1095, 2001

[3.3] D. C. Jiles, “Introduction to magnetism and magnetic materials”, Chapman & Hall, London, 1991

[3.4] H. Bittel, “Noise of ferromagnetic materials”, IEEE Transactions on Magnetics, Vol 5, No 3, 1969

[3.5] G. V. Lomaev, S. V. Malyshev, A. P. Degterev, “Use of Barkhausen effect for non destructive testing (review)”, Sov. Journal Non-destructive Testing, 20, 189, 1984

[3.6] M. Kersten, “Grundlagen einer theorie der ferromagnetischen hysterese und der koerzitivkraft”, Physik Z, Vol 44, 63-77, 1943

[3.7] L. Ceniga, L. Novak, E. Kisdi-Koszo, “The influence of heat treatment on the Barkhausen effect in the Fe-Cr-B amorphous alloy”, Journal Magnetism and Magnetic Material, 196-197, 154-155, 1999

[3.8] V. Moorthy, B. A. Shaw, P. Hopkins, “Surface and sub-surface stress evaluation in case-carburised steel using high and low frequency magnetic Barkhausen emission measurements”, Journal Magnetism and Magnetic Material, 299, 362-375, 1999

[3.9] V. Moorthy, B. A. Shaw, P. Mountford, P. Hopkins, “Magnetic Barkhausen emission technique for evaluation of residual stress alteration by grinding in case-carburised En36 steel”, Acta Materialia, Vol 53, 4997-5006, 2006

[3.10] D. J. Craik, R. S. Tebble, “Ferromagnetism and ferromagnetic domains”, Amsterdam: North-Holland Publishing Co., 1965

[3.11] H. D. Bush, R. S. Tebble, “The Barkhausen effect”, Proceedings Physical Society, 60, 370, 1948

[3.12] R. Tebble, S. Skindmore, L. Corner, “The Barkhausen effect”, Proceedings Physical Society, A63, 739, 1950

[3.13] E. Stoner, “The analysis of magnetisation curve”, Reviews of Modern Physics, Vol 25, Issue 1, 2, 1953

[3.14] C. G. Gardner, G. A. Matzkanin, D. L. Davidson, “The influence of mechanical stress on magnetisation processes and Barkhausen jumps in ferromagnetic material”, Journal of Non-destructive Testing, Vol 3, 131, 1971

[3.15] S. Tiitto, "On the influence of microstructure on magnetisation transitions in steel", Applied Physics Series No 119, 1, 1977

[3.16] O. Sundström, K. Törrönen, "The use of Barkhausen noise analysis in non-destructive testing", Materials Evaluation, 51, 1979

[3.17] L. P. Karjalainen, M. Moilanen, R. Rautioaho, "Influence of tensile and cyclic loading upon Barkhausen noise in a mild steel", Materials Evaluation, Vol 37, 45, 1979

[3.18] E. Puppin, M. Zani, D. Vallaro, A. Venturi, "A double coil apparatus for Barkhausen noise measurements", Review of science instruments, Vol 72, No 4, 2001

[3.19] D. C. Jiles, "The effect of stress on magnetic Barkhausen activity in ferromagnetic steels", IEEE Transactions on Magnetics, Vol 25, No 5, 1989

[3.20] Z. J. Chen, A. Strom, D. C. Jiles, "Micromagnetic surface measurements for evaluation of surface modifications due to cyclic stress", IEEE Transactions on Magnetics, Vol 29, No 6, 1993

[3.21] D. C. Jiles, L Suomien, "Effects of surface stress on Barkhausen effect emission: model predictions and comparison with X-ray diffraction studies", IEEE Transaction on Magnetics, Vol 30, No 6, 1994

[3.22] Y. Tomita, Kiyoshi, Hashimoto, N. Osawa, "Non-destructive estimation of fatigue damage for steel by Barkhausen noise analysis", NDT&E International, Vol 29, No 5, 275-280, 1996

[3.23] P. Rodriquez, B. Raj, "Development of in-service inspection techniques for nuclear power plants in India", International Journal Pres Ves & Piping 73, 59-68, 1997

[3.24] V. Moorthy, B. K. Choudhary, S. Vaidyanathan, T. Jayakumar, K. B. S. Rao, B. Raj, "An assessment of low cycle fatigue damage using magnetic Barkhausen emission in 9Cr-1Mo ferritic steel", International Journal of Fatigue, Vol 21, No. 3, 263-269, 1999

[3.25] D. K. Bhattacharya, S. Vaidyanathan, "Effect of the demagnetisation factor on the Barkhausen noise signal", Journal of Magnetism and Magnetic Materials, Vol 166, 1-2, 111-116, 1997

[3.26] V. Moorthy, B. A. Shaw, K. Brimble, I. Atkins, "Evaluation of Heat treatment and Deformation Induced Changes in Material", 3rd International Conference on Barkhausen Noise and Micromagnetic Testing, 2001

[3.27] M. Zergoug, N. Boucherrou, A. Haddad, A. Benchaala, B. Moulti, H. Tahraoui, F. Sellidj, A. Hammouda, "Thermally affected characterisation region by Barkhausen noise", Ultrasonics 37, 703-707, 2000

[3.28] C. G. Stefanita, D. L. Atherton, L. Clapham, "Plastic versus elastic deformation effects on magnetic Barkhausen noise in steel", Acta Materialia 48, 3545-3551, 2000

[3.29] A. Dhar, L. Clapham, D. L. Atherton, "Influence of uniaxial plastic deformation on magnetic Barkhausen noise in steel", NDT&E International, Vol 34, 507-514, 2001

[3.30] J. Anglada-Rivera, L. R. Padovese, J. Capo-Sanchez, "Magnetic Barkhausen noise and hysteresis loop in commercial carbon steel: influence of applied tensile stress and grain size", Journal of Magnetism and Magnetic Materials, 231, 299-306, 2001

[3.31] L. Santi, A. D. C. Viegas, A. M. H. de Andrade, R. L. Sommer, R. Grossinger, R. Sato Turtelli, "Barkhausen noise measurements in Finemet type materials", Journal Magnetism and Magnetic Materials, 226-230, 1484-1486, 2001

[3.32] Kee-Ok Chang, Se-Hwan Chi, Kwon-Jae Choi, Byeong-Chul Kim, Sam-Lai Lee, "Changes in magnetic parameters of neutron irradiated RPV Linde80 high copper weld surveillance specimens", International Journal of Pressure Vessels and Piping 79, 753-757, 2002

[3.33] V. E. Iordache, F. Ossart, E. Hug, "Magnetic characterisation of elastically and plastically tensile strained non-oriented Fe 3.2%Si steel", Journal of Magnetism and Magnetic Materials, 254-255, 57-59, 2003

[3.34] B. D. Cullity, "Introduction to magnetic materials", Addison-Wesley, London, 1972

[3.35] J. A. Perez-Benitez, L. R. Padovese, J. Capo-Sanchez, J. Anglada-Rivera, "Investigation of the magnetic Barkhausen noise using elementary signals parameters in 1000 commercial steel", Journal of Magnetism and Magnetic Materials, 263, 72-77, 2003

[3.36] S. Desvaux, M. Duquennoy, J. Gualandri, M. Ourak, "The evaluation of surface residual stress in aeronautic bearings using the Barkhausen noise effect", NDT & E International, Vol 37, 9, 2004

[3.37] G. Manson, G. Hoffmann de Visme, "The frequency spectrum of Barkhausen noise", Journal of Applied Physics, Vol 5, 1389, 1972

[3.38] A. Dhar, D. L. Atherton, "Influence of magnetising parameters on the magnetic Barkhausen noise", IEEE Transactions on Magnetics, Vol 28, No 6, 3363-3366, 1992

[3.39] R. Ranjan, D. C. Jiles, "Magnetic properties of decarburized steels: An investigation of the effects of grain size and carbon content", IEEE Transactions on Magnetics, Vol 23, No 3, 1987

[3.40] A. Mitra, M. R. Govindaraju, D. C. Jiles, "Influence of microstructure on micromagnetic Barkhausen emissions in AISI 4140 steel", IEEE Transactions on Magnetics, Vol 31, No 6, 1995

[3.41] D. O'Sullivan, M. Cotterell, D. A. Tanner, I. Mészáros, "Characterisation of ferritic stainless steel by Barkhausen techniques", NDT & International 37, 489-496, 2004

[3.42] V. Moorthy, S. Vaidyanathan, T. Jayakumar, B. Raj, "Microstructural characterisation of quenched and tempered 0.2% carbon steel using magnetic Barkhausen noise analysis", Journal of Magnetism and Magnetic Materials, 171, 179-189, 1997

[3.43] S. Yamaura, Y. Furuya, T. Watanabe, "The effect of grain boundary microstructure on Barkhausen noise in ferromagnetic materials", Acta Materialia Inc 49, 3019-3027, 2001

[3.44] J. Blachnio, J. Dtkiewicz, A. Salamon, "The effect of cyclic deformation in a 13% Cr ferritic steel and structure and Barkhausen noise level", Material Science and Engineering A323, 83-90, 2002

[3.45] M. A. Negley, D. C. Jiles, "Imaging surface conditions of ferromagnetic steel using Barkhausen technique", IEEE Transactions on Magnetics, Vol 30, No 6, 4509-4511, 1994

[3.46] M. Komatsubara, J. L. Porteseil, "Influence of the magnetising frequency on the Barkhausen noise power of non-oriented Si-steel sheets", Journal de Physique, Vol 46, C6-173, 1985

[3.47] M. Komatsubara, J. L. Porteseil, "Barkhausen noise behaviour in grain oriented 3%Si-Fe and the effect of local strain", IEEE Transactions on Magnetics, Vol 22, 496-498, 1986

[3.48] M. Birsan and J. A. Szpunar, "Correlation between the Barkhausen noise power and the total power losses in 3% Si-Fe", Journal of Applied Physics, Vol 79 (8), 6042, 1996

[3.49] T. W. Krause, L. Clapham, D. L. Atherton, "Characterisation of the magnetic easy axis in pipeline steel using magnetic Barkhausen noise", Journal of Applied Physics, Vol 75 (12), 7983, 1994

[3.50] A. Mitra, L. B. Sipahi, M. R. Govindaraju, D. C. Jiles, "Effects of magnetoelastic anisotropy on hysteresis and Barkhausen emissions in amorphous metals", Journal of Magnetism and Magnetic Materials, Vol 153, 231, 1995

[3.51] M. L. Lobanov, I. P. Sysolyatina, V. K. Christyakov, Yu. L. Gobov, E. S. Gorkunov, S. M. Zadvorkin, G. S. Korzunin, A. G. Lavrent'ev, D. V. Perov, A. B. Rinkevich, V. A. Sandovskii, "On possibility of non-destructive testing of the grain size in the intermediate stages of manufacturing electrical steel", Russian Journal of Non-destructive Testing, Vol 39, No 8, 2003

[3.52] A. Gündel, A. M. Severino, F. J. G. Landgraf, R. L. Sommer, "Barkhausen noise and high induction losses in non-oriented electrical steel", Journal of Magnetism and Magnetic Materials, 272-276, 561-562, 2004

[3.53] A. J. Moses, F. J. G. Landgraf, K. Hartmann, T. Yonamine, "Correlation between angular dependence of A.C. Barkhausen noise and hysteresis loss in non-orientated electrical steel", Stahleisin Dusseldorf, 215-219, 2004

[3.54] G. Durin, S. Zapperi, "An introduction to the Barkhausen effect", Atti della III scuola brasiliana di magnetismo EBM2001, Porto Alegre (Brasile), 2001

[3.55] G. Durin, S. Zapperi, "On the power spectrum of magnetisation noise", Journal Magnetism and Magnetic Material, 242-245, 1085-1088, 2002

[3.56] G. Durin, S. Zapperi, "Barkhausen noise in soft amorphous magnetic materials under applied stress", Journal of Applied Physics, Vol 85 (8), 5196, 1999

[3.57] S. Zapperi, G. Durin, "New perspectives for the Barkhausen effect", Computational Materials Science 20, 436-442, 2001

[3.58] G. Durin, S. Zapperi, "Barkhausen noise in soft amorphous magnetic materials under applied stress", Journal of Applied Physics, Vol 85, No 8, 5196-5198, 1999

[3.59] G. Durin, S. Zapperi, "Complex dynamics of magnetic domain walls", Physica A 314, 230-243, 2002

[3.60] D. Spasojevic, S. Bukvic, S. Milosevic, H. E. Stanley, "Barkhausen noise: Elementary signals, power laws, and scaling relations", Physical Review E, Vol 54, No 3, 1996

[3.61] P. Cizeau, S. Zapperi, G. Durin, H. G. Stanley, "Dynamics of a ferromagnetic domain wall and the Barkhausen effect", Physics Review letters, Vol 79, No 23, 1997

[3.62] M. Babiana, B. Koiller, A. L. A. de Queiroz, J. C. Denardin, R. L. Sommer, "Domain size effects in Barkhausen noise", Physical Review E, Vol 59, No 4, 1999

[3.63] M. De Wulf, J. Melkebeek, "On the advantage and drawbacks of using digital acquisition systems for the determination of magnetic properties of electrical steel sheet and strip", Journal of Magnetism and Magnetic Materials 196-197, 940-942, 1999

[3.64] K. Hartmann, A. J. Moses, T. Meydan, "A system for measurement of AC Barkhausen noise in electrical steels", Journal of Magnetism and Magnetic Materials 254-255, 318-320, 2003

[3.65] J. Pal'a, J. Bydžovský, P. Švec, "Influence of magnetising frequency and construction of pick-up coil on Barkhausen noise", Journal of Electrical Engineering, Vol 55, No10/S, 38-40, 2004

CHAPTER 4

DESIGN & DEVELOPMENT OF THE BARKHAUSEN NOISE MEASUREMENT SYSTEM

4.1. Introduction

The purpose of Barkhausen noise measurements is to obtain a better understanding of the phenomenon, which component of power loss the Barkhausen noise is related to and how the Barkhausen noise varies with different measurement conditions. The aim of this investigation is to identify a relationship between Barkhausen noise and the hysteresis component of total power loss. Standard measurements are carried out under sinusoidal magnetic induction however, the measurement system developed in this work can also magnetise samples with triangular, trapezoidal and arbitrary waveform conditions.

Barkhausen noise in strips, 300 mm long × 30 mm wide, of grain-oriented 3%SiFe electrical steel cut at 0°, 55°, 90° to the rolling direction, and non-oriented 0.2%, 0.3%, 1.3%, 1.8%, 3%, 5.5%, 6.5% SiFe electrical steel, was measured over a magnetising frequency range of 5 Hz - 100 Hz at sinusoidal flux densities from 0.1 T to 1.8 T.

In addition, an ancillary study was conducted on cold-rolled low carbon steel with 0-40% rolling reduction, of charpy, plate and picture frame shapes. Also, thermally aged iron copper with different ageing times (0-5000 minutes), of charpy and ring shape was investigated.

4.2. Flux density sensor

The spatial average change in flux density can be detected by means of a search coil also known as a "B-coil" or "pick-up coil". A voltage in induced across a coil surrounding a sample proportional to the rate of change of internal flux density. The law that relates flux density and instantaneous induced voltage, v, is [4.1]:

$$v = -N_B \cdot A_B \cdot \frac{dB}{dt} \qquad [\mathrm{V}] \qquad (4.1)$$

where, N_B - number of turns of the coil; A_B - cross sectional area of the coil; dB/dt - rate of change of flux density with respect to time

The flux density can be calculated by integrating the voltage induced in the coil:

$$B = -\frac{1}{N_B \cdot A_B} \cdot \int v_B \; dt \qquad [\mathrm{T}] \qquad (4.2)$$

In this investigation, a B-coil was wound on a 1 mm thick plastic former that slides over the sample. The coil has 80 turns, wound with 0.06 mm diameter enamelled copper wire. The coil was wound as uniformly as possible. Once the coil winding was complete, araldite was poured over it to protect against wear. For the charpy and plate samples in the ancillary study, an 80 turn, 0.06 mm diameter enamelled copper wire B-coil was wound directly on to the sample. B-coils with 90 and 180 turns of 0.1 mm diameter enamelled copper wire were wound on the ring and picture frame samples respectively.

4.3. Magnetic field sensor

The tangential component of surface magnetic field strength, H, on a sample can be determined by using an H-coil sensor. The magnetic field strength can be determined from the voltage induced in a coil, which is uniformly wound around a non-magnetic former. The former needs to be very thin so the sensor can be as close as possible to the surface of the sample under test. When using an H-coil, it is assumed that the tangential component of the magnetic field strength close to the surface is the same as that just inside the sample. Figure 4.1 shows a typical H-coil placed on the surface of a strip of steel.

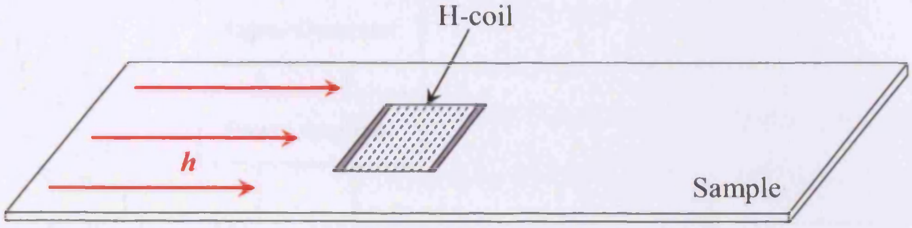

Figure 4.1. H-coil placed on the surface of a strip of steel

A 0.1 mm thick × 20 mm wide glass former was wound with a 500 turn coil of 0.03 mm diameter enamelled copper wire. The instantaneous tangential component of the magnetic field strength, H, was calculated from:

$$H = -\frac{1}{\mu_0 \cdot N_H \cdot A_H} \cdot \int v_H \quad dt \qquad [\text{A/m}] \qquad (4.3)$$

where, μ_o - permeability of free space; A_H - cross sectional area of the H-coil; N_H - number of turns of the H-coil; v_H - instantaneous voltage induced in the H-coil

Before any measurement was taken, the H-coil was calibrated. A known magnetic field strength, H_{cc}, was generated along the axis of a long solenoid, when a current, i_c, was passed through its winding. The uniform magnetic field, H_{cc}, at its centre, was calculated with the following equation [4.1]:

$$H_{cc} = \frac{N_c \cdot i_c}{L_c} \qquad (4.4)$$

where, N_c - the number of turns of the solenoid; L_c - the length of the solenoid

A schematic diagram of the calibration system is shown in figure 4.2. Where the signal generator connected to a power amplifier applies a current to the solenoid, which creates a field along its axis. The H-coil is placed at the centre of the solenoid, with the coil placed at 90° to the field. By using the shunt resistor, the current applied to the solenoid is measured. By using eq. 4.4 the field applied is calculated, and the H-coil voltage is measured using the DAQ card at the same time. A linear relationship exists between both signals and a calibration factor is calculated.

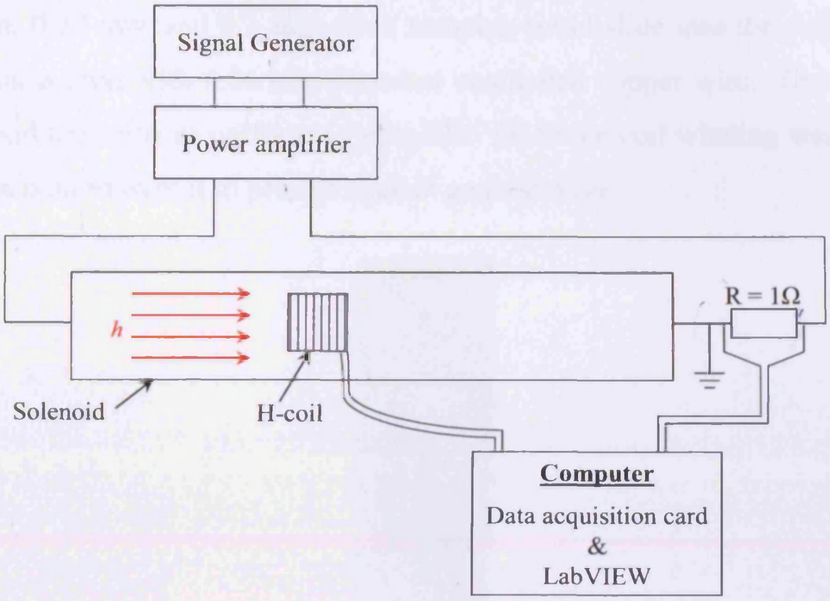

Figure 4.2. H-coil calibration system

The H-coil was calibrated over a frequency range from 25 to 100 Hz and a peak magnetic field range from 100 to 3000 A/m. The voltage measured from the H-coil was integrated so that the values given in the program are directly proportional to the peak instantaneous applied magnetic field strength.

The calibration constant was calculated at each frequency and the average calibration constant, N·A, for the H-coil was found to be 0.00589 m^2. This value was used to calculate the magnetic field strength for all experiments in this investigation.

4.4. Barkhausen noise sensors

Various types of sensors can be used to measure Barkhausen noise, in this investigation three main types of sensors described below were investigated.

4.4.1. Single coil Barkhausen sensor

Barkhausen noise can be measured using a single flux-sensing coil [4.2]. A single coil Barkhausen sensor (figure 4.3) was wound on a former made from plastic. The plastic former is 1 mm thick and slides over the sample. Three formers of dimensions 30 mm wide by 15 mm length with three spacing thicknesses were designed so that the 0.5 mm, 0.27 mm and 0.1 mm thick samples could slide into the coil. The coil had 80 turns wound with 0.06 mm diameter enamelled copper wire. Great care was taken to wind the turns as uniform as possible. Once the coil winding was complete, araldite was poured over it to protect against general wear.

Figure 4.3. Single coil Barkhausen noise sensor

4.4.2. *Double coil Barkhausen sensor*

When a single coil Barkhausen noise sensor is used for ac magnetisation, the frequency component (i.e. flux density) swamps most of the Barkhausen noise information. A better approach is to use two detection coils connected in series opposition [4.3]. Such an arrangement cancels out the predominant Faraday emf and the remaining Barkhausen noise component is then detected using a higher resolution range of the data acquisition (DAQ) card. Apart from improved voltage resolution, the double flux-sensing coil also effectively senses a greater volume of sample, which may lead to differences in Barkhausen noise compared to the single coil method. The double coil Barkhausen sensor (figure 4.4) was wound on a plastic former, with the same dimensions as the single coil sensor.

Figure 4.4. Double coil Barkhausen noise sensor

Two 80 turn coils each wound with 0.06 mm enamelled copper wire, separated by a distance of 5 mm between the adjacent ends, were wound on the former. The Barkhausen noise component is only partially cancelled out since each coil picks up a slightly different Barkhausen contribution, discussed in more detail in chapter 4.12.1.

4.4.3. Surface Barkhausen sensor

The surface Barkhausen noise sensor measures the Barkhausen noise component perpendicular to the sample surface unlike the previous two search coil sensors that measure the in-plane component of the sample. The sensor components supplied by Stresstech Oy comprised three pieces of 3 mm diameter (type 3B1) ferrite (figure 4.5) of lengths 10.0, 12.9 and 24.7 mm, and two bobbins with 1000 and 500 turns of 0.06 mm enamelled copper wire. The dimensions of the bobbins are shown in figure 4.6.

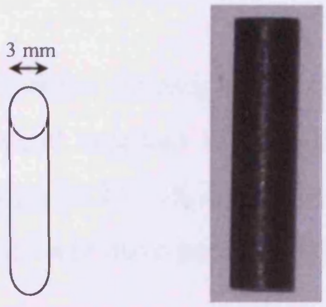

Figure 4.5. Ferrite core for surface Barkhausen noise sensor

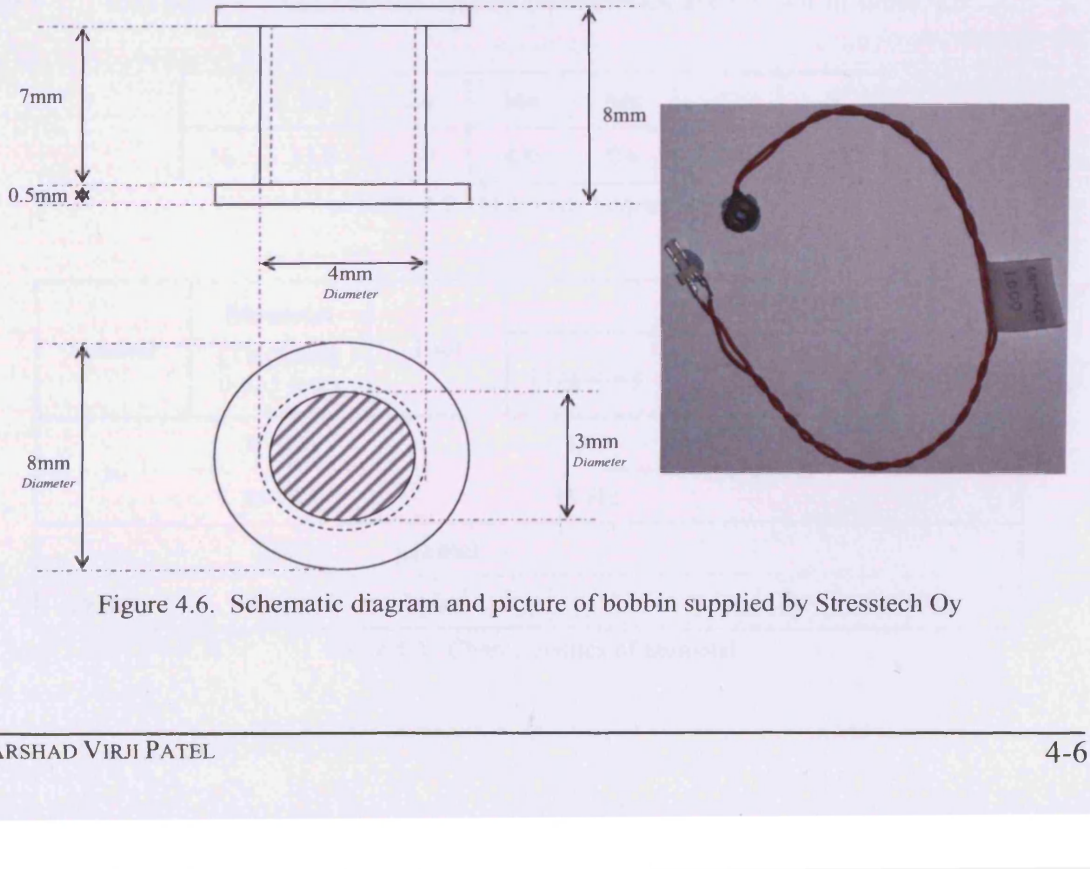

Figure 4.6. Schematic diagram and picture of bobbin supplied by Stresstech Oy

The ferrite is inserted inside the bobbin to magnetically amplify the low voltage Barkhausen noise signal. The ferrite amplifies the magnetic flux density inside the bobbin by a factor directly proportional to the ferrite's relative permeability (using Eq. 2.2) [4.1]. The relative permeability, μ_r, of the ferrite core is 900 (table 4.1), therefore, the magnetic flux density is amplified 900 times.

Symbol	**Ferrite Type 3B1**	**Unit**	**CONDITIONS**		
			Frequency	Induction/field strength	Temperature
μ_r	900 ± 20%		≤ 10 kHz	0.1 mT	25 °C
B_{peak}	330	mT	10 kHz	250 A/m	25 °C
	200				100 °C
ρ	0.2	Ωm	DC		25 °C
Density	4800	kg/m^3			25 °C

Table 4.1. Characteristics of ferrite 3B1

Other potential core materials were investigated. These were a pure iron rod produced by arc melting, mumetal supplied by Carpenter Technology Corporation and nano-crystalline samples supplied by MK Magnetics. The iron rod was 10.8 mm long by 2 mm in diameter and had a relative permeability of ~2000 [4.1].

The mumetal sample composition is shown in table 4.2. It was 10 mm long with a 2.5 mm × 2.5 mm square cross section. Its characteristics are shown in table 4.3.

	Fe	Cu	Mo	Mn	C	S
%	13.8	5.0	4.0	0.6	0.010	0.002

Table 4.2. Mumetal composition

Symbol	**Mumetal** (Thickness 0.635 mm)	**Unit**	**CONDITIONS**		
			Frequency	Induction/field strength	Temperature
μ_r	50 000		DC	3200 A/m	25 °C
	35 000		60 Hz		
ρ	580	μΩ mm			
Density	8747	kg/m^3			

Table 4.3. Characteristics of mumetal

The nano-crystalline sample composition is given in table 4.4. It was 6.4 mm long with a 3.1 × 3.3 mm square cross section. The nano-crystalline sample is made of laminations glued together as shown in figure 4.7. Its important characteristics are shown in table 4.5.

	Fe	Si	B	Nb	Cu
%	73.5	13.5	9.0	3.0	1.0

Table 4.4. Nano-crystalline composition

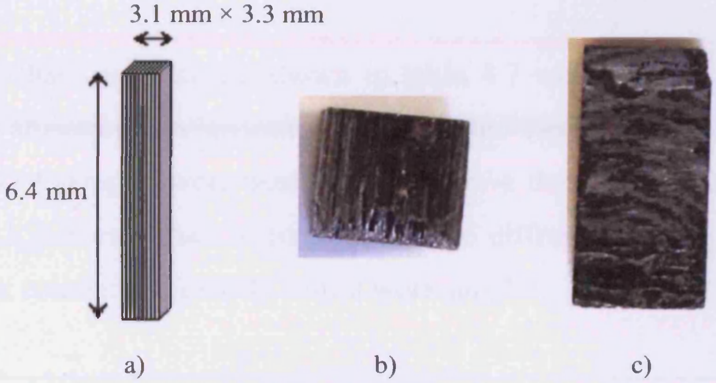

Figure 4.7. Nano-crystalline core for Barkhausen noise sensor, a) schematic diagram, b) top view of sample, c) side view of the sample

Symbol	**Nana-crystalline**	**Unit**	**CONDITIONS**		
			Frequency	Induction/field strength	Temperature
μ_r	70 000		400 Hz	8000 A/m	25 °C
ρ	120	μΩ cm	DC		25 °C
Density	7300	kg/m^3			

Table 4.5. Characteristics of the nano-crystalline material

4.5. Test Specimens

4.5.1. Electrical Steels

Table 4.6 shows details of the Epstein samples used in the investigation of Barkhausen noise versus flux density and frequency.

Sample	**Cut direction to rolling direction**	**Silicon content** *(%)*	**Density** *(kg/m³)*	**Width** *(mm)*	**Length** *(mm)*	**Thickness** *(mm)*
GO	0°	3.0	7650	30.0	305	0.27
GO	55°	3.0	7650	30.0	305	0.27
GO	90°	3.0	7650	30.0	305	0.27
NO	-	3.0	7650	30.0	305	0.50
NO	-	6.5	7430	30.0	305	0.10

Table 4.6. Samples used in Barkhausen noise versus flux density and frequency measurements, density and silicon content supplied by manufacturer (GO - grain-oriented electrical steel sample, NO - non-oriented electrical steel sample)

Samples whose characteristics are shown in table 4.7 were used to investigate the influence of the anisotropic behaviour of non-oriented electrical steel on Barkhausen noise. Two sets of samples were used, they both have the chemical composition, Fe 3.2%Si 0.77%Al, however their average grain size differs (C1 = 53 μm, C2 = 180 μm). The silicon content and density values were supplied.

Sample	**Cut direction to rolling direction**	**Silicon content** *(%)*	**Density** *(kg/m³)*	**Width** *(mm)*	**Length** *(mm)*	**Thickness** *(mm)*
NO	0°	3.2	7600	30.0	305	0.5
NO	15°	3.2	7600	30.0	305	0.5
NO	30°	3.2	7600	30.0	305	0.5
NO	45°	3.2	7600	30.0	305	0.5
NO	60°	3.2	7600	30.0	305	0.5
NO	75°	3.2	7600	30.0	305	0.5
NO	90°	3.2	7600	30.0	305	0.5

* Two sets of samples with the parameters as above were used, the only difference being that the average grain size of sample C1 was 53 μm, and C2 was 180 μm.

Table 4.7. Epstein samples properties cut at different angles to the rolling direction.

Detail of samples of non-oriented electrical steel with various silicon contents, chosen to investigate the relationship between Barkhausen noise and hysteresis is shown in table 4.8.

Sample	Silicon content *(%)*	Density *(kg/m^3)*	Width *(mm)*	Length *(mm)*	Thickness *(mm)*	Resistivity *(Ωm)*
S1	0.2	7850	30.0	280	0.5	1.67×10^{-7}
S2	0.3	7850	30.0	280	0.5	1.79×10^{-7}
S4	1.3	7800	30.0	280	0.5	3.06×10^{-7}
S5	1.8	7700	30.0	280	0.5	3.77×10^{-7}
S6	3	7650	30.0	305	0.5	5.48×10^{-7}
S7	6.5	7430	30.0	280	0.1	8.24×10^{-7}
S9	5.5	7530	30.0	280	0.1	7.35×10^{-7}
S10 (no coating)	3	7650	30.0	305	0. 216	5.48×10^{-7}

Table 4.8. Samples used in Barkhausen noise and hysteresis loss measurements

A grain-oriented 3%SiFe electrical steel sample with an average grain size of 10 mm was used for the Barkhausen scanning measurements (table 4.9).

Sample	Cut direction to rolling direction	Silicon content *(%)*	Density *(kg/m^3)*	Width *(mm)*	Length *(mm)*	Thickness *(mm)*
GO	0°	3.0	7650	30.0	305	0.27

Table 4.9. Description of sample used for Barkhausen scanning measurements

4.5.2. Ancillary study samples

The ancillary study was conducted on cold-rolled low carbon steel with different rolling reductions and thermally aged iron copper with different ageing times. Prof S. Takahashi (from the NDE and Science Research Centre, Japan) supplied the samples, which were part of a round robin test. Tables 4.10 and 4.11 shows the chemical composition and properties of the cold-rolled low carbon steel. Table 4.12 shows properties of the thermally aged Fe 1wt%Cu alloy. Figure 4.8 shows the shape and sizes of the samples.

	C	Si	Mn	Fe
wt. %	0.15 ~ 0.20	0.15 ~ 0.35	0.30 ~ 0.60	bal.

Table 4.10. Chemical composition of low-carbon steel samples

Cold-rolled low carbon steel

Sample identity	**Shape**	**Coil**	**Rolling reduction** *(%)*
A1	Charpy (V-notched)		0
A2	Charpy (V-notched)		5
A3	Charpy (V-notched)		10
A4	Charpy (V-notched)		20
A5	Charpy (V-notched)		40
Af1	Picture Frame	N1 = 220, N2 = 180	0
Af2	Picture Frame	N1 = 220, N2 = 180	5
Af3	Picture Frame	N1 = 220, N2 = 180	10
Af4	Picture Frame	N1 = 220, N2 = 180	20
Af5	Picture Frame	N1 = 220, N2 = 180	40
Ap1	Plate		0
Ap2	Plate		5
Ap3	Plate		10
Ap4	Plate		20
Ap5	Plate		40

Table 4.11. Properties of the low carbon steel samples

Thermally aged Fe 1wt% Cu alloy

Sample identity	**Shape**	**Coil**	**Rolling reduction** *(%)*	**Aging time at 723K** *(min)*
B1	Charpy (V-notched)		0	0
B2	Charpy (V-notched)		0	50
B3	Charpy (V-notched)		0	500
B4	Charpy (V-notched)		0	5000
Bb1	Bar (not notched)		0	0
Br1	Ring	N1 = 60, N2 = 90	0	0
Br2	Ring	N1 = 60, N2 = 90	0	50
Br3	Ring	N1 = 60, N2 = 90	0	500

Br4	Ring	N1 = 60, N2 = 90	0	5000
C1	Charpy (V-notched)		10	0
C2	Charpy (V-notched)		10	50
C3	Charpy (V-notched)		10	500
C4	Charpy (V-notched)		10	5000
Cr1	Ring	N1 = 60, N2 = 90	10	0
Cr2	Ring	N1 = 60, N2 = 90	10	50
Cr3	Ring	N1 = 60, N2 = 90	10	500
Cr4	Ring	N1 = 60, N2 = 90	10	5000

* Fe-Cu alloys were annealed at 1123K for 5 hours, followed by water quenching. Then, Fe-Cu samples were cold rolled and isothermally aged at 723 K for 0 – 5000 min.

** The long axis of the charpy and bar samples corresponds to rolling direction.

*** N1 and N2 represent the number of turns in the exciting and pick-up coils, respectively.

Table 4.12. Properties of the thermally aged iron copper samples

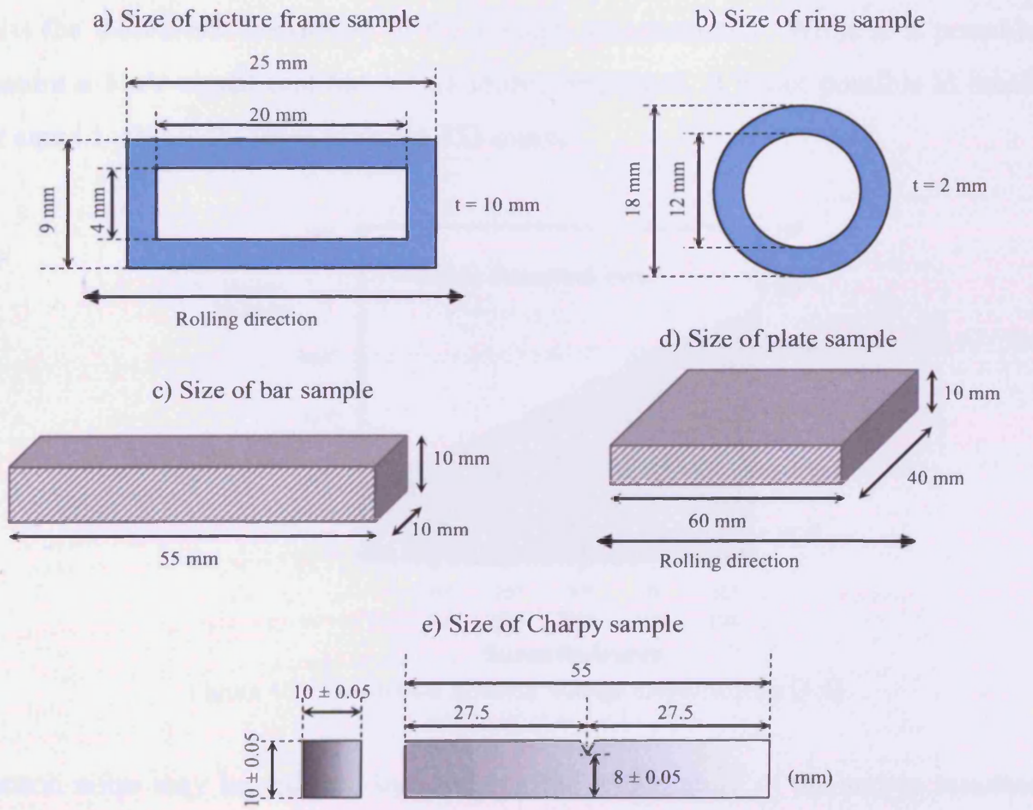

a) Size of picture frame sample

b) Size of ring sample

c) Size of bar sample

d) Size of plate sample

e) Size of Charpy sample

Figure 4.8. Shapes and sizes of a) picture frame sample b) ring sample c) bar sample d) plate sample e) charpy sample

4.6. Noise reduction

Sources such as Johnson noise and stray magnetic fields can be superimposed on to circuitry, thus inducing errors in measurement. Therefore, when developing the system it was necessary to have an understanding of the sources so that they could be minimised.

Johnson or thermal noise, defines the ultimate limit of resolution in an electrical measurement. This noise is generated by the thermal agitation of the charge carriers (the electrons) inside an electrical conductor at equilibrium, which happens regardless of any applied voltage. All voltage sources develop Johnson noise because of their internal resistance.

The theoretical limit of sensitivity in any measurement is determined by the noise generated by the resistances present in the circuit [4.4]. Figure 4.9 shows the theoretical voltage measurement limits at room temperature. High source resistance limits the theoretical sensitivity of the voltage measurement. While it is possible to measure a 1 μV signal that has a 1 Ω source resistance, it is not possible to measure that same 1 μV signal level from a 1 TΩ source.

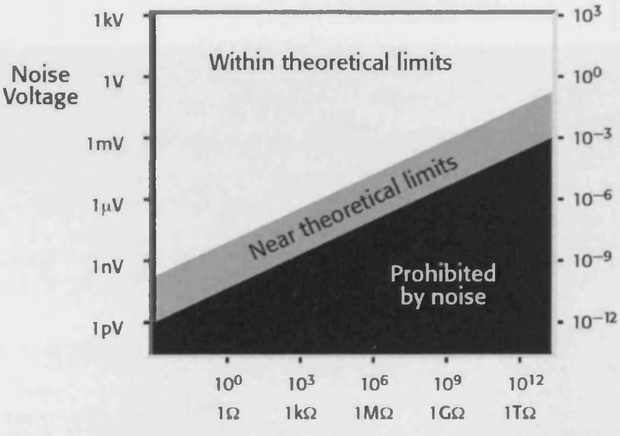

Figure 4.9. Theoretical limits of voltage measurements [4.4]

Johnson noise may be reduced by lowering the temperature of the source resistance. Cooling the devices from room temperature would be inconvenient and costly. Cooling fans were placed near to the power amplifier, DAQ cards and isolation transformer to keep the devices near room temperature.

A changing flux induces a voltage in the coil, which is proportional to the rate of change of flux. Connecting wires are twisted together to avoid any unintentional loops that enclose some stray magnetic field affecting the voltage measured by the measuring device. For this method to work most effectively, the loops were wound as uniformly as possible [4.5]. To minimise the affects of stray fields all the connecting wires were wound using a small electrical motor, which gave a high degree of dense, uniform twisting.

The earth's magnetic field can generate nano-volts in dangling leads [4.4], so signal wires were kept as short as possible. To further reduce environmental electrical noise, the yokes, the sample and the search coil carrier were placed in a grounded aluminium box and the computer monitor was placed over a metre from the measurement system. Furthermore, the magnetising windings were enwrapped in grounded copper foil to minimise the effects of stray fields, from the magnetising yokes, on the measurement sensors. A low noise DAQ card was also chosen to minimise the influence of thermal noise. Figure 4.10 shows the designed system and its noise protection.

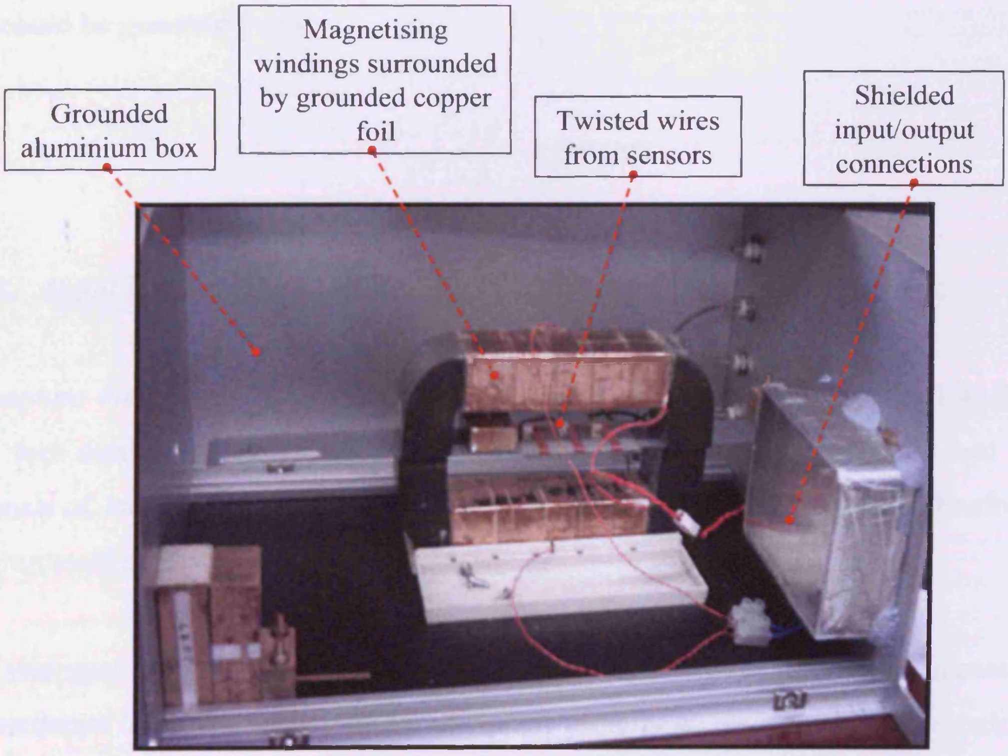

Figure 4.10. Barkhausen noise measurement system with noise protection employed

4.7. Data acquisition cards

Two cards were used in the development of the magnetising and measuring system: one for generation of the magnetising voltage waveforms, which were fed to the power amplifiers and the other was used for acquisition of the sensor signals i.e. Barkhausen noise sensors, H-coil, B-coil and magnetising current waveform.

The PC's specification was: Pentium 3 clocked at 933 MHz, 1280 MB of memory, 37 GB hard drive, floppy drive, network card, graphic and sound card integrated with the motherboard.

4.7.1. Output DAQ card (NI 6731)

All digital to analogue converters generate staircase-like waveforms [4.6], and therefore choosing a high resolution DAQ card is essential. A 16-bit resolution card with a sampling rate of 1 MS/s was chosen for Barkhausen measurements. The output has a range of -10 to +10 V, therefore the smallest change of output voltage that could be generated was:

$$\frac{10-(-10)}{2^{16}-1} = 305\mu V$$

4.7.2. Input DAQ card (NI 4552)

To capture the signals from sensors a National Instruments dynamic signal analyser card was used which is plugged in at the PCI bus in the PC. The card had four channels of 16-bit resolution and all channels are simultaneously sampled at software programmable rates up to 204.4 kS/s [4.7].

The analogue inputs have both analogue and real-time digital filters implemented in the hardware to prevent aliasing. Input signals initially go through low-pass analogue filters to attenuate frequency components beyond the range of the analogue to digital converters (ADC). Then digital anti-aliasing filters automatically adjust their cut-off frequency to remove frequency components above half of the programmed sampling rate. Because of this input design, there was no need to add any other filters to prevent aliasing.

The card has a software-programmable switch that determines whether a capacitor is placed in the signal path. If the switch is set for dc, the capacitor is bypassed and any dc offset present in the source signal is passed to the analogue to digital converters. If the source has a significant amount of unwanted offset (bias voltage), the ac coupling switch had to be set to place the capacitor in the signal path and take full advantage of the input signal range. Within the measurement program, the dc coupling switch was set.

The 90 dB dynamic range of the measurement card makes high-accuracy measurements possible. The card has amplitude flatness of ±0.1 dB, and has a maximum total harmonic distortion (THD) specification of -92 dB at 1 kHz and a worst case THD of -80 dB at higher frequencies.

State-of-the-art, 128-times oversampling, delta-sigma modulating ADCs achieve low noise and low distortion. Because these ADCs sample at 128 times the specified sampling rate with 1-bit resolution, they produce nearly perfect linearity. Extremely flat, linear-phase, low-pass digital filters then remove the quantisation noise from outside the band of interest, divide the sample rate by 128, and increase the resolution to 16 bits. Using the delta-sigma modulating ADCs, the card is immune to the differential nonlinearity distortion associated with conventional data acquisition devices.

The input range of this card is software selectable and can be set for each channel independently. Table 4.13 shows the input range and precision according to the gain used.

Linear gain	**Gain** *(dB)*	**Input range** *(V)*	**Precision*** *(μV)*
0.1	-20	± 42.4 (± 100) **	3051.8 **
0.316	-10	± 31.6	965.05
1	0	± 10	305.18
3.16	10	± 3.16	96.505
10	20	± 1	30.518
31.6	30	± 0.316	9.6505
100	40	± 0.1	3.0518
316	50	± 0.0316	0.96505
1000	60	± 0.01	0.30518

* Value of voltage increment of one LSB of 16-bit counter

** Input range by design ±100V, but test and certified for ±42.4V

Table 4.13. Overall input range and precision according to the input range configuration and gain used

The input range selected depends on the expected size of the incoming signal. For best results, the input range was matched as closely as possible to the expected range of the input signal, explained in detail in chapter 4.8.5.

4.7.3. Signal processing

Barkhausen noise peaks had an amplitude of approximately 130 μV (using the double B-coil sensor, for a grain-oriented electrical steel sample magnetised at 50 Hz at 1 T) and at the same time a ground offset of ~32 mV occurred. Then the range of the data acquisition system had to be set to the highest occurring voltage in order not to damage the card or to clip the reading. In the case of the data acquisition card used in this investigation the resolution was switched from 300 nV to 3 μV. To avoid such a problem differential inputs were used. To provide differential reading the signals of interest are connected via shielded twisted pair cables to a BNC 2140 connector socket (figure 4.11) that has the option to switch between grounded (single ended) and differential mode. This socket acts as the signal conditioning unit, which is connected, to the data acquisition board.

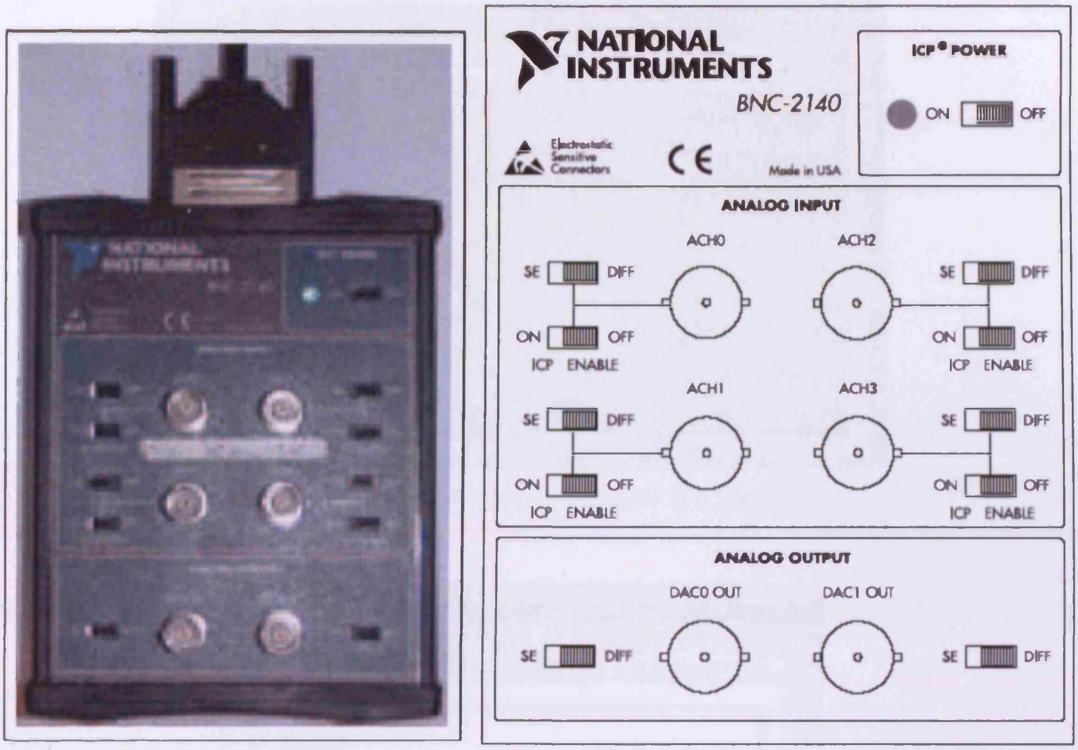

Figure 4.11. BNC 2140 connector block

4.8. LabVIEW program

National Instruments LabVIEW 7.0™ is a graphical programming language [4.8], which was used to develop the Barkhausen noise measurement system. A program in LabVIEW is called a *vi* ("virtual instrument") and always consists of two windows, a graphical user interface ("Front Panel", figure 4.12) and a graphical program code ("Block Diagram", figure 4.13).

The front panel is the user interface of the *vi*, the user builds the front panel with controls and indicators, which are the interactive input and output terminals of the *vi*, respectively. The block diagram contains the graphical source code, such as functions, libraries, calculations and structures from built-in LabVIEW *vi* libraries. So called 'wires' connect each of the nodes on the block diagram, including control and indicator terminals, functions, and structures.

LabVIEW uses dataflow programming, where the flow of data determines execution. Large amounts of different control and indicator elements make it easy to form an attractive and structured graphical user interface.

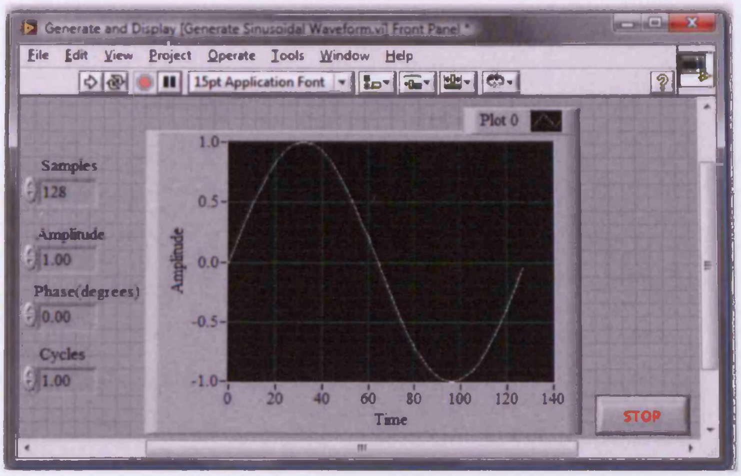

Samples 128
Amplitude 1.00
Phase(degrees) 0.00
Cycles 1.00

Figure 4.12. Example of a front panel view in a LabVIEW *vi*

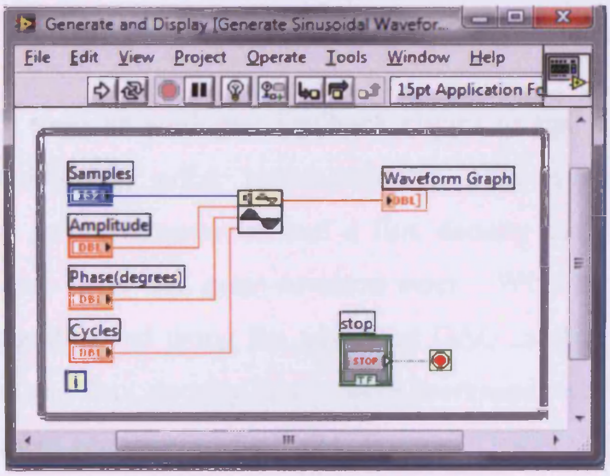

Figure 4.13. Example of a block diagram view in a LabVIEW *vi*

4.8.1. Magnetising current sensor

The digital feedback algorithm requires that as well as the shape of the flux density waveform, the magnetising current to the solenoid had to be detected (for a full description see chapter 4.8.2). To detect this current, a shunt resistor was inserted between the transformer and the magnetising yokes. A connection diagram showing how the shunt resistor was inserted into the measurement system is shown in figure 4.14.

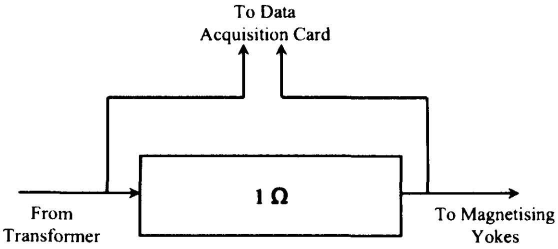

Figure 4.14. Connection diagram from shunt resistor

4.8.2. *Digital feedback algorithm*

To be able to have repeatable and comparable measurements the shape of the flux density waveform must be controlled. This can be done by either an analogue feedback circuit or a digital feedback algorithm.

Hartmann et al [4.3] used an analogue feedback circuit to magnetise electrical steel samples for ac Barkhausen noise measurements. The system could measure Barkhausen noise at power frequencies and a flux density not exceeding 1.2 T for non-oriented steel and 1.4 T for grain-oriented steel. With the development of a digital feedback algorithm and using the advanced DAQ cards in this investigation, the frequency range and flux density levels were increased, while at the same time improving measurement accuracy and speed.

The 'Hartmann system' was modified to incorporate digital feedback. The system developed uses an automated digital feedback technique capable of controlling flux density not only under sinusoidal conditions, but also under triangular, trapezoidal and even arbitrary conditions. The flux density range increased to 1.8 T (for grain-oriented 3%SiFe electrical steel), 1.5T (for non-oriented electrical steel) and the magnetisation frequency range was significantly widened from 5 to 100 Hz.

The block diagram of the developed digital feedback system used for the control of the magnetisation waveform is shown in figure 4.15.

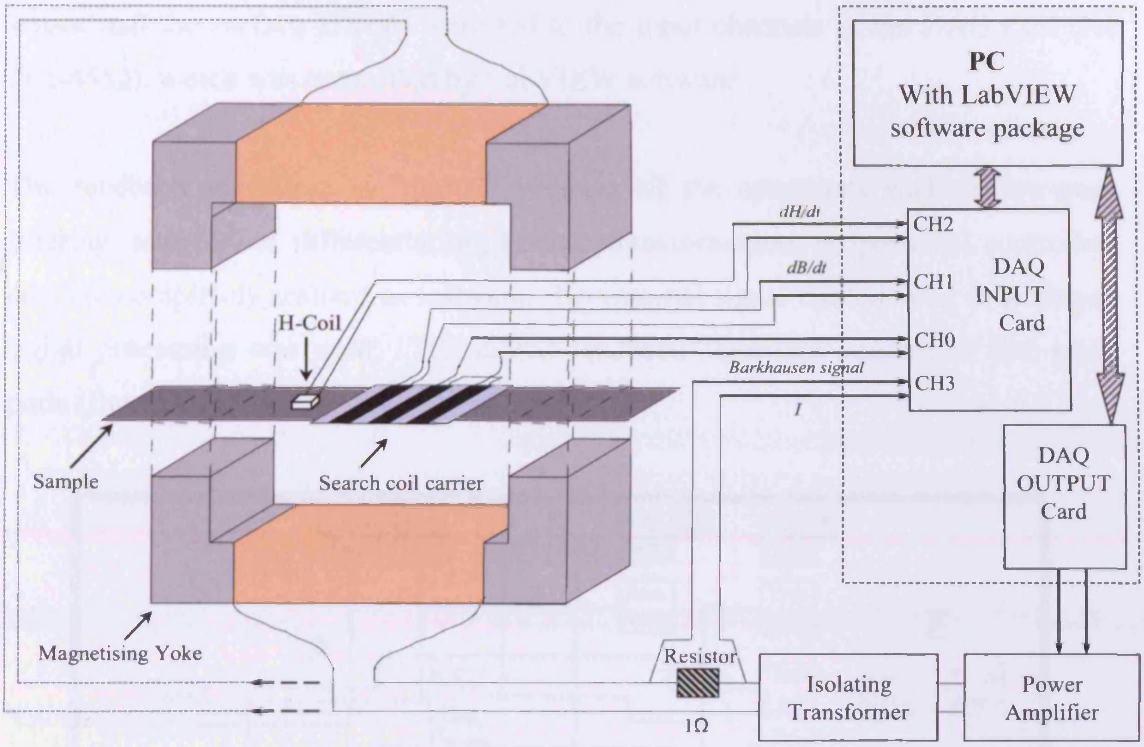

Figure 4.15. Block diagram of the Barkhausen Noise Measurement System

A computer with National Instruments LabVIEW and a data acquisition and generation card (NI PCI-6711) generates the output voltage waveforms to control the applied flux density. This output waveform was fed through a power amplifier, which acted like a low-pass filter [4.9]. An isolating transformer was used to remove any dc component in the magnetising current.

The DC-300A II power amplifier yields ultralow distortion through a wide range of frequencies from DC (0 Hz) to 20 kHz. The amplifier has output transistors that are "direct coupled" to the load so there are no output capacitors or transformers to compromise its integrity. The output power of the DC-300A II enables it to deliver balanced 70 volt output in Bridge-Mono mode without using costly "stepup" transformers.

The system uses a closed circuit magnetising yoke similar to that used in a single sheet tester [4.10]. The magnetising yoke was 167 mm long and 32 mm wide with a square cross section and was suitable for use with Epstein samples. Signals measured (i.e. voltage across resistor, enwrapping B-coil, enwrapping Barkhausen double coil sensor and the surface H-coil) were fed to the input channels of the DAQ card (NI PCI-4552), which was controlled by LabVIEW software.

The feedback algorithm is "digital" because all the operations such as low-pass filtering, integration, differentiation, Fourier transformation, proportional controller, etc., are completely realised in software. No external signal conditioning or analogue signal processing was used. The digital feedback algorithm consists of five main parts (figure 4.16).

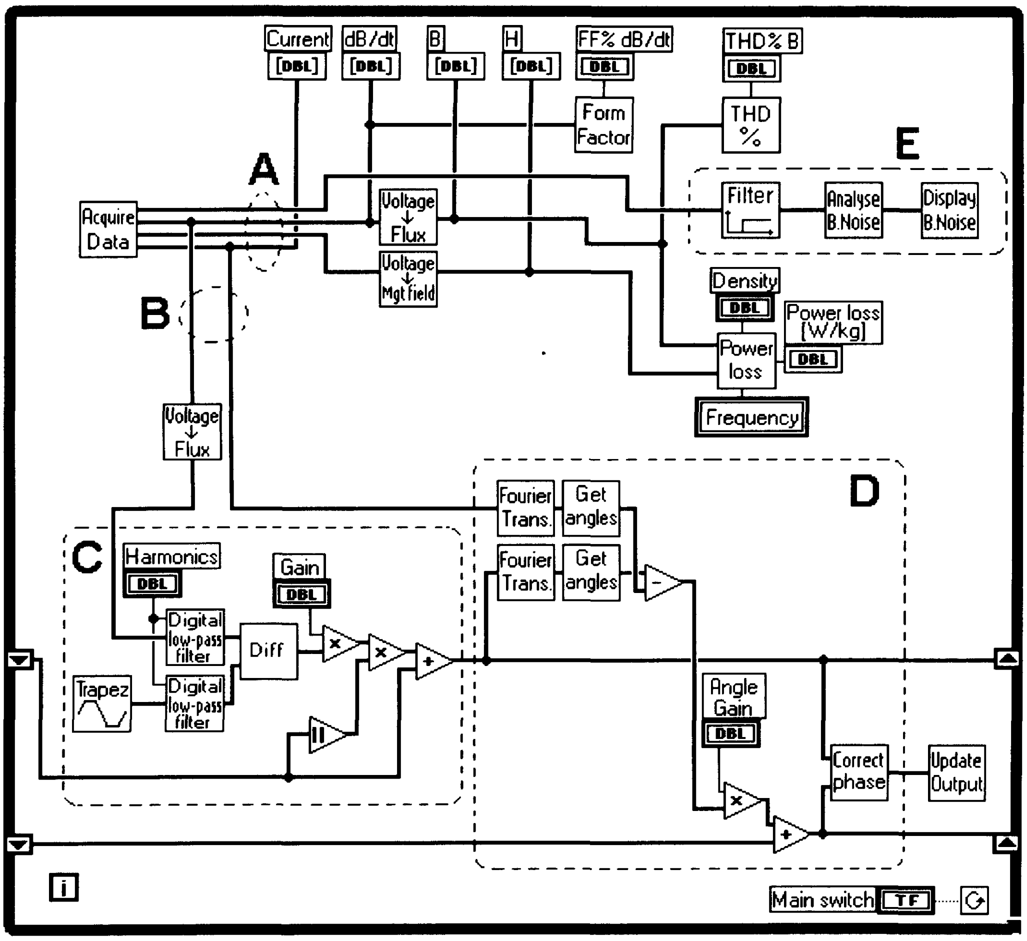

Figure 4.16. Simplified adaptive digital feedback algorithm written in LabVIEW (not all modules are shown): (A) measurement thread; (B) control thread; (C) proportional controller; (D) adaptation module; (E) Barkhausen noise analysis module

The first thread (**A** in figure 4.16) is the measuring thread, in which acquired signals are used to calculate the peak flux density, B [T], peak applied magnetic field strength, H [A/m], and power loss per unit mass, P [W/kg]. This also feeds **E** in figure 4.16, which filters, analyses and displays the Barkhausen noise signal (described more in detail in chapter 4.9).

The second thread (**B** in figure 4.16) is responsible only for digital feedback and utilises the same acquired data as the measuring thread. However, additional calculations were implemented for digital feedback, such as digital filtering and computation of the relative difference between reference and real B (Eq. (4.5)) [4.11]:

$$\mathrm{Diff}_{(i)} = \frac{B_{ref} - B_{real(i)}}{\hat{B}_{ref}} \tag{4.5}$$

where, Diff - waveform of relative difference between reference and real waveforms; B_{ref} - reference (ideal) instantaneous flux density waveform; B_{real} - real (measured) instantaneous flux density waveform; $\hat{B}_{ref}$ - peak value of reference flux density waveform; i - current iteration value

Before the DAQ card generates the output voltage, the waveform computed by the proportional controller (**C** in figure 4.16) is fed to the correct phase element (**D** in figure 4.16) (a module that calculates the phase lead/lag between the output voltage generated by the DAQ card and actual magnetising current for each harmonic that is implemented). This provides a Fourier transform of the waveform, modifies the phase of each harmonic, and then calculates an inverse Fourier transform. This artificially "distorted" voltage output waveform is then generated by the DAQ card and "converted" through the non-linear components (low-pass filter, power amplifier, isolation transformer, yoke and sample) to the desired shape of the flux density waveform in this case sinusoidal.

In each iteration, the waveform Diff is used to modify the generated output voltage waveform accordingly (C in figure 4.16), until the difference between the expected and real waveform is equal to or less than the user defined value.

The algorithm initially assumes that the flux density, ***B***, depends linearly on the magnetising current, ***i***. The non-linearity between measured ***B*** and ***i*** is strongly dependent on the shape and magnetic properties of the yoke and the sample. The passive low-pass filter and power amplifier introduces a phase lag, up to several tens of degrees for each harmonic. The phase lead/lag functions of the low-pass filter and the power amplifier can be found relatively easily, but the magnetising yoke, the random air-gaps, as well as the B-H characteristics of the sample cause the transfer function of the whole system to continually change. In order to compensate for this, a module that calculates the phase lead/lag between the output voltage generated by the data acquisition card and each harmonic of the actual magnetising current is implemented (**D** in figure 4.16).

The array of phase shifts for all harmonics was continuously adapted for all subsequent iterations. Before the data acquisition card generates the output voltage, the waveform computed by the proportional controller (**C** in figure 4.16) is fed to the *Correct phase* element (**D** in figure 4.16), which provides a Fourier transform of the waveform, modifies the phase of each harmonic, and then calculates an inverse Fourier transform.

As the permeability of the sample under investigation changes very rapidly throughout the magnetisation cycle, a greater modification of the controlled signal than predicted by the feedback may occur in some regions of the magnetising curve. This would lead to oscillations of the magnitude of the controlled waveform. In practice, feedback gains equal to 0.3 or less successfully prevented this (these are shown as *Gain* and *Angle Gain* icons in **C** and **D** in figure 4.16, respectively).

Since in general (taking into consideration the influence of the staircase effect [4.12]) data acquisition cards acquire a different number of points per magnetisation cycle than they generate, there is a module responsible for rendering the waveform to another number of points (this is shown as *Change points* icon in figure 4.16).

A simplified block diagram of the adaptive digital feedback system is presented in figure 4.17. Where a reference $\dot{B}$ is fed to a proportional control unit, which controls the shape of the B waveform. Then this signal feeds into the adaptation module, which adjusts the angle at which it lags/leads by. Then the signal feeds into a low pass filter (*LPF*), power amplifier (*PA*), isolating amplifier (*IT*) which then feeds to the magnetisation yokes.

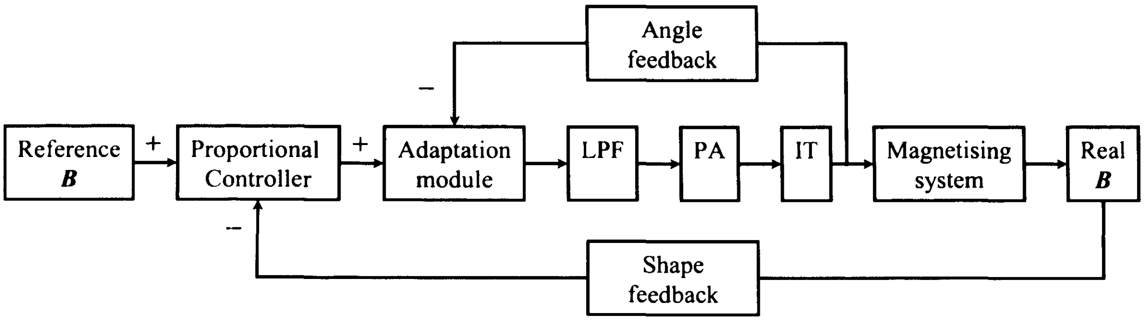

Figure 4.17. Block diagram of digital adaptive feedback system [4.11]

The equation for calculating the output voltage waveform in subsequent iterations is:

$$\boldsymbol{Out}_{(i)} = \boldsymbol{F}_{(i)}(\boldsymbol{Out'}_{(i)}) \tag{4.6}$$

where, i - current iteration; ***Out*** - voltage waveform generated by the DAQ; ***Out'*** - is the output waveform calculated for i^{th} iteration by the proportional controller as

$$\boldsymbol{Out'}_{(i)} = \boldsymbol{Out}_{(i-1)} + \boldsymbol{G} \cdot \left|\boldsymbol{Out}_{(i-1)}\right| \cdot \boldsymbol{Diff}_{(i)} \tag{4.7}$$

where, ***G*** - gain of the proportional controller (shown as *Gain* icon in **C** in figure 4.17); ***Diff*** - difference waveform calculated from equation (4.5); i-1 - previous iteration

The waveform ***Out'*** from equation (4.7) is one period of a continuous function and can also be expressed as a finite Fourier series

$$\boldsymbol{Out'}_{(i)} = \sum_{k=1} [A_{(k)} \cdot \cos(k \cdot 2 \cdot \pi \cdot f \cdot t + \varphi_{(k)})]_{(i)} \tag{4.8}$$

where, k - harmonic number; A - magnitude of the k^{th} harmonic; f - magnetising frequency; t - time; φ - phase shift of the k^{th} harmonic

The symbol ***F*** in equation (4.6) denotes a function of phase lead/lag for all harmonics. It is applied by module *Correct phase* in **D** in figure 4.16 as

$$\boldsymbol{Out}_{(i)} = \sum_{k=1} [A_{(k)} \cdot \cos(k \cdot 2 \cdot \pi \cdot f \cdot t + \varphi_{(k)} + \alpha_{(k)})]_{(i)} \tag{4.9}$$

where, α - is the phase lead/lag of the k^{th} harmonic calculated as

$$\alpha_{(k,i)} = \alpha_{(k,i-1)} + G_{\alpha} \cdot (\alpha_{B(k,i)} - \alpha_{I(k,i)}) \tag{4.10}$$

where, G_{α} - gain of angle feedback (shown as *Angle Gain* icon in **D** in figure 4.16); α_B - phase of the k^{th} harmonic of flux density waveform; α_I - phase of the k^{th} harmonic of magnetising current

Hence, the array of phase shifts for all harmonics, which is fed to the module *Correct phase*, can be written as

$$\boldsymbol{\alpha} = [\alpha_{(1)}, \alpha_{(2)}, \ \dots \ , \ \alpha_{(n)}] \tag{4.11}$$

where, $\boldsymbol{\alpha}$ - is an array of phase shifts for all analyzed harmonics; α - phase shift for a given harmonic; n - total number of analysed harmonics

During the controlling process, any mutual dependencies between magnetising channels are corrected automatically. This makes the feedback "adaptive", since there is no need to know how the magnetising channels interact with each other.

Data processing can only be carried out once a complete cycle of the magnetising waveform has been acquired. Therefore, the time of each iteration and thus the convergence time is dependent on the magnetising frequency. As the frequency decreases the time of the cycle grows accordingly, but the number of iterations necessary to achieve a controlled state of magnetisation remains approximately the same (see figure 4.18). Figure 4.18a shows for non-oriented electrical steel at 1 kHz magnetising frequency it takes approximately 130 iterations to control the sinusoidal flux density waveform up to 1.6 T, which is approximately 0.13 seconds. For grain-oriented electrical steel at 50 Hz it takes 3.20 seconds to control it to 1.5 T (figure 4.18b). For this reason, it would take several hours to approach the required conditions for frequencies below 1 Hz.

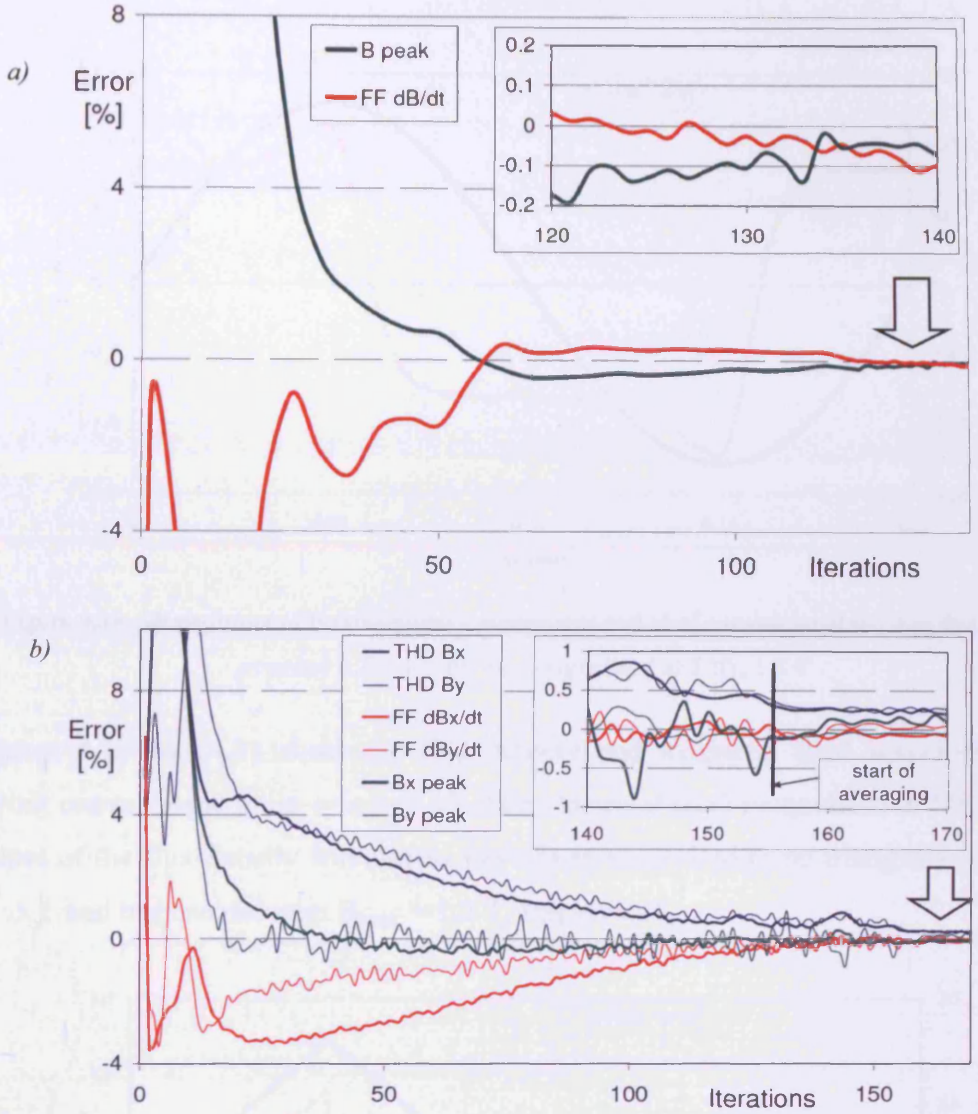

Figure 4.18. Typical graphs of the performance of the adaptive digital feedback: a) alternating magnetisation at 1 kHz, 1.6 T, non-oriented electrical steel sheet, b) 2D rotational magnetisation at 50 Hz, 1.5 T, conventional grain-oriented electrical steel. (The insets show the magnifications of the final part of the controlling process. The inset in Fig. 4.18b shows the influence of averaging of the readings from 25 periods.) [4.11]

Figure 4.19 shows the flux density and magnetic field waveforms obtained when testing conventional non-oriented 0.2% silicon iron electrical steel magnetised at 5 Hz. The shape of the flux density waveform has been controlled to be sinusoidal with $B_{peak} = 1.3$ T.

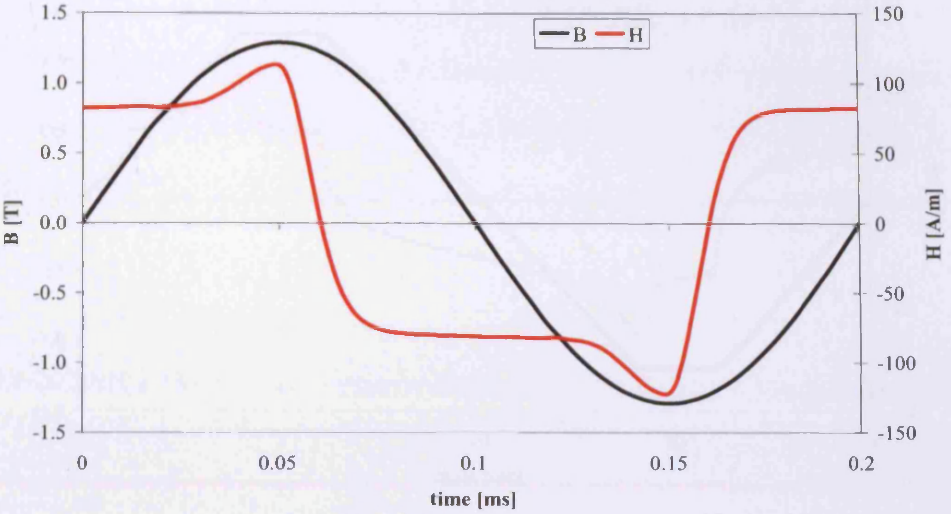

Figure 4.19. Waveforms of B (sinusoidal - controlled) and H of conventional 0.5 mm thick non-oriented 0.2% silicon iron magnetised at 5 Hz, 1.3 T

Figures 4.20 and 4.21 show the flux density and magnetic field waveforms from testing conventional grain-oriented 3%SiFe electrical steel magnetised at 50 Hz. The shapes of the flux density waveforms have been controlled to be triangular with $B_{peak} = 1.3$ T and trapezoidal with $B_{peak} = 1.2$ T, respectively.

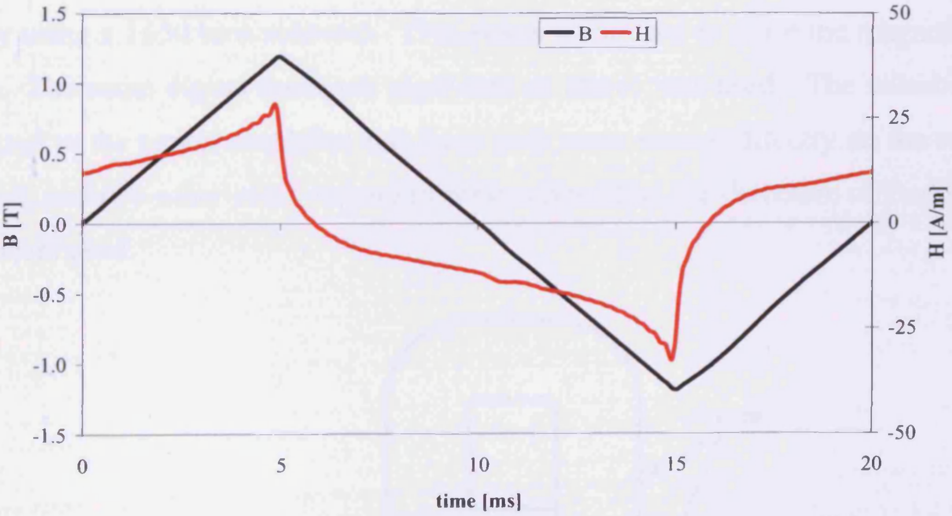

Figure 4.20. Waveforms of B (triangular - controlled) and H of conventional 0.27 mm thick grain-oriented 3% silicon iron magnetised at 50 Hz, 1.3 T

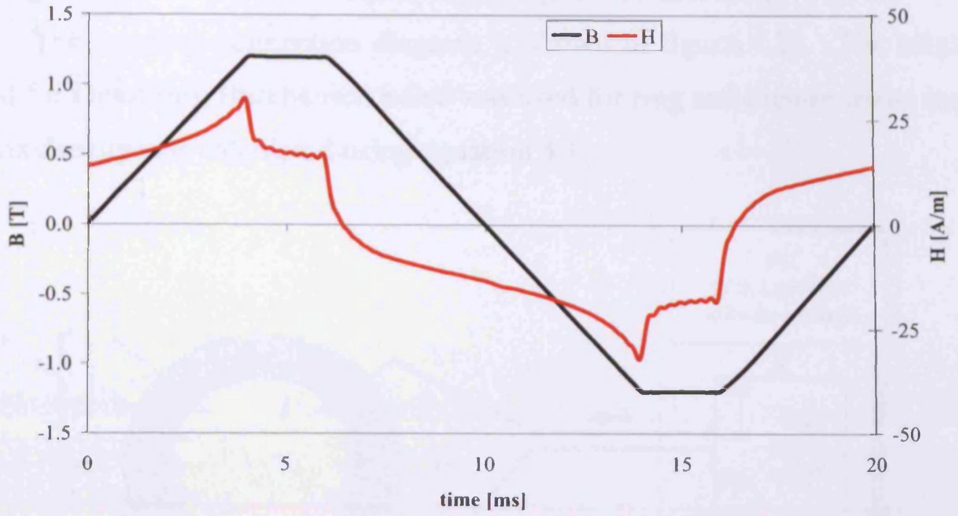

Figure 4.21. Waveforms of B (trapezoidal - controlled) and H of conventional 0.27 mm thick grain-oriented 3% silicon iron magnetised at 50 Hz, 1.2 T

4.8.3. *Magnetisation configuration for ancillary study samples*

The charpy, bar (not notched), and plate samples were magnetised using the yoke configuration shown in figure 4.22. Due to the thickness of the samples, the previous method of flux injection could not be used, therefore the samples were magnetised directly using a 1650 turn solenoid. Two yokes were used to close the magnetisation circuit. The same digital feedback algorithm as above was used. The solenoid was connected to the power amplifier and three coils were wound directly on the sample. A B-coil, and two other coils, wound in series opposition for detection of Barkhausen noise, were used.

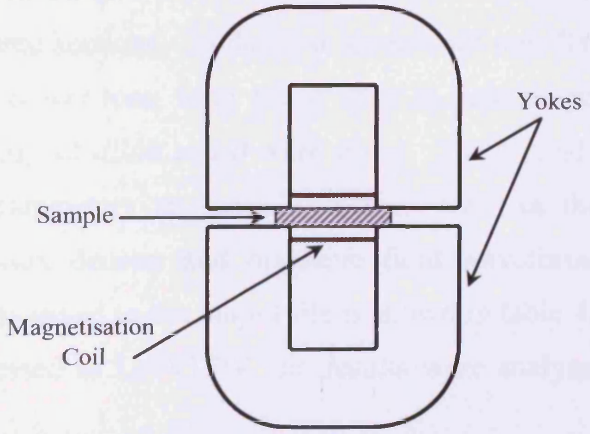

Figure 4.22. Yoke configuration for charpy, bar (not notched), and plate samples

The Ring and Picture Frame samples were magnetised according to BS EN 60404-6 [4.13]. The winding connection diagram is shown in figure 4.23. The single coil method for measuring Barkhausen noise was used for ring and picture frame samples. The flux density was calculated using equation 4.1.

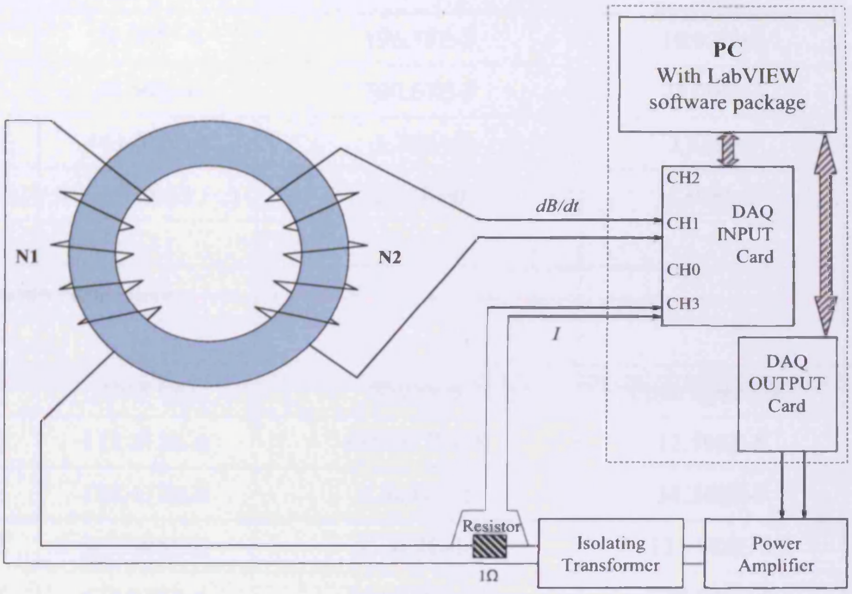

Figure 4.23. Ring sample magnetisation configuration (the same configuration was used for the picture frame shape sample)

4.8.4. *Storing of the measured and calculated results*

The program designed for feedback and measurements was equipped with auto saving of the measured and calculated results to an output file. All the results were appropriately formatted and saved together with all other important measurement data to text files, which were exported, to Microsoft Excel or a LabVIEW program. The file was split into three sections. In the first section, all non-Barkhausen parameters such as B_{max}, H_{max}, power loss, form factor error in percentage and total harmonic distortion in percentage of *dB/dt* and *B* were saved. The second section included the Barkhausen noise parameters as seen in chapter 4.9. In the third section, the Barkhausen noise, flux density and magnetic field waveforms were saved. An example of the results saved to the output file is shown in table 4.14. Once, all of the data had been processed in LabVIEW, the results were analysed and plotted using Microsoft Excel.

Original file	Bark- NO-Power Loss Test-1- 50.0Hz Sine B Control 27 Mar 2006.txt			
Table of Power Losses and all factors:				
Bmax [T]	Hmax [A/m]	Power Loss [W/kg]	Permeability	...
3.0E-01	16.32E+0	78.88E-3	14.62E+3	...
5.0E-01	21.03E+0	196.73E-3	18.92E+3	...
1.0E+00	34.56E+0	700.67E-3	23.00E+3	...
1.50E+0	461.06E+0	1.79E+0	2.58E+3	...
1.60E+0	1.19E+3	2.11E+0	1.07E+3	...
				...
Barkhausen Noise data:				...
				...
TSA3	RMS (V)	Kurtosis	Pow. Spec (W)	...
169.677E-3	112.213E-6	699.053E-18	12.594E-9	...
283.192E-3	185.417E-6	4.964E-15	34.389E-9	...
563.474E-3	363.005E-6	65.789E-15	131.788E-9	...
889.219E-3	570.820E-6	380.816E-15	325.940E-9	...
950.151E-3	612.471E-6	526.618E-15	375.279E-9	...
				...
Barkhausen Noise Waveform with B Waveform :				...
Points	BN	B (T)	H (A/m)	...
000.000E+0	213.547E-6	363.908E-6	12.808E+0	...
1.000E+0	27.534E-6	1.361E-3	12.836E+0	...
2.000E+0	-1.075E-6	2.281E-3	12.863E+0	...
3.000E+0	-91.746E-6	3.201E-3	12.889E+0	...
...	...	...	...	...

Table 4.14. Typical data output from LabVIEW, which is saved into a text file

4.8.5. Automatic input range selection

As described in chapter 4.7, a large input range can accommodate a large signal variation but reduces the voltage resolution and choosing a smaller input range improves the voltage resolution but can result in the signal being clipped. Therefore, for best results the input range was matched as closely as possible to the expected range of the input signal. The measurement DAQ card (NI-4552) had software selectable input ranges. The developed program, included a independent checking algorithm that read the input voltage to determine the most appropriate voltage range for optimum resolution.

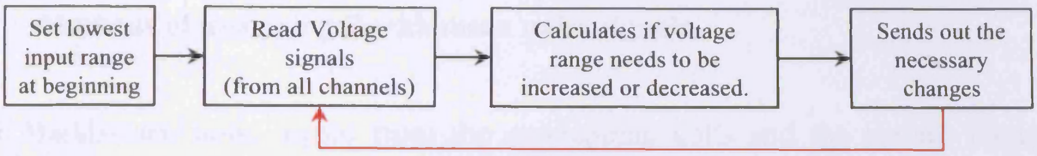

Figure 4.24. Block diagram of automatic input range algorithm

Figure 4.24 shows a block diagram of the input range algorithm implemented in the software. The algorithm works such that if the input range is set to ±1 V and the measured input voltage reaches within 10% of the next range (3.16 V or 0.316 V) then it will increase or decrease the input range accordingly.

4.8.6. Sample demagnetisation

Simply switching off the applied field would leave a sample in a magnetised state. The process of demagnetisation by reversals of *H* is widely used for demagnetising magnetic materials. In this process, the field *H* is cycled over successively smaller ranges obtaining a series of hysteresis loops of decreasing size. The process may be continued until the excursion of *H* approaches zero, leaving the specimen essentially demagnetised [4.14].

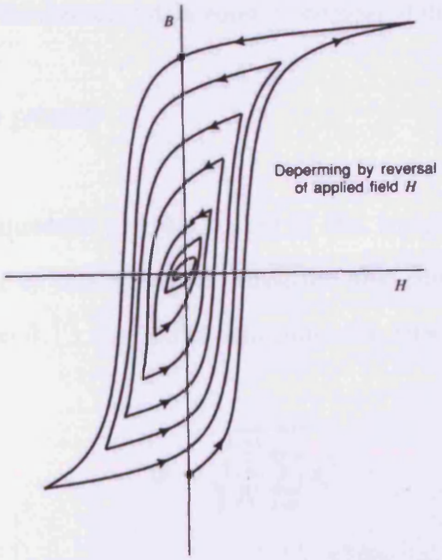

Figure 4.25 Normal magnetisation curve passing through the tips of successive hysteresis loops

This method was implemented into the LabVIEW *vi*, and once the set magnetic flux density was reached, the applied voltage was decreased in 200 steps using the same demagnetising frequency as magnetising frequency.

4.9. Methods of analysing Barkhausen noise signals

The Barkhausen noise signal from the enwrapping coils and the surface mounted sensor was acquired and analysed with aid of LabVIEW software. High-pass filters including the Equi-ripple filter, Chebyshev filter, Elliptic filter, Bessel filter and IIR Butterworth were tested for filtering out unwanted emf components. A fifth order Butterworth high-pass filter with a cut off frequency of 3.5 kHz was found to be the most effective.

Due to the stochastic nature of Barkhausen noise, the signal was analysed statistically, after filtering, using root mean square, total sum of amplitudes, kurtosis, power spectrum, arithmetic mean, standard deviation, variance, median, mode, skewness, and total number of peaks, all of which are described below. The absolute values were obtained by averaging over ten cycles:

$$\overline{x} = \frac{1}{n} \cdot \sum_{i=1}^{n} x_i \tag{4.12}$$

where, $\overline{x}$ - calculated average; n - this is set to ten to indicate that the measurement is taken ten times; x - absolute value of the measured data point; i - number of iterations

4.9.1. Root mean square (RMS)

The rms value Ψ of a sequence can be found if the input sequence elements x are squared, the mean is taken of this squared sequence and finally the square root of this quantity is taken. Equation 4.13 is used to calculate the rms value.

$$\psi = \sqrt{\frac{1}{N} \sum_{i=0}^{N=1} x_i^2} \tag{4.13}$$

where, N - number of elements in the input sequence

4.9.2. *Total sum of amplitudes (TSA)*

The following equation describes the mathematical method for calculating TSA for each of the different amplitudes.

$$TSA = Positive\ \ Sum\ \ of\ \ Amplitudes + \left|\ Negative\ \ Sum\ \ of\ \ Amplitudes\ \right| \quad (4.14)$$

The Barkhausen noise signal is stored as an array of 2048 values. Eq. 4.15 demonstrates how the different values in the array are added.

$$TSA = 5 + 8 + 12 + 15 + 20 + 18 + 15 + 10 + 5 + 2 + \\ \left|(-2)+(-6)+(-10)+(-15)+(-18)+(-24)+(-20)+(-17)+(-14)+(-9)+(-5)\right| = 250 \quad (4.15)$$

4.9.3. *Total number of peaks (TNP)*

A peak is described in this case, as a large number with lower numbers either side of it. This is true in the case of positive peaks or negative peaks. An example of positive and negative peaks can be seen in figure 4.26, the red peaks are counted to give the absolute total number of peaks.

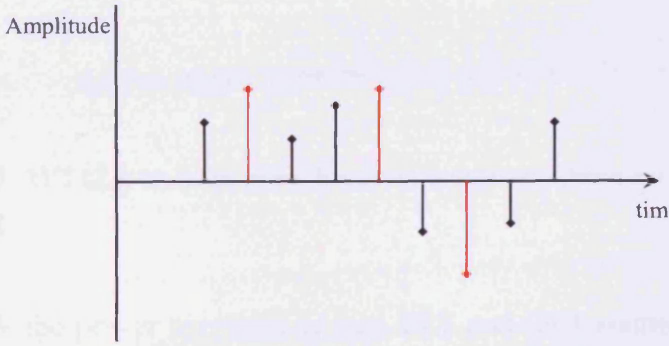

Figure 4.26. Example of positive and negative peaks in the Barkhausen noise signal

4.9.4. Kurtosis

Kurtosis is a measure of the degree of flattening near the centre of a normal distribution. Similar to the skewness, the value for the kurtosis is obtained using the following equation.

$$\sigma^4 = \frac{1}{N}\sum_{i=0}^{N-1}(X_i - \mu)^4 \tag{4.16}$$

where, N - is the number of elements in X; μ - represents the mean value of the sequence

4.9.5. Power spectrum

The power spectrum computes the harmonic power content of a signal. If X represents the actual measurements in volts, the power spectrum *vi* expresses the normalised units of the output sequence power spectrum in watts on a 1 Ohm basis (P = V^2/R, with R = 1Ω).

The Discrete Fourier Transform (DFT) or the Fast Fourier Transform (FFT) of a real signal is a complex number. The power in each frequency component is obtained by squaring the magnitude of that frequency component. The plot showing the power in each of the frequency components is known as the power spectrum. The power spectrum $S_k(f)$ of a function $x(t)$ is defined as:

$$S_k(f) = X_k(f)\cdot X_k^{compl.conj.}(f) = |\ X_k(f)\ |^2 \tag{4.17}$$

where, $X_k(f)$ - FFT (X_k); k - index of the frequency component (harmonic) where the power has been calculated [4.6]

Within LabVIEW the power spectrum *vi* uses FFT and DFT routines to compute the power spectrum. When the number of samples within the input array is a power of two, the power spectrum *vi* computes the FFT instead of using the DFT algorithm. This FFT computation is very fast and memory efficient.

4.9.6. Arithmetic mean

The arithmetic mean value μ is calculated using the following equation.

$$\mu = \frac{1}{n}\sum_{i=0}^{n-1} X_i \tag{4.18}$$

where, μ - is the mean; n - is the number of elements in X

This is simply the sum of all samples, *x,* in a sequence divided by the number, *n*, of samples.

4.9.7. Standard deviation

The standard deviation σ is calculated using the following equation.

$$\sigma = \sqrt{\frac{1}{n}\sum_{i=0}^{n-1} (X_i - \mu)^2} \tag{4.19}$$

where, μ - is mean; n - is the number of elements in X

4.9.8. Variance

The variance measures the spread or dispersion of the sample values. The variance value σ^2 is calculated from:

$$\sigma^2 = \frac{1}{n}\sum_{i=0}^{n-1} (X_i - \mu)^2 \tag{4.20}$$

where, n - is the number of elements in X; μ - represents the mean value of the sequence calculated according equation 4.18.

Note that the variance values are the same as for the power spectrum. This happens when the mean value μ is small compared to the elements within the input sequence. The other condition providing the same results for both parameters is that the power spectrum is obtained by squaring the magnitude of its frequency components without using the phase information. Commonly the phase information is not considered when calculating power spectrum results. When a signal needs to be assembled the phase information is necessary.

4.9.9. Median

The median value is the "middle value" of a list. The smallest number such that at least half the numbers in the list are no greater than it. If the list has an odd number of entries, the median is the middle entry in the list after sorting the list into increasing order. If the list has an even number of entries, the median is equal to the sum of the two middle (after sorting) numbers divided by two. The median value is found by input sequence X sorting the values of X and selecting the middle element(s) of the sorted array.

$$\text{Median} = \begin{cases} s_i & \text{if } n \text{ is odd} \\ 0.5\,(s_{k-1} + s_k) & \text{if } n \text{ is even} \end{cases}$$

where, n - is the number if elements in the input sequence X; s - is the sorted sequence of X; $i = \frac{n-1}{2}$; $k = \frac{n}{2}$

4.9.10. Mode

The mode is the most frequently occurring value in a sequence of numbers. For example, if the input sequence is

$$X = \{0, 1, 3, 3, 4, 4, 4, 5, 5, 7\}$$

the mode of X is four because that is the value that most often occurs in X. However, instead of finding the true mode of the input sequence, this *vi* uses a histogram to divide the input sequence into bins, or intervals, and returns the centre value of the bin containing the most values from the input sequence.

The *vi* calculates the mode by generating a discrete histogram *h(x)* with the specified number of intervals of the input sequence *X*. Each bin, specified by intervals covers a range of floating-point numbers. The *vi* scans *h(x)* for the interval Δ_i that has the maximum count. After the *vi* identifies the interval, it selects the centre value of the interval as the mode of the input sequence *X*.

$$h(\mathrm{mod}\,e) = \max[h(x)] \tag{4.21}$$

4.9.11. Skewness

The Skew of a signal is a description of its asymmetry. If the value for Skewness, σ^3, is greater than zero, i.e. positive skewness, the signal has a tail to the right. Negative skewness is an indication that the signal has a tail to the left. The skew of an input data set can be calculated using the following equation.

$$\sigma^3 = \frac{1}{n}\sum_{i=0}^{n-1}(X_i - \mu)^3 \tag{4.22}$$

where, N - is the number of elements in X; μ - represents the mean value of the sequence

This computation, which is also called "moment about mean", is a measure of the deviation of the elements in the sequence from the mean.

4.10. Methods of reducing the noise produced due to an iron-cored transformer

A transformer can be made of a stack of electrical steel laminations as shown in figure 4.27.

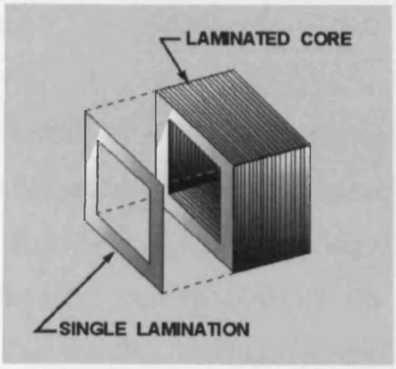

Figure 4.27. Typical transformer made of electrical steel laminations

The basic construction of a transformer consists of a ferromagnetic core surrounded by primary and secondary coils. The ac voltage in the primary coil induces an alternating magnetic flux that flows around the core, which in turn induces an ac voltage in the secondary coil. The ratio of the primary to secondary voltages is equal to the ratio of the number of turns in their windings, or alternatively, the voltage per turn is the same for both windings.

$$r = \frac{N_s}{N_p} = \frac{V_s}{V_p} \qquad (4.23)$$

where, N_s - number of turns of secondary coil; N_p - number of turns in primary coil; V_s – voltage of secondary coil; V_p - voltage of primary coil; r - is the ratio between the primary and secondary

The main reason for using a transformer in the measurement circuit is to block any dc component produced by the power amplifier [4.15]. The power amplifier [4.9] did not have a capacitive output, therefore produced a very small dc offset voltage, which affects the magnetisation circuit. However, usually the transformer has a ferromagnetic core, which produces its own Barkhausen noise. This is then carried in the magnetising current and passed into the magnetising yokes, thus to the sample, which is then measured and analysed with the Barkhausen noise signal. To reduce this effect, two methods were investigated. Firstly, an air-cored transformer was investigated, the removal of the ferromagnetic core would reduce the noise passed to the magnetising yokes and secondly an ac coupling capacitor would produce lower noise.

4.10.1. Air-core transformer

An air-cored transformer consists of two concentric coils, with just air linking the coils. The advantage of this is that the magnetising current has the same waveform as the primary voltage [4.16]. However, it has a very significant disadvantage that it is difficult to produce high magnetic flux to generate the appropriate secondary emf. The second disadvantage is that the flux linking the windings of a ferromagnetic core is largely contained within the core. However, an air-cored transformer produces stray flux that can be induced in nearby circuits. Hence, the air-cored transformer needs ferromagnetic shields to contain the flux.

The coupling coefficients of two winding configurations were investigated. Figure 4.28 shows the two winding configurations investigated. Figure 4.28(a) simply has the primary winding wound over the secondary winding, therefore magnetic flux created by the primary winding generates an emf in the secondary coil, having the secondary coil inside the primary gives better coupling for the transformer. Figure 4.28(b) is a more complex winding configuration with the primary winding and the secondary winding inter-layered. This enables the primary and second winding to be closer.

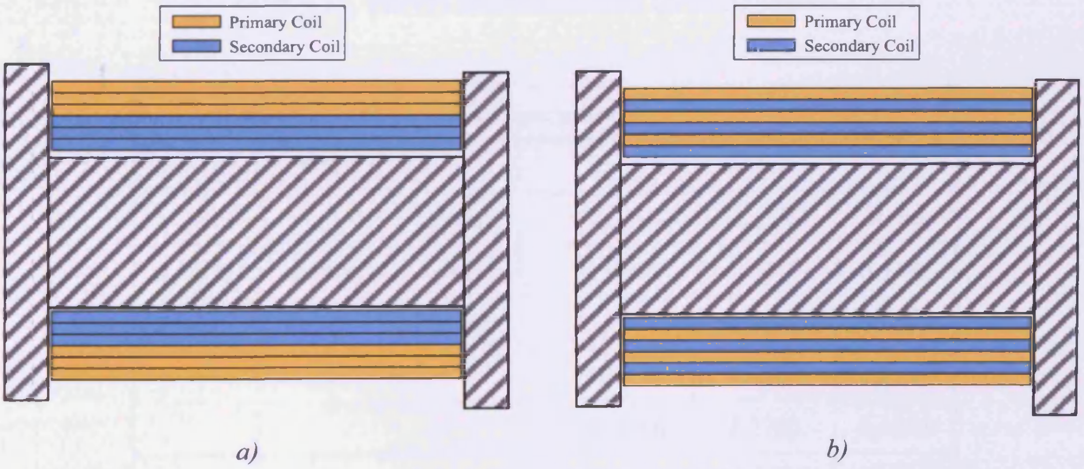

Figure 4.28. Winding configurations of air-cored transformer a) primary winding on the outside and secondary wind on the inside b) inter layered windings with primary and secondary winding layered.

No-load tests were carried out on both transformers. A schematic diagram of the no-load test apparatus is shown in figure 4.29.

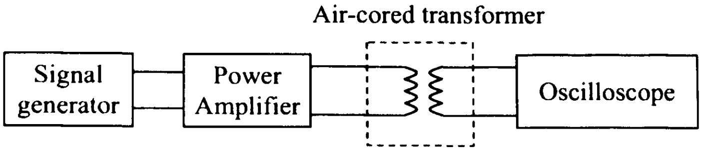

Figure 4.29. Schematic diagram of no-load test for air-cored transformer

Results were obtained at 5 and 50 Hz. The input voltage was increased in steps until the maximum voltage from the power amplifier had been reach and the emf of the secondary was measured. The average coupling ratios under no-load are displayed in tables 4.15 and 4.16 for configuration 1 and configuration 2 respectively.

Configuration 1					
5 Hz			**50 Hz**		
V_{in} (V)	V_{out} (V)	Ratio	V_{in} (V)	V_{out} (V)	Ratio
1.0720	0.0039	0.0036	1.0800	0.0071	0.0065
5.0410	0.0051	0.0010	3.1260	0.0196	0.0063
			5.0050	0.0304	0.0061
			10.4600	0.0649	0.0062
			20.5100	0.1237	0.0060
			Average Ratio		**0.0051**

Table 4.15. Results from no-load test for configuration 1

Configuration 2					
5 Hz			**50 Hz**		
V_{in} (V)	V_{out} (V)	Ratio	V_{in} (V)	V_{out} (V)	Ratio
1.0800	0.0882	0.0817	1.0440	0.5410	0.5182
4.9720	0.3111	0.0626	3.1140	1.6140	0.5183
			5.0770	2.6180	0.5157
			10.1900	5.2700	0.5172
			20.0400	10.3200	0.5150
			Average Ratio		**0.3898**

Table 4.16. Results from no-load test for configuration 2

It can be concluded that the interlayer windings of the configuration have a far higher coupling ratio. Figure 4.30(a) shows the bobbin created to make the air-cored transformer, and figure 4.30(b) shows the air-cored transformer after construction.

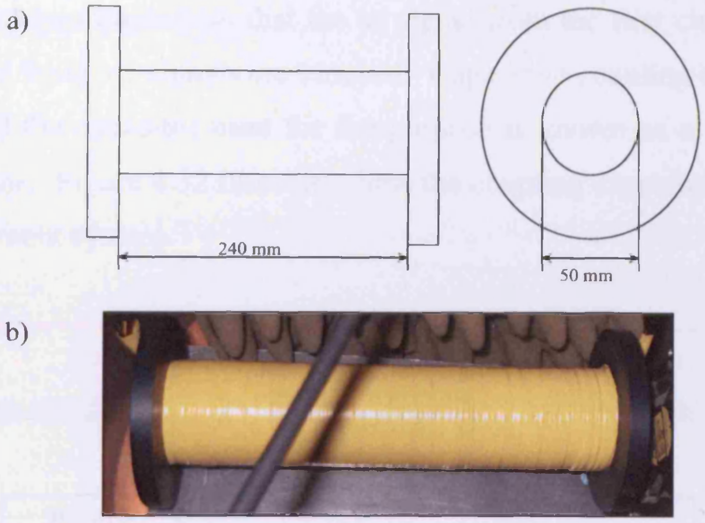

Figure 4.30. Diagram of the a) bobbin created for the air-cored transformer b) air-cored transformer once constructed

Once the air-cored transformer was built, it was placed inside a ferromagnetic shielding tube as shown in figure 4.31 together with a cooling fan.

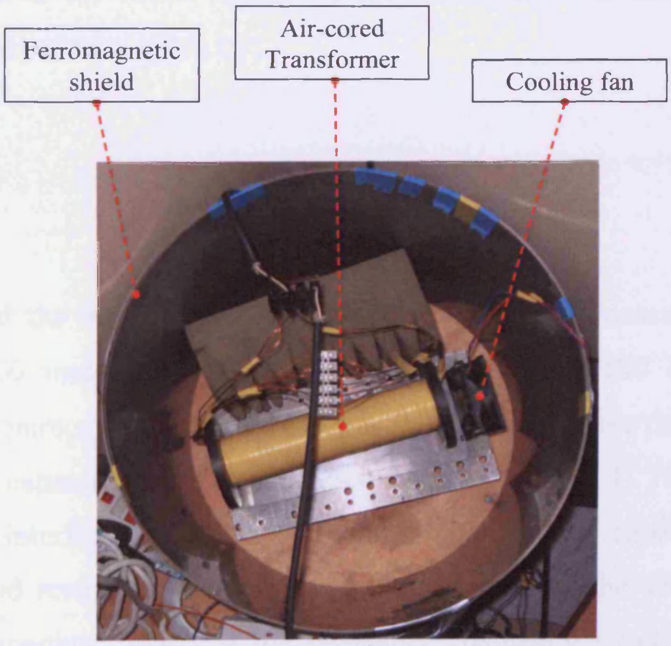

Figure 4.31. Air-cored transformer inside a ferromagnetic shielding tube, with a cooling fan

4.10.2. AC coupling capacitor

Because capacitors pass ac signals but block dc signals, they are often used to separate ac and dc components of a signal. In analogue circuits, a coupling capacitor is used to connect two circuits so that the ac signal from the first circuit can pass to the second circuit while dc signals are blocked. Capacitive coupling is also known as *AC coupling* and the capacitor used for the purpose is known as a *coupling* or *DC blocking capacitor*. Figure 4.32 illustrates how the coupling capacitor is incorporated into the measurement system.

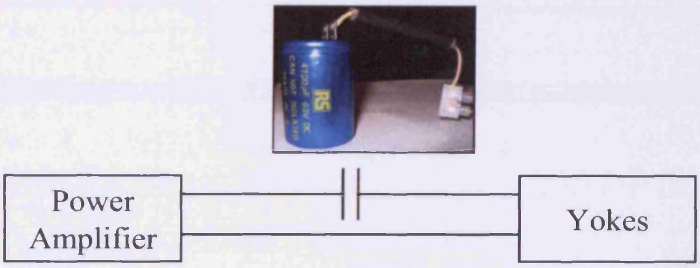

Figure 4.32. Connection diagram for coupling capacitor

However, a major disadvantage of introducing a capacitor into the circuit is the unintentional forming of a resonance circuit. The inductance of the windings on the yokes combines with the circuit resistance and the capacitor to form an RLC circuit with a resonance frequency given by:

$$f_{resonance} = \frac{1}{2 \cdot \pi \cdot \sqrt{L \cdot C}} \qquad (4.24)$$

The inductance of the windings on the yokes was 3 mH as measured using a LCR Wayne Kerr B605 meter. A frequency range of 5 Hz - 100 Hz was required, therefore, any resonance frequency within this range would make the digital feedback fail. A 4700 μF capacitor gave a resonance frequency of 42.41 Hz, which was too low and would interfere with the frequency range. The capacitance could be decreased to avoid resonance however this would decrease the voltage that can be applied on the capacitor. Also, if the resonance frequency is increased it must be ensured that no harmonic of the input voltage has the same frequency as the resonance frequency. Therefore, a capacitance of the order 0.12 F that gave a resonance frequency of 1 Hz would have been required but it was not possible to obtain one.

4.10.3. Summary of reducing the noise produced due to the iron-cored transformer

Measurements of Barkhausen noise using the double coil sensor were compared using iron-cored transformer, air-cored transformer and coupling capacitor. The rms of the Barkhausen noise signal was calculated and is shown in figure 4.33.

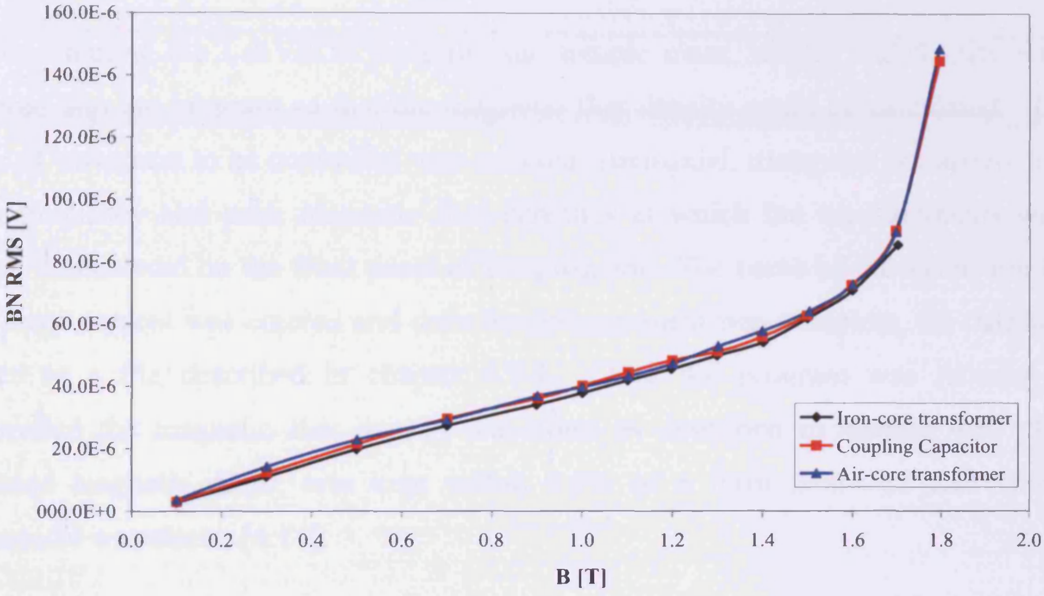

Figure 4.33. RMS Barkhausen noise, BN RMS, against magnetic flux density, *B*, at 50 Hz magnetising frequency, for grain-oriented electrical steel cut at 0° to the rolling direction, 0.27 mm thick, measured with the double B-coil sensor

It is not possible to distinguish between the three sets of measurements. It was expected that the iron-cored transformer would produce a higher rms Barkhausen noise than the air-core transformer or coupling capacitor. However, the coupling capacitor and air-cored transformer did enable measurements to be conducted at 1.8 T on grain-oriented electrical steel rather than 1.7 T with the iron-cored. The coupling capacitance was not high enough to avoid resonance and measurements could not be made below 40 Hz. Therefore, the air-cored transformer was chosen and installed into the Barkhausen noise measurement system.

4.11. Experimental procedure for Barkhausen noise measurement

The mass of each sample to be tested was measured and the cross-sectional area was calculated assuming the density provided by the manufacturer. The sample was then placed through the single flux density search coil. Depending on the sensor chosen, the sample was placed through the double coil Barkhausen noise sensor carrier or alternatively the surface sensor was placed onto the sample. The sample was then placed on one yoke and the second yoke was placed on top before the H-coil sensor was placed on the sample.

Before running the LabVIEW program, the sample mass, length, and density were entered into the program so that the magnetic flux density could be calculated. The type of waveform to be controlled was selected (sinusoidal, triangular or trapezoidal). The frequency and peak magnetic flux densities at which the measurements were taken was entered on the front panel of the program. The name of the saved file for the measurement was entered and once the measurement was complete, the data was saved to a file described in chapter 4.8.4. Once the program was running, it controlled the magnetic flux density waveform as described in chapter 4.8. The induced magnetic d*B*/d*t*, was kept within 0.5% of a form factor of 1.11 (for a sinusoidal waveform) [4.14].

Due to the use of digital feedback, the form factor could easily be set, however the d*B*/d*t* waveform would not be perfectly sinusoidal, even though it met international power loss standards by keeping within 1% of the form factor. A further limit was introduced into the program and that was to calculate the Total Harmonic Distortion (*THD*) of d*B*/d*t*. The *THD* is defined as the ratio of the rms sum of the harmonics to the amplitude of the fundamental waveform (equation 4.25).

$$THD = \frac{V_2^2 + V_3^2 + V_4^2 + \ldots\ldots + V_n^2}{V_1^2} \qquad (4.25)$$

where, V_n - the RMS voltage of harmonic n

Figure 4.34a shows the waveform of d*B*/d*t* once the form factor reaches 0.3% of 1.11, and the *THD* is equal to 7.5 %. Figure 4.34b shows the d*B*/d*t* waveform once the form factor is 0.01% of 1.11 and *THD* reaches 1.1%.

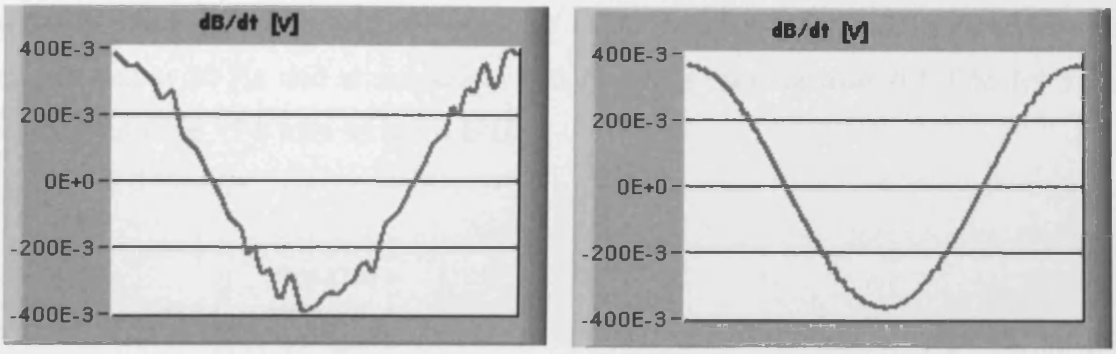

a) *b)*

Figure 4.34. d*B*/d*t* waveforms a) with *FF* of 0.3% and *THD* of 7.5%, b) with *FF* of 0.01% and *THD* of 1.1%

It is clearly seen that the d*B*/d*t* waveform was significantly distorted when using only the form factor as a limit. The waveform was clearly more sinusoidal with the reduction of *THD*. The program was set to reduce the *THD* to ±2% [4.17] and once the *THD* and *FF* of d*B*/d*t* has reached the set limits, measurements were taken.

In addition to the Barkhausen analysis described in chapter 5.10, the program also calculates the total power loss (Eq. 4.26) of the sample, and the relative permeability (Eq. 4.27) at each flux density.

$$Total\ \ Power\ \ Loss\ = \frac{f}{D}\cdot\int(H\cdot\frac{dB}{dt})\ \ dt \tag{4.26}$$

$$\mu_r = \frac{B_{peak}}{4\cdot\pi\cdot10^{-7}\cdot H_{peak}} \tag{4.27}$$

Once the measured peak flux density was within 0.2% of the set peak flux density, and the *THD* and *FF* were within the set limits, the results were saved to a temporary file. Once all set measurements were taken at each peak flux density, the temporary files were read and data was inserted into a single file (chapter 4.8.4), which was used for further data analysis in Excel.

4.11.1. Dependence of sampling frequency

Figures 4.35a and 4.35b show the variation of rms Barkhausen noise with peak flux density and sampling frequency, *fs*, respectively. A (305 × 30 × 0.27) mm sample of grain-oriented 3%SiFe electrical steel cut at 90 degrees to its rolling direction was magnetised at 50 Hz and at sinusoidal flux densities ranging from 0.1 T to 1.4 T. *fs* was varied from 12.8 kHz to 102.4 kHz.

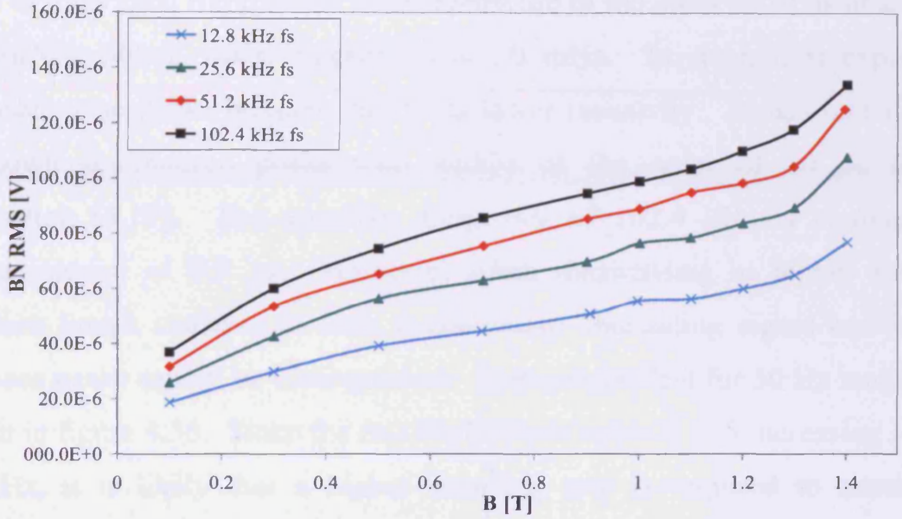

(a)

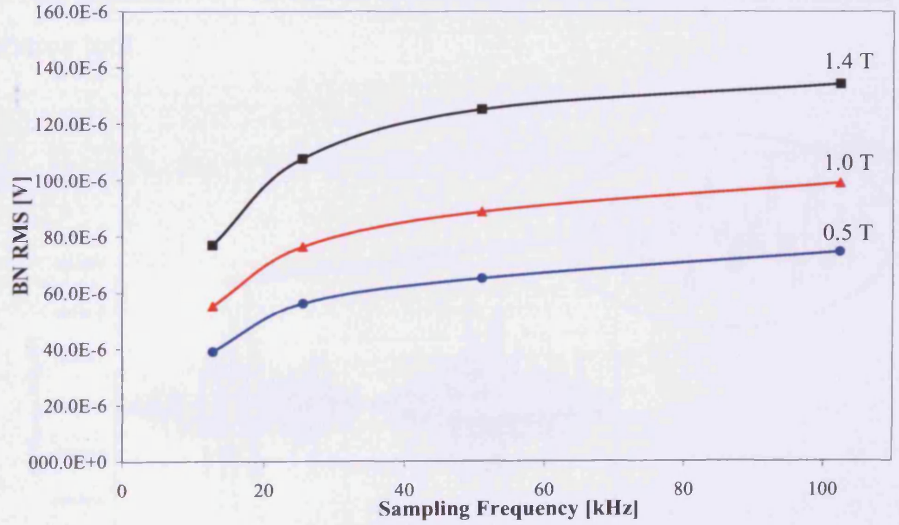

(b)

Figure 4.35. Variations of BN rms signal at 50 Hz magnetisation (a) with peak flux density at various values of *fs* (b) with *fs* at different values of peak flux density.

The rms value, total sum of amplitudes, power spectrum and kurtosis were determined for the Barkhausen noise signal. Similar trends were seen for each analysis method so only the rms analysis is shown.

As *fs* increases, the rms Barkhausen noise also increases but then begins to plateau as *fs* approaches 100 kHz as indicated in figure 4.35b. This suggests that Barkhausen noise peaks are missed at lower sampling frequencies but that the majority are captured when an *fs* of 100 kHz was used. Puppin et al [4.18] has shown that the duration of individual Barkhausen noise events are of the order of 10 μs in amorphous $Fe_{63}B_{14}Si_8Ni_{15}$ ribbon when magnetised at 50 mHz. In steel, it is expected that Barkhausen noise peaks broaden due to its lower resistivity. Measurements on iron have shown Barkhausen peaks with widths of the order of 50 μs for 3 Hz magnetisation [4.19]. The sampling frequency of 102.4 kHz is equivalent to a sampling interval of 9.8 μs. However, when magnetising at higher frequencies Barkhausen jumps coalesce to form a continuous fluctuating signal and individual Barkhausen peaks cannot be distinguished. This was evident for 50 Hz magnetisation as shown in figure 4.36. Since the rms Barkhausen noise is still increasing slightly at 102.4 kHz, it is likely that a higher sampling rate is required to maximise the measured Barkhausen noise signal. In practice, this is not a major problem with regard to non-destructive evaluation applications since Barkhausen analysis is mostly a comparative tool.

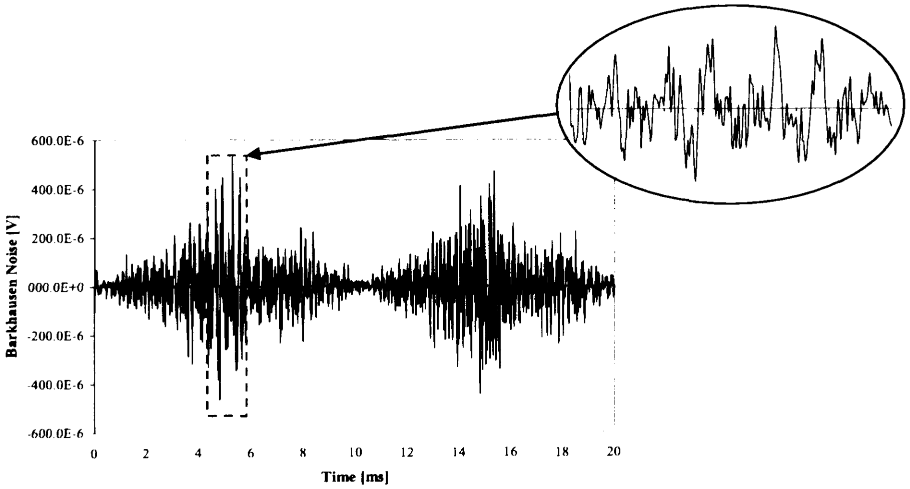

Figure 4.36. Magnified view of the Barkhausen spectrum for 50 Hz magnetisation frequency at 1.0 T for grain-oriented SiFe electrical steel

From figure 4.35a it is clear that the rms Barkhausen noise follows a similar trend with varying flux densities for various *fs*, therefore comparative measurements will be informative provided *fs* is constant. Therefore, *fs* was kept constant for all measurements at any given magnetising frequency i.e. for 50 Hz measurements the *fs* was kept constant at 102.4 kHz and for 100 Hz measurements the *fs* was kept constant at 204.8 kHz. The DAQ card does this by keeping the number of points constant for each magnetisation frequency. The maximum number of points available from the DAQ card was 2048; therefore, the maximum magnetising frequency was limited to 100 Hz because the maximum *fs* for the DAQ card was 204.8 kHz. The relationship between the number of data points measured per cycle and *fs* at a given magnetising frequency is given by:

$$Magnetising\ frequency = \frac{fs}{Number\ of\ data\ points\ per\ cycle} \qquad (4.28)$$

Therefore, the magnetisation frequency range was limited to between 5 Hz and 100 Hz.

4.12. Investigation of Barkhausen noise sensors

Parameters of the two Barkhausen noise sensors used in the investigation were investigated. With the double B-coil wound in series opposition, the effect of the separation distance between the two coils on the Barkhausen noise signal was investigated. With the ferrite surface sensor, the effects of changing the ferrite length was investigated.

4.12.1. Effect of the separation distance between the two coils on the Barkhausen noise signal

The double B-coil configuration picks up higher Barkhausen noise over a greater sample volume than the single coil method. However, it has been found that increasing the distance between the coils increases the Barkhausen noise signal [4.17]. Puppin et al. [4.18] used two independent coils to detect Barkhausen noise and found that the signals induced in the coils were very similar when the coils were close and a progressive decrease of their correlation was observed when the coils were moved apart as shown in figure 4.37.

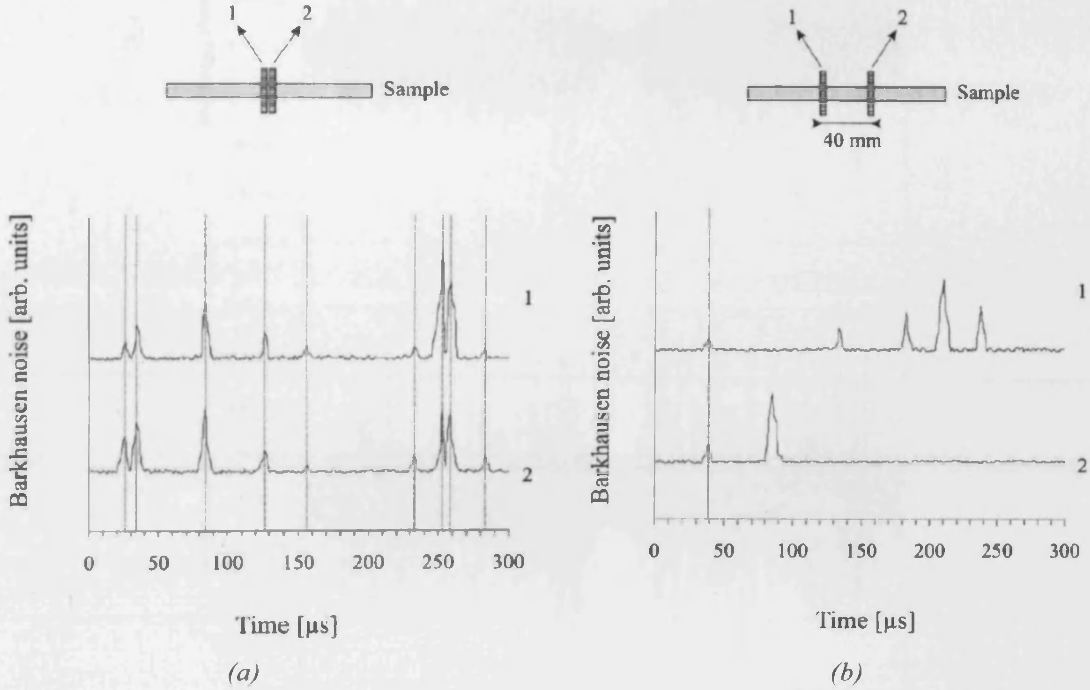

(a) *(b)*

Figure 4.37. Amorphous ribbon $Fe_{53}B_{14}Si_8Ni_{15}$, at magnetising frequency of 0.05 Hz (a) Signals when the coils are positioned nearby (b) Signals when the coils are placed at a distance of 40 mm [4.18]

The result of this effect was also observed in this investigation using the double B-coil sensor. When the distance between the coils was increased, the effective cancellation of the Barkhausen noise signal decreased resulting in an overall increase in the Barkhausen noise signal.

A strip of grain oriented 3%SiFe electrical steel (303 mm × 30 mm × 0.27 mm) cut parallel to its rolling direction, was magnetised sinusoidally at 50 Hz and at peak flux densities in the range 0.3 - 1.8 T. The separation distance between the adjacent ends of the two pick-up coils was varied from 5 mm to 40 mm. Two identical single search coils with dimensions described in chapter 4.4.1 were used.

Figure 4.38 shows Barkhausen noise distributions for two coil separations. Larger Barkhausen noise amplitudes are seen for a 40 mm coil separation. The difference was even clearer when rms values were calculated. For a 5 mm separation distance, the rms Barkhausen noise was 36.1 μV compared to 91.0 μV for a 40 mm separation.

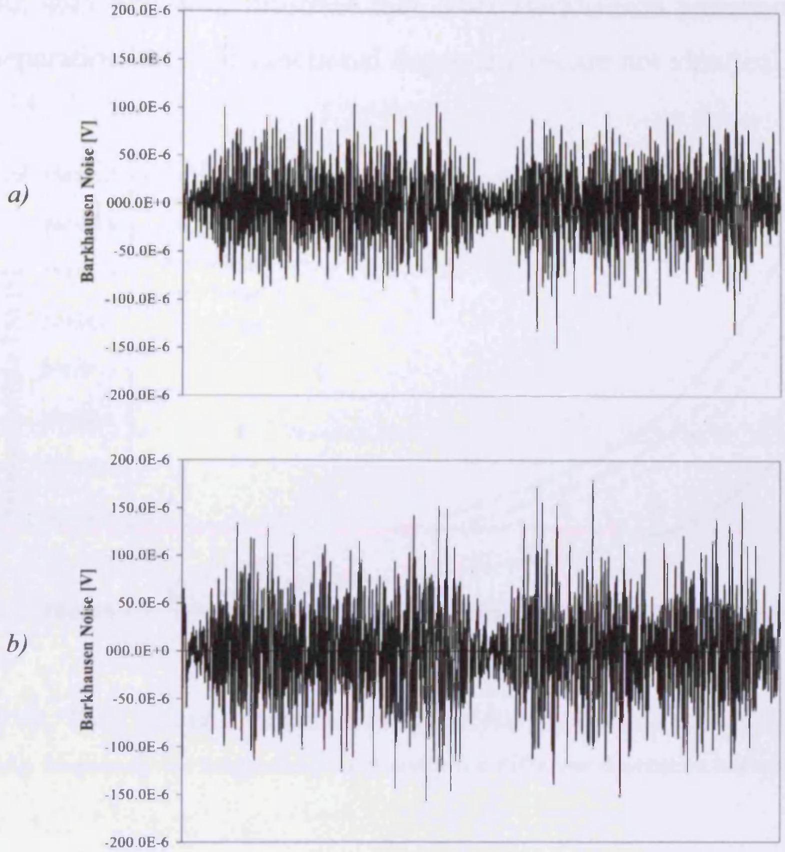

Figure 4.38. Barkhausen noise spectrum at 50 Hz magnetising frequency and 1.2 T (a) separation distance of 5 mm (b) 40 mm

Figure 4.39 shows the variation of rms Barkhausen noise with peak flux density. The noise increases significantly as the separation between the two pick-up coils increases.

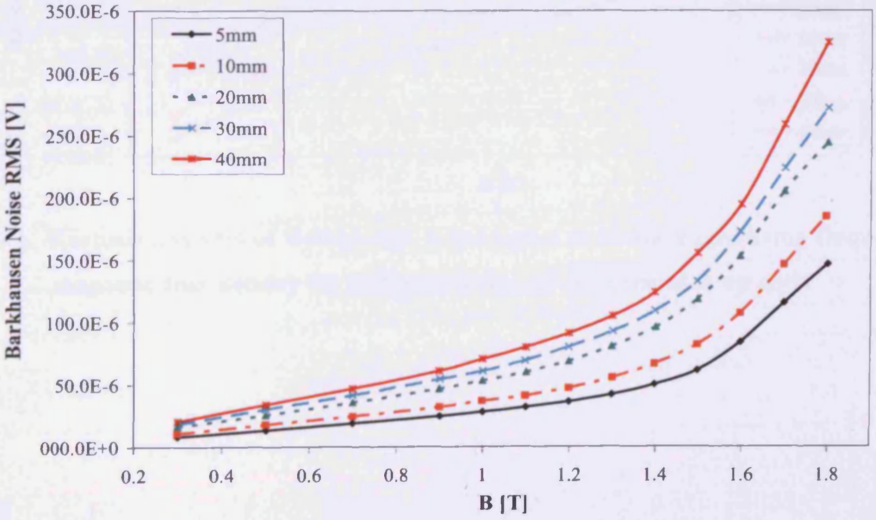

Figure 4.39. RMS analysis of Barkhausen noise signal at 50 Hz magnetising frequency vs. magnetic flux density for different distances between pick up coils

Figure 4.40, 4.41 and 4.42 illustrate that other Barkhausen parameters also change with coil separation but their functional dependencies are not identical.

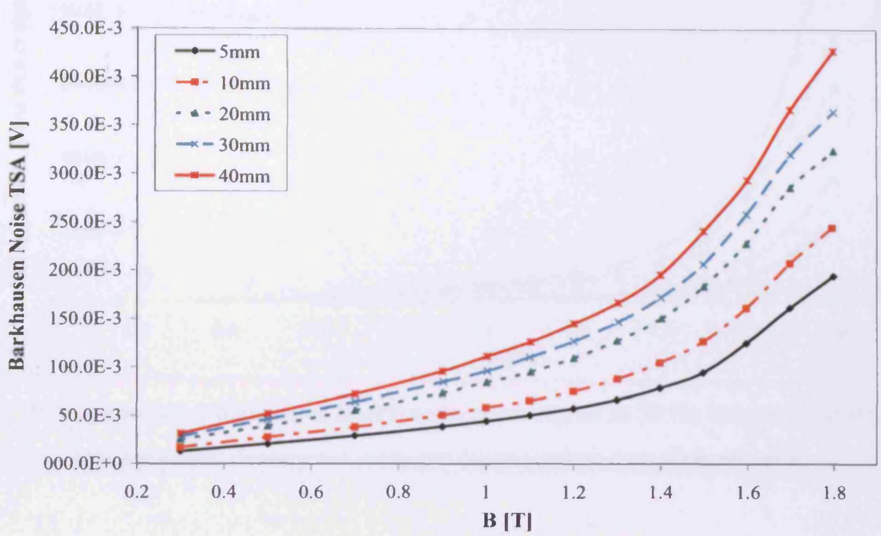

Figure 4.40. Total sum of amplitudes (TSA) analysis of Barkhausen noise signal at 50 Hz magnetising frequency vs. magnetic flux density for different distances between pick up coils

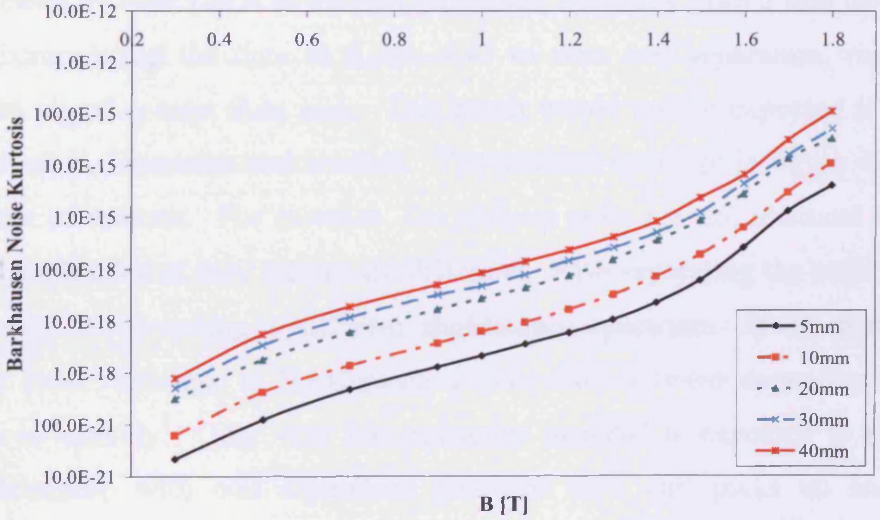

Figure 4.41. Kurtosis analysis of Barkhausen noise signal at 50 Hz magnetising frequency vs. magnetic flux density for different distances between pick up coils

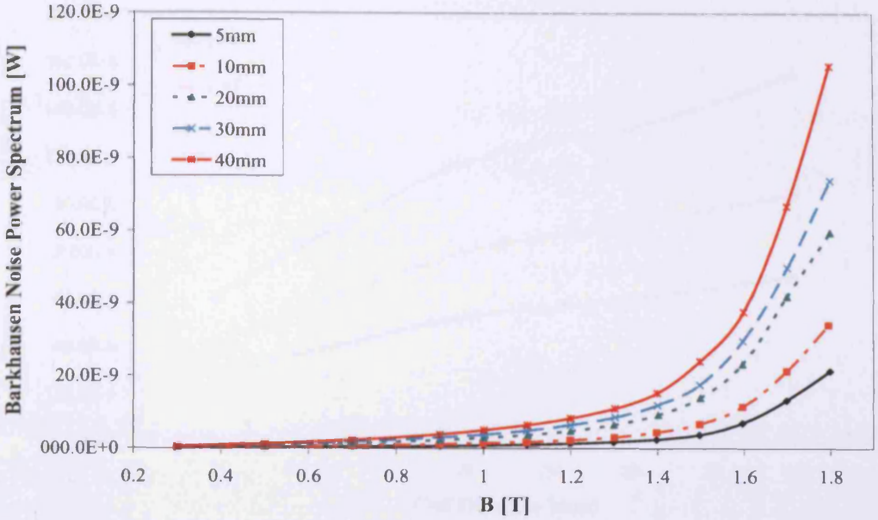

Figure 4.42. Power spectrum analysis of Barkhausen noise signal at 50 Hz magnetising frequency vs. magnetic flux density for different distances between pick up coils

The results shown in figure 4.40 are indicative of a spatially varying Barkhausen noise spectrum, as previously stated [4.18]. In this case, the degree of Barkhausen noise cancellation decreases with coil separation. For example, the rms Barkhausen noise increases by over 120% as the coil separation increases from 5 mm to 40 mm at 1.8 T. Extrapolating the data in figure 4.43 to zero coil separation, results in a Barkhausen signal greater than zero. This result would not be expected if the coils were identical in dimension and location. The positive intercept in figure 4.43 is due to a number of reasons. For instance, the pick-up coils are not identical therefore, measured amplitudes of their output are different. Also separating the coils naturally leads to each coil detecting a different Barkhausen spectrum. If the material has significant local variations in Barkhausen activity then a linear dependence on coil separation is unlikely. Only very homogeneous material is expected to produce a linear relationship with coil separation provided each coil picks up an average Barkhausen emission, which is representative of the material as a whole.

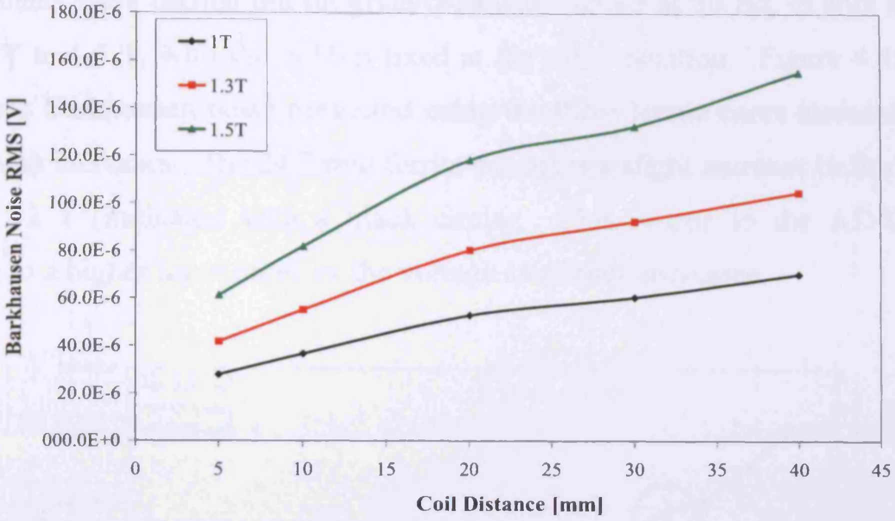

Figure 4.43. RMS analysis of Barkhausen noise signal at 50 Hz magnetising frequency vs. distance between pick up coils at 1 T, 1.3 T and 1.5 T

4.12.2. *Effect of changing the ferrite core length on the Barkhausen noise signal*

The surface ferrite sensor detects the Barkhausen noise component in the Z-plane (i.e. plane perpendicular to the sample surface) of the sample. The sensor supplied by Stresstech Oy had interchangeable ferrite cores of lengths 10.0, 12.9 and 24.7 mm and diameter of 3.0 mm, as shown in figure 4.44. The two bobbins were 8.0 mm in height and wound with 1000 and 500 turns of 0.06 mm diameter enamelled copper wire. It was assumed that the measured voltage signal from the coil was not affected by the ferrite length as long as the ferrite is of the same diameter. The validity of this assumption was tested, as described below.

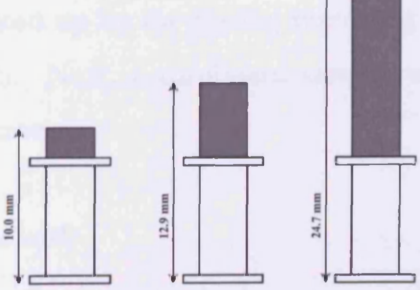

Figure 4.44. Ferrite cores used in the investigation

Measurements were carried out on grain-oriented 3%SiFe at 50 Hz, at flux densities from 0.1 T to 1.5 T, with the bobbin fixed at the same position. Figure 4.45 shows that the rms Barkhausen noise measured using the three ferrite cores increases as the ferrite length increases. The 24.7 mm ferrite produces a slight increase in Barkhausen noise at 1.2 T (indicated with a black circle). This is due to the AD/DA card switching to a higher input range as the voltage amplitude increases.

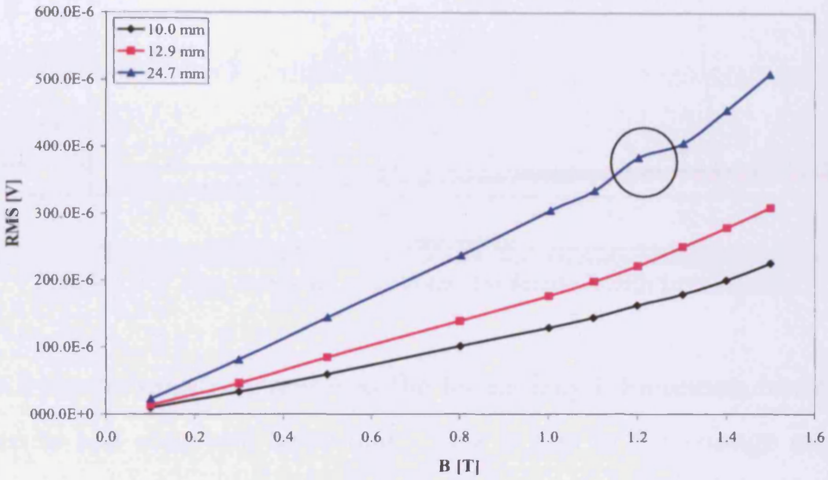

Figure 4.45. Variation of RMS Barkhausen noise with flux density (50 Hz) using the three ferrite core lengths

The measured voltage amplitude unexpectedly increases with the ferrite core length. The sample was replaced by a non-magnetic material to investigate if this effect is due to the double yoke configuration. By using a non-magnetic sample, low flux was introduced at the lower end of the ferrite (nearest to the sample) hence, any induced signal would be from any stray field received from the top yoke (nearest to the top of the ferrite core). Next, the top yoke was removed and only the bottom yoke was in place when the grain-oriented 3%SiFe sample was magnetised. If any stray field from the top yoke had been picked up by the ferrite, removing it would cause no voltage increase with ferrite length. Next, a cardboard sample was used to investigate the reason for the voltage increase.

4.12.2.1. Non-magnetic sample

A cardboard sample was cut to the dimensions as an Epstein strip. A sinusoidal 50 Hz input voltage was increased from 1 V to 10 V, in 0.5 V steps. The bobbin was placed at the centre of the sample. Figure 4.46 shows how the signal from the ferrite varies with length.

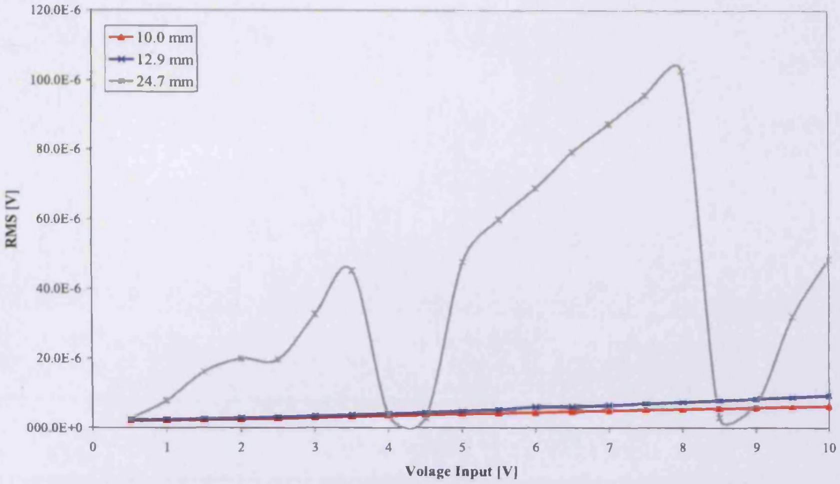

Figure 4.46. Non-magnetic sample test for ferrite length investigation

The voltage from the sensor increases as the ferrite length increases, however the 24.7 mm long ferrite had abnormal behaviour. This is due to the voltage increase in the sensor, hence the voltage range on the measurement card changing. This voltage range changing is obviously a major problem with this DAQ card.

4.12.2.2. Using a single yoke system to investigate the effect of changing the ferrite core length on the Barkhausen noise signal

A grain-oriented 3%SiFe sample was magnetised at 50 Hz from 0.2 T to 1.7 T, using a single yoke whose dimensions are given in chapter 4.8.2.

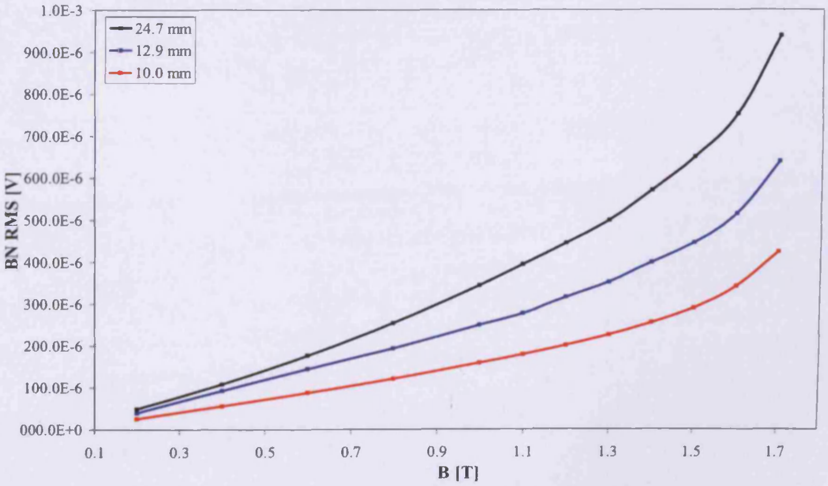

Figure 4.47. Ferrite length test with a single yoke configuration

The same correlation can be seen with the single core test (figure 4.47) as was seen with the double yoke configuration (figure 4.45). From this result, it can be concluded, that there is no stray field influence from the top yoke. Next, Finite Element Modelling (FEM) was undertaken to investigate the reason for the voltage increase.

4.12.2.3. Using finite element modelling to investigate the effect of changing the ferrite core length on the Barkhausen noise signal

The Vector Fields OPERA-3d finite element package was used for this analysis. This commercial FEM packages have three main elements [4.20]:

1. A ***pre-processor***, which enables the user to define the problem's geometry and specify boundary conditions and sources.

2. A ***solver***, for constructing the system of algebraic equations, which model the physical situation mathematically, and producing solutions. There are three main types covering the power frequency area, the Magnetostatic solver, the Time-harmonics solver and the Transient solver. In this investigation, the Magnetostatic solver [4.21] was used. The field equations are time invariant magnetic field equations where the source field is constant with no induced current.

3. A ***post-processor***, allows the analysis of results and enables the calculated fields to be visualised and manipulated.

Modelling the problem involves a number of issues related to the geometry of the device under consideration and the expected characteristics of the fields. Therefore, planning of the model is a relevant part of the modelling process. The analysis of the entire structure is computationally expensive and a great deal of time was saved due to the symmetry of the problem, a quarter model of the magnetic circuit was implemented.

Figure 4.48 shows the post-processor ¼ diagram of the model. The sample parameters used in the model were of non-oriented 3%SiFe electrical steel (30 mm × 300 mm × 0.5 mm), magnetised at 1.47 T, with a sensor ferrite core length of 24 mm. The yoke material modelled was 3%SiFe grain-oriented electrical steel.

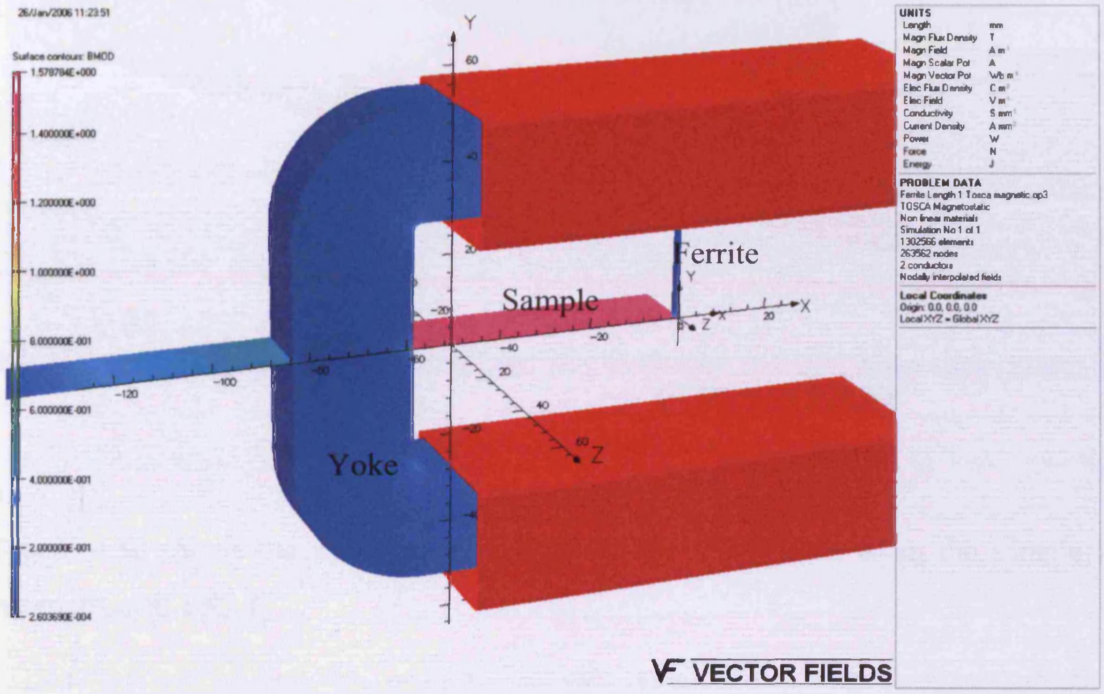

Figure 4.48. Post-processor diagram of ¼ model, sample magnetised at 1.47 T

Figure 4.49 shows an expanded image of the ferrite sensor on the top surface of the sample. It can be seen that the magnetic flux density below the ferrite is slightly less than the sample's average peak flux density of 1.47 T.

Figure 4.49. Ferrite sensor on sample, expanded image

Figure 4.50 shows the flux density vectors in the ferrite core when the sample is magnetised at 1.47 T.

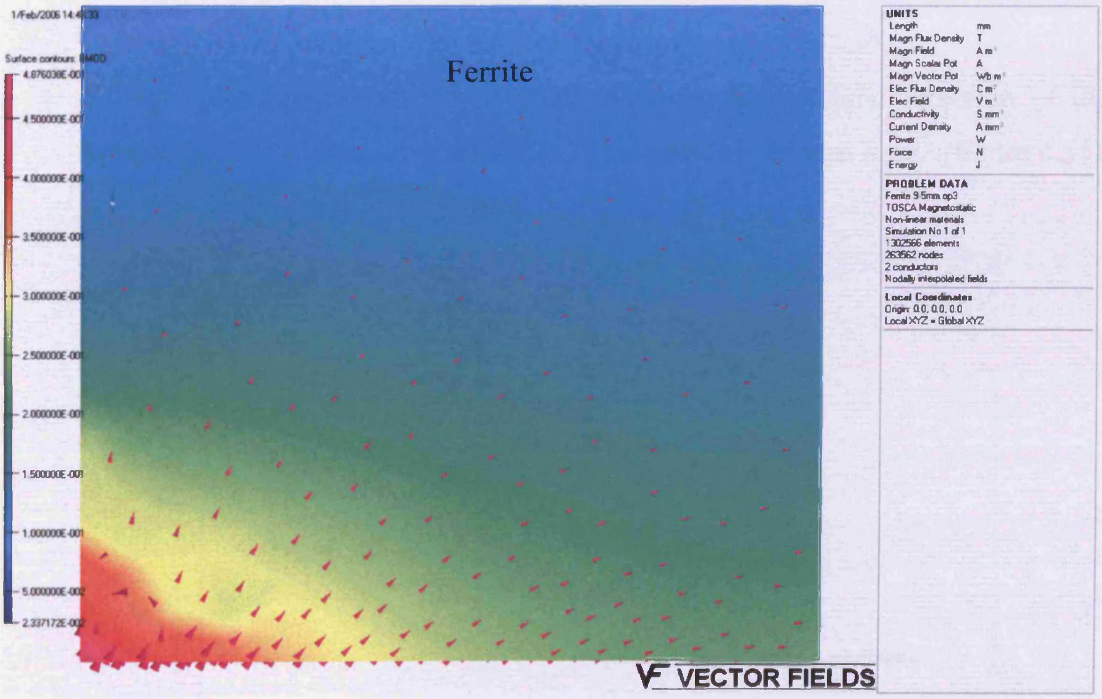

Figure 4.50. Flux density distribution in the ferrite core

Magnetic flux density variation along chosen paths was obtained using the path investigation method. Four locations, two on the sample and two on the ferrite sensor, were chosen as shown in figure 4.51.

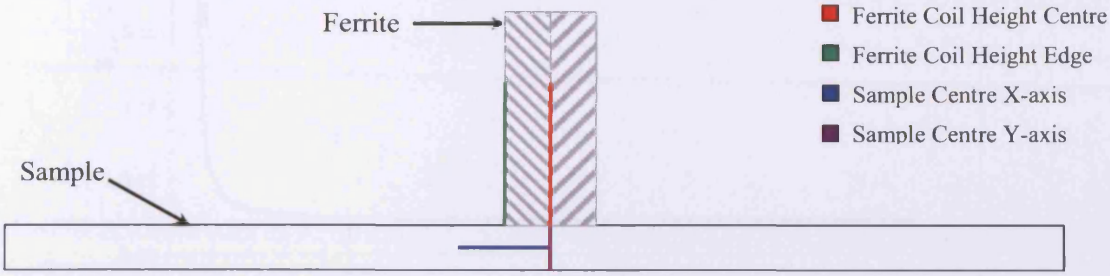

Figure 4.51. Locations of paths chosen for presentation of flux density variation

The reasons for choosing these locations and the definition of the paths are:

1. "Ferrite coil height centre", is that the path is on the axis of the bobbin along the ferrite length. The path is 8 mm long. (figure 4.52)
2. "Ferrite coil height edge", is along the outer vertical surface of the ferrite length. The path is 8 mm long. (figure 4.53)
3. "Sample centre x-axis", is that the path that is centrally along the longitudinal direction of the sample. The path is 3 mm long. (figure 4.54)
4. "Sample centre y-axis", is the path along the longitudinal direction of the sample, on the surface of the sample. The path is 0.46 mm long. (figure 4.55)

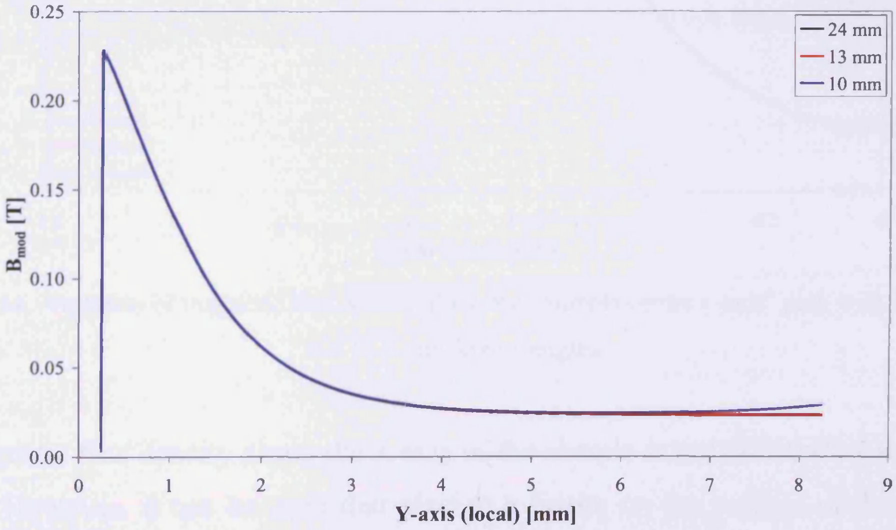

Figure 4.52. Variation of magnetic flux density along the "Ferrite Coil Height Centre" path with 24.7, 12.9 and 10.0 mm ferrite lengths

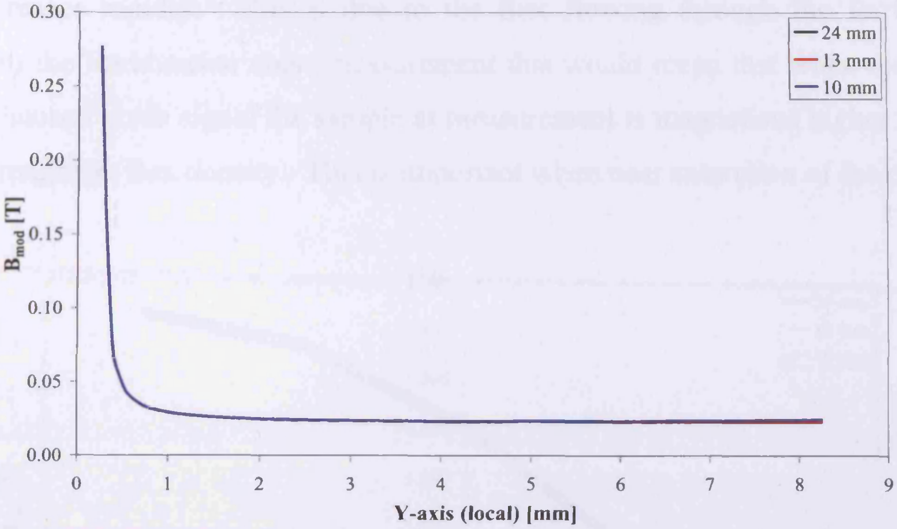

Figure 4.53. Variation of magnetic flux density along the "Ferrite Coil Height Edge" path with 24.7, 12.9 and 10.0 mm ferrite lengths

The same characteristics are apparent along the central vertical axis and outside surface of the ferrite for all ferrite lengths. The flux density is high within the ferrite near the sample and decreases with increasing distance from the sample.

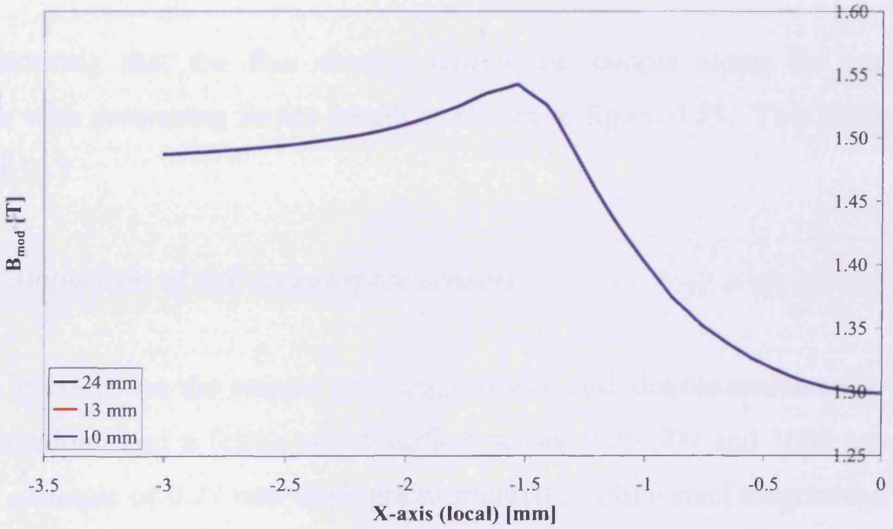

Figure 4.54. Variation of magnetic flux density along the "Sample centre x-axis" path with 24.7, 12.9 and 10.0 mm ferrite lengths

The magnetic flux density along the x-axis of the sample is not affected by the ferrite length. However, it can be seen that placing a ferrite on the surface of the sample, causes the magnetic flux density in the sample to increase to a peak on its edge and then decreases rapidly. This is due to the flux flowing through the ferrite also. Related to the Barkhausen noise measurement this would mean that when measuring the Barkhausen noise signal the sample at measurement is magnetised higher than the average magnetic flux density. This is important when near saturation of the material.

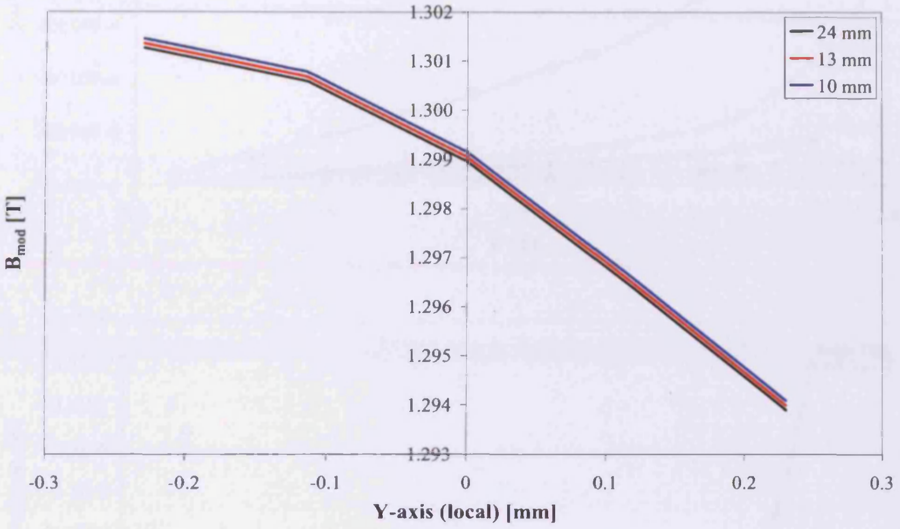

Figure 4.55. Variation of magnetic flux density along the "Sample centre y-axis" path with 24.7, 12.9 and 10.0 mm ferrite lengths (the ferrite is at +0.22 mm)

It is interesting that the flux density within the sample along the vertical axis decreases with decreasing ferrite length as shown in figure 4.55. This is discussed in chapter 4.12.3.

4.12.3. Comparison of coil and surface sensors

Figure 4.56 compares the outputs of a single search coil, double search coils wound in series opposition and a ferrite cored surface sensor with 500 and 1000 turn pick-up coils for a sample of 0.27 mm thick grain-oriented 3%SiFe steel magnetised from 0.3 T to 1.8 T at 50 Hz (the results from kurtosis and TSA analysis were similar).

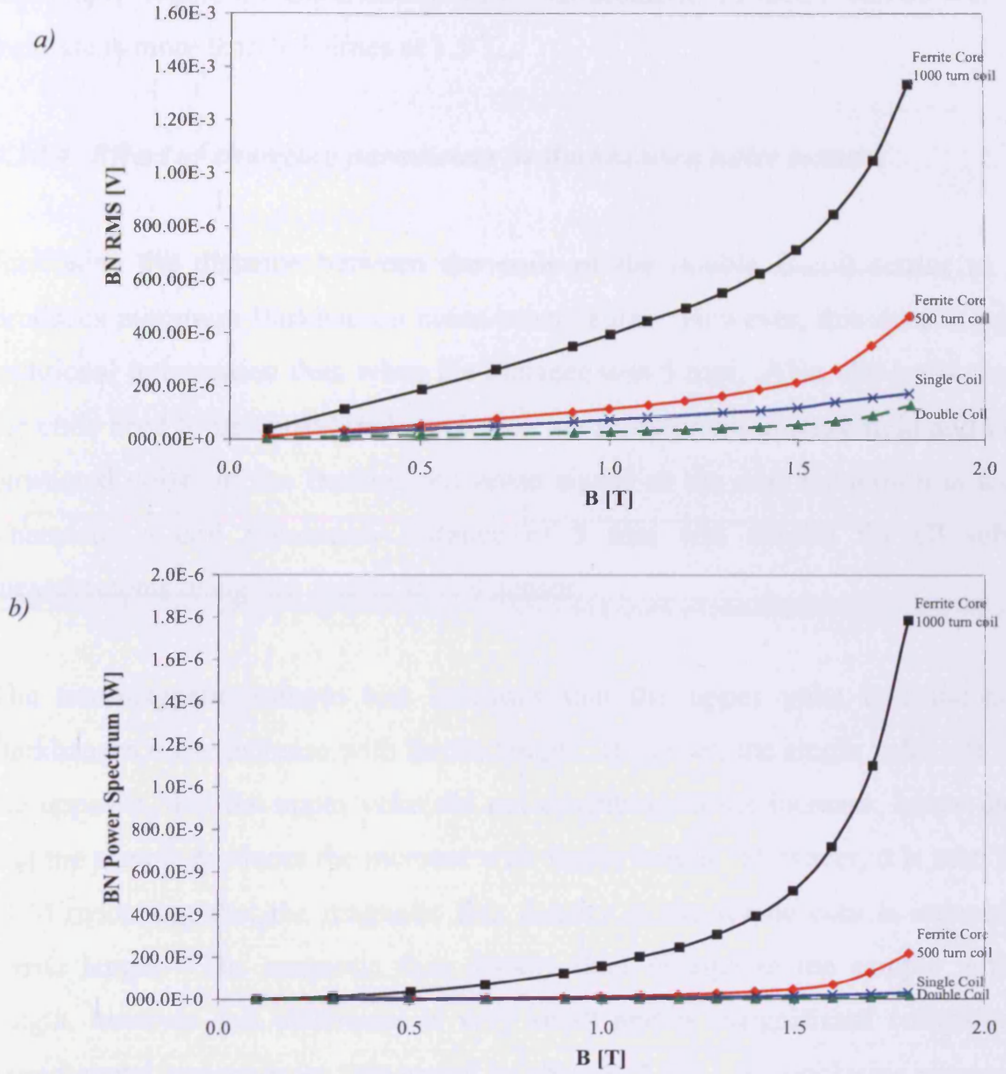

Figure 4.56. Variation of a) BN RMS b) BN power spectrum outputs of the sensors with flux density at 50 Hz in grain-oriented 3% silicon steel (core length of 13 mm in both ferrite sensors)

The magnitude of the output signal depends on the sensor characteristics as well as the Barkhausen noise events so the results are normalized as shown in figure 4.56. The trends with the ferrite cored surface probe are very similar to those of the enwrapping coils although they are oriented perpendicular to each other. The change of rms Barkhausen noise value with flux density detected by the ferrite cored sensor with 1000 turn pick-up coil is highest whereas the double search coil is the lowest. The ferrite cored sensor outputs increase rapidly at high flux density indicating that the different sensors are effectively picking up different Barkhausen noise events. In the case of the double coil, some events will be lost in the subtraction. Also increasing the number of turns in the ferrite cored sensor from 500 to 1000 turns does not simply double the Barkhausen noise measurement. In fact, it can be seen that the increase is more than 3.3 times at 1.5 T.

4.12.4. Effect of changing parameters in Barkhausen noise sensors

Increasing the distance between the coils of the double B-coil sensor to 40 mm produces minimum Barkhausen noise cancellation. However, this does not give any additional information than when the distance was 5 mm. Also, the leads connecting the coils need to be considered since they are more prone to stray field and increased unwanted noise on the Barkhausen noise signal as the coil separation is increased. Therefore, a coil separation distance of 5 mm was chosen for all subsequent measurements using the double B-coil sensor.

The non-magnetic sample test indicates that the upper yoke contributes to the Barkhausen noise increase with ferrite length. However, the single yoke test indicates the opposite, that the upper yoke did not contribute to the increase, hence indicating that the sample produces the increase with ferrite length. However, it is seen from the FEM modelling that the magnetic flux density in the ferrite core is independent of ferrite length. The magnetic flux density does change in the sample with ferrite length, however this difference is very small and is insignificant compared to the experimental uncertainties (discussed in chapter 4.15). A conclusive answer cannot be derived from this FEM analysis, therefore further modelling is required. In addition, it needs to be determined whether the permeability of each ferrite core was same since this can influence the Barkhausen noise signal measured. Because of the voltage range changes with the 24 mm ferrite length measurements and the small 4 mm gap between the ferrite and the above yoke, the 12.9 mm ferrite was used for all subsequent measurements.

The increase in turns from 500 to 1000 does not simply double the Barkhausen noise signal in the surface sensor. This may be due to the area enclosed by the coil being larger and the Barkhausen noise signal is magnetically amplified with more turns hence the data acquisition card can measure more Barkhausen noise jump signals. There may be other factors (e.g. coil construction) that increase the Barkhausen noise signal, further investigation is needed.

4.13. Uniformity of magnetisation in the sample

A common method of magnetising an electrical steel sample is by means of a solenoid [4.22]. However, in this investigation yokes were magnetised and used to inject flux into the sample. By using this method, the sample and not the sensor core (i.e. ferrite) is magnetised. The uniformity of the flux density, *b*, was measured along the length of sample. Figure 4.57 shows the locations of an 80 turn search coil placed around the 3%SiFe electrical steel sample. All three coils were connected to a DAQ card and processed in LabVIEW.

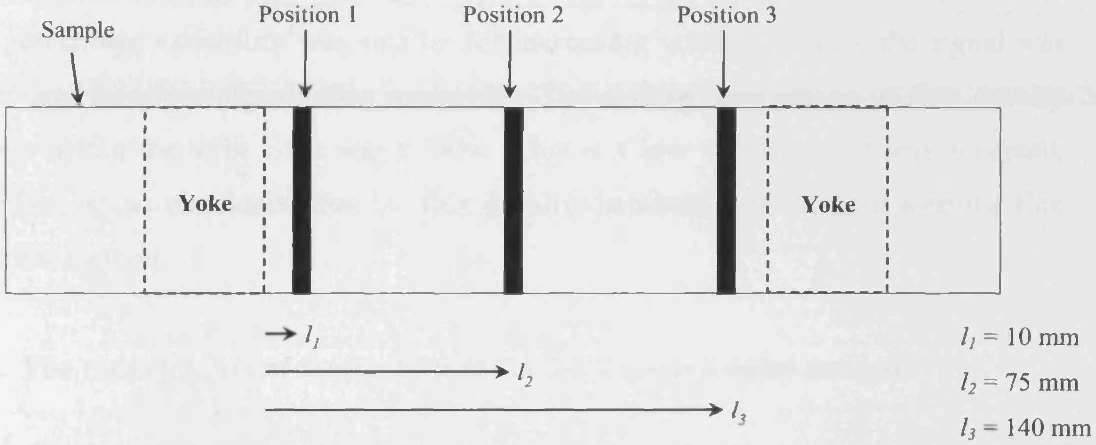

Figure 4.57. Diagram of the position of the B-coils for the flux density uniformity test

The input voltage to the yokes was increased from 0.1 V to 1.5 V at 50 Hz, which was found to be stable to 0.05%, the flux density was calculated using LabVIEW. Table 4.17 shows the results measured.

Voltage Input *(V)*	**Position**	**B** *(T)*
0.1	1	0.0337
	2	0.0337
	3	0.0334
0.5	1	0.2882
	2	0.2862
	3	0.2859

1.0	1	0.7082
	2	0.7026
	3	0.7045
1.5	1	1.0995
	2	1.0968
	3	1.0959

Table 4.17. Table of flux density measurements along the sample, with 3 search coils

It can be seen that the three coils measure a percentage difference of 0.48%, 0.44%, 0.40%, and 0.17% for input voltage of 0.1 V, 0.5 V, 1.0 V and 1.5 V, respectively. The percentage variability was smaller for increasing voltage because the signal was larger and therefore signal/noise improves. The average percentage of flux density change within the three coils was 0.38%. This is a low variation and was accepted, therefore, it was concluded that the flux density distribution is uniform with the flux injection method.

4.14. The repeatability of methods used for Barkhausen noise analysis

A sinusoidal waveform can be defined by its amplitude and frequency. Unfortunately, this cannot be applied to Barkhausen noise since it has a stochastic and deterministic component. Nevertheless, a parameter must be found to simply and clearly quantify the Barkhausen noise occurring in a given magnetising cycle. The data shown in the figures in this section quantify the repeatability of each of the statistical methods used, and a repeatability of better than 98% was set being acceptable. For all analysis methods, the total percentage error from the mean at each flux density was calculated using equation 4.29, and then combined using equation 4.30.

$$S_R = \frac{1}{\bar{x}} \cdot \sqrt{\frac{\sum_{i=1}^{n_u}(x_i - \bar{x})^2}{(n_u - 1)}} \times 100 \qquad (4.29)$$

where, S_R – estimated standard deviation (in percentage), x_i - is the measured value; $\bar{x}$ - is the mean of the measured value; n_u - is the number of measurements made

$$U_S = \sqrt{U_{S1}^2 + U_{S2}^2 + U_{S3}^2 + \ldots} \tag{4.30}$$

The data presented in the figures in chapter 4.14 were obtained by measuring Barkhausen noise in grain-oriented 3%SiFe electrical steel at 50 Hz with the double B-coil sensor. The measurements were repeated five times for each set of B_{max} values.

- ***Root mean square***

Figure 4.58 shows that the rms value of Barkhausen noise is repeatable.

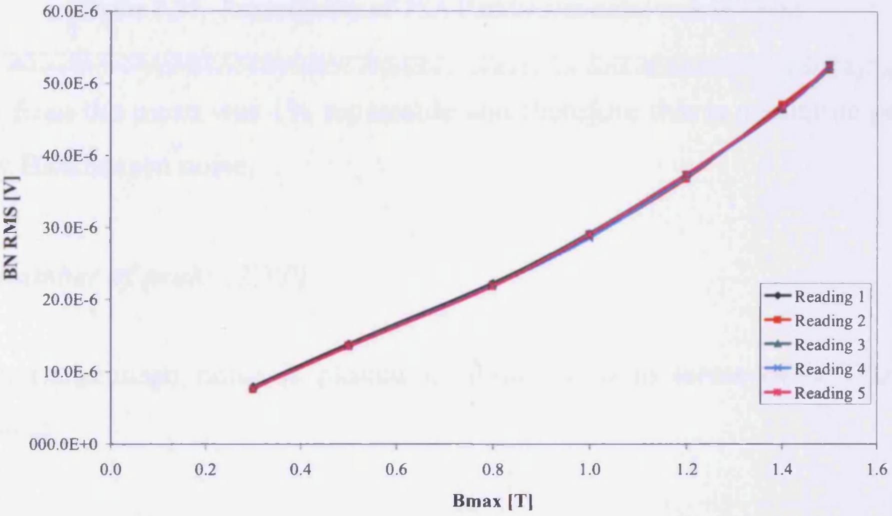

Figure 4.58. Repeatability of rms Barkhausen noise measurement

The error from the mean was 1% and therefore is a suitable parameter to classify Barkhausen noise.

- ***Total sum of amplitudes (TSA)***

The same Barkhausen noise is plotted in figure 4.59 in terms of it TSA values measurement.

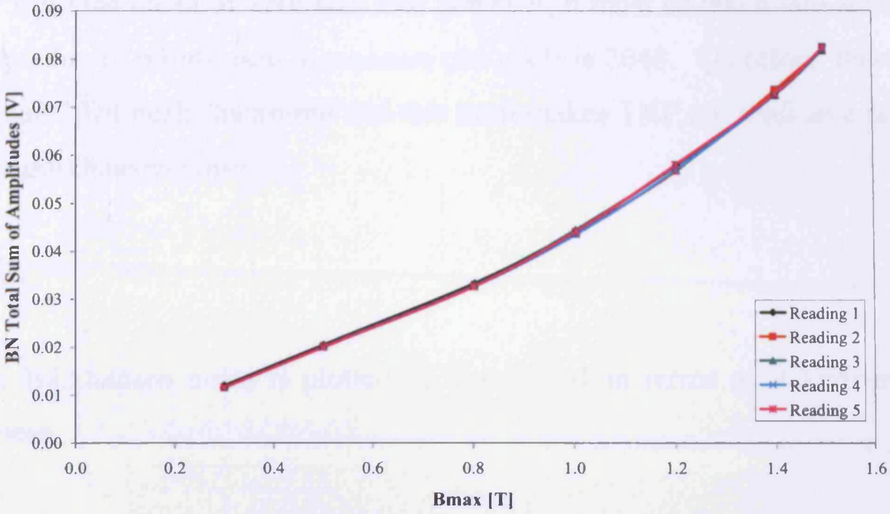

Figure 4.59. Repeatability of TSA Barkhausen noise measurement

The error from the mean was 1% repeatable and therefore this is a suitable parameter to classify Barkhausen noise.

- ***Total number of peaks (TNP)***

The same Barkhausen noise is plotted in figure 4.60 in terms of it TNP values measurement.

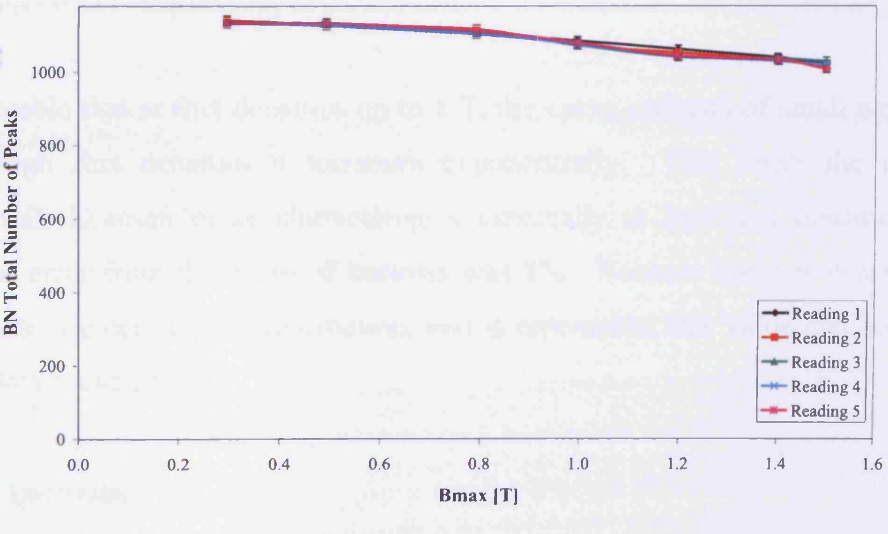

Figure 4.60. Repeatability of TNP Barkhausen noise measurement

The error from the mean of TNP was 1%; however, it must be taken into account that the total number of points used to measure one cycle is 2048. Therefore, there cannot be more than 1024 peaks measured and this limit makes TNP not a suitable parameter to classify Barkhausen noise.

- ***Kurtosis***

The same Barkhausen noise is plotted in figure 4.61 in terms of it kurtosis values measurement.

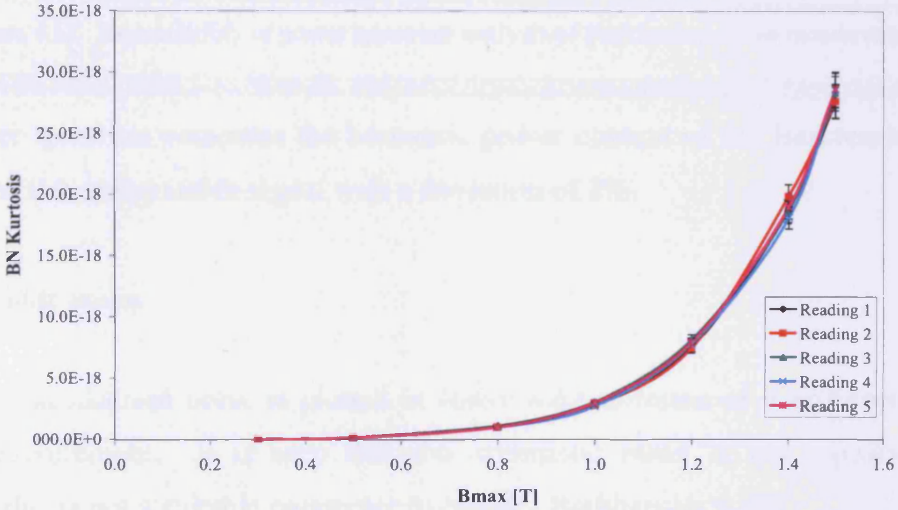

Figure 4.61. Repeatability of kurtosis analysis of Barkhausen noise measurement

It is noticeable that at flux densities up to 1 T, the curve consists of small amplitudes and for high flux densities it increases exponentially. This limits the usage to determine Barkhausen noise characteristics especially at low flux densities. The percentage error from the mean of kurtosis was 5%. Because kurtosis describes the flatness near the centre of a distribution, and is repeatable, this value can be used to classify Barkhausen noise.

- ***Power spectrum***

The same Barkhausen noise is plotted in figure 4.62 in terms of it power spectrum values measurement.

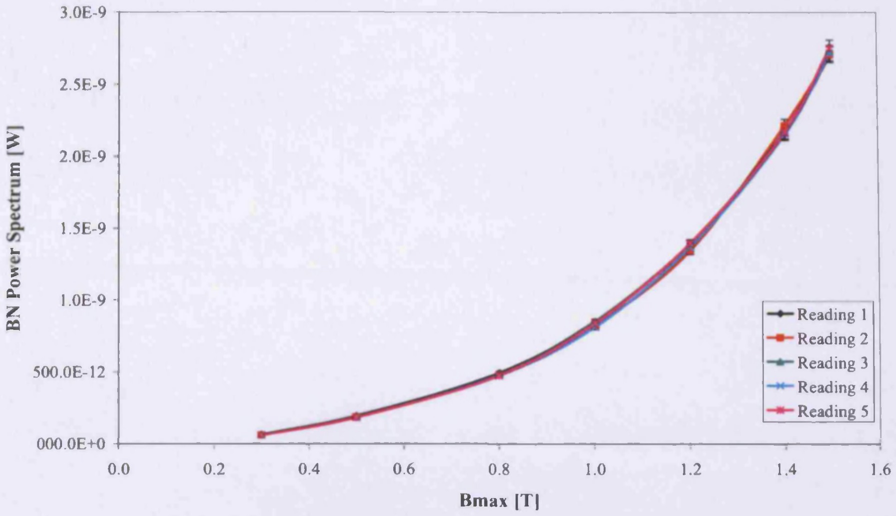

Figure 4.62. Repeatability of power spectrum analysis of Barkhausen noise measurement

The power spectrum computes the harmonic power content of the Barkhausen noise signal, and it is a repeatable signal with a deviation of 2%.

- ***Arithmetic mean***

The same Barkhausen noise is plotted in figure 4.63 in terms of it arithmetic mean values measurement. It is seen that the arithmetic mean is not repeatable and therefore this is not a suitable parameter to classify Barkhausen noise.

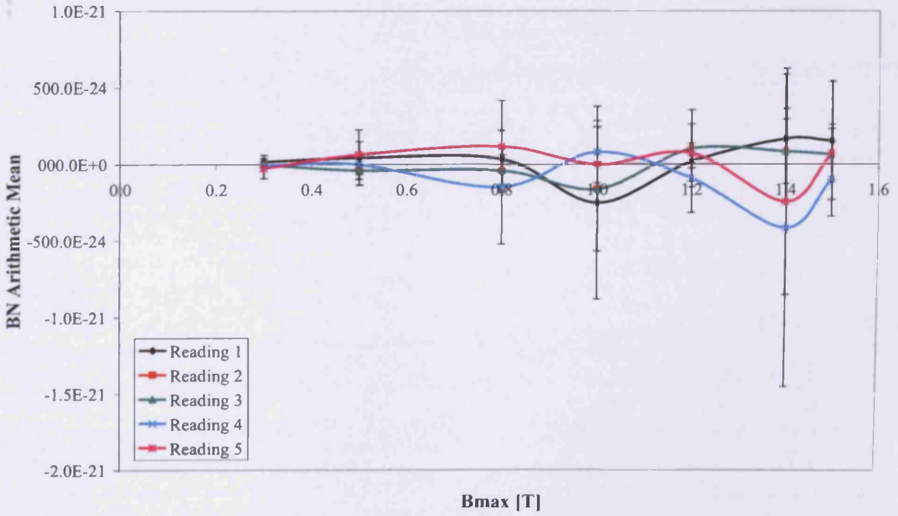

Figure 4.63. Repeatability of arithmetic mean analysis of Barkhausen noise measurement

- ***Standard deviation***

The same Barkhausen noise is plotted in figure 4.64 in terms of it standard deviation values measurement.

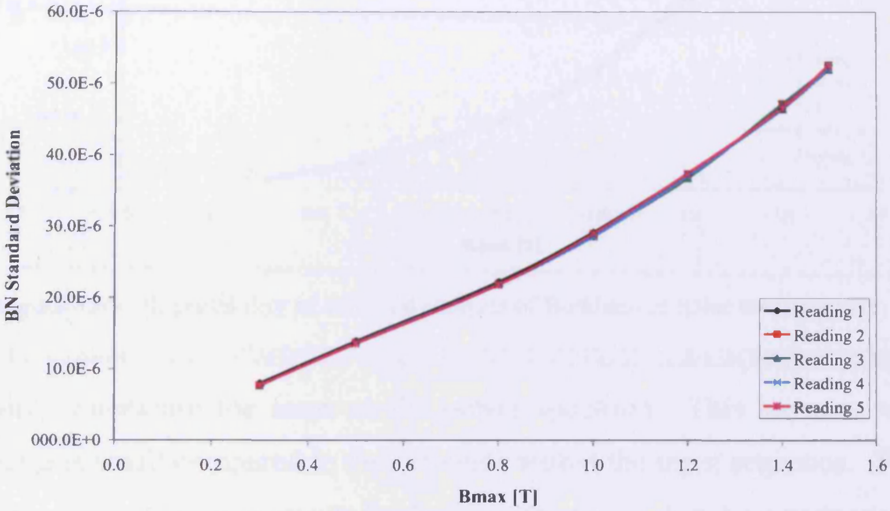

Figure 4.64. Repeatability of standard deviation analysis of Barkhausen noise measurement

The error from the mean was 1%. However, for small mean values μ, the standard deviation provides the same results as the rms calculations. The standard deviation will not produce any additional information compared to that provided by rms analysis, therefore, the standard deviation value was not used.

- ***Variance***

The same Barkhausen noise is plotted in figure 4.65 in terms of it variance values measurement.

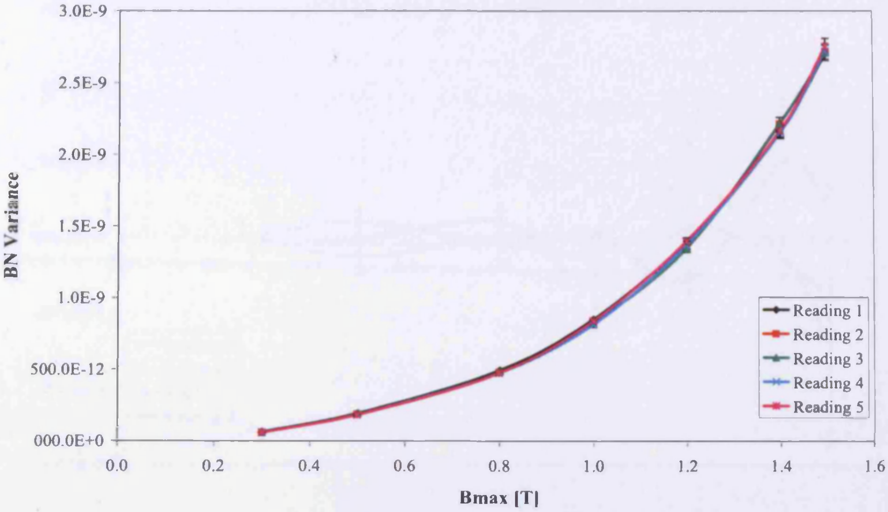

Figure 4.65. Repeatability of variance analysis of Barkhausen noise measurement

The variance values are the same as the power spectrum. This happens when the mean value μ is small compared to the elements within the input sequence. The other condition providing the same results for both parameters is that the power spectrum is obtained by squaring the magnitude of its frequency components without using the phase information. Commonly the phase information is not considered when calculating the power spectrum. The error from the mean was 2%, but because it is the same as the power spectrum it will not be used for Barkhausen noise analysis in this investigation.

- ***Median***

The same Barkhausen noise is plotted in figure 4.66 in terms of it median values measurement.

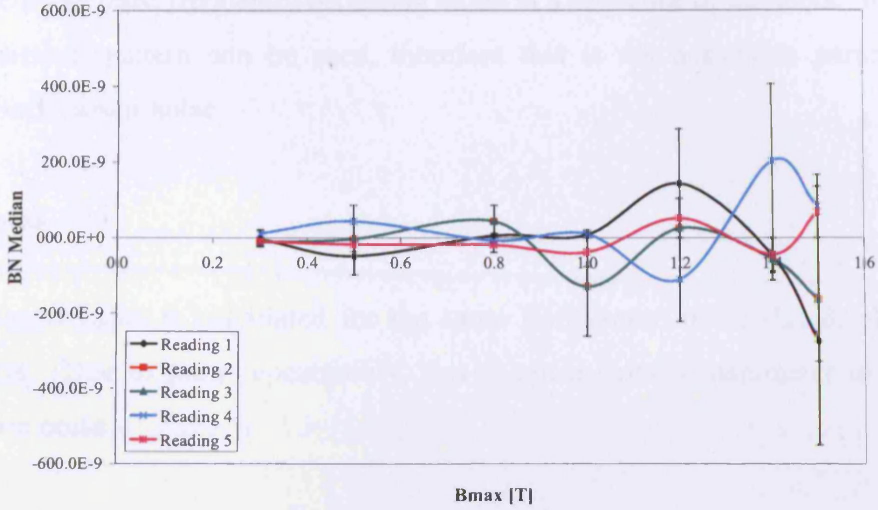

Figure 4.66. Repeatability of median analysis of Barkhausen noise measurement

Due to the stochastic nature of the Barkhausen noise signal the median value would not be repeatable.

- ***Mode***

The mode values of the measurement of the same Barkhausen noise is plotted in figure 4.67 in terms of it mode values measurement.

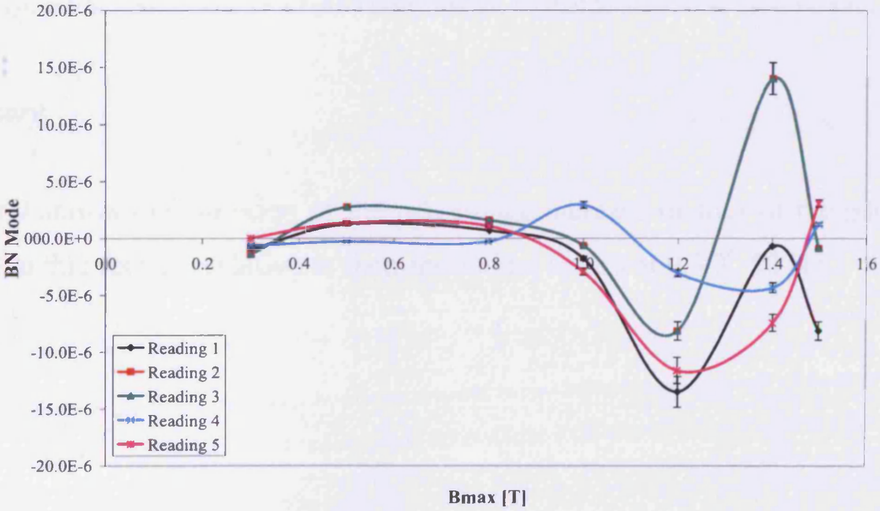

Figure 4.67. Repeatability of mode analysis of Barkhausen noise measurement

The mode is the most frequently occurring value in a sequence of numbers. It is clear that no distinct pattern can be seen, therefore this is not a suitable parameter to classify Barkhausen noise.

- ***Skewness***

The skewness value is calculated for the same Barkhausen noise signal, plotted in figure 4.68. Due to poor repeatability, this is not a suitable parameter to classify Barkhausen noise.

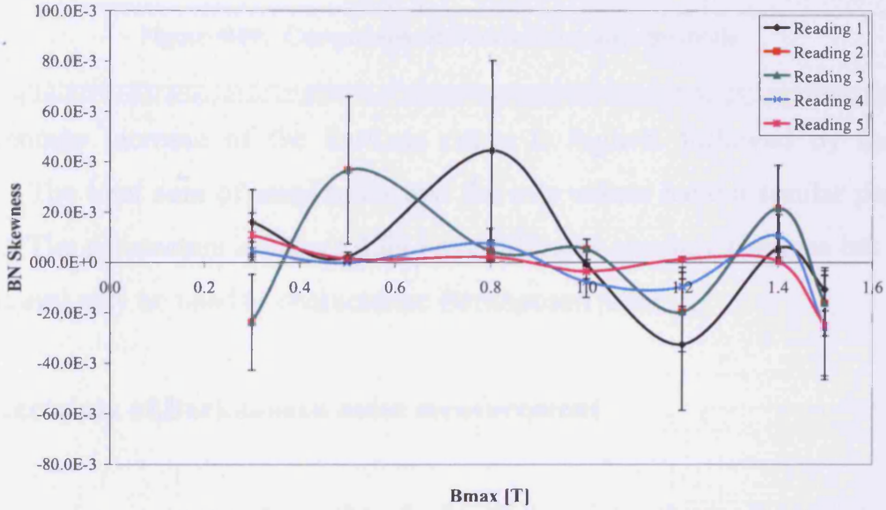

Figure 4.68. Repeatability of skewness analysis of Barkhausen noise measurement

- ***Summary***

Figure 4.69 shows the variation of the percentage increase of four of the parameters presented in this section, relative to their individual values at 0.5 T, 50 Hz.

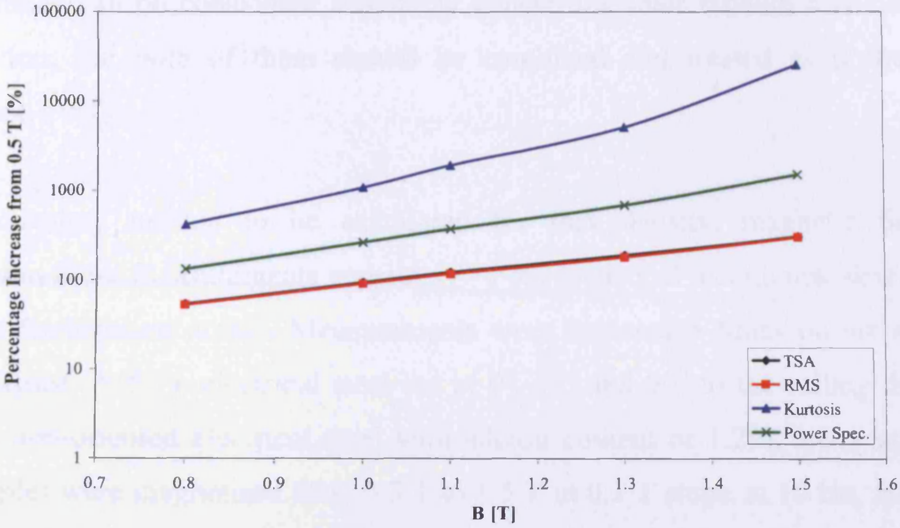

Figure 4.69. Comparison of Barkhausen noise methods

The percentage increase of the kurtosis curve is highest followed by the power spectrum. The total sum of amplitudes and the rms values have a similar percentage increases. The parameters in figure 4.69 have different absolute changes but they are repeatable and may be used to characterise Barkhausen noise.

4.15. Uncertainty of Barkhausen noise measurement

Uncertainty of measurement is the doubt that exists about the result of any measurement [4.23]. The effect that gives rise to uncertainty in measurements can be divided into two forms [4.24]: The estimation of uncertainties in the Barkhausen noise measurements is based on the types of evaluation given by the British Measurement and Testing Association [4.24].

Random – where repeating the measurement gives a randomly different result. If so, the more measurements that are made, and then averaged, a better estimate can be expected [4.23].

Systematic – where the same influence affects the result for each of the repeated measurement. In this case, nothing extra is learnt by repeating measurements. Other methods are needed to estimate uncertainties due to systematic effect, e.g. different measurements, calculations [4.23].

Uncertainties can be considered separately concerning their random and systematic contribution, but both of them should be combined and treated as if they were equivalent.

The uncertainty needed to be calculated for flux density, magnetic field and Barkhausen noise measurements separately. Four statistical techniques were used to calculate Barkhausen noise. Measurements were repeated 5 times on six samples, grain-oriented 3%SiFe electrical steel cut at 0°, 55° and 90° to the rolling direction, and also non-oriented electrical steel with silicon content of 1.2%, 3.0% and 6.5%. The samples were magnetised from 0.3 T to 1.5 T in 0.1 T steps, at 10 Hz, 50 Hz and 100 Hz magnetising frequency.

4.15.1. Random uncertainties

The estimated standard deviation (in percentage), S_R, of the measured results was calculated from equation 4.29. From S_R, the estimated standard uncertainty, u_R, of the mean was calculated from:

$$u_R = \frac{S_R}{\sqrt{n_u}} \tag{4.31}$$

However, equation 4.31 is applicable if a large number of repeat readings were taken. In this case, each measurement was repeated only 5 times ($n_u = 5$) and therefore, the uncertainty calculations need to be extended by multiplying it by the student t-factor, t, and a coverage factor, k.

Student t-factor is a statistical distribution table defined by, the ratio of the deviation of the mean of a sample of size n from an expected value, to its standard deviation. Coverage factor, k, is a number added to the measured result to give a guaranteed power level for a particular level of confidence.

The S_R was assumed to be a normal distribution with a certain level of confidence. If the confidence level is 95%, equivalent $k = 2$. The t-student factor corresponding to five measurements is given as 1.44 for coverage factor k = 2 [4.23]. Therefore, the extended uncertainty can be calculated from:

$$U_R = t \times k \times u_R \tag{4.32}$$

The calculated random uncertainty was:

Magnetic flux density uncertainty, $U_{R\text{-}B}$ = 0.07 % (4.33a)

Magnetic field uncertainty, $U_{R\text{-}H}$ = 0.97 % (4.33b)

Barkhausen noise rms uncertainty, $U_{R\text{-}BNRMS}$ = 1.39 % (4.33c)

Barkhausen noise TSA uncertainty, $U_{R\text{-}BNTSA}$ = 1.25 % (4.33d)

Barkhausen noise kurtosis uncertainty, $U_{R\text{-}BNKurtosis}$ = 7.50 % (4.33e)

Barkhausen noise power spectrum uncertainty, $U_{R\text{-}BNPower}$ = 2.79 % (4.33f)

4.15.2. Systematic uncertainties

The uncertainty associated with inherited instruments and measurement procedure errors had to be evaluated and combined into a resultant uncertainty at a desired level of confidence. These uncertainties are inherited from the instruments and measurement methods chosen. All the uncertainties contributed from each component used in the measurement system were collected and are given in table 4.18.

Type	**Origin**	**Error contribution** *(%)*
From Barkhausen (Channel 0)		
Voltage Measurement	From the certificate of calibration DAQ card	0.05
Error in coil construction	Estimated error in coil construction	0.1
From B-Coil (Channel 1)		
Mass	From the certificate of weighting scale	0.1
Length	Calculated error due to ruler	0.67
Air Flux	Calculated error due to 1 mm thick plastic carrier	0.1

Voltage Measurement	From the certificate of calibration DAQ card	0.05
From H-Coil (Channel 2)		
Calibration	Calculated error from calibration	1
Voltage Measurement	From the certificate of calibration DAQ card	0.05
Angle between coils	Estimated error between each turn in H-coil	0.5
Angle Rotation of H-Coil	Estimated error due to angle placement of H-coil	1

Table 4.18. Systematic uncertainties in the measurement system

The total uncertainties are combined using equation 4.30, and the uncertainties were calculated for magnetic flux density, magnetic field and for Barkhausen noise measurements.

The calculated systematic uncertainty is:

Magnetic flux density uncertainty, $U_{S\text{-}B} = 0.69\ \%$ (4.34a)
Magnetic field uncertainty, $U_{S\text{-}H} = 1.50\ \%$ (4.34b)
Barkhausen noise uncertainty, $U_{S\text{-}BN} = 0.11\ \%$ (4.34c)

4.15.3. Total uncertainty

Then the total uncertainty of the system is calculated by the addition of random and systematic uncertainty, using equation 4.35.

$$U_{TOT} = \sqrt{U_R^2 + U_S^2} \tag{4.35}$$

The calculated total uncertainty was:

Magnetic flux density uncertainty, $U_{TOT\text{-}B} = 0.69\ \%$ (4.36a)
Magnetic field uncertainty, $U_{TOT\text{-}H} = 1.79\ \%$ (4.36b)

Barkhausen noise rms uncertainty, $U_{TOT\text{-}BNRMS} = 1.39\ \%$ (4.36c)
Barkhausen noise TSA uncertainty, $U_{TOT\text{-}BNTSA} = 1.25\ \%$ (4.36d)

Barkhausen noise kurtosis uncertainty, $U_{TOT\text{-}BNKurtosis} = 7.50\ \%$ (4.36e)

Barkhausen noise power spectrum uncertainty, $U_{TOT\text{-}BNPower} = 2.79\ \%$ (4.36f)

The total uncertainties for various measuring systems given in [4.25] are within a range from 3.6% to 11%. It can be seen the total uncertainties in the investigation are well below 11% with the highest being total uncertainty of kurtosis with 7.5%, which in this investigation is within the limits given in [4.25].

References to chapter 4

[4.1] D. C. Jiles, “Introduction to magnetism and magnetic materials”, Chapman & Hall, London, 1991

[4.2] V. E. Iordache, E. Hug, N. Buiron, “Magnetic behaviour versus tensile deformation mechanisms in a non-oriented Fe-(3wt.%)Si steel”, Material of Science and Engineering, A359, 62-74, 2003

[4.3] K. Hartmann, A. J. Moses, T. Meydan, “A system for measurement of ac Barkhausen noise in electrical steels”, Journal of Magnetism and Magnetic Materials, 254-255 318-320, 2003

[4.4] J. F. Keithley, “Low level measurements handbook”, Sixth edition, Keithley Instruments Inc, 2004

[4.5] G. Spadacini, D. Bellan, S. A. Pignari, “Impact of Twist Non-Uniformity on Crosstalk in Twisted-Wire Pairs”, IEEE International Symposium on Electromagnetic Compatibility, Vol 2, 483-488, 2003

[4.6] Data acquisition, Analog output series help, National Instruments, 2004

[4.7] NI 4551/4552 user manual, National Instruments, dynamic signal acquisition instrument for PCI, 1999

[4.8] National Instruments LabVIEW^{TM} user manual, 2001

[4.9] Amcron, DC-300A series II power amplifier, in: reference manual, Amcron, 1996

[4.10] BS EN 10280, “Magnetic materials - Methods of measurement of the magnetic properties of electrical sheet and strip by means of a single sheet tester”, 2001

[4.11] S. Zurek, P. Marketos, T. Meydan, A. J. Moses, “Use of novel adaptive digital feedback for magnetic measurements under controlled magnetising conditions”, IEEE Transactions on Magnetics, Vol 41, 4242-4249, 2005

[4.12] K. Matsubara, T. Nakata, N. Takahashi, K. Fujiwara, M. Nakano, H. L. Zhu, H. Aoki, “Effect of staircase output voltage waveform of a D/A converter on iron losses measured using an H-coil”, Journal of Magnetism and Magnetic Materials, Vol 160, 185-186, 1996

[4.13] BS EN 60404-6, “Magnetic materials - Part 6: Methods of measurement of the magnetic properties of magnetically soft metallic and powder materials at frequencies in the range 20 Hz to 200 kHz by the use of ring specimens”, 2003

[4.14] J. D. Kraus, “Electromagnetics”, McGraw-Hill, Fourth edition, 1992

[4.15] C. R. Paul, S. A. Nasar, L. E. Unnewehr, “Introduction to electrical engineering”, McGraw Hill, Second edition, 1992

[4.16] E. Hughes, “Hughes electrical technology”, Prentice Hall, Seventh edition, 1995

[4.17] A. J. Moses, H. V. Patel, P. I. Williams, "AC Barkhausen noise in electrical steels: Influence of sensing technique on interpretation of measurements", Journal of Electrical Engineering, Vol 57, No. 8/S, (Special issue), 2006

[4.18] E. Puppin, M. Zani, D. Vallaro, A. Venturi, "A double coil apparatus for Barkhausen noise measurements", Review of Science Instruments, Vol 72, No 4, 2001

[4.19] G. Manson, G. HoffMann de Visme, "The frequency spectrum of Barkhausen noise", Journal of Physics D: applied physics, Vol 5, 1389-1395, 1972

[4.20] Vector Fields Opera 3d user guide, 2004

[4.21] Vector Fields Opera 3d reference manual, 2004

[4.22] BS EN 60404-2, "Magnetic materials - Part 2: Methods of measurement of the magnetic properties of electrical steel sheet and strip by means of an Epstein frame", 1998

[4.23] S. Bell, "A beginner's guide to uncertainty measurement", Measurement good practice guide, No 11, National Physical Laboratory, 1999

[4.24] K. Birch, "Estimating uncertainties in testing", Measurement good practice guide n36, British Measurement and Testing Association, 2001

[4.25] J. Sievert, H. Ahlers, M. Birkfeld, B. Conmut, F. Fiorillo, K. A. Hempel, T. Kochmann, A. Lebouc, T. Meydan, A. J. Moses, A. M. Rietto, "Intercomparison of measurements of magnetic losses in electrical sheet steel under rotation flux conditions", Commission of the European communities, Report EUR 16255 EN, EC Brussels, Luxembourg, 1995

CHAPTER 5

SCANNING BARKHAUSEN MEASUREMENT SYSTEM

5.1. Introduction

Barkhausen noise scanning measurements were carried out on an Epstein strip of grain-oriented electrical steel. The surface field on a 0.27 mm thick, 3%SiFe grain-oriented electrical steel sample with an average grain size of 10 mm diameter was measured. The purpose of Barkhausen noise scanning measurements was to non-destructively identify the influence of features such as the position of grain boundaries under the insulating surface coating. Impurity and defect distributions vary from grain to grain and within grain boundaries [5.1, 5.2, 5.3] and thus cause differences in domain wall pinning, hence Barkhausen noise.

A 40 mm × 20 mm area in the centre of the sample was scanned at peak flux densities of 0.5 T and 1.0 T at magnetising frequencies of 25 Hz and 50 Hz. A block diagram of the Barkhausen noise scanning measurement system is shown in figure 5.1. The main components are the magnetising system, a precision (X-Y-Z) position control system with an on board microprocessor, and a block of perspex designed to accommodate the ferrite sensor.

The precision positioning control system (PC-2) runs on a separate PC to that of the magnetisation system (PC-1). They were connected through a digital input/output connection described in section 5.3.1.

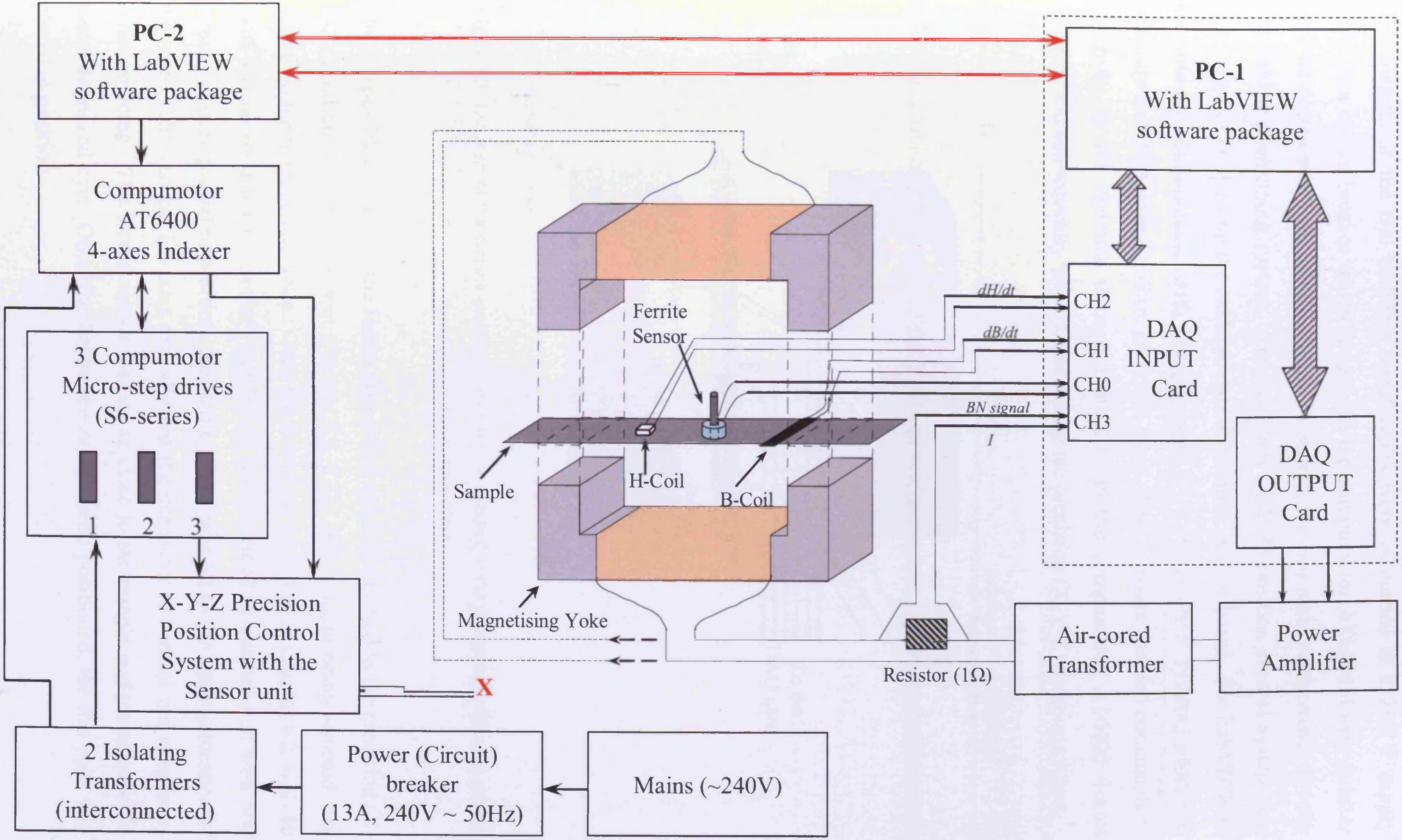

Figure 5.1. Block diagram of the Barkhausen Noise Scanning Measurement System

The outputs of the two isolating transformers were connected to a 240 V supply through a circuit breaker which feeds both the compumotor AT6400 4-axes indexer and the compumotor microstep drives (S6 series), the two main components directly control the positioning system. The precision (X-Y-Z) position control system was connected to PC-1 using the analogic data acquisition system board. For LabVIEW to be able to communicate with the precision (X-Y-Z) position system, additional software called Motion Toolbox [5.4] was used. This software enabled commands to be given by the operator through LabVIEW to the compumotor AT6400 4-axes indexer, and subsequently was carried out by the precision (X-Y-Z) position system.

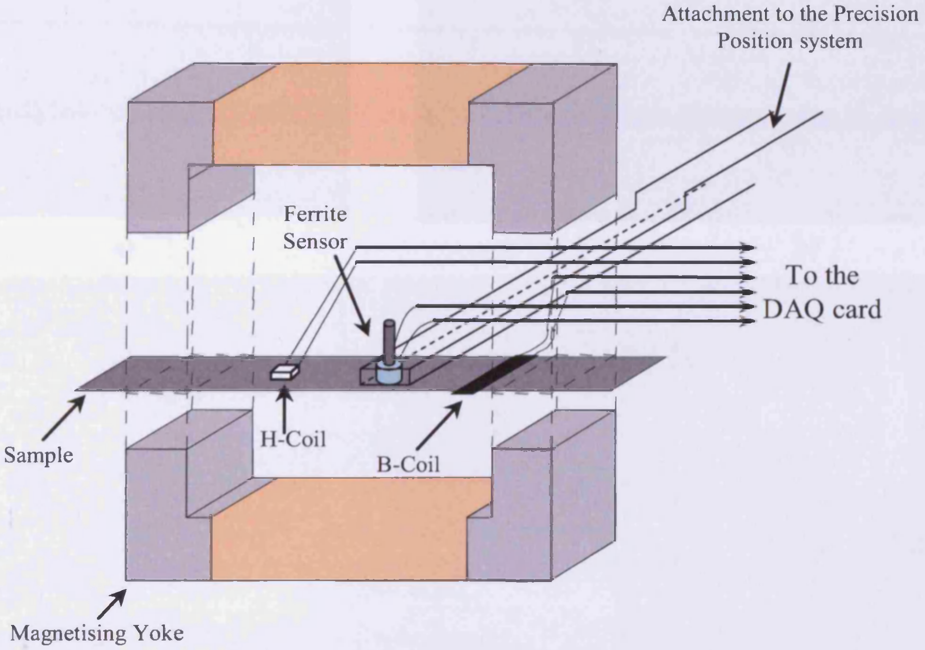

Figure 5.2. Diagram of the surface mounted ferrite sensor attached to the precision positioning control system with the perspex block

The perspex block housing the ferrite sensor had one end attached to the precision (X-Y-Z) positioning control system (figures 5.2, 5.3). The sample being scanned was placed on the magnetising yoke. Once the B-coil (as described in chapter 4.2, with 80 turns wound on a plastic carrier) and H-coil (as described in chapter 4.3, with 500 turns) had been placed in position, the ferrite sensor was set to the starting location of the scan. The vertical (Z-axis) axis allowed the computer to control the sample-to-sensor spacing. The ferrite sensor was set as close to the sample surface as possible using the naked eye. Once the ferrite sensor had been positioned, the top yoke was placed in position.

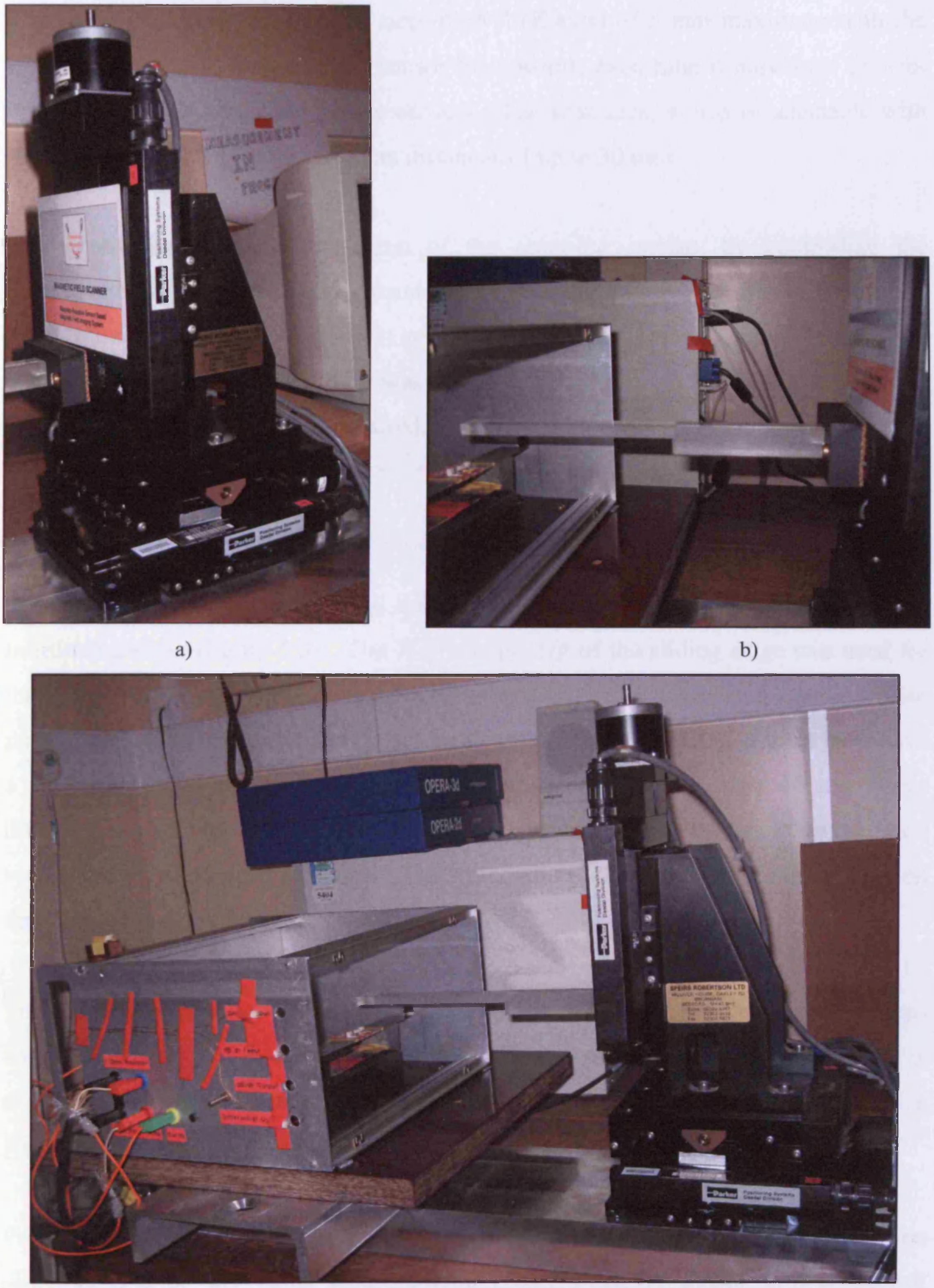

a) b)

c)

Figure 5.3. Photograph of the a) precision (X-Y-Z) positioning system b) perspex block housing the ferrite sensor c) precision (X-Y-Z) positioning system with the perspex block housing the ferrite sensor and the magnetising set-up

The user can specify the vertical step interval (Z-axis) of 5 mm maximum with the LabVIEW program (to make the sensor lift upwards each time it moves, to prevent the sample being scratched by the sensor). The scan area, which is selectable with independent X and Y-axes, can scan distances of up to 30 mm.

PC-1 controlled the full operation of the scanning system, by controlling the magnetisation of the sample (explained in chapter 4), and then communicating with PC-2 to move the sensor to the next appropriate location. Once the specified area had been scanned, the measured data was saved to a text file. A separate LabVIEW *vi* was used to analyse the data measured.

5.2. Positioning system

The positioning stage comprises three stepper motors arranged in a three axis positioning stage (figure 5.3). The X-Y component of the sliding stage was used for raster scanning a sensor over a stationary sample and the Z component allows precise positioning of the sensor height above the sample surface. The X-Y-Z axes each have a sliding range of 60 mm respectively and are able to transverse a 30 mm linear distance in a minimum time of 1 second. However, throughout the investigation a scan speed of 10 mm/sec was used. This speed allows the ferrite sensor to stabilise on the sample before readings are taken.

The advantage of using a slower scan speed is that acceleration and deceleration steps are unnecessary to overcome initial inertia. Also, due to slower scan speeds there is no whiplash caused by abrupt start/stop motion. However, the disadvantage is a longer scan time.

For simplicity of control, the raster scan method was chosen for the Barkhausen scanning system. The raster scan operation requires that the sensor be first scanned forwards a set distance along the X-axis. Upon completion of the X-axis forwards motion, the direction is reversed and the sensor returned to its start position. The Y-axis motion is incremented and the X-axis scan motion proceeds again. This process is repeated until the Y-axis has incremented a set distance.

The stepper motors have a maximum step resolution of 100 μm. A scan made over a 40 mm × 20 mm area at a step resolution of 100 μm in both axes resulted in 80 000 data points. The number of data points (hence total scan time) could be reduced by making the step size larger, however, at the expense of poorer resolution Barkhausen images. Alternatively, the scan area could be reduced to keep the number of data points to a minimum and to reduce the total scan time. This was not of concern because the sensor diameter was 3 mm, so a small step resolution was not required. The scan area in this investigation never exceeded 40 mm × 20 mm with a minimum step size of 1 mm.

The precision (X-Y-Z) positioning control system consists of a microprocessor based four axis indexer known as the compumotor AT6400 [5.5]. AT6400 inserts hardware registers for motor position, I/O, and system status. The AT6400 was inserted into a single 16-bit enhanced industry standard architecture expansion slot in the PC. The AT6400 provides multi-axis control of the positioner through the motion control language. A separate auxiliary board simplifies connection by interfacing the stepper motors to the AT6400.

5.3. LabVIEW programs

Parker Hannifin Corporation manufactured the precision (X-Y-Z) positioning control. Although the version used required the application of the LabVIEW software package, the main software package for the system was the Motion Toolbox. This package is a library of LabVIEW virtual instruments for the compumotor's 6000 series of motion controllers [5.6]. Motion Toolbox supported both the compumotor AT6400 four axes (drivers) and the three axis indexers.

Because the precision (X-Y-Z) positioning control system was ran from PC-2 and the magnetisation system ran from PC-1, two LabVIEW programs ran on each PC, simultaneously. On PC-2, all the scanning system settings for the scan were entered on the front panel, in LabVIEW. The settings included parameters such as step resolution, sampling resolution, area of scan and the vertical step interval. LabVIEW created an array that sets out the area of the sample surface to be scanned. On PC-1, all the magnetisation system settings were set on the front panel. The settings included sample length, sample mass, sample density, magnetisation frequency, and magnetic flux density.

However, the magnetisation system *vi* (PC-1) required the number of data points to be measured for scanning measurements i.e. 40 mm × 20 mm with a step size of 1 mm gave a total of 800 data points. The program acquired 800 data points and saved the measured Barkhausen noise results to a text file.

5.3.1. Communication between both systems

PC-1 was installed with the PCI-6731 [5.7] DAQ card that was fed to a connection block (NI CB-68LP) that generated the output voltage waveform to control the applied magnetic flux density. This card had eight input/out digital lines. PC-2 was installed with a data acquisition card (NI PCI-6034E) [5.8] fed to a connection block (NI CB-68LP); this DAQ card also had eight digital input/output lines. Only two digital lines were used from each DAQ card, one to send a digital signal and the other to receive a digital signal.

Within both main LabVIEW *vi*'s this communication was incorporated. Digital line 1 of PC-1 and line 2 of PC-2 were set to output a digital logic "1" or "0", and line 2 of PC-1 and line 1 of PC-2 were set to read a digital signal. Once all the limits had been reached (as described in chapter 4.8) by the flux density waveform, the results were saved to a temporary file, and then a digital signal (logic "1") was sent to PC-2 via line 1. When the digital signal of logic "1" is read (line 1 PC-2) by the precision (X-Y-Z) positioning control system *vi*, it increments the data point location by 1 and the sensor is moved to the next location. Once the sensor had been moved, the precision (X-Y-Z) positioning control system *vi* sent a digital logic "1" back to the magnetisation *vi* via line 2. When the magnetisation *vi* sent out the logic "1" to move to the next point it waited until logic "1" was read in line 2. Once a logic "1" had been read in line 2 of PC-1, it controlled the magnetic flux density to the set limits, saved the data to a temporary file and sent out another logic "1" to move the sensor, this was repeated until all data points had been reached. Once all set data points are completed, the temporary files are read and data is inserted into one single file, which was later used for further data analysis in Microsoft Excel and another LabVIEW program. The format of the file saved is shown in chapter 4.10.3. Once all data points are completed, the precision (X-Y-Z) positioning control system *vi* also moved the sensor back to its starting location, this gave repeatable results if it was necessary to scan areas more than once.

5.3.2. Data analysis vi

Once all the data had been saved to a text file, it was read by a visualisation *vi*, also created in LabVIEW. The visualisation *vi* read the final data file, put the data in an organised array, and then plotted the data on an 3d surface graph. All the images were then labelled and saved to an individual files (.jpg). A typical .jpg image of the rms Barkhausen noise data is shown in figure 5.4.

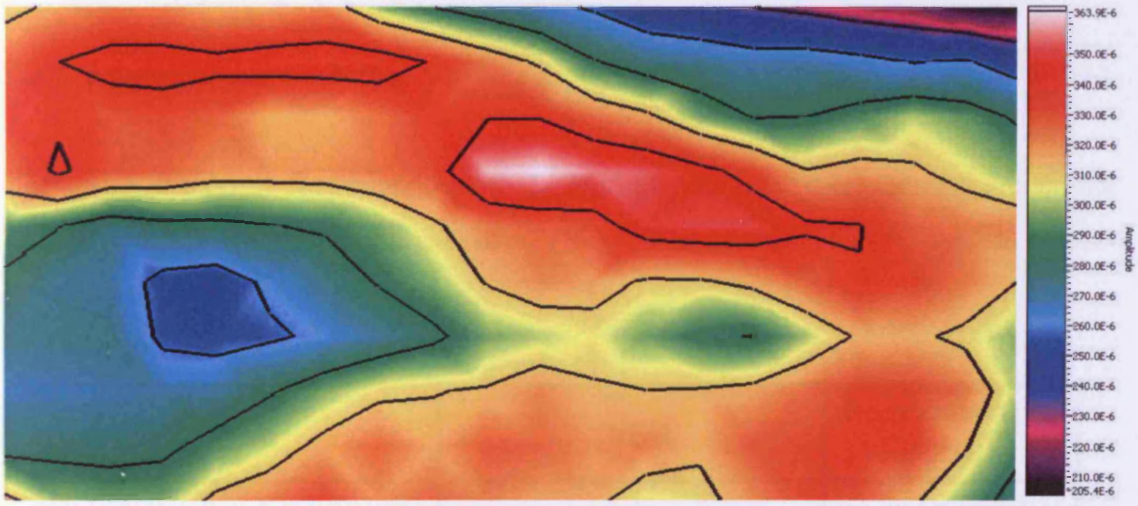

Figure 5.4. Typical image of rms Barkhausen noise scanned over, 40 mm × 20 mm, with a step size of 1 mm, on a grain-oriented electrical steel sample at magnetising frequency of 50 Hz and peak flux density of 1 T

5.4. Uncertainty of scanning measurements

Uncertainties [5.9] of the scanning measurements were assessed in the manner discussed in chapter 4.15. The uncertainty of the Barkhausen noise scanning measurements were calculated for a single grain-oriented 3%SiFe electrical steel sample with an average grain diameter of 10 mm. Each measurement was repeated 5 times, magnetised at 0.5 T and 1 T, at magnetising frequencies of 25 Hz and 50 Hz. An area of 40 mm × 20 mm was scanned with 2 mm and 1 mm steps.

5.4.1. Random uncertainties

The estimated standard uncertainty, u_R, was calculated, a confidence level of 95% was chosen. This is equivalent to k = 2. The t-student factor corresponding to five measurements is given as 1.44.

Using the above information the random uncertainty was calculated to be:

Magnetic flux density uncertainty, $U_{R\text{-}B} = 0.02\ \%$ (5.1a)
Barkhausen noise rms uncertainty, $U_{R\text{-}BNRMS} = 1.92\ \%$ (5.1b)
Barkhausen noise TSA uncertainty, $U_{R\text{-}BNTSA} = 2.00\ \%$ (5.1c)
Barkhausen noise kurtosis uncertainty, $U_{R\text{-}BNKurtosis} = 8.75\ \%$ (5.1d)
Barkhausen noise power spectrum uncertainty, $U_{R\text{-}BNPower} = 3.83\ \%$ (5.1e)

5.4.2. Systematic uncertainties

The systematic errors that contribute to the Barkhausen noise measurement are shown in table 5.1. The error in the precision (X-Y-Z) positioning control system is also shown.

Type	**Origin**	**Error contribution** *(%)*
From B-Coil (Channel 1)		
Mass	From the certificate of weighting scale	0.1
Length	Calculated error due to ruler	0.67
Air Flux	Calculated error due to 1 mm thick plastic carrier	0.1
Voltage Measurement	From the DAQ card calibration certificate	0.05
From Barkhausen (Channel 0)		
Voltage Measurement	From the DAQ card calibration certificate	0.05
Error in coil construction	Estimated error in construction	0.1

From precision (X-Y-Z) positioning control system		
Precision (X-Y-Z) positioning	Calculated error due to positioning	0.01

Table 5.1. Systematic uncertainties in the scanning Barkhausen measurement system

The total uncertainties are added using:

$$U_S = \sqrt{U_{S1}^2 + U_{S2}^2 + U_{S3}^2 + \dots} \tag{5.2}$$

The calculated systematic uncertainty is:

Magnetic flux density uncertainty, $U_{S\text{-}B} = 0.69\ \%$ (5.3a)

Barkhausen noise uncertainty, $U_{S\text{-}BN} = 0.11\ \%$ (5.3b)

5.4.3. Total uncertainty

Then the total uncertainty of the system is calculated by the addition of random and systematic uncertainty, using equation 5.4.

$$U_{TOT} = \sqrt{U_R^2 + U_S^2} \tag{5.4}$$

The calculated total uncertainty was:

Magnetic flux density uncertainty, $U_{TOT\text{-}B} = 0.69\ \%$ (5.5a)

Barkhausen noise rms uncertainty, $U_{TOT\text{-}BNRMS} = 1.92\ \%$ (5.5b)

Barkhausen noise TSA uncertainty, $U_{TOT\text{-}BNTSA} = 2.00\ \%$ (5.5c)

Barkhausen noise kurtosis uncertainty, $U_{TOT\text{-}BNKurtosis} = 8.75\ \%$ (5.5d)

Barkhausen noise power spectrum uncertainty, $U_{TOT\text{-}BNPower} = 3.83\ \%$ (5.5e)

References to chapter 5

[5.1] R. Ranjan, D. C. Jiles, “Magnetic properties of decarburized steels: An investigation of the effects of grain size and carbon content”, IEEE Transactions on Magnetics, Vol 23, No 3, 1869-1876, 1987

[5.2] S. Yamaura, Y. Furuya, T. Watanabe, “The effect of grain boundary microstructure on Barkhausen noise in ferromagnetic materials”, Acta Materialia Inc 49, 3019-3027, 2001

[5.3] M. L. Lobanov, I. P. Sysolyatina, V. K. Christyakov, Yu. L. Gobov, E. S. Gorkunov, S. M. Zadvorkin, G. S. Korzunin, A. G. Lavrent’ev, D. V. Perov, A. B. Rinkevich, V. A. Sandovskii, “On possibility of non-destructive testing of the grain size in the intermediate stages of manufacturing electrical steel”, Russian Journal of Non-destructive Testing, Vol 39, No 8, 615-628, 2003

[5.4] Motion Toolbox user guide, “A library of LabVIEW virtual instruments for motion control”, Snider consultants Inc, 1997

[5.5] Compumotor division of Parker Hannifin corporation, 6000 series software reference guide, Document No: 88-012966-01D, 5500 Business Park Drive, Rohnert Park, CA94928, USA, 1992

[5.6] National Instruments LabVIEW^{TM} user manual, 2001

[5.7] NI PCI-6731, National Instruments data sheet

[5.8] NI PCI-6034, National Instruments data sheet

[5.9] S. Bell, “A beginner’s guide to uncertainty measurement”, Measurement good practice guide No 11, National Physical Laboratory, 1999

CHAPTER 6

DISCUSSION

6.1. Introduction

The magnetic Barkhausen effect was discovered at the beginning of the last century but its origin and interpretation is still not fully understood. It is generally accepted to be due to microscopic discontinuities in domain wall motion due to the presence of defects [6.1]. Various methods of measurement based on detecting induced voltages caused by Barkhausen jumps within a material have been developed. Because of the stochastic nature of Barkhausen noise, a variety of statistical methods can be used to analyse the signals using root mean square, sum of amplitudes, kurtosis and power spectrum methods. Definite trends are found in the influence of factors such as texture and microstructure on Barkhausen noise under different magnetising conditions in electrical steels and some direct connection with hysteresis loss appears to exist [6.2].

The majority of measurements were carried out on Epstein strips of non-oriented and grain-oriented electrical steels. Samples of fully processed, non-oriented electrical steels, comprised two types of 0.1 mm thick material with 5.5%Si and 6.5%Si; five types of 0.5 mm thick material with 0.2%Si, 0.3%Si, 1.3%Si, 1.8%Si, and 3.0%Si; and two groups of seven types of 0.5 mm thick with 3.0%Si cut at 0°, 15°, 30°, 45°, 60°, 75°, and 90° to the rolling direction, one group with an average grain size 53 μm and the other group with an average grain size of 180 μm. In addition, grain-oriented electrical steel with 3%Si, 0.27 mm thick, cut at 0°, 55°, and 90° to the rolling direction were tested.

In addition, an ancillary study was conducted on cold-rolled low carbon steel with 0-40% rolling reduction, of charpy, plate and picture frame shapes. Also, thermally aged iron copper with different ageing times (0-5000 minutes), of charpy and ring shape was investigated.

6.2. Basic understanding of measurement parameters under ac conditions

Barkhausen noise has been researched over many years under near dc conditions however recently ac Barkhausen noise has also been investigated. A basic understanding of the parameters measured under ac conditions is required to allow understanding of results shown in this study.

In order to observe experimentally well separated Barkhausen jumps, a near dc magnetising frequency would have to be applied. Where statistical characterisation of Barkhausen noise remains stable and its amplitude is high enough to permit efficient collection of Barkhausen jumps [6.3]. Figure 6.1 shows a typical Barkhausen noise signal at 20 mHz for a Co-base amorphous alloy [6.4].

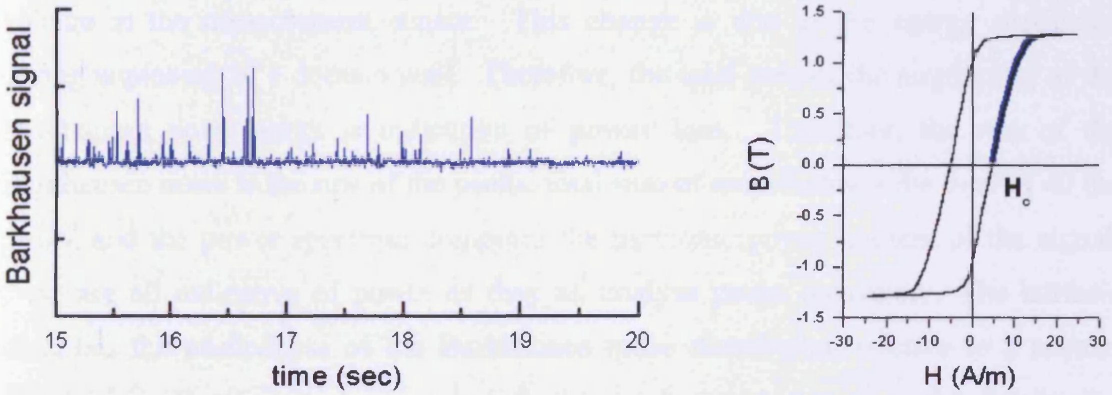

Figure 6.1. Barkhausen noise signal for Co-base amorphous alloy, magnetised at 20 mHz [6.4]

At this frequency, clear Barkhausen peaks can be observed which makes statistical analysis simpler to understand. Individual peaks can be seen, therefore counted, which then gives a direct relation to inclusions in a material [6.3]. Also, the height of the peaks gives a relation to the size of the inclusion [6.3]. However, peaks that are measured at power frequencies begin to coalesce. Figure 6.2 shows a typical Barkhausen noise signal at 1 Hz, and it can be seen that individual peaks are smaller and have started to coalesce. Therefore, it is less meaningful to count the number of peaks, as the number of peaks does not indicate the true number of Barkhausen jumps.

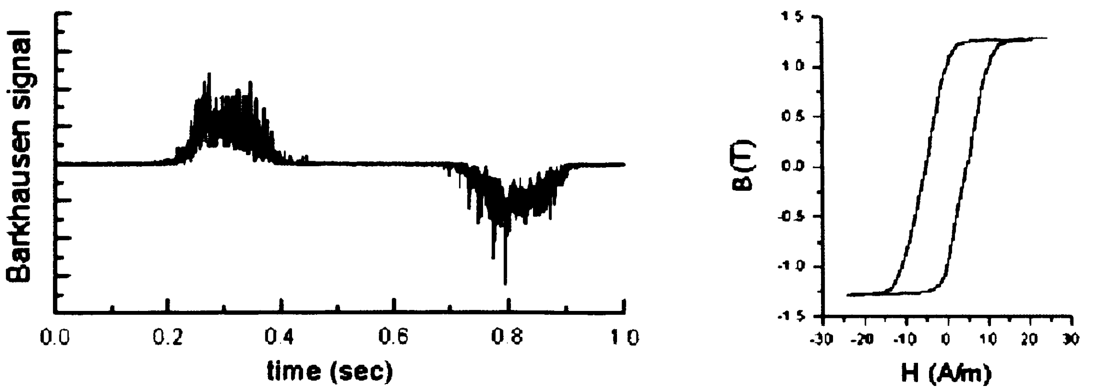

Figure 6.2. Barkhausen noise signal for Co-base amorphous alloy, magnetised at 1 Hz [6.4]

Domain walls are pinned on non-magnetic inclusions, grain boundaries, oxides, etc. The domain wall stays pinned to the inclusion until the wall energy (applied field) is high enough for it to snap away, when this happens the domain wall accelerates suddenly, and thus energy is wasted. The abrupt change in magnetisation induces a voltage in the measurement sensor. This change is due to the energy dissipated during unpinning of a domain wall. Therefore, the total sum of the amplitudes of the Barkhausen noise peaks is indicative of **power loss**. Therefore, the rms of the Barkhausen noise is the rms of the peaks, total sum of amplitudes is the total of all the peaks, and the power spectrum computes the harmonic power content of the signal, these are all indicative of power as they all analyse peaks measured. The kurtosis describes the peakedness of the Barkhausen noise distribution relative to a normal distribution. Kurtosis is not directly linked to peak sizes but more to the distribution of peaks. An increase in kurtosis would show an increase in peakedness of the Barkhausen noise distribution.

6.3. Comparison of various core materials used in the surface sensor

An Epstein strip of 3%SiFe grain-oriented electrical steel cut at 0° to the rolling direction was used as the sample to measure the dependence of the Barkhausen noise measurement with the core material used in the surface sensor. A magnetising frequency of 50 Hz (f_{mag}) and a peak flux density (B_{peak}) ranging from 0.1 T to 1.5 T was used. Four cores were investigated (iron, ferrite, mumetal and nano-crystalline) to observe the influence of the core material on the performance of the Barkhausen noise surface sensor. The main parameters of the core materials are listed in table 6.1

(the values have been taken from chapter 4.4.3). Also as a reference, an air-cored coil was used to measure Barkhausen noise.

Core material	μ_r	**Shape and size**	**Turns**
Ferrite	900	Circular 3 mm diameter 12·9 mm length	1000
Iron	~2 000	Circular 2 mm diameter 10·8 mm length	1000
Mumetal	35 000	Square 2·5 × 2·5 mm 10 mm length	1000
Nano-crystalline	70 000	Square 3·1 × 3·3 mm 6·4 mm length	800

Table 6.1. Parameters of core material used for surface sensor

Based on the working principle of the ferrite sensor (described in chapter 4.4.3) it was anticipated that the iron, mumetal and nano-crystalline cores would amplify the Barkhausen noise signal more than the ferrite core due to their greater relative permeability. However, the resultant measurements (Barkhausen noise was analysed using root mean square (RMS) (figure 6.3), total sum of amplitudes (figure 6.4), kurtosis (figure 6.5) and power spectrum (figure 6.6)) show this is not the case.

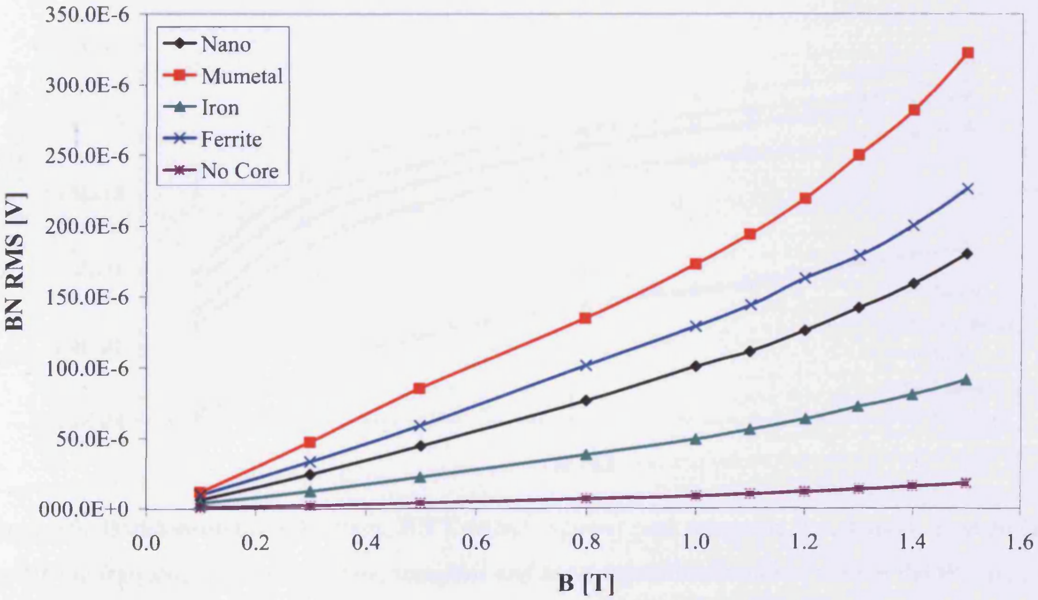

Figure 6.3. RMS Barkhausen noise, BN RMS, against peak magnetic flux density, *B*, at 50 Hz magnetising frequency, for iron, ferrite, mumetal and nano-crystalline material used in the Barkhausen noise surface sensor

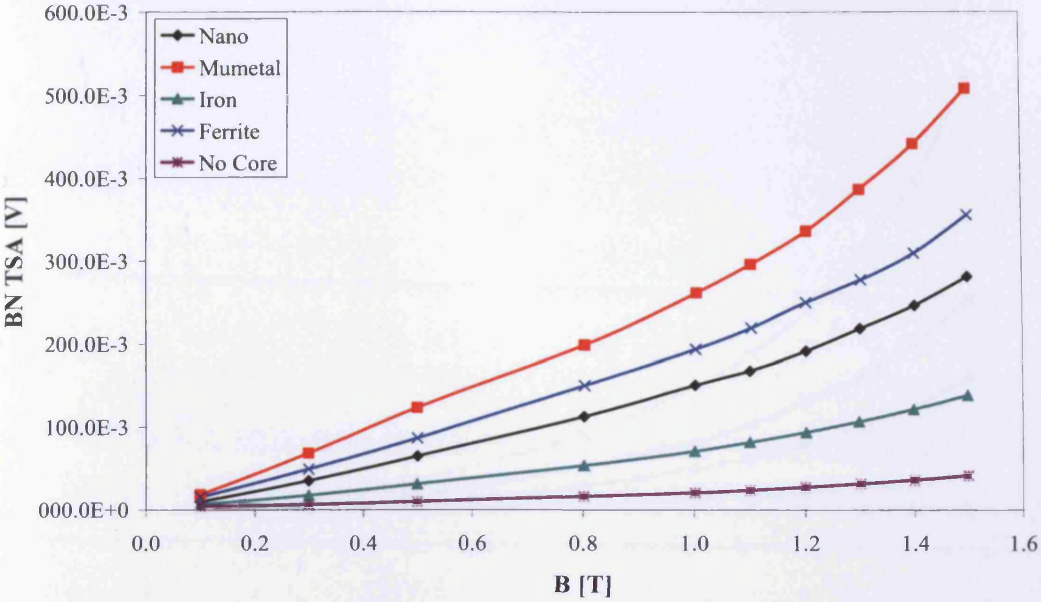

Figure 6.4. Barkhausen noise total sum of amplitudes, BN TSA, against peak magnetic flux density, *B*, at 50 Hz magnetising frequency, for iron, ferrite, mumetal and nano-crystalline material used in the Barkhausen noise surface sensor

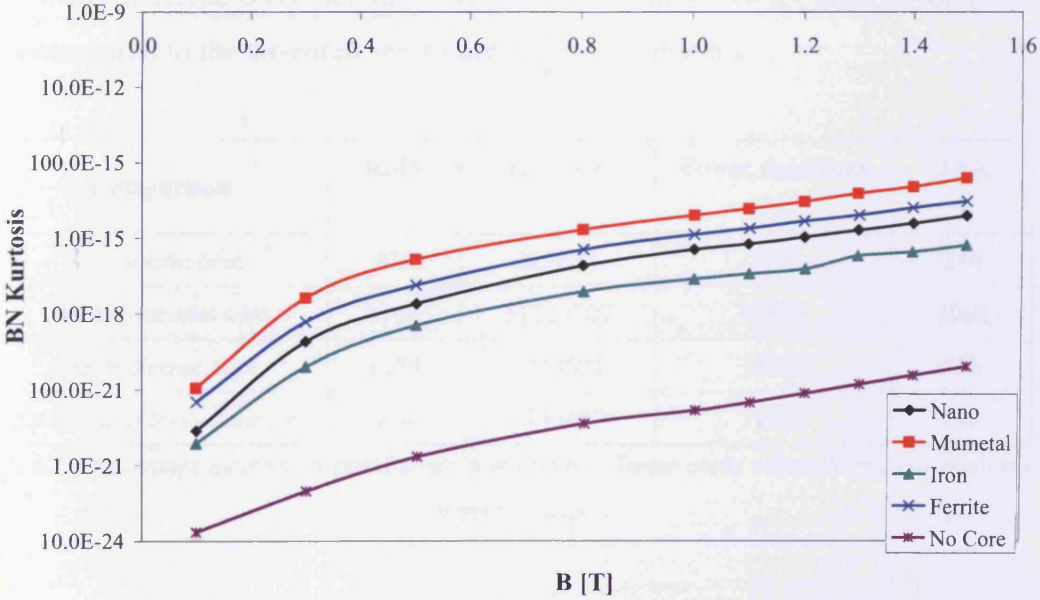

Figure 6.5. Barkhausen noise kurtosis, BN Kurtosis, against peak magnetic flux density, *B*, at 50 Hz magnetising frequency, for iron, ferrite, mumetal and nano-crystalline material used in the Barkhausen noise surface sensor

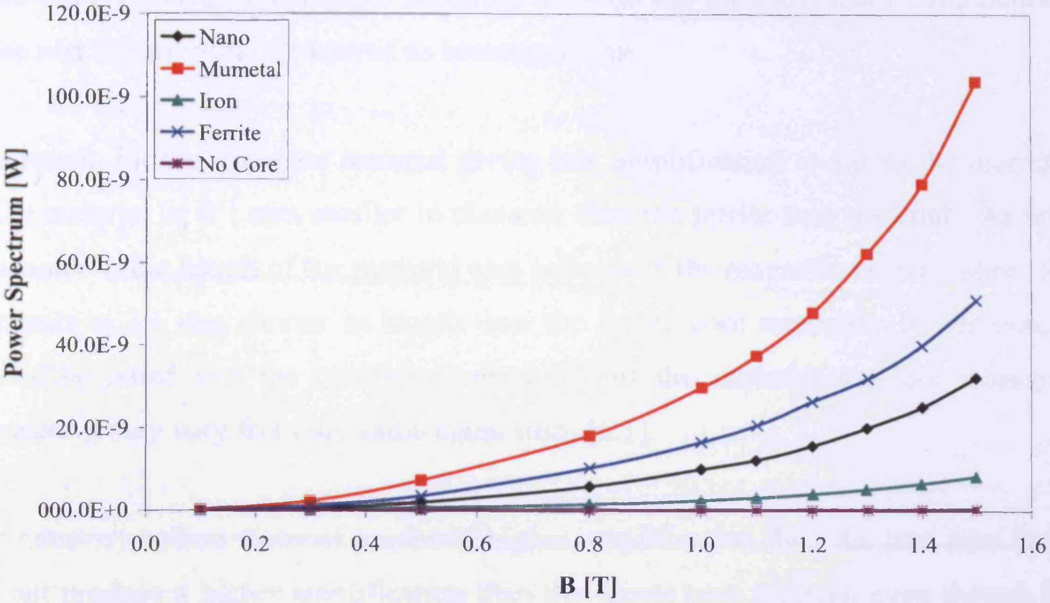

Figure 6.6. Barkhausen noise power spectrum, BN power spectrum, against peak magnetic flux density, *B*, at 50 Hz magnetising frequency, for iron, ferrite, mumetal and nano-crystalline material used in the Barkhausen noise surface sensor

The iron and nano-crystalline cores both produce Barkhausen noise signal amplitudes lower than the ferrite cored sensor. The percentage increases for each of the material cores compared to the air-cored sensor are shown in table 6.2.

Comparison	**RMS** *(%)*	**Kurtosis** *(%)*	**Power spectrum** *(%)*	**TSA** *(%)*
Air to Iron core	434	222633	2748	218
Air to Mumetal core	1767	11123707	34845	1068
Air to Ferrite core	1259	3078691	18428	748
Air to Nano-crystalline core	954	1183677	11025	557

Table 6.2. Percentage increase of Barkhausen noise with different cores with reference to an air cored surface sensor

From table 6.2 it is seen that the mumetal core amplifies the Barkhausen noise signal most and the iron core the least for all the analysis methods. There are three factors that affect the amplification of Barkhausen noise signal using the surface sensor. First the size of the core material e.g. thickness and length, secondly the number of turns on the coil used to pick up the signal and thirdly the contact that the core material has with the sample material surface. However, it is not known how great an influence these effects (except for number of turns) have on the measurement of Barkhausen noise and further work is required to investigate this.

The reason for the iron core material giving low amplification is due to the diameter of the material, it is 1 mm smaller in diameter than the ferrite core material. As seen in chapter 4, the length of the material also influences the magnetic amplification; the iron core is 2.1 mm shorter in length than the ferrite core material. In addition, it should be noted that the relative permeability of the material was not measured therefore it may vary from the value taken from [6.1].

The nano-crystalline material produced higher amplification than the iron core but it did not produce a higher amplification than the ferrite core material even though the material has a higher relative permeability than the ferrite core material. However, factors that need to be taken into account are that the nano-crystalline material is much shorter in length than the ferrite core and the pickup coil has 200 turns less. (See chapter 4.12.3 on how changing the number of turns effects Barkhausen noise measurement.) Another important factor is that the nano-crystalline core is made of thin laminations unlike the other materials and it is not fully understood how laminations would effect the measurement of Barkhausen noise. In addition, the nano-crystalline material did not have a smooth surface so that sensor contact to sample surface was not good. With all the factors taken into account it is concluded that the nano-crystalline material would not perform as well as the ferrite core material, unless a better quality of finish was supplied.

Mumetal is a non-oriented 77% nickel-iron molybdenum alloy that offers high initial permeability, high maximum permeability, low coercivity and low saturation induction. With this composition, the magnetocrystalline anisotropy is almost zero. Consequently, there is a reduction in the energy of Bloch walls, reducing the pinning forces exerted by the inclusions [6.5]. Because the magnetostriction is also very weak, the movement of the walls is not hindered by the appearance of stress at the scale of the domains. These two characteristics are responsible for high permeability. However, the mumetal core did produce higher amplification than the ferrite core material but the increase was only approx 40% more for rms Barkhausen analysis. With the large difference in the relative permeability, a far higher increase of

Barkhausen noise was expected. With a 3 mm length difference and approx 0.5 mm thickness change, a small decrease can be accounted by this, however not all can be due to size differences.

Ferrites contain four nonmagnetic ions (oxygen) for every three magnetic ions in the spinel structure [6.5]. Compared to metals, the initial permeability and the maximum permeability at low frequency are also lower, sometimes by several orders of magnitude. The coercive field is higher. A characteristic of the ferrites is that they have small losses at high frequencies. The presence of ferrous ions may be avoided here by producing a slight iron deficit with respect to the theoretical value of two ions per molecule. The result is a resistivity greater by several orders than metal, making the eddy current loss completely negligible in most cases [6.5]. Losses related to the presence of imperfections inside the grains are also small because the grains are so small that often they only form a single magnetic domain. Polarisation is therefore only established by rotation and any dissipative mechanism related to movement of the Bloch wall is avoided. Unfortunately, the initial permeability is reduced because of this.

The most important factor is that Barkhausen noise created by the ferrite and the mumetal is minimal, and therefore addition and/or cancellation of Barkhausen noise is avoided. However, it must be noted that mumetal does have higher Barkhausen noise than ferrite. With this characteristic, these two samples are ideal for use as a Barkhausen noise sensor. However, the ferrite has a further advantage of having small losses at higher frequencies, due to reduction of eddy current losses. Barkhausen noise occurs at high frequencies in the kHz range or more, thus any reduction of micro-eddy currents would be advantageous. A reduction in eddy currents would mean a reduction in damping of the Barkhausen noise signal, which is advantageous. The mumetal does have a high relative permeability however, from the measurements it can be seen that the higher relative permeability is not vastly advantageous, due to mumetal having higher self Barkhausen noise than the ferrite material. Also, mumetal has higher high-frequency losses, which would damp the Barkhausen noise signal. Thus, the ferrite material is the most suitable material to be used in a Barkhausen noise surface sensor.

6.4. Barkhausen noise versus flux density & magnetising frequency

The influence of magnetic flux density and magnetising frequency on Barkhausen emissions in electrical steel samples (table 4.6) was investigated in this section.

6.4.1. *Barkhausen noise versus flux density*

The variation of rms Barkhausen noise with peak flux density at f_{mag} = 50 Hz in the five samples of electrical steel is shown in figure 6.7. The double B-coil sensor was used for the measurement of Barkhausen noise in all the samples. (The total sum of amplitudes, power spectrum and kurtosis show similar trends.)

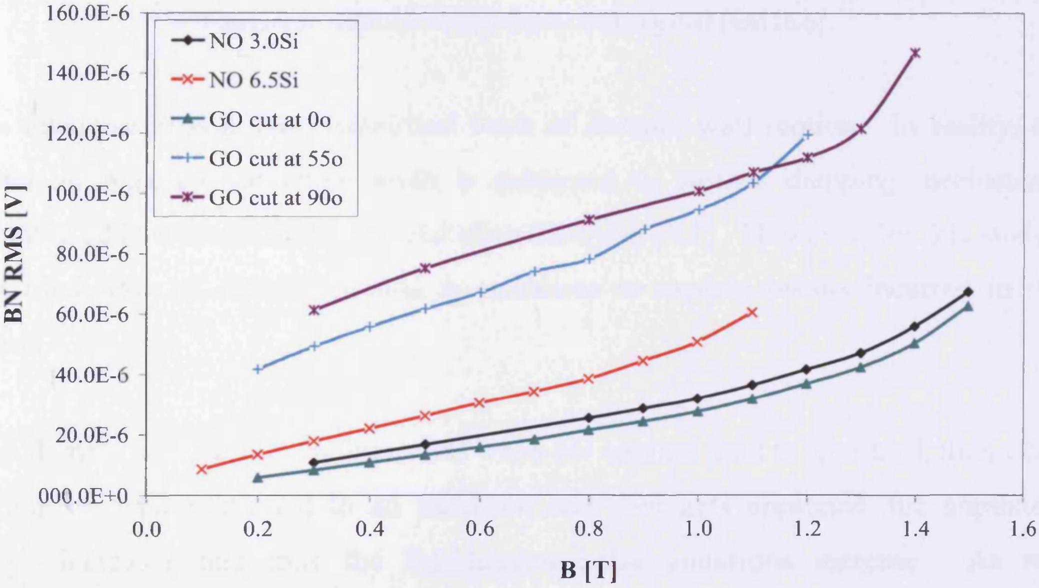

Figure 6.7. Variation of rms Barkhausen noise with peak flux density, *B*, at 50 Hz magnetising frequency, for non-oriented 3%Si and 6.5%Si, grain-oriented 3%Si cut at 0°, 55° and 90° to the rolling direction, measured with the double B-coil sensor

An increase in magnetic flux density increases the Barkhausen noise signal linearly (figure 6.7). This increase in Barkhausen noise is due to the velocity of the domain wall, which is governed by the size of the applied field according to a relationship of the form [6.6]:

$$velocity = k(H - H_C) \tag{6.1}$$

where, H - is the applied field; H_c - is the coercive force; k - is the mobility of the domain wall. Figure 6.8 illustrates this response.

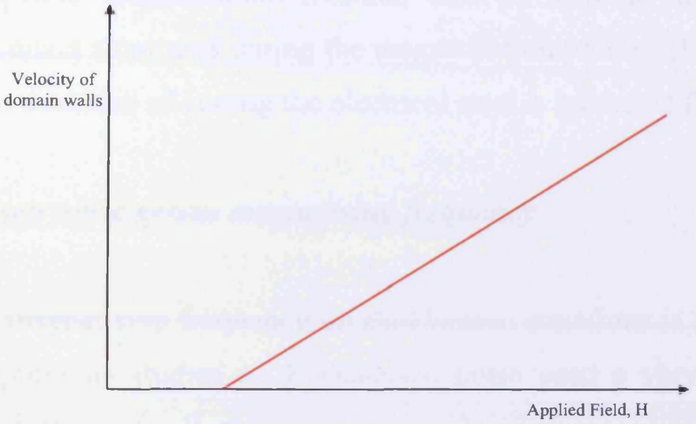

Figure 6.8. Domain wall velocity with applied field [6.6]

This relationship is a very simplified form of domain wall motion. In reality, the motion of magnetic domains walls is subjected to various damping mechanisms including eddy currents and spin relaxation damping [6.1]. However, for this study a simplified form of domain motion is sufficient to explain results incurred in this section.

If the domain wall velocity is increased when the applied field is increased, then when the domain wall is pinned to an inclusion and then gets unpinned, the unpinning energy increases and thus the Barkhausen noise emissions increase. As rms Barkhausen noise is an indication of power this shows that there is an increase in power lost during unpinning when the applied field is increased. Also, the Barkhausen noise increases linearly with flux density however close to saturation of the material this is no longer a linear behaviour. This is due to the domain rotation process.

Also figure 6.7 shows that the grain-oriented steel cut at 0° produces the least rms Barkhausen noise. Grain-oriented electrical steel cut at 90° produces the highest rms Barkhausen noise. This is due to the 0° sample being magnetised in the easy direction where magnetisation is least difficult. In the 90° direction, the domains are aligned

90° to the magnetisation direction and therefore more domains than 0° sample must be rotated hence the increase in rms Barkhausen noise. Also an increase in grain-oriented (cut at 0°) to non-oriented (3%SiFe) can be seen. This increase in non-oriented electrical steels is associated with an increase in irreversible 90° domain walls and irreversible magnetisation rotation, thus an increase in nucleation and annihilation of domain structures during the magnetisation process [6.7]. This is also the case when the direction of cutting the electrical steel is increased from 0° to 90°.

6.4.2. Barkhausen noise versus magnetising frequency

The influence of magnetising frequency on Barkhausen emissions is explained in this section. Many previous studies on Barkhausen noise used a very slow changing magnetisation, which made Barkhausen noise observation easier than under ac conditions. Sipahi and co-workers [6.8] found that an ac excitation field to generate Barkhausen jumps gives a much more reproducible Barkhausen signal.

There is considerable experimental evidence to show that the domain wall spacing in single crystals of 3%SiFe is a function of the frequency of the applied field. Houze [6.9] observed that the average domain wall spacing decreases with increasing frequency, although the reason for this was not apparent. The results of similar measurements (made at a high peak flux density) by Haller and Kramer [6.10] show that the mean domain wall spacing is inversely proportional to the square root of the frequency ($1/f^{1/2}$). It would seem logical to expect that the domain size changes might be an attempt by the system to minimise its energy. In a later paper, Haller and Kramer [6.11] attempted to explain their observations by using a thermodynamic approach and applying the principle of minimum entropy production; that is, minimisation of the system losses. Although the observations above the thresholds were accurately predicted, the theory did not explain the discontinuity, but predicted infinite spacing at zero frequency.

Rankis and co-workers [6.12] found that Barkhausen jumps decreased by almost 50% in number during long duration quasi-static cyclic magnetisation. The effect took place in nickel ferrite under a sawtooth field with a period of 20 to 60 minutes. Measurements taken within this research comprised of the mean rms Barkhausen noise calculated from an average of 10 cycles but a decrease of Barkhausen noise with increasing frequency was not observed. It should be noted in this work that different materials have been examined and the magnetising frequency and waveform were different compared to the work in [6.12]. This research did not observe individual pulses because at magnetising frequencies of just a few Hertz, overlapping of pulses takes place and a clear distinction between pulses is not possible. Therefore, a direct comparison between [6.12] and this study may not be possible but as the number of pulses and the calculated Barkhausen noise parameters are linked together a decrease of pulses would be recognised by a decreasing Barkhausen noise parameter value.

Dhar and Atherton [6.13] examined low carbon 1%Mn pipeline steel and they found that with increasing flux density in the sample the Barkhausen activity initially increased but finally started to decrease at higher magnitudes of flux density. Also, it was shown that the Barkhausen noise increased with increasing frequency. A sinusoidal magnetising waveform with magnetising frequencies up to 50 Hz was used to magnetise the sample up to a flux density of 1.5T. The rms value of the Barkhausen noise was the parameter, which showed the decrease of Barkhausen noise with flux density at magnetising frequencies of 12 Hz, 25 Hz and 50 Hz. The rms value of Barkhausen noise in this research at different magnetising frequencies versus peak flux density in figure 6.9, 6.10, 6.11, 6.12, 6.13, 6.14 and 6.15 curves show a linear characteristic. (Again, the total sum of amplitudes, power spectrum and kurtosis show similar trends.) The Barkhausen noise increases with increasing flux density and increasing magnetising frequency. As the main difference between [6.13] and this work is the material tested, the cause for these dissimilarities must be sought for within the material texture.

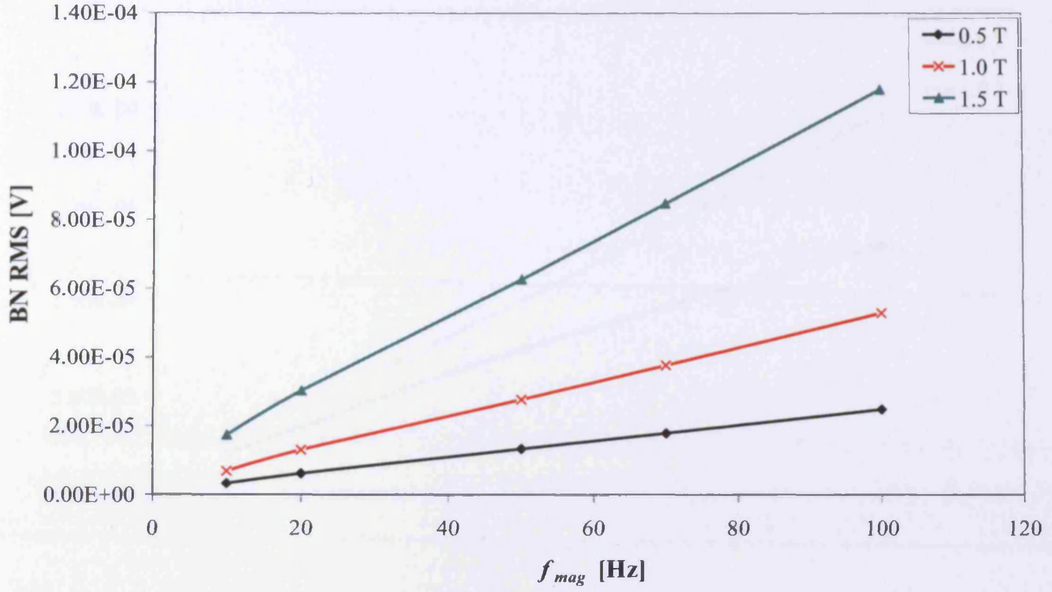

Figure 6.9. Variation of rms Barkhausen noise with magnetising frequency, f_{mag}, at 0.5 T, 1.0 T, 1.5 T magnetic flux density, for grain-oriented electrical steel cut at 0° to the rolling direction, 0.27 mm thick, measured with the double B-coil sensor

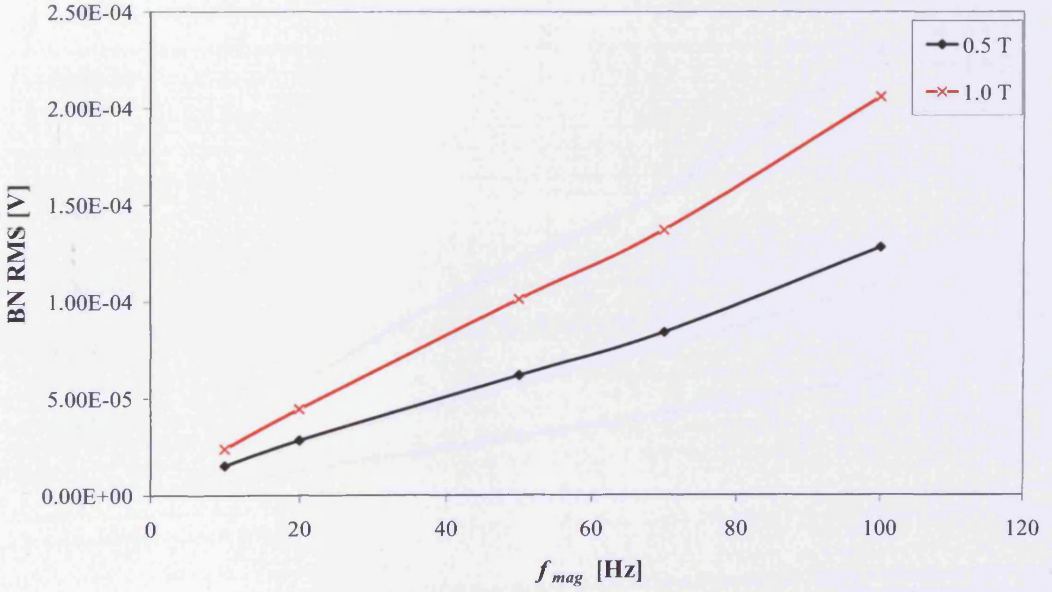

Figure 6.10. Variation of rms Barkhausen noise with magnetising frequency, f_{mag}, at 0.5 T, 1.0 T magnetic flux density, for grain-oriented electrical steel cut at 55° to the rolling direction, 0.27 mm thick, measured with the double B-coil sensor

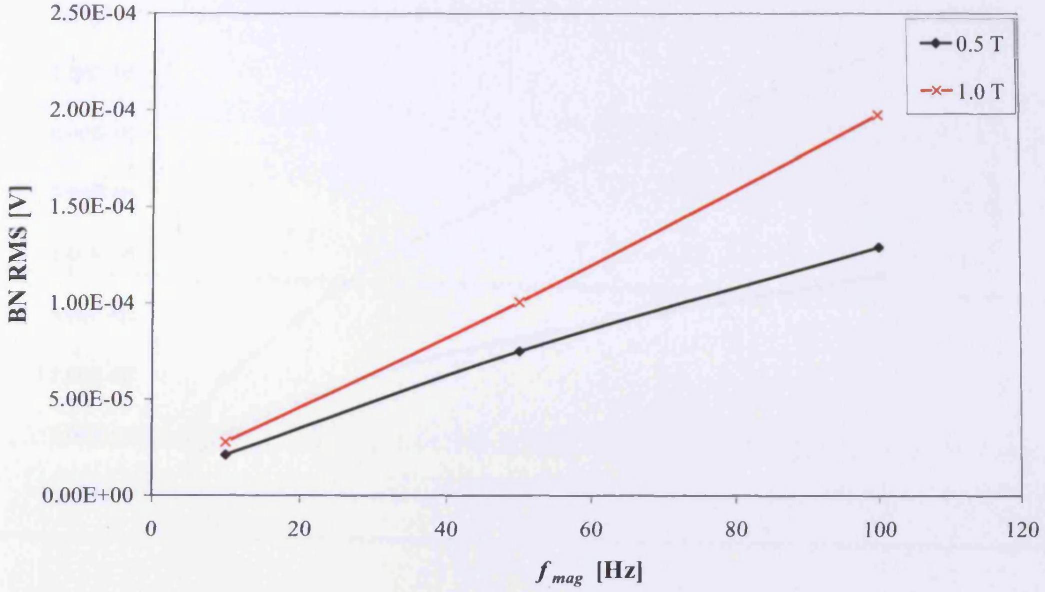

Figure 6.11. Variation of rms Barkhausen noise with magnetising frequency, f_{mag}, at 0.5 T, 1.0 T magnetic flux density, for grain-oriented electrical steel cut at 90° to the rolling direction, 0.27 mm thick, measured with the double B-coil sensor

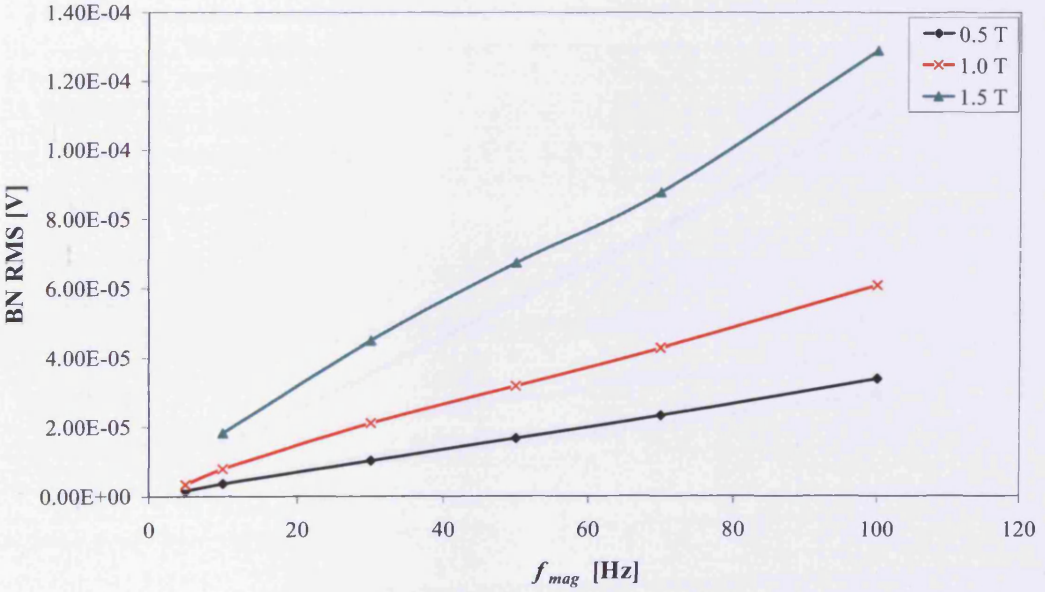

Figure 6.12. Variation of rms Barkhausen noise with magnetising frequency, f_{mag}, at 0.5 T, 1.0 T, 1.5 T magnetic flux density, for non-oriented electrical steel with 3%Si and 0.5 mm thick, measured with the double B-coil sensor

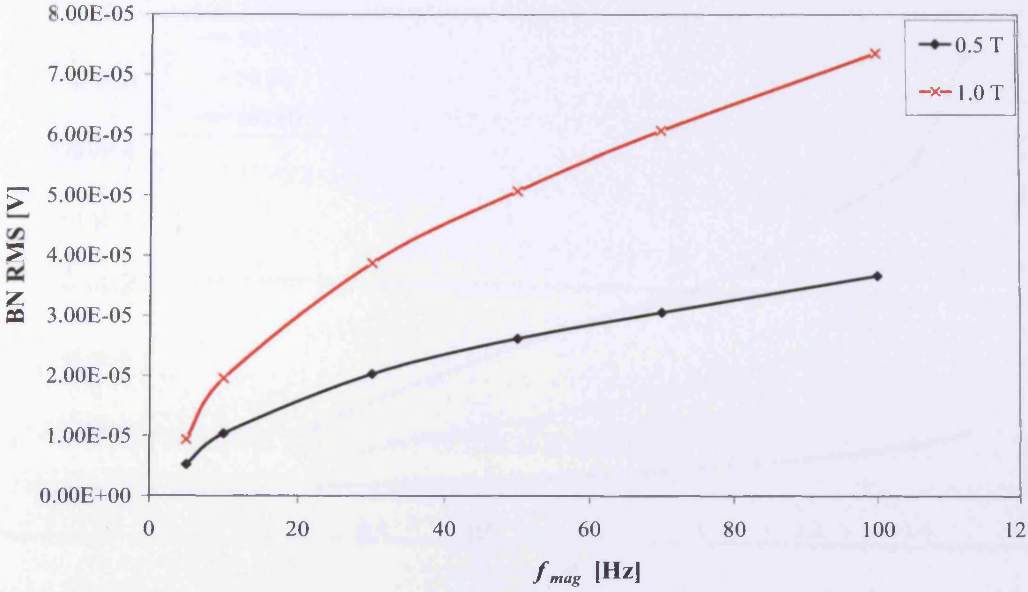

Figure 6.13. Variation of rms Barkhausen noise with magnetising frequency, f_{mag}, at 0.5 T, 1.0 T magnetic flux density, for non-oriented electrical steel with 6.5%Si and 0.1 mm thick, measured with the double B-coil sensor

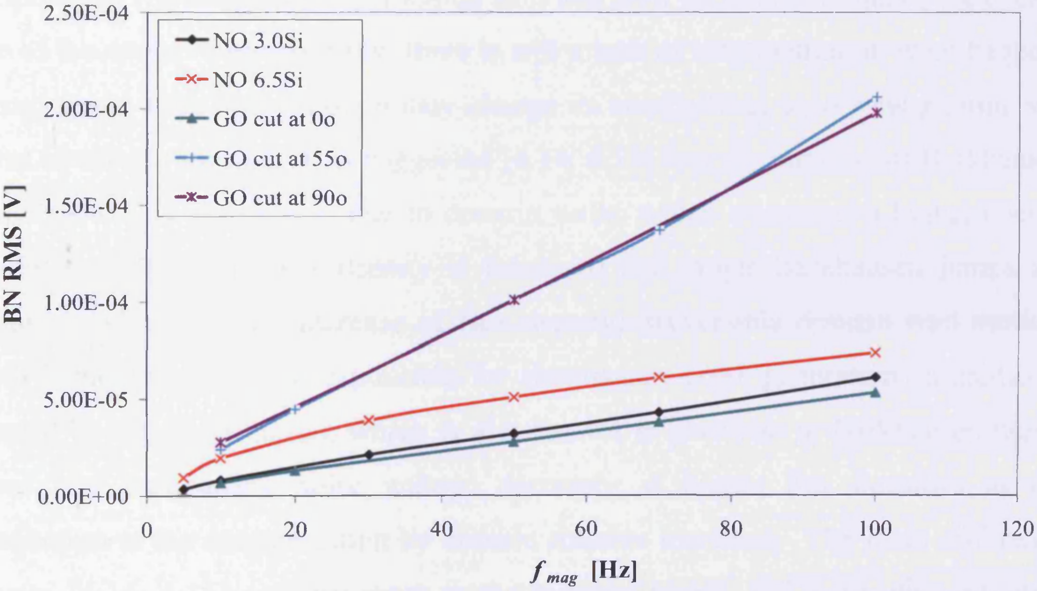

Figure 6.14. Variation of rms Barkhausen noise with magnetising frequency, f_{mag}, at 1.0 T magnetic flux density, for non-oriented electrical steel with 3%Si and 0.5 mm thick, non-oriented electrical steel with 6.5%Si and 0.1 mm thick, grain-oriented 3%Si electrical steel cut at 0°, 55° and 90° to the rolling direction and 0.27 mm thick, all measured with the double B-coil sensor

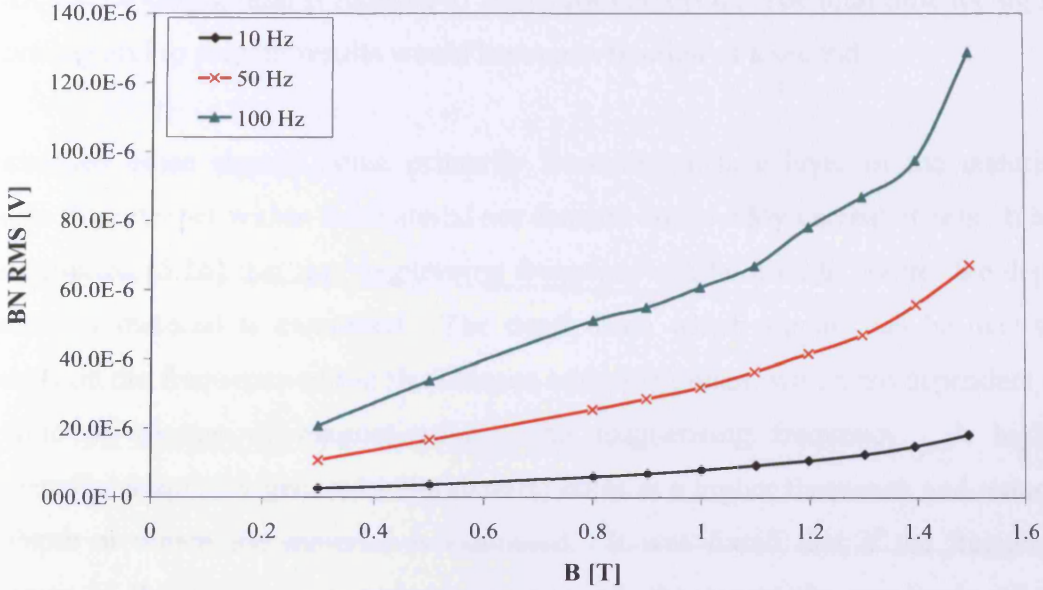

Figure 6.15. Variation of rms Barkhausen noise with peak magnetic flux density, *B*, at 10, 50 and 100 Hz magnetising frequency, for non-oriented electrical steel with 3%Si and 0.5 mm thick, all measured with the double B-coil sensor

The amplitude of Barkhausen emission depends on the energy of the domain wall that is unpinned. The distribution of pinning sites and their number determines the energy state of the walls. Unfortunately, there is still a lack of information on what happens when domain walls move, how it may change its energy level or to what pinning site it pins to once in motion. It is suggested [6.14, 6.15] that the increase of Barkhausen noise at low flux densities is due to domain walls, which overcome a higher energy pinning site while the flux density is increased and larger Barkhausen jumps are possible. With a further increase of flux density, irreversible domain wall motion, which is the main process responsible for Barkhausen noise generation, is gradually replaced by domain rotation, which is also known to give rise to Barkhausen noise. Hence, the Barkhausen noise voltage decreases at higher flux densities as the contribution to the magnetisation by domain rotation increases. The main difference between [6.14, 6.15] and this work is the material tested, and again dissimilarities must be sought from within the materials.

One advantage of a higher magnetising frequency is simply the fact that the time needed to capture a cycle is reduced significantly. With a magnetising frequency of

50 Hz, the capturing time is reduced to 20 ms for one cycle. The total time for signal processing and to present results would become a fraction of a second.

Barkhausen noise signals come primarily from the surface layer of the material. Signals from deeper within the material are damped due to eddy current effects. It has been reported [6.16] that the magnetising frequency can be used to control the depth at which a material is examined. The depth from which signals can be detected depends on the frequency of the Barkhausen emission pulses, which are dependent on the rate of change of magnetisation - the magnetising frequency. A higher magnetising frequency generates Barkhausen noise at a higher frequency and reduces the depth at which the material is examined. It was found that if the frequency spectrum of the Barkhausen noise was analysed, the larger the amplitude of the Barkhausen noise signal is, the lower is its frequency of emission [6.8, 6.17]. This means that the harmonic components within a Barkhausen noise signal decreases with increasing analysing frequency.

The increase of Barkhausen noise with increasing magnetising frequency is shown in figure 6.15, this is an advantage for data acquisition systems as higher Barkhausen signals are less problematic to capture. Unfortunately, with increasing magnetising frequency the observation of single Barkhausen jumps becomes less feasible as overlaying effects of pulses takes place.

6.5. Non-oriented electrical steel samples cut at various different directions to the rolling direction

Non-oriented steel is very nearly isotropic making it very suitable for rotating electrical machines. However, the material does have a very small anisotropy induced due to rolling. Anisotropy of losses in non-oriented electrical steels is mainly confined to the hysteresis component of loss [6.16]. It has been proposed that the hysteresis loss can be split into two components, a *high induction component*, which follows the texture behaviour, and a *low induction component*, which increases monotonically with the angle from the rolling direction [6.17]. Different energy mechanisms are acting on these two regions of the hysteresis loop; at low induction it is well accepted that domain wall motion is a major source of loss; however, at high induction the main energy dissipation is not clear, whether it is irreversible domain rotation (most likely), domain annihilation and nucleation or (less likely) simply more domain wall movement. Moses et al [6.18] correlated the high and low induction hysteresis components and Barkhausen noise in non-oriented electrical steel. It verified the influence of anisotropy of inter-inclusion distances on angular dependence of losses in non-oriented steel.

To verify these conclusions two stacks of different texture materials were investigated, both non-oriented electrical steel with parameters the same (table 4.7) (e.g. density, size, silicon content, etc), each stack had seven strips of 0.5 mm thick, electrical steel with 3.0%Si cut at 0°, 15°, 30°, 45°, 60°, 75° and 90° to the rolling direction. However, the average grain size was different, sample C1, with 53 μm and sample C2, with 180 μm. The total power loss and rms Barkhausen noise were measured at 50 Hz magnetising frequency and flux densities of 0.5 T and 1.0 T. The total power loss and rms Barkhausen noise are plotted against angle of rolling direction in figure 6.16 and figure 6.17 respectively. It was found that the power loss increased as the angle increased from 0° to 90° (figure 6.16). At 0° the power loss at 1.0 T, 50 Hz was 0.68 W/kg and at the same conditions for the 90° sample the power loss was 0.96 W/kg. This is due to the material's domains having to rotate due to material anisotropy induced during rolling, thus increasing the hysteresis component of loss. Moses et al [6.18] found a peak to occur at 60° where as in this investigation a peak was observed at 45°. This discrepancy is due to the different processing of the materials as they also used electrical steel samples (0.47 mm thick, non-oriented electrical steel). Clearly, there is a different texture dependence above and below this cutting angle.

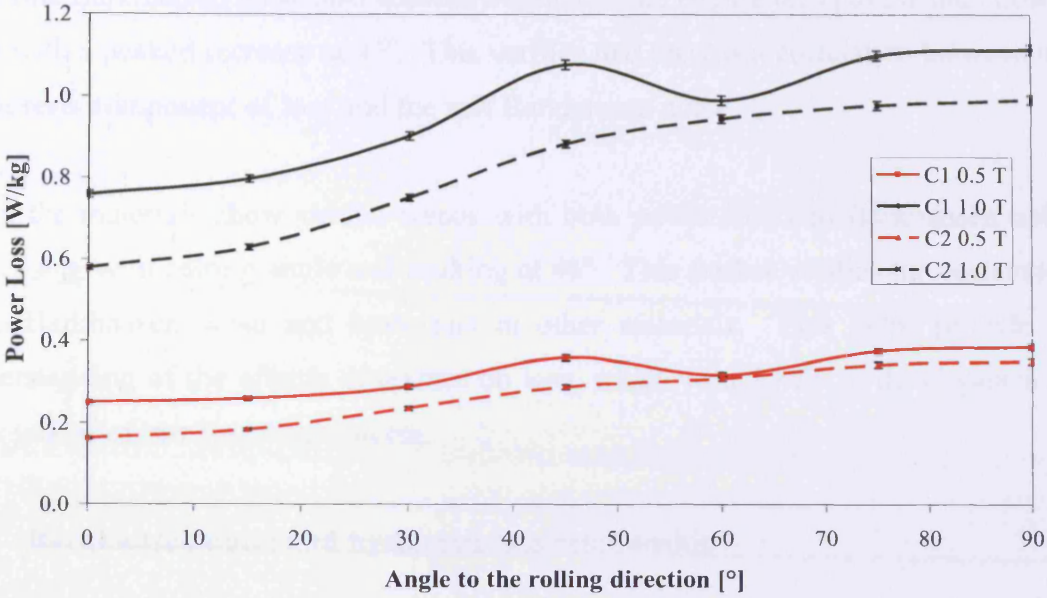

Figure 6.16. Variation of total power loss with angle of sample to the rolling direction, at 50 Hz magnetising frequency, at 0.5 T and 1.0 T magnetic flux density, for non-oriented electrical steel with 3%Si, 0.5 mm thick, C1 with average grain size of 53 μm, C2 with average grain size of 180 μm

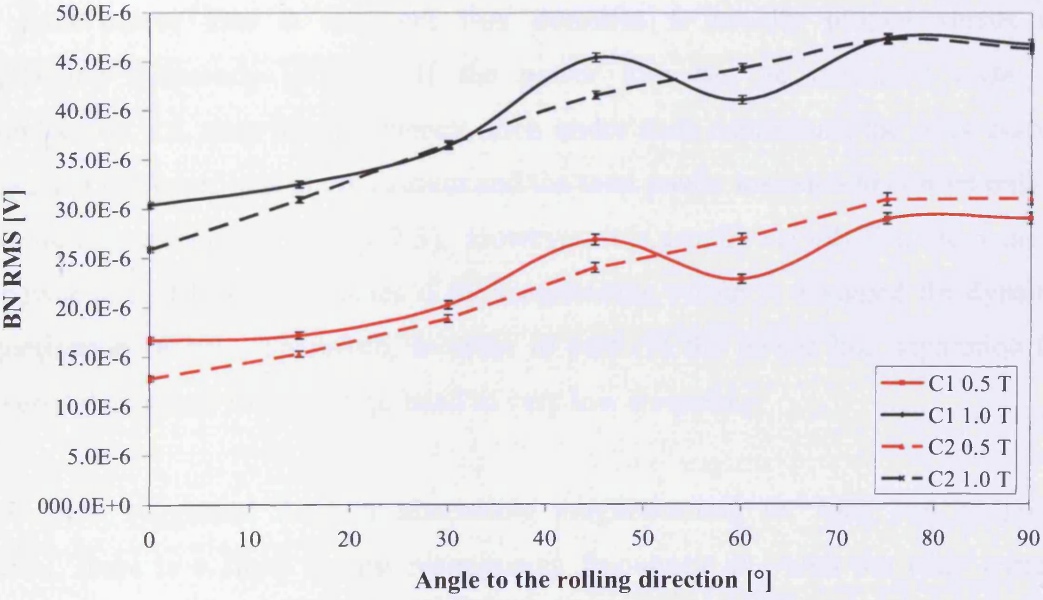

Figure 6.17. Variation of rms Barkhausen noise with angle of sample to the rolling direction, at 50 Hz magnetising frequency, at 0.5 T and 1.0 T magnetic flux density, for non-oriented electrical steel with 3%Si, 0.5 mm thick, C1 with average grain size of 53 μm, C2 with average grain size of 180 μm

The rms Barkhausen noise also showed a similar trend (figure 6.17) to the total power loss with a peaked increase at 45°. This verifies that there is a correlation between the hysteresis component of loss and the rms Barkhausen noise.

Both the materials show similar trends with both power loss and Barkhausen noise increasing with cutting angle and peaking at 45°. This further verifies the correlation with Barkhausen noise and hysteresis in other materials. This helps provide an understanding of the effects of texture on loss, which would help in development of new grades of low loss motor steels.

6.6. Barkhausen noise and hysteresis loss relationship

The hysteresis component is due to the work of the braking forces acting on the Bloch walls in motion [6.5]. They are greatest when the pinning forces are greatest. Therefore, there is expected to be a relationship between hysteresis loss and Barkhausen noise.

The total power loss at different flux densities is usually plotted versus the magnetising frequency [6.19]. If the power loss can be measured under dc magnetisation, i.e. very low frequency, then under such conditions, the eddy current component of power loss is not present and the total power loss should consist only of the hysteresis component (figure 2.3). However, it is usually very difficult to measure the power loss at low frequencies if the magnetising set-up is designed for dynamic magnetisation [6.20]. Therefore, in order to perform the power loss separation the measured data needs to be extrapolated to very low frequency.

It has been suggested that for alternating magnetisation, for each soft magnetic material, there is a finite lowest magnetising frequency at which the eddy current contribution to the total power loss can be neglected [6.21]. This finite frequency for most materials is in the range between 0.1 - 5 Hz [6.21]. This frequency can be found relatively simply, if the power loss is measured at a range from quasi-static to dynamic frequencies (Figure 6.18). The power loss separation method based on the principle described has been used frequently [6.19].

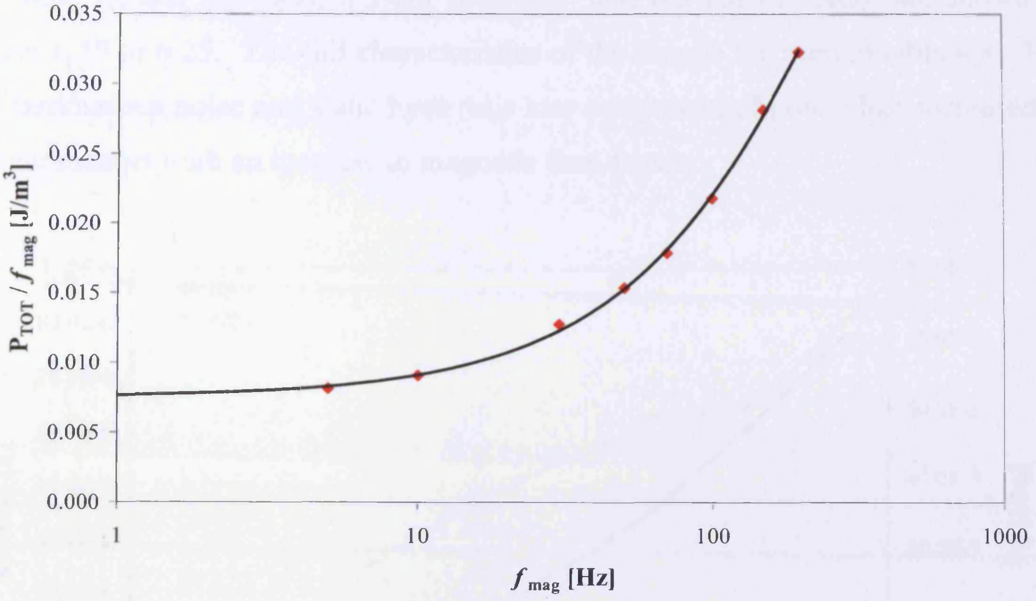

Figure 6.18. Power loss measured for different magnetising frequencies and the approximating function (the black line)

The non-oriented electrical steel samples (S1, S2, S3, S4, S5, S6 and S7) with various silicon contents were magnetised in the frequency range from 5 Hz to 200 Hz. The measured power losses were divided by the frequency to obtain the loss per cycle and plotted versus the frequency. Then, the approximation functions have been found through the automatic curve fitting available in LabVIEW. The approximating functions were second order polynomials ($y = A_2 \cdot x^2 + A_1 \cdot x + A_0$), with the coefficients found by the least-square method. Each level of magnetic flux density was approximated by different functions, the A_0 coefficient is the most dominant at low frequencies and if the frequency approaches zero then this can be treated as the number that represents the hysteresis component of power loss.

The Barkhausen noise was measured (using the double coil sensor) over 1 averaged cycle (the average over 10 cycles was calculated) at 50 Hz magnetising frequency and therefore a relationship between Barkhausen noise and static hysteresis loss could be investigated.

The static hysteresis loss component of power loss and Barkhausen noise variation with peak magnetic flux density under 50 Hz sinusoidal magnetisation in non-oriented electrical steels, with 0.2%Si (S1-NO), 0.3%Si (S2-NO), 1.3%Si (S3-NO), 1.8%Si

(S4-NO), 3.0%Si (S5-NO), 5.5%Si (S6-NO) and 6.5%Si (S7-NO), are shown in figures 6.19 to 6.25. The full characteristics of the sample are seen in table 4.8. The rms Barkhausen noise and static hysteresis loss component of power loss increased in a linear manner with an increase in magnetic flux density.

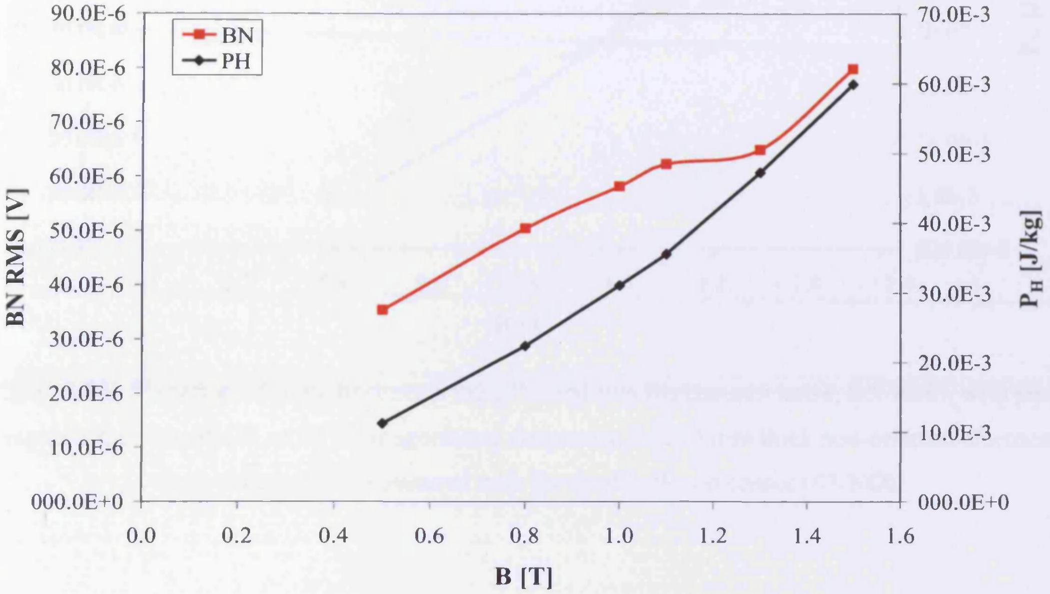

Figure 6.19. Variation of static hysteresis loss, P_H, and rms Barkhausen noise, BN RMS, with peak magnetic flux density, B, at 50 Hz magnetising frequency, for 0.5 mm thick non-oriented electrical steel with 0.2%Si, measured with the double B-coil sensor (S1-NO)

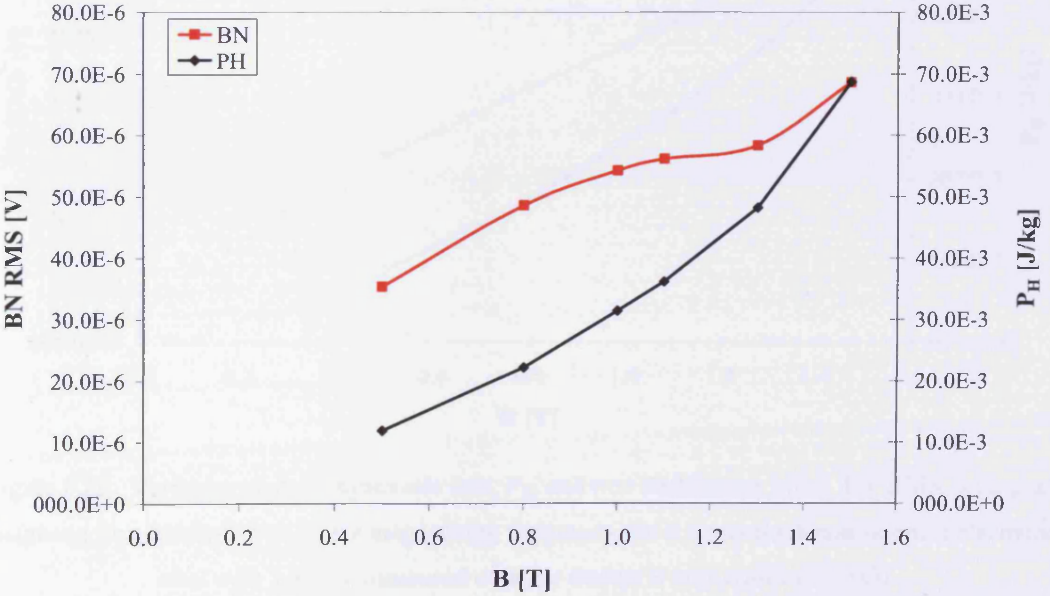

Figure 6.20. Variation of static hysteresis loss, P_H, and rms Barkhausen noise, BN RMS, with peak magnetic flux density, B, at 50 Hz magnetising frequency, for 0.5 mm thick non-oriented electrical steel with 0.3%Si, measured with the double B-coil sensor (S2-NO)

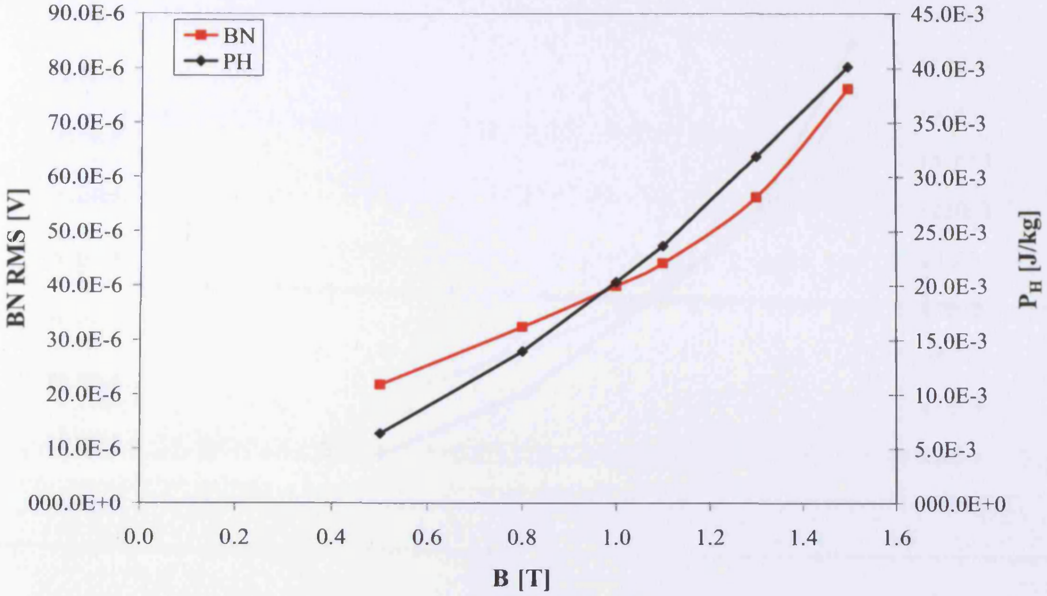

Figure 6.21. Variation of static hysteresis loss, P_H, and rms Barkhausen noise, BN RMS, with peak magnetic flux density, B, at 50 Hz magnetising frequency, for 0.5 mm thick non-oriented electrical steel with 1.3%Si, measured with the double B-coil sensor (S3-NO)

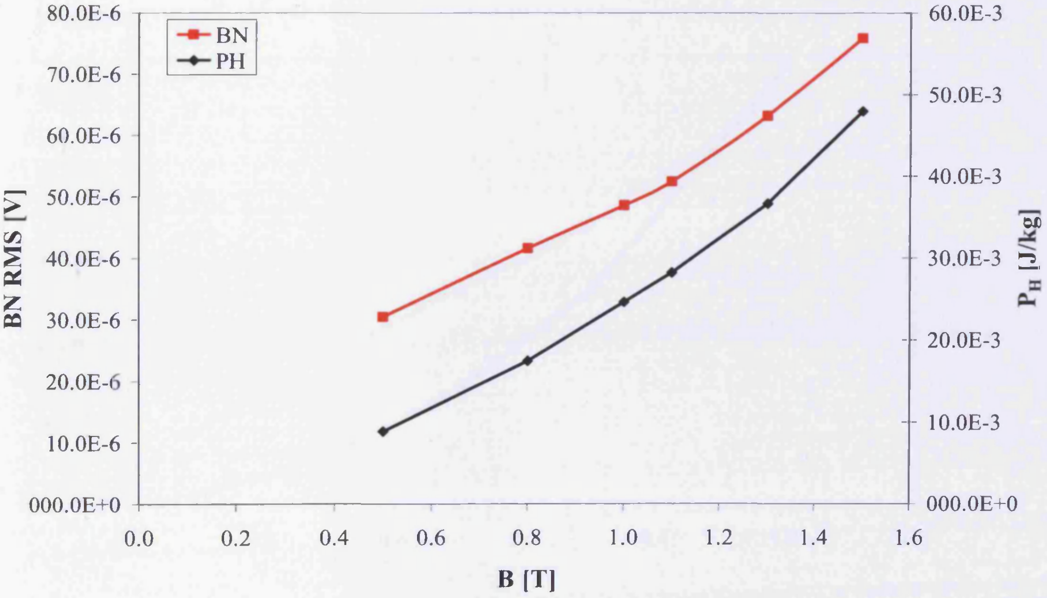

Figure 6.22. Variation of static hysteresis loss, P_H, and rms Barkhausen noise, BN RMS, with peak magnetic flux density, B, at 50 Hz magnetising frequency, for 0.5 mm thick non-oriented electrical steel with 1.8%Si, measured with the double B-coil sensor (S4-NO)

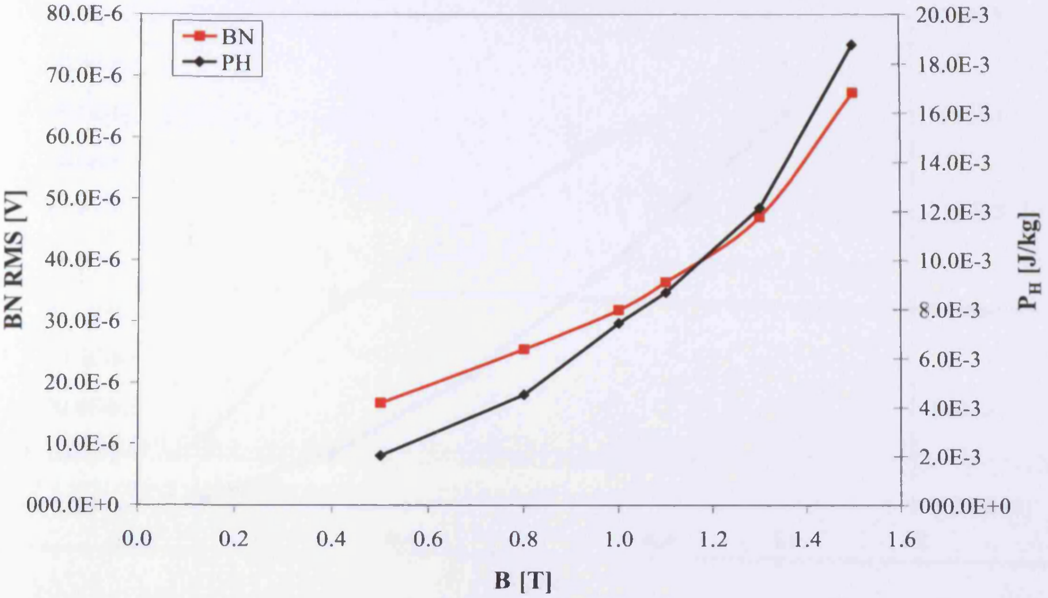

Figure 6.23. Variation of static hysteresis loss, P_H, and rms Barkhausen noise, BN RMS, with peak magnetic flux density, B, at 50 Hz magnetising frequency, for 0.5 mm thick non-oriented electrical steel with 3.0%Si, measured with the double B-coil sensor (S5-NO)

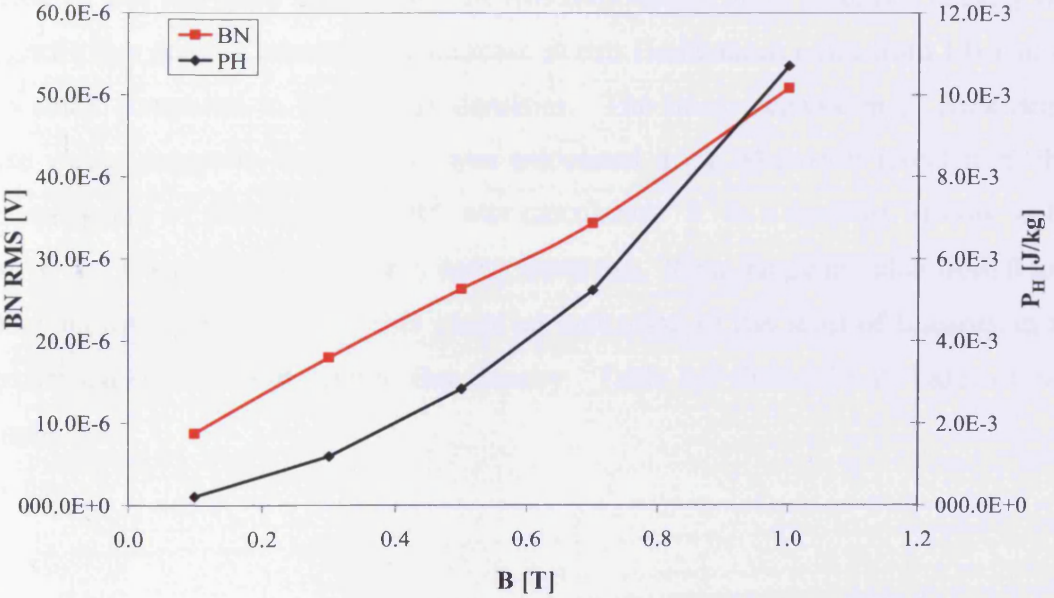

Figure 6.24. Variation of static hysteresis loss, P_H, and rms Barkhausen noise, BN RMS, with peak magnetic flux density, B, at 50 Hz magnetising frequency, for 0.1 mm thick non-oriented electrical steel with 5.5%Si, measured with the double B-coil sensor (S6-NO)

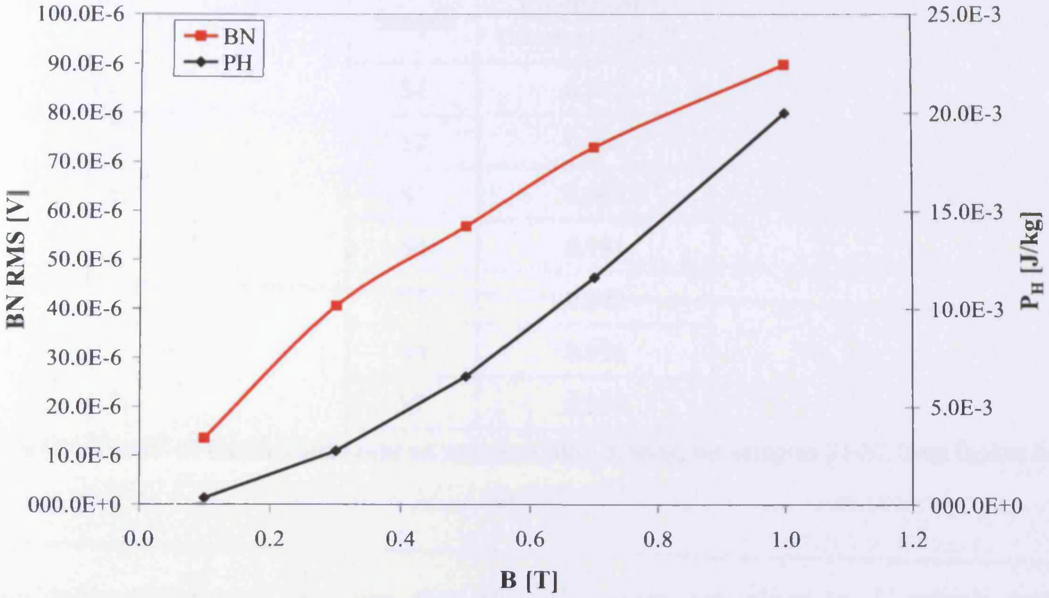

Figure 6.25. Variation of static hysteresis loss, P_H, and rms Barkhausen noise, BN RMS, with peak magnetic flux density, B, at 50 Hz magnetising frequency, for 0.1 mm thick non-oriented electrical steel with 6.5%Si, measured with the double B-coil sensor (S7-NO)

In non-oriented electrical steel with 0.2%Si (figure 6.19) and 0.3%Si (figure 6.20), the hysteresis loss increases linearly and the rms Barkhausen noise increases linearly with magnetic flux density however the increase in rms Barkhausen noise from 1.0 T to 1.3 T is small compared to lower flux densities. The linear regression of Barkhausen noise versus magnetic flux density was calculated using Microsoft Excel from this, the coefficient of determination, R^2, was calculated. R^2 is a measure of how well a best-fit line fits to the data that it is being fitted too. It can range in value from 0 to 1, with 1 indicating perfect fit. This gives an indication of the level of linearity in the Barkhausen noise with magnetic flux density. Table 6.3 shows the R^2 value of each sample.

Sample	Coefficient of determination, R^2
S1	0.972
S2	0.961
S3	0.943
S4	0.981
S5	0.922
S6	0.996
S7	0.969

Table 6.3. The R^2 of Barkhausen noise vs. magnetic flux density, for samples S1-S7 from figures 6.19 to 6.25

From table 6.3 it can be seen that the R^2 values are close to 1, which means Barkhausen noise follows a linear relationship with magnetic flux density. The Barkhausen noise of non-oriented electrical steel samples with 1.3% (figure 6.21), 1.8% (figure 6.22), 3.0% (figure 6.23), 5.5% (figure 6.24), and 6.5% Si (figure 6.25) increased linearly with magnetic flux density and no discrepancies like 0.2%Si (S1-NO) (figure 6.19) and 0.3%Si (S2-NO) (figure 6.20) samples are observed. As this discrepancy is only observed in low silicon content (<1%Si) electrical steel, it is concluded that at high magnetisation the Barkhausen noise in low silicon content electrical steel samples does not increase linearly. This is due to a reduction in domain rotation thus reducing the rms Barkhausen noise.

Some correlation has previously been found between Barkhausen noise under ac magnetisation and the static hysteresis component of power loss [6.2]. In all the materials tested the rms Barkhausen noise at 50 Hz rises with static hysteresis confirming the general trend found previously in a wider range of materials. It is recognised today that loss separation in this way is artificial; however, the result does indicate that a close relationship between Barkhausen noise and static hysteresis loss does exist.

An investigation into the influence of silicon content to Barkhausen noise was also investigated. Figure 6.26 shows the total power loss measured in all non-oriented electrical steel samples against silicon content. A 2nd order polynomial approximation function is used to show the general trend of the results. It can be seen that the total power loss decreases with an increase in silicon content. At 5.5%Si the power loss does increase compared to the non-oriented 3.0%Si electrical steel. This difference is due to the processing of 5.5%Si electrical steel. The main methods for commercially producing high silicon content non-oriented electrical steel is by chemical vapour deposition and the rolling methods [6.22]. Also, it must be noted that the 5.5% and 6.5% Si non-oriented electrical steel samples are 0.1 mm thick compared to the others that are 0.5 mm thick. However, the 5.5%SiFe non-oriented electrical steel sample at 50 Hz magnetisation frequency, at 1.0 T flux density, had a total power loss of 1.06 W/kg whereas the 6.5%SiFe non-oriented sample gave 0.76 W/kg at the same magnetising frequency and flux density. This does indicate that the processing of the 5.5%SiFe sample increased the Barkhausen noise content.

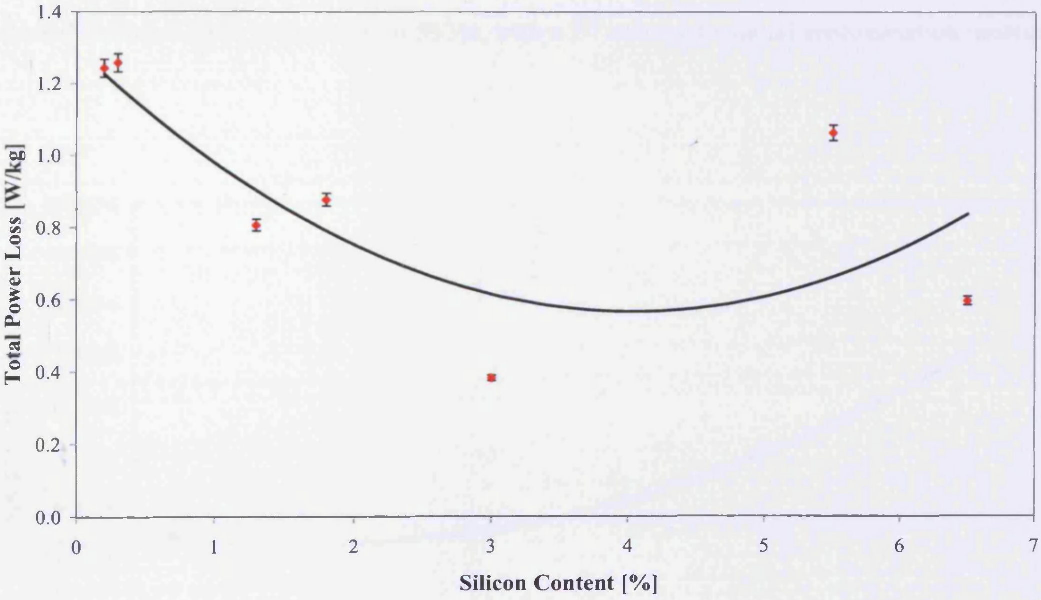

Figure 6.26. Total power loss against silicon content in 0.2%Si (S1-NO), 0.3%Si (S2-NO), 1.3%Si (S3-NO), 1.8%Si (S4-NO), 3.0%Si (S5-NO), 5.5%Si (S6-NO) and 6.5%Si (S7-NO) non-oriented electrical steel, magnetised at 50 Hz, with a 2nd order polynomial approximation function

The hysteresis loss component was extrapolated from the results above (figure 6.26) and it can be seen from figure 6.27 that the hysteresis loss component decreases with silicon content and then increases at 5.5%Si. If the rms Barkhausen noise versus silicon content is plotted (figure 6.28) it can be seen that the Barkhausen noise signal follows a close relationship with the hysteresis loss component.

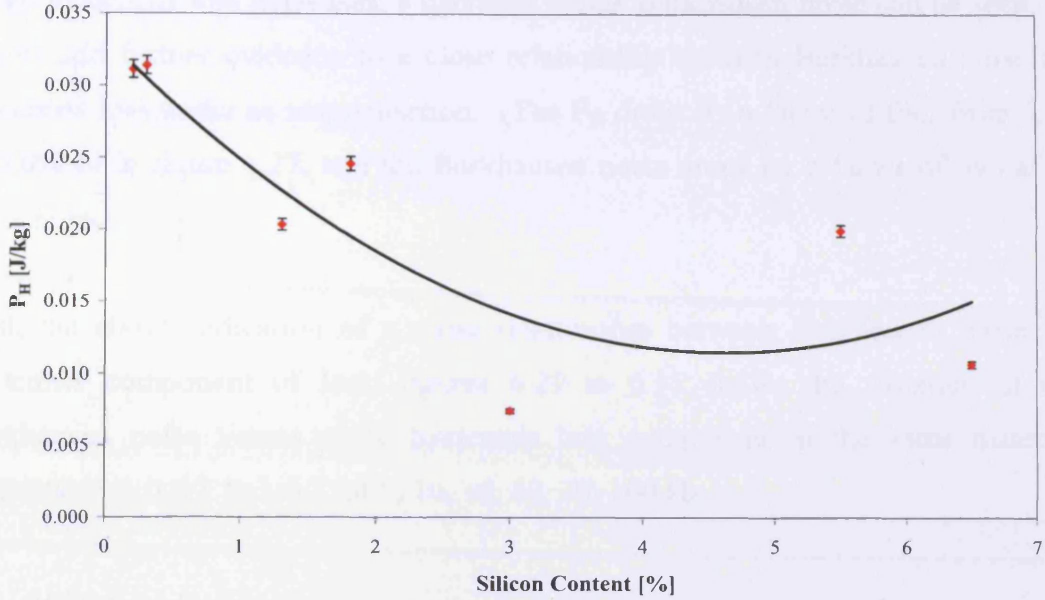

Figure 6.27. Static hysteresis loss, P_H, against silicon content in 0.2%Si (S1-NO), 0.3%Si (S2-NO), 1.3%Si (S3-NO), 1.8%Si (S4-NO), 3.0%Si (S5-NO), 5.5%Si (S6-NO) and 6.5%Si (S7-NO) non-oriented electrical steel, magnetised at 50 Hz, with a 2nd order polynomial approximation function

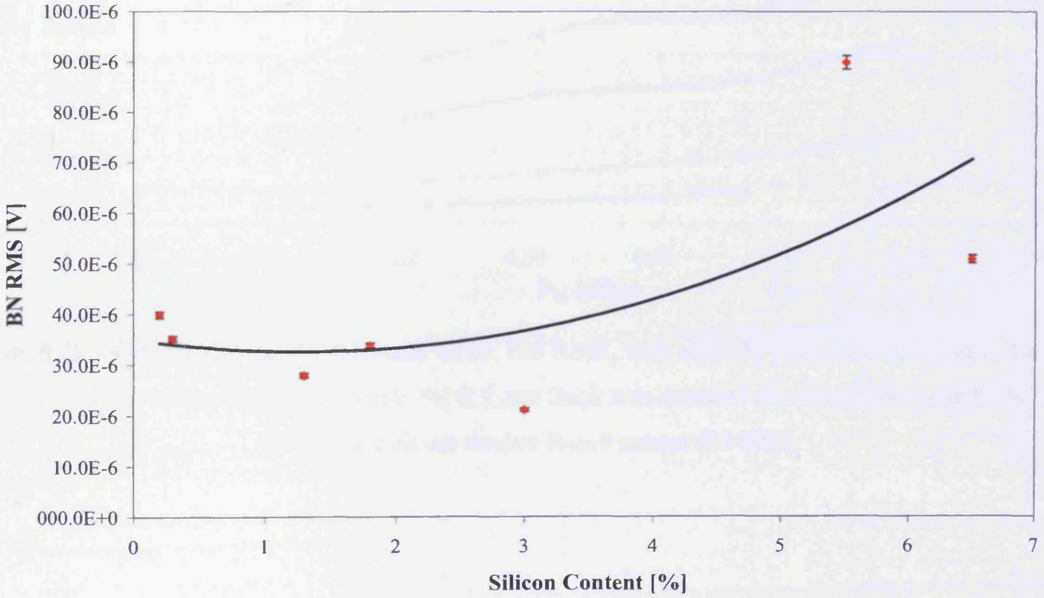

Figure 6.28. RMS Barkhausen noise, BN RMS, against silicon content in 0.2%Si (S1-NO), 0.3%Si (S2-NO), 1.3%Si (S3-NO), 1.8%Si (S4-NO), 3.0%Si (S5-NO), 5.5%Si (S6-NO) and 6.5%Si (S7-NO) non-oriented electrical steel, magnetised at 50 Hz, with a 2nd order polynomial approximation function

When hysteresis loss decreases, a decrease in rms Barkhausen noise can be seen; the results add further evidence to a close relationship between Barkhausen noise and hysteresis loss under ac magnetisation. (The P_H drops by a factor of four from 0.2% to 3.0% Si in figure 6.27, and the Barkhausen noise drops by a factor of two at the same points.)

With the above indication of a close relationship between Barkhausen noise and hysteresis component of loss, figures 6.29 to 6.35 shows the variation of rms Barkhausen noise versus static hysteresis loss component in the same materials magnetised at 0.5 T to 1.5 T, at 5, 10, 30, 50, 70, 100 Hz.

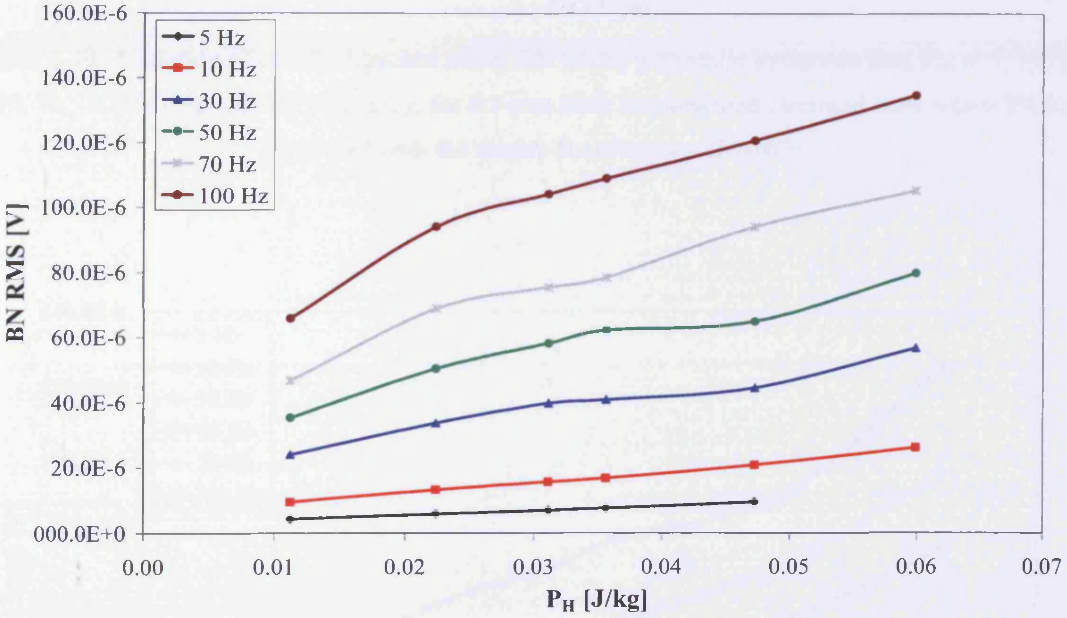

Figure 6.29. Variation of rms Barkhausen noise, BN RMS, with static hysteresis loss, P_H, at 5, 10, 30, 50, 70, 100 Hz magnetising frequency, for 0.5 mm thick non-oriented electrical steel with 0.2%Si, measured with the double B-coil sensor (S1-NO)

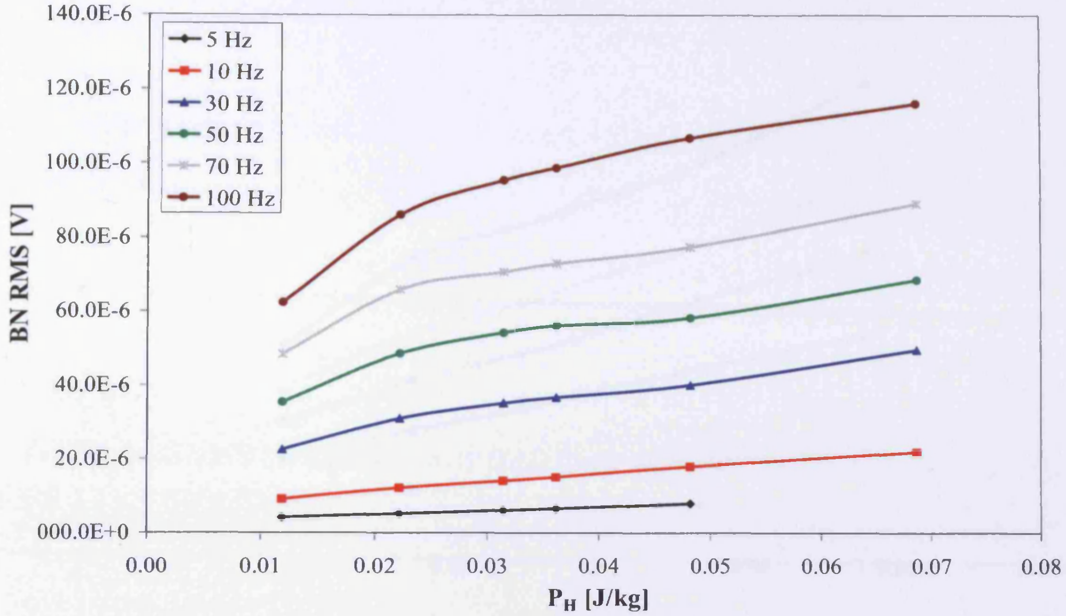

Figure 6.30. Variation of rms Barkhausen noise, BN RMS, with static hysteresis loss, P_H, at 5, 10, 30, 50, 70, 100 Hz magnetising frequency, for 0.5 mm thick non-oriented electrical steel with 0.3%Si, measured with the double B-coil sensor (S2-NO)

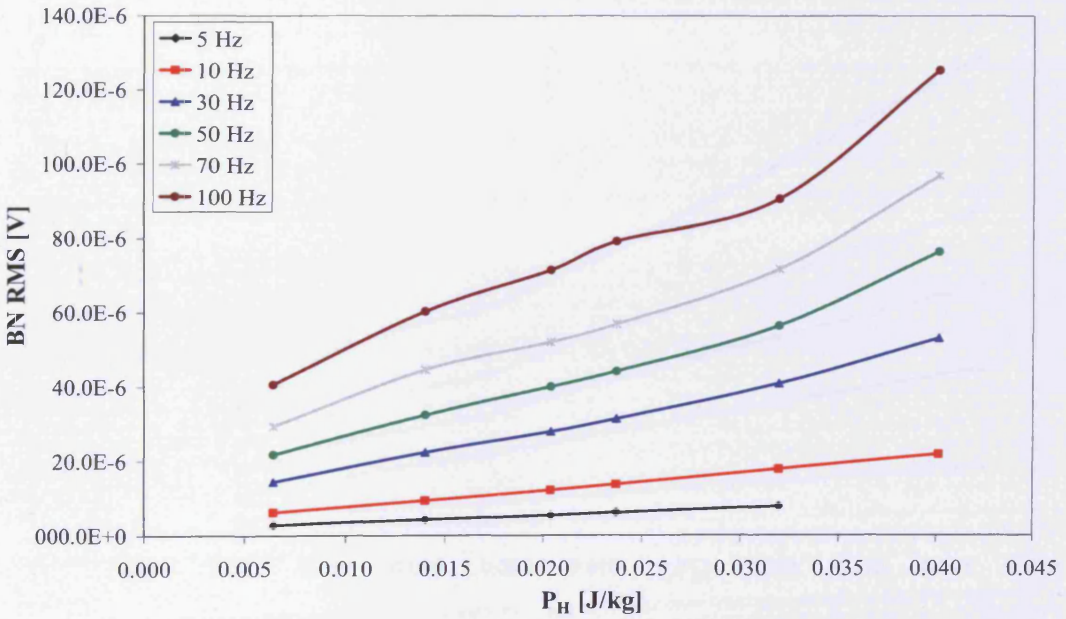

Figure 6.31. Variation of rms Barkhausen noise, BN RMS, with static hysteresis loss, P_H, at 5, 10, 30, 50, 70, 100 Hz magnetising frequency, for 0.5 mm thick non-oriented electrical steel with 1.3%Si, measured with the double B-coil sensor (S3-NO)

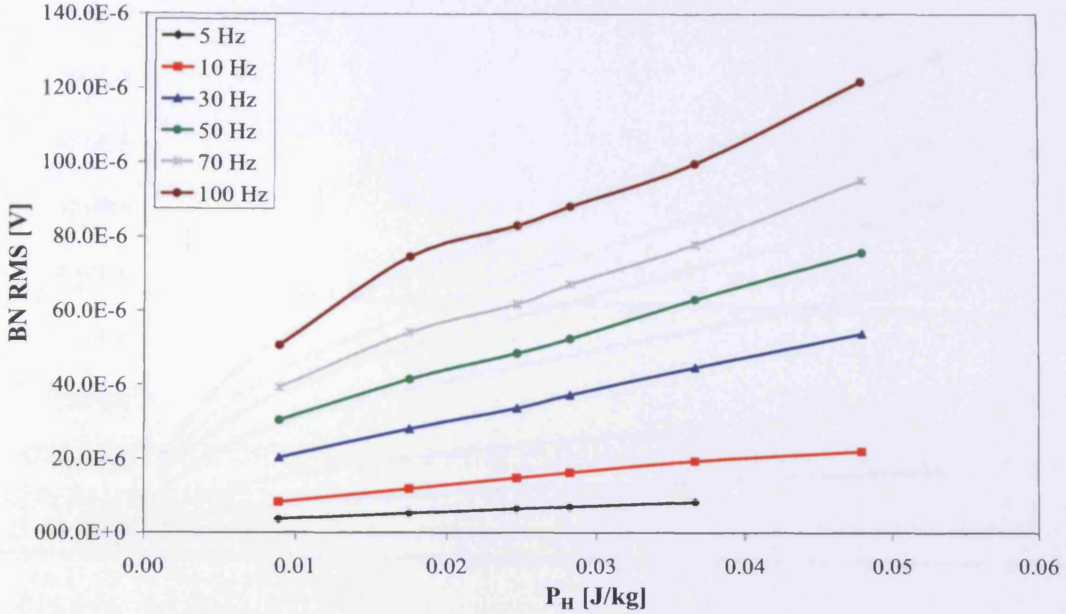

Figure 6.32. Variation of rms Barkhausen noise, BN RMS, with static hysteresis loss, P_H, at 5, 10, 30, 50, 70, 100 Hz magnetising frequency, for 0.5 mm thick non-oriented electrical steel with 1.8%Si, measured with the double B-coil sensor (S4-NO)

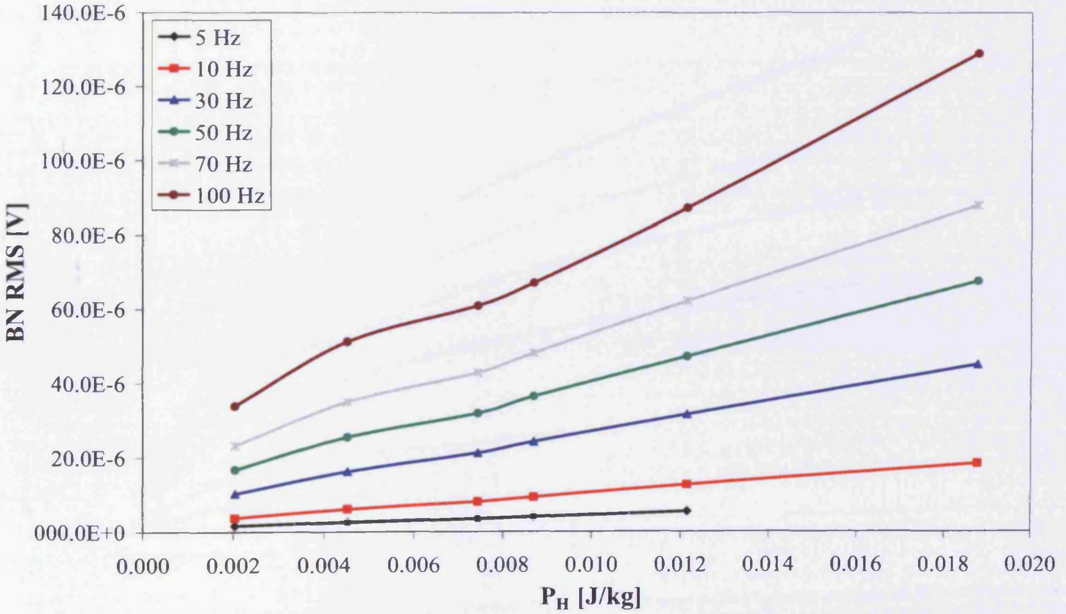

Figure 6.33. Variation of rms Barkhausen noise, BN RMS, with static hysteresis loss, P_H, at 5, 10, 30, 50, 70, 100 Hz magnetising frequency, for 0.5 mm thick non-oriented electrical steel with 3.0%Si, measured with the double B-coil sensor (S5-NO)

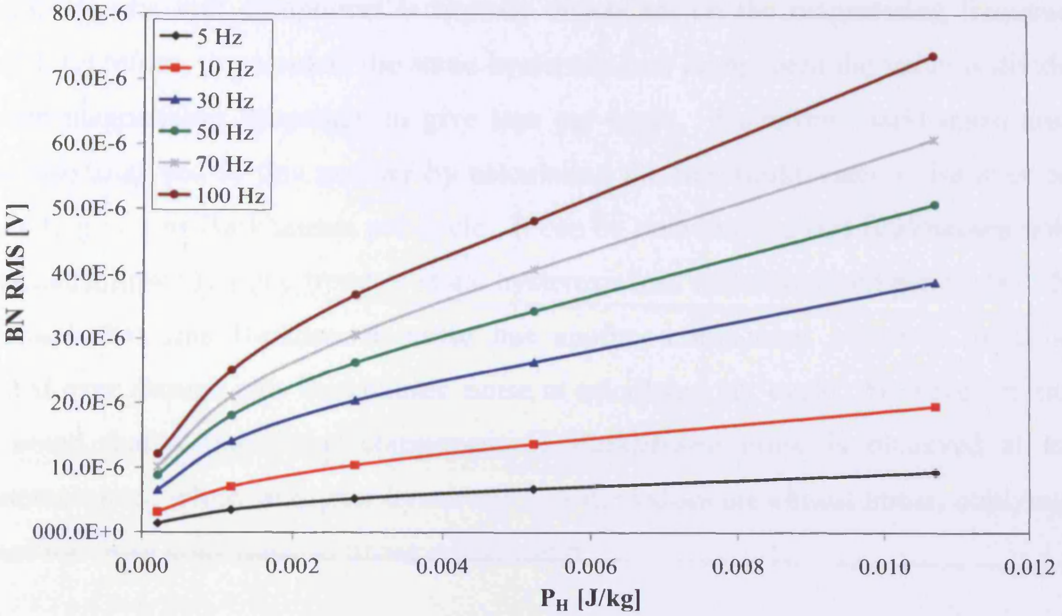

Figure 6.34. Variation of rms Barkhausen noise, BN RMS, with static hysteresis loss, P_H, at 5, 10, 30, 50, 70, 100 Hz magnetising frequency, for 0.1 mm thick non-oriented electrical steel with 5.5%Si, measured with the double B-coil sensor (S6-NO)

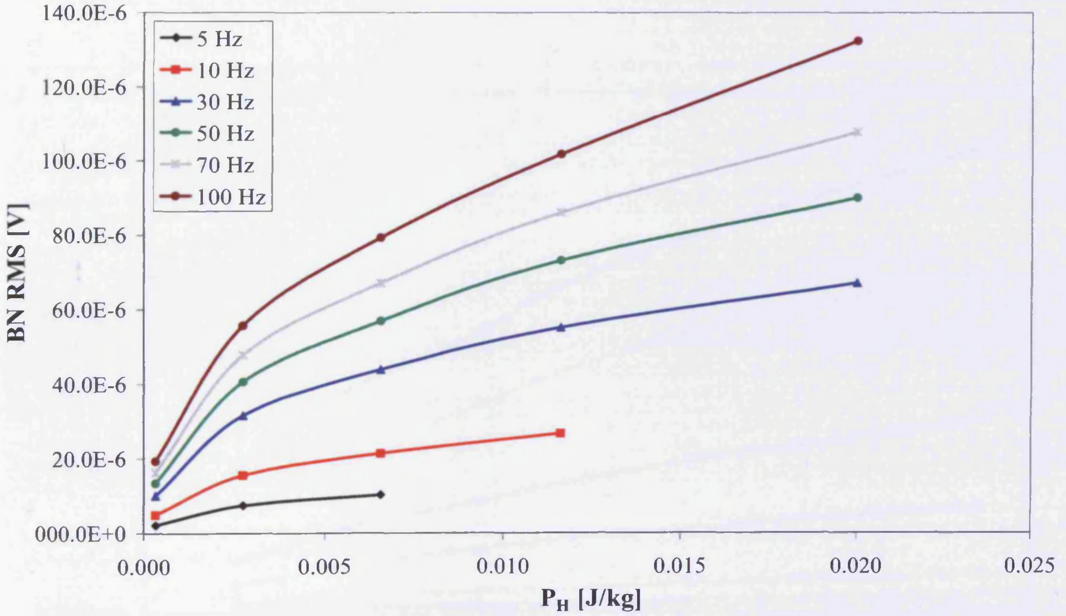

Figure 6.35. Variation of rms Barkhausen noise, BN RMS, with static hysteresis loss, P_H, at 5, 10, 30, 50, 70, 100 Hz magnetising frequency, for 0.1 mm thick non-oriented electrical steel with 6.5%Si, measured with the double B-coil sensor (S7-NO)

The hysteresis loss component is linearly dependent on the magnetising frequency [6.19]; therefore, to calculate the static hysteresis loss component the value is divided by the magnetising frequency to give loss per cycle. Therefore, Barkhausen noise was also analysed in this manner by calculating the rms Barkhausen noise over one cycle to give rms Barkhausen per cycle. It can be seen that the rms Barkhausen noise does not follow the same trend as static hysteresis loss when analysed per cycle. This indicates that rms Barkhausen noise has another component which is frequency related even though rms Barkhausen noise is calculated per cycle. However, it must be noted that a non-linear component of Barkhausen noise is observed at low hysteresis loss; while, at higher hysteresis loss the values are almost linear, implying a transition from non-linear to linear relationship.

The above measurements were also conducted with the surface ferrite sensor (figure 6.36) and the same trends can be seen with the surface sensor. The surface measurement of Barkhausen noise gives the same result as the wound coil method, which indicates that the perpendicular component of Barkhausen noise also gives the same relationship with the hysteresis loss component.

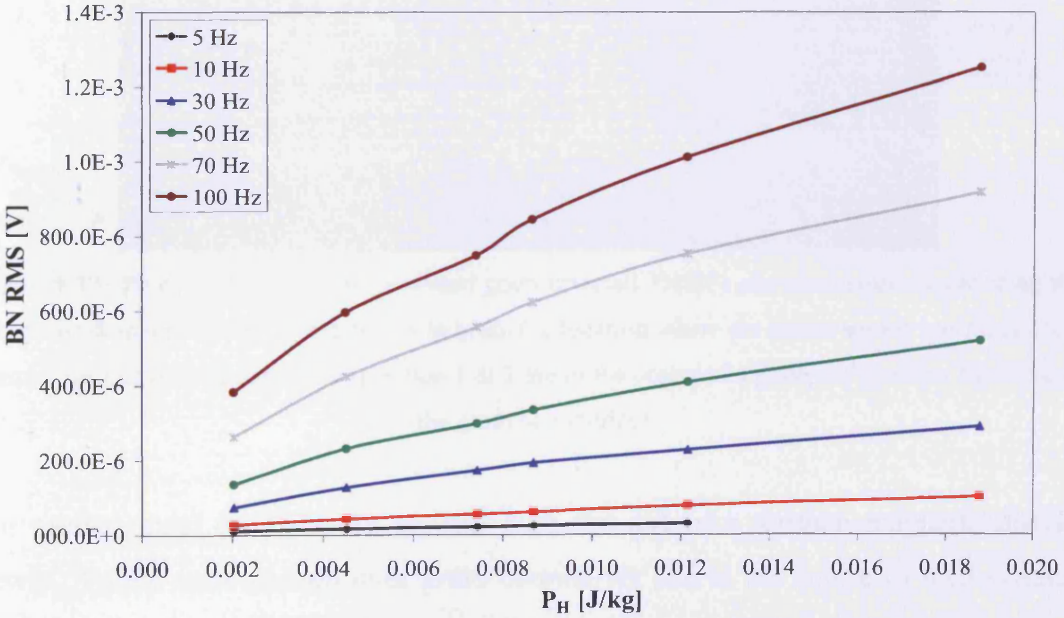

Figure 6.36. Variation of rms Barkhausen noise, BN RMS, with static hysteresis loss, P_H, at 5, 10, 30, 50, 70, 100 Hz magnetising frequency, for 0.5 mm thick non-oriented electrical steel with 3.0%Si, measured with the ferrite sensor (S5-NO)

The results presented in this section indicate that a relationship between Barkhausen noise and hysteresis component of loss is present. However, there is also another component (e.g. frequency component) present in the Barkhausen noise signal measured. Further investigation is required to understand the full information stored within a Barkhausen noise signal.

6.7. Grain-to-grain variation of Barkhausen noise

The coating applied to the surface of grain-oriented electrical steel not only provides interlaminar insulation in assembled cores but it induces a beneficial stress into the steel, which reduces losses in the steel [6.23]. The Barkhausen noise before and after chemical removal of the coating of a 0.27 mm thick, grain-oriented 3%SiFe steel was measured using the ferrite cored sensor (length 12.9 mm) at 4 points on the surface, at 50 Hz in the range 0.3 T to 1.4 T (figure 6.37 illustrates the locations of the measurements taken).

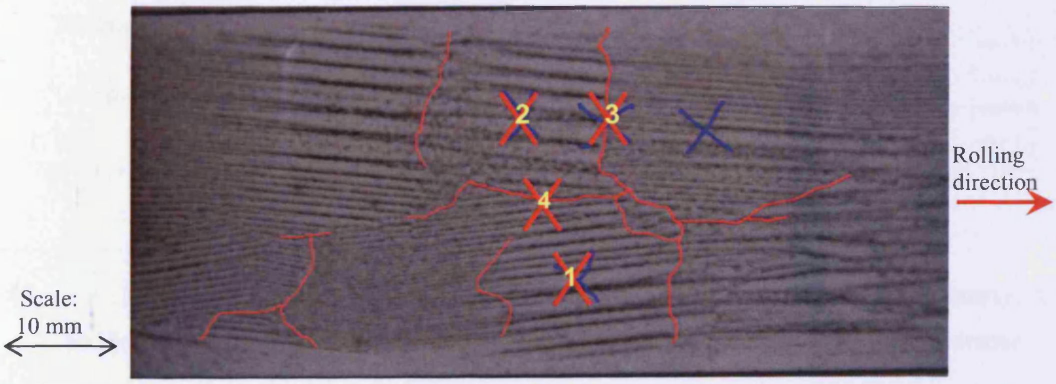

Figure 6.37. Photo of the grains in the coated grain-oriented 3%SiFe electrical steel sample using the magnetic domain viewer. The numbers indicate the location where the ferrite sensor was placed for measurement of Barkhausen noise (position 1 & 2 are in the centre of a grain and position 3 & 4 are on the grain boundaries)

The measurement points were chosen with the aid of a surface magnetic domain viewer. Points were chosen over grain boundaries and in the centre of well-oriented grains of average diameter 10 mm. The total measurement uncertainty of rms Barkhausen noise signals was a maximum of ±5% over the measurement range.

The coating was removed by dipping in hydrochloric acid at a room temperature of 20 °C for 30 minutes; once the coating was removed; the sample was annealed in a vacuum at 810 °C for 2 hours, to relieve the sample of any stresses incurred during coating removal.

Figure 6.38 shows the measured rms Barkhausen noise signal for the coated sample and figure 6.39 shows the measured rms Barkhausen noise signal after coating removal, with peak flux density across the sample.

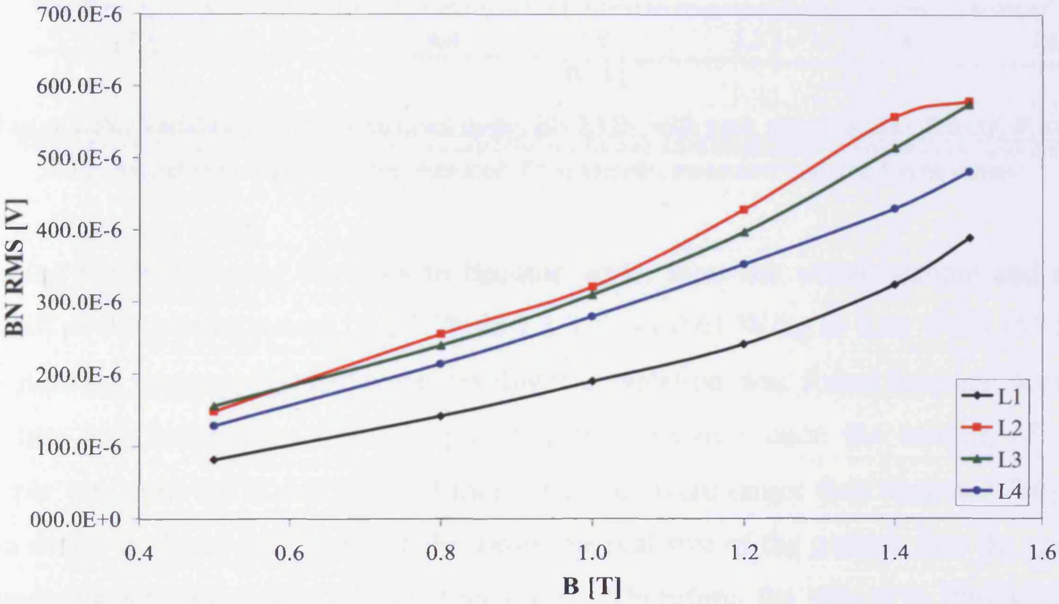

Figure 6.38. Variation of rms Barkhausen noise, BN RMS, with peak magnetic flux density, *B*, at 50 Hz magnetising frequency, for coated 3%Si sample, measured with the ferrite sensor

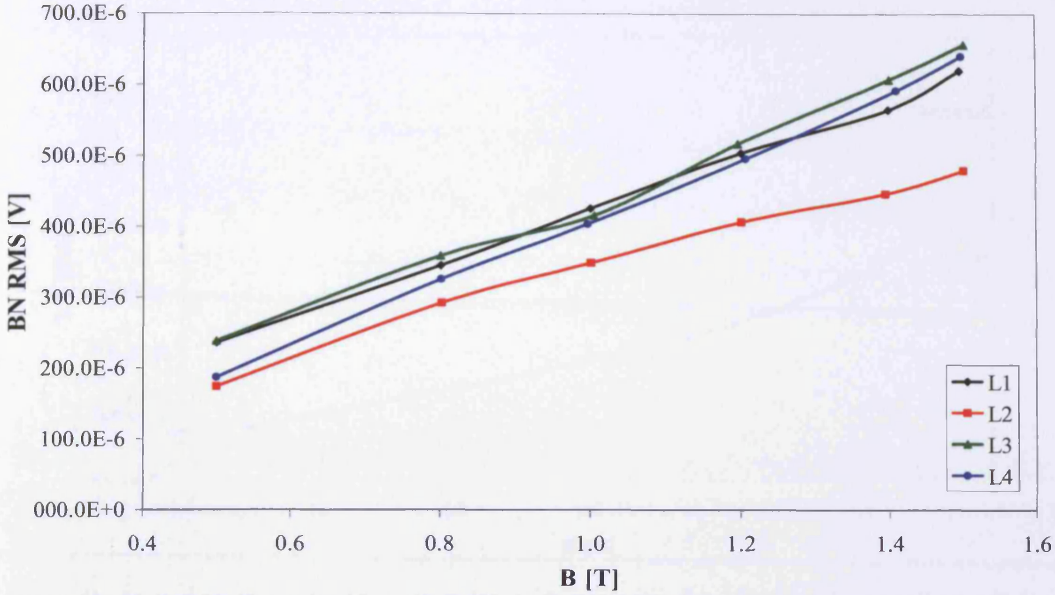

Figure 6.39. Variation of rms Barkhausen noise, BN RMS, with peak magnetic flux density, *B*, at 50 Hz magnetising frequency, for uncoated 3%Si sample, measured with the ferrite sensor

Coating removal caused domains to become wider over the whole sample and the overall power loss increased by 25.2% at 1.4 T from 0.61 W/kg to 0.81 W/kg (50 Hz magnetising frequency). However, no direct correlation was found between sensor position and Barkhausen noise output, this was because once the coating of the sample was removed it was realised that the grains were larger than expected (larger than shown in figure 6.37, figure 6.40 shows the real size of the grains), thus the grain boundaries not lying in the expected locations. Therefore, the effects to Barkhausen noise and power loss with a coated and uncoated electrical steel sample were investigated. The Barkhausen noise variation between a coated and uncoated electrical steel sample can be seen in figure 6.41.

Figure 6.40. Photo of the domains in the uncoated grain-oriented 3%SiFe electrical steel sample using the magnetic domain viewer

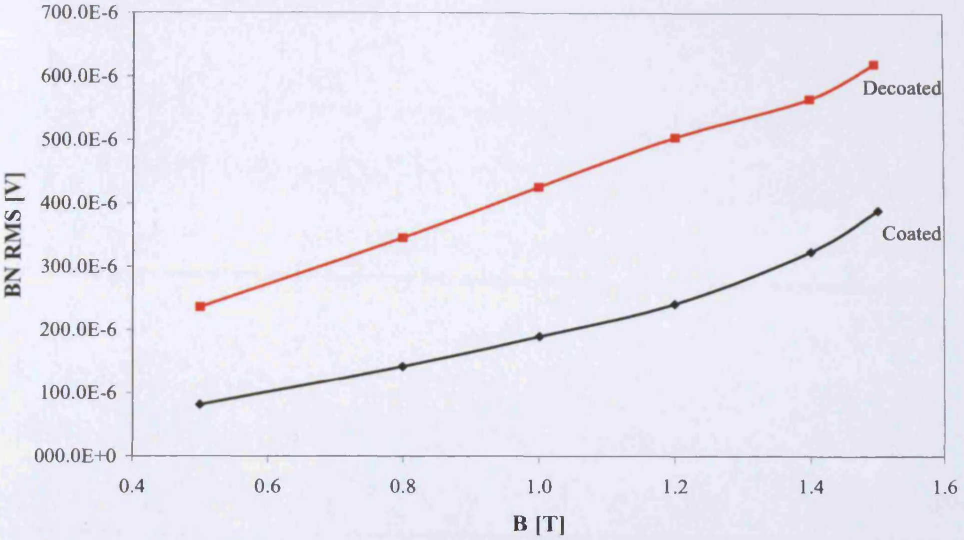

Figure 6.41. Variation of rms Barkhausen noise, with magnetic flux density, B, at position 1 (L1), at 50 Hz magnetising frequency, in 0.27 mm thick, 3%Si grain-oriented steel before and after coating removal, measured with the ferrite sensor

Removal of the coating and the subsequent annealing has resulted in 180° domain refinement leading to the observed widening of domain wall spacing (figure 6.40), thus the average rms Barkhausen noise increased by up to 25% due to coating removal (as can be seen in figure 6.41). Changes in Barkhausen noise under applied stress are primarily attributable to changes in 180° domain walls, thus it is not unexpected to see an increase in rms Barkhausen noise. With a relatively large change in Barkhausen noise (25%) and a similar amount in power loss (25.2%) this indicates a strong correlation between power loss and Barkhausen noise.

After removing the coating, the grains were found to be larger than first indicated with the magnetic domain viewer, which showed that the magnetic domain viewer method was not the best method to observe the grain size. Therefore, a further 9 points were chosen to investigate the variation of Barkhausen noise inside individual grains of an uncoated grain-oriented 3%SiFe (figure 6.42).

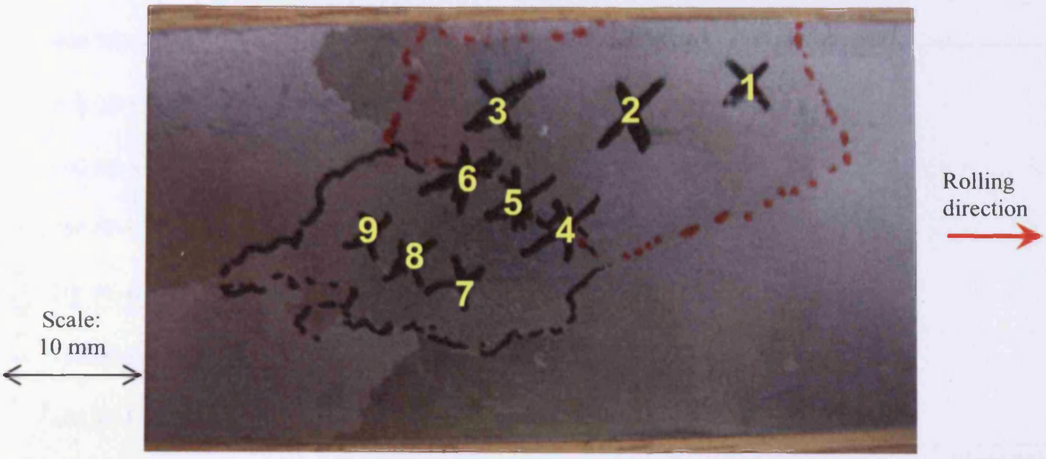

Figure 6.42. Photo of the uncoated grain-oriented 3%SiFe electrical steel sample. The numbers indicate the location where the ferrite sensor was placed for measurement of Barkhausen noise (1 is P1 in figures, etc)

Figure 6.43 shows points 1-3, the variation of rms Barkhausen noise with peak flux density in a single grain (grain 1) using the ferrite cored sensor. Figure 6.44 shows points 4-6, the variation of rms Barkhausen noise at the grain boundary. Figure 6.45 shows points 7-9, the variation of rms Barkhausen noise with peak flux density in a single grain (grain 2) adjacent to grain 1. Figure 6.46 shows all 1-9 points to show the variations of rms Barkhausen noise from grain-to-grain and grain-to-grain boundary.

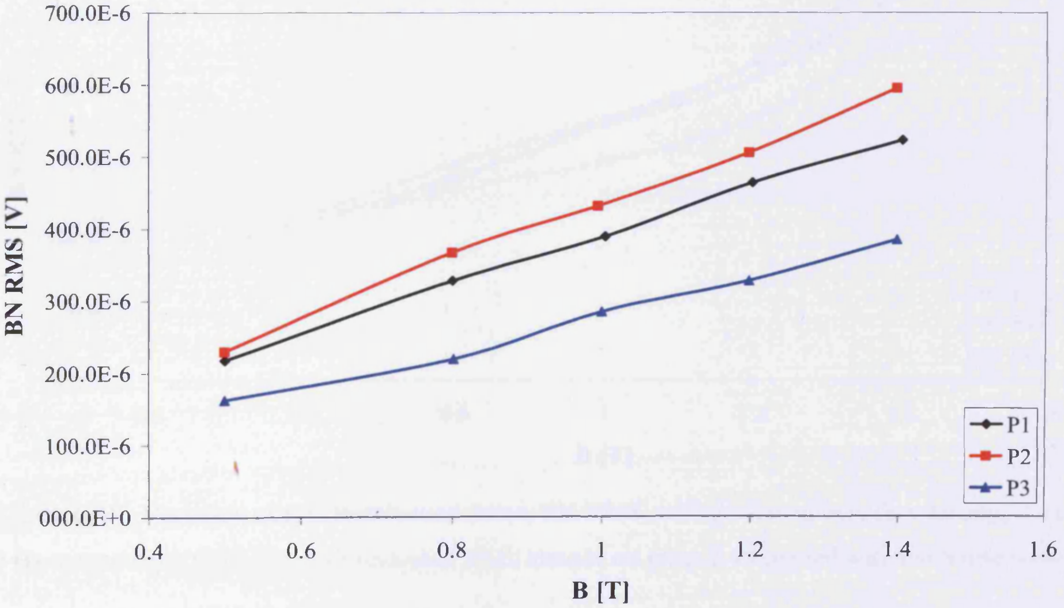

Figure 6.43. Variation of rms Barkhausen noise, BN RMS, with peak magnetic flux density, *B*, at 50 Hz magnetising frequency, for uncoated 3%Si sample on grain 1, measured with the ferrite sensor

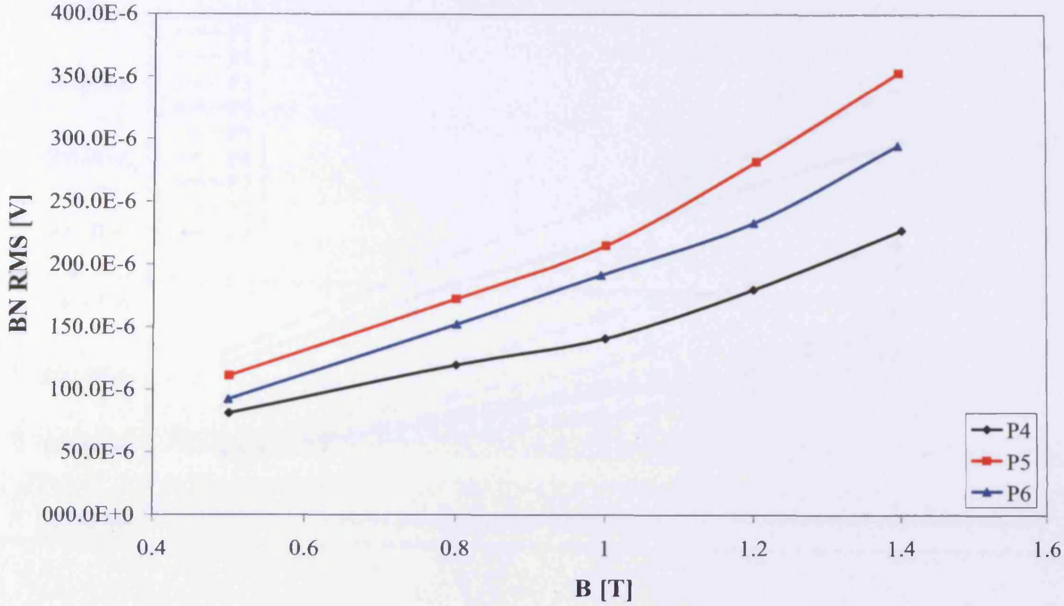

Figure 6.44. Variation of rms Barkhausen noise, BN RMS, with peak magnetic flux density, *B*, at 50 Hz magnetising frequency, for uncoated 3%Si sample on the grain boundary, measured with the ferrite sensor

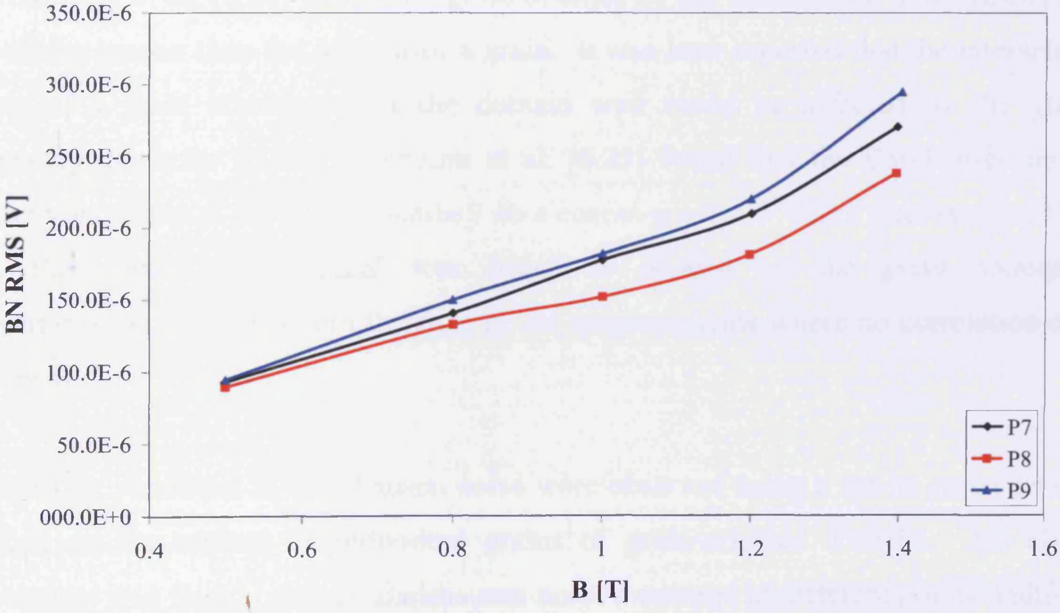

Figure 6.45. Variation of rms Barkhausen noise, BN RMS, with peak magnetic flux density, *B*, at 50 Hz magnetising frequency, for uncoated 3%Si sample on grain 2, measured with the ferrite sensor

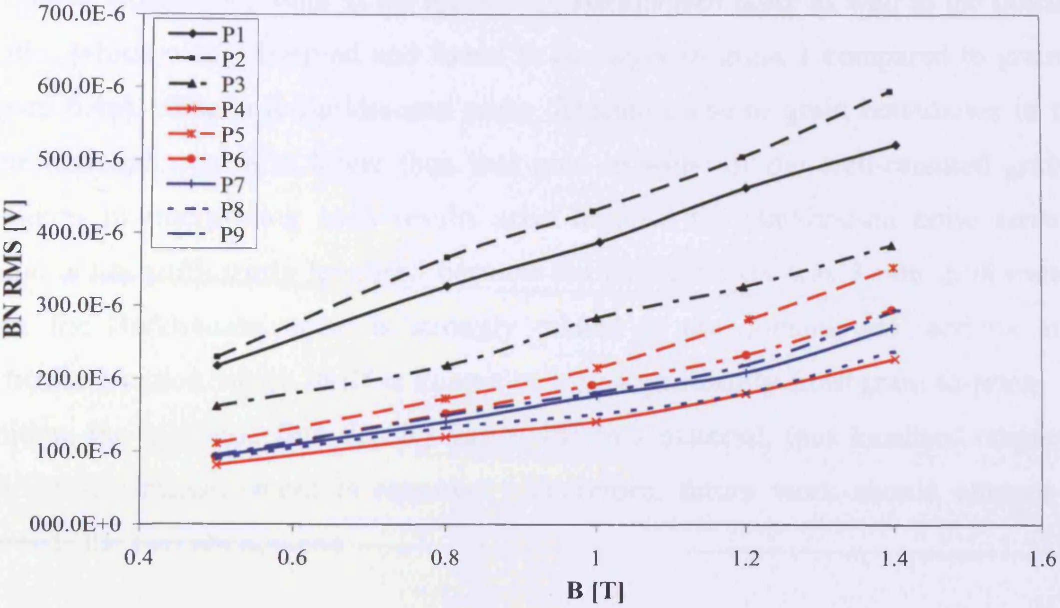

Figure 6.46. Variation of rms Barkhausen noise, BN RMS, with peak magnetic flux density, *B*, at 50 Hz magnetising frequency, for uncoated 3%Si sample on grain 1, grain 2 and the grain boundary, measured with the ferrite sensor

Due to grain boundaries composed entirely of lattice defects, it was reported by Kavecansky et al. [6.24] that at the grain boundaries the Barkhausen noise emissions would be greater than the interior of a grain. It was later reported that the interaction between a grain boundary and the domain wall could be affected by the grain boundary character [6.24]. Yamaura et al. [6.25] found that the Barkhausen noise activity increases at the grain boundary on a coarse-grained 3%SiFe steel sample, also the Barkhausen noise signal was found to depend on the grain boundary misorientation. This was not the case in our measurements where no correlation can be seen.

Interesting variations in Barkhausen noise were observed using a ferrite cored sensor placed on the surface of individual grains of grain-oriented 3%SiFe. No close agreement was found between Barkhausen noise measured at different points within a single grain at 50 Hz magnetisation, and within another grain of similar size and orientation. Barkhausen noise varied by more than 50% between grain 1 and grain 2. Grain 1 had a length along the rolling direction of ~30 mm with a width of ~15 mm, and a misorientation angle of ~-1°, whereas grain 2 had a length of ~20 mm with a width of ~12 mm, and a misorientation angle of ~+0.5°. These differences between the grains would contribute to the increase in Barkhausen noise as well as the domain widths, which were observed and found to be larger in grain 1 compared to grain 2 (figure 6.46). The rms Barkhausen noise detected close to grain boundaries in the same material was 40% lower than that seen in some of the well-oriented grains. Problems in interpreting such results arise because the Barkhausen noise sensing region is not sufficiently localised because the ferrite sensor was 3 mm in diameter. Also, the Barkhausen noise is strongly related to the domain wall activity at a particular location which itself is known to vary significantly from grain-to-grain. In addition, the magnetic flux density varies within a material, thus localised magnetic flux density measurement is required. Therefore, future work should attempt to correlate the two phenomena.

The results presented in this section indicate Barkhausen noise does not increase near grain boundaries as expected. Due to the sensor size more localised measurements were not able to be taken. However, it was found that power loss and Barkhausen noise have a close relationship, as when coating was removed the power loss and Barkhausen noise increased by a similar amount.

6.8. Surface scanning of Barkhausen noise on grain-oriented electrical steel

A Barkhausen noise scanning system was developed to observe evidence of Barkhausen variation across the surface in a more systematic manner (the measurement system is described in chapter 5). A 0.27 mm thick, grain-oriented 3%SiFe electrical steel sample from the same stack as the above sample was chosen with large grains of ~13 mm diameter. The reason for choosing a sample with large grains is that the sensor size was large i.e. 3 mm diameter.

Measurements were made using the ferrite sensor of length 12.9 mm, over an area of 40 mm × 20 mm, over a coated 0.27 mm thick grain-oriented 3%SiFe electrical steel sample. A step size of 2 mm was chosen due to the size of the sensor however, one set of measurements was also conducted at a 1 mm step size to investigate if there is any change in results due to step size.

Figures 6.47 to 6.50 show the Barkhausen noise measured over the specified area at 50 Hz magnetising frequency, at 1.0 T magnetic flux density, with a step size of 2 mm. The rms, total sum of amplitudes, kurtosis and power spectrum analysis of Barkhausen noise respectively are all plotted.

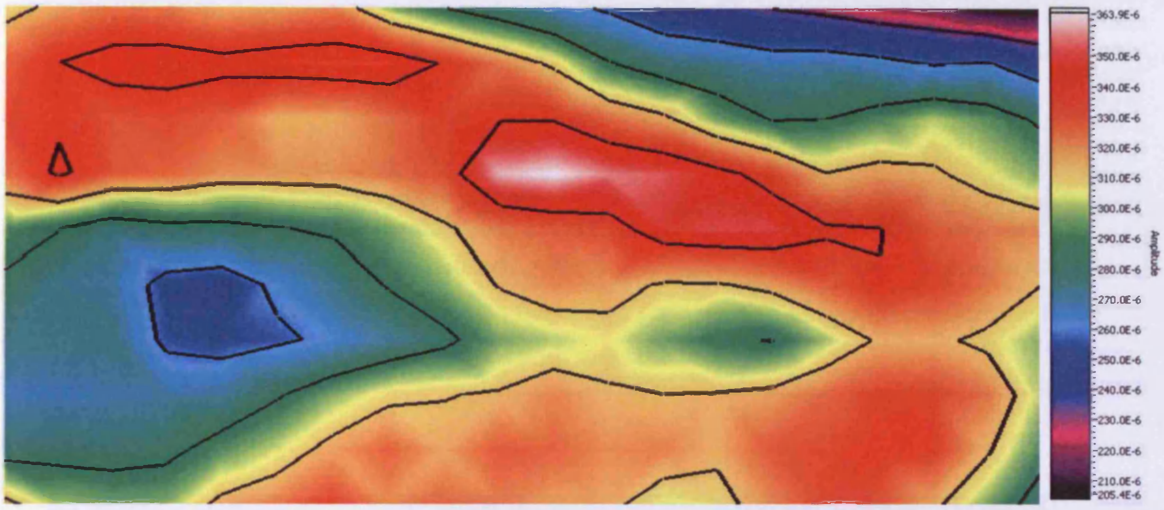

Figure 6.47. Surface scan of rms Barkhausen noise, area scanned 40 mm × 20 mm, at 1.0 T magnetic flux density, at 50 Hz magnetising frequency, for coated 3%Si sample, measured with the ferrite sensor, with step scan of 2 mm

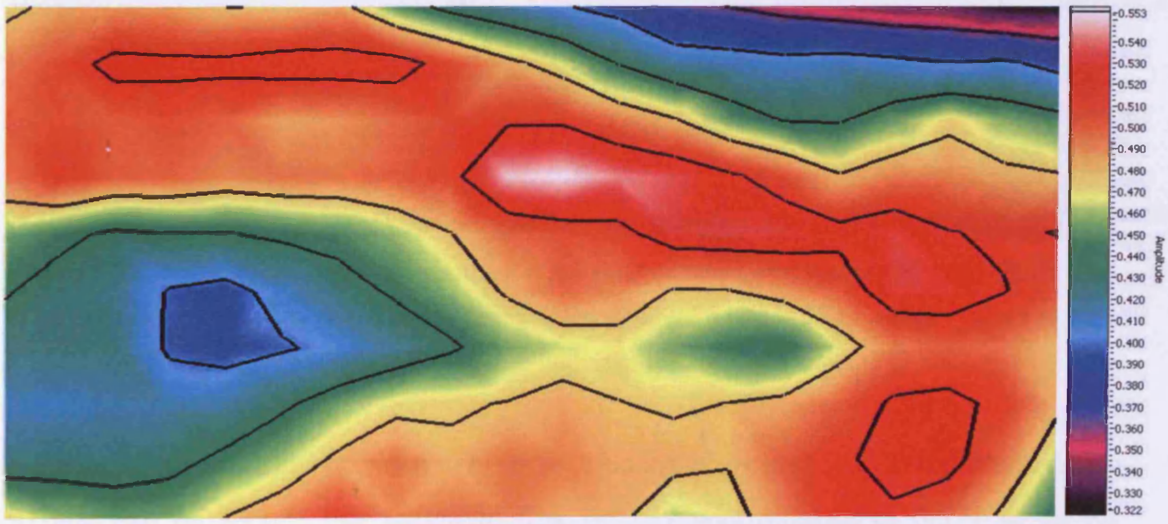

Figure 6.48. Surface scan of total sum of amplitudes of Barkhausen noise, area scanned 40 mm × 20 mm, at 1.0 T magnetic flux density, at 50 Hz magnetising frequency, for coated 3%Si sample, measured with the ferrite sensor, with step scan of 2 mm

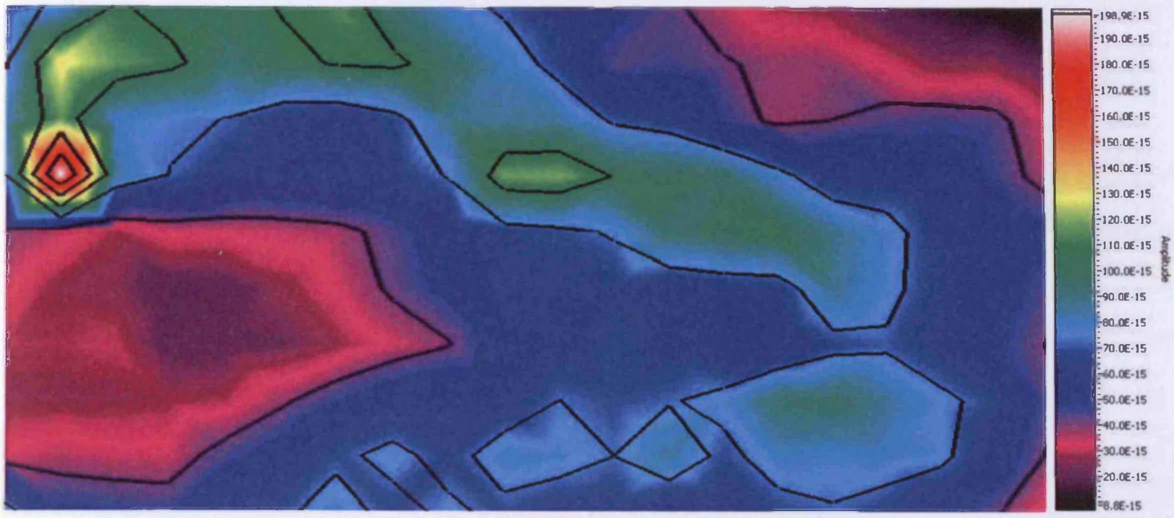

Figure 6.49. Surface scan of kurtosis Barkhausen noise, area scanned 40 mm × 20 mm, at 1.0 T magnetic flux density, at 50 Hz magnetising frequency, for coated 3%Si sample, measured with the ferrite sensor, with step scan of 2 mm

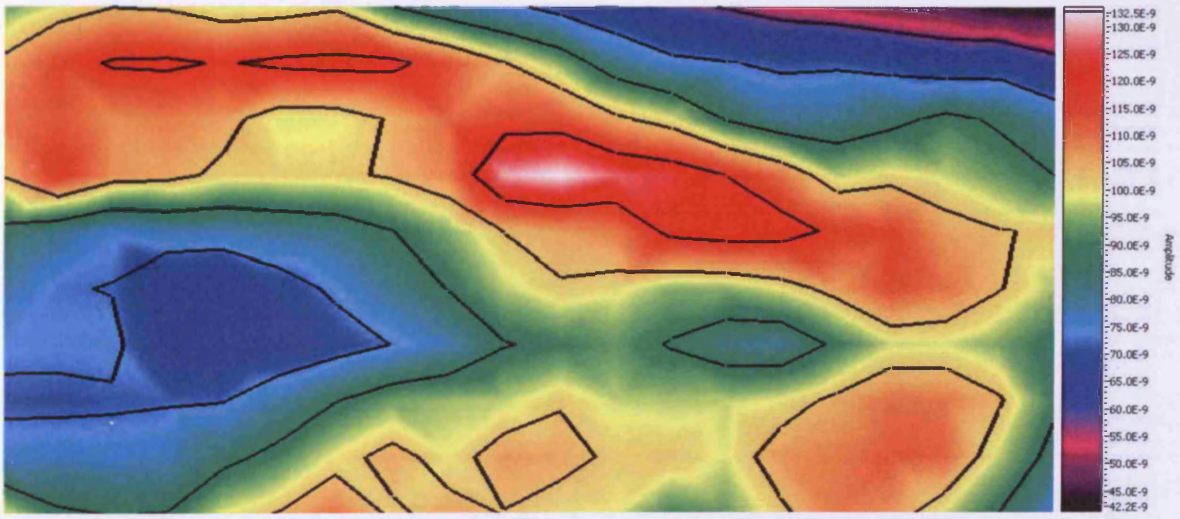

Figure 6.50. Surface scan of power spectrum of Barkhausen noise, area scanned 40 mm × 20 mm, at 1.0 T magnetic flux density, at 50 Hz magnetising frequency, for coated 3%Si sample, measured with the ferrite sensor, with step scan of 2 mm

A definite pattern can be seen where regions of high and low Barkhausen noise activity can be seen. The magnetic flux density was reduced to 0.5 T at 50 Hz magnetising frequency and the scans were repeated. Similar regions of high and low Barkhausen noise activity can be seen in figures 6.51 to 6.54.

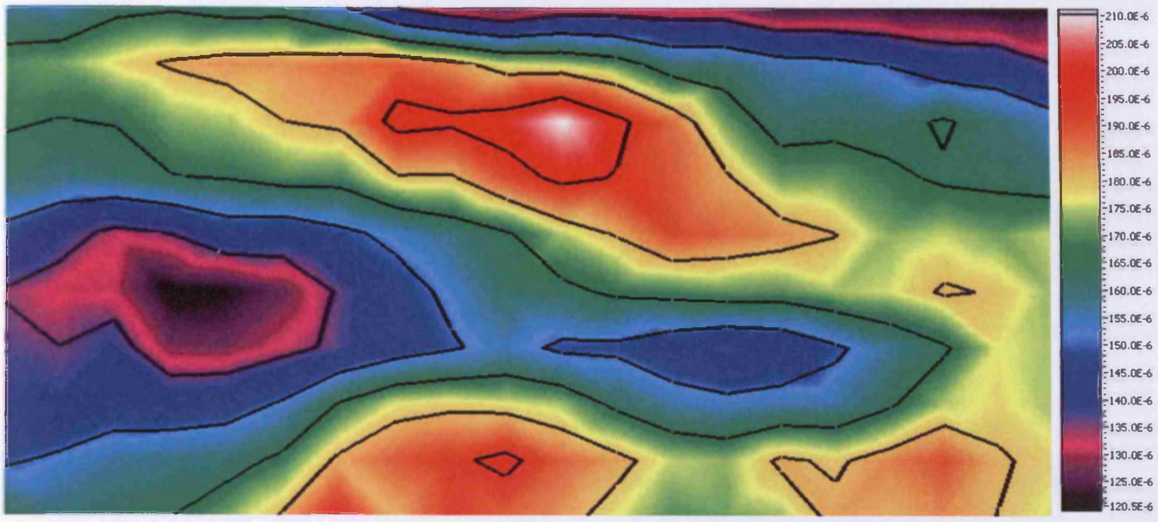

Figure 6.51. Surface scan of rms Barkhausen noise, area scanned 40 mm × 20 mm, at 0.5 T magnetic flux density, at 50 Hz magnetising frequency, for coated 3%Si sample, measured with the ferrite sensor, with step scan of 2 mm

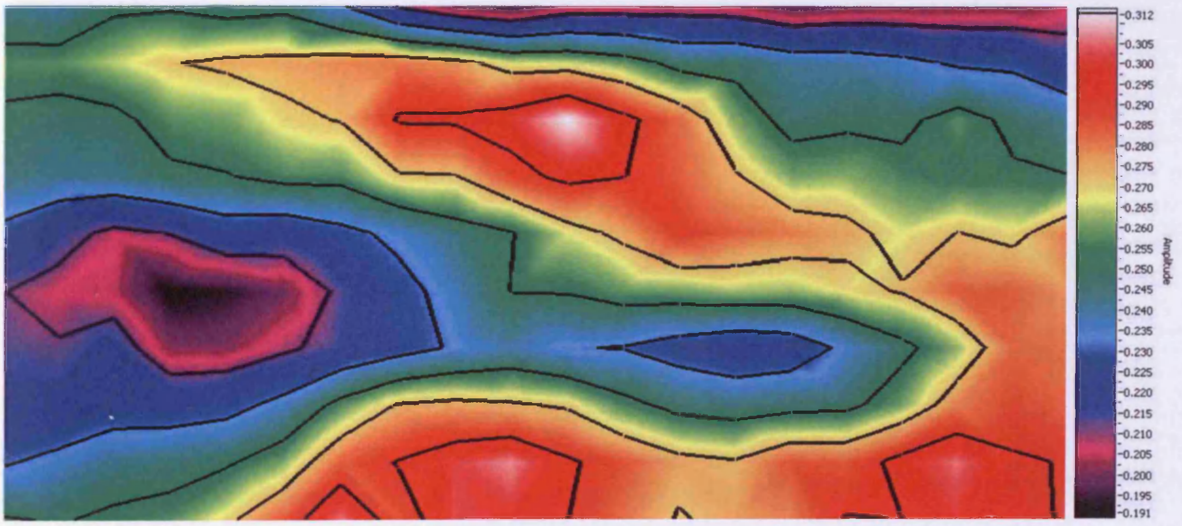

Figure 6.52. Surface scan of total sum of amplitudes of Barkhausen noise, area scanned 40 mm × 20 mm, at 0.5 T magnetic flux density, at 50 Hz magnetising frequency, for coated 3%Si sample, measured with the ferrite sensor, with step scan of 2 mm

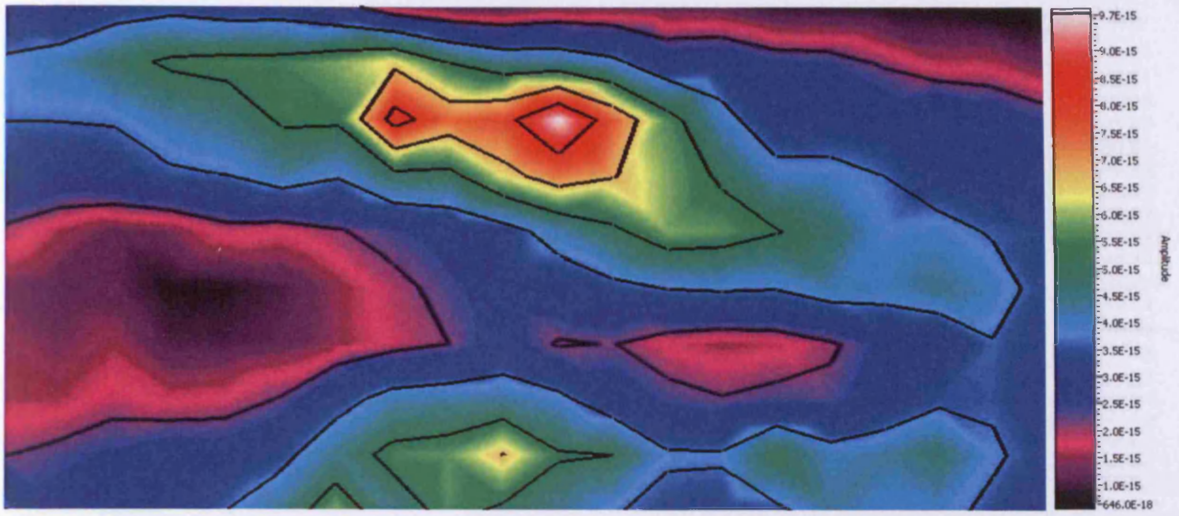

Figure 6.53. Surface scan of kurtosis Barkhausen noise, area scanned 40 mm × 20 mm, at 0.5 T magnetic flux density, at 50 Hz magnetising frequency, for coated 3%Si sample, measured with the ferrite sensor, with step scan of 2 mm

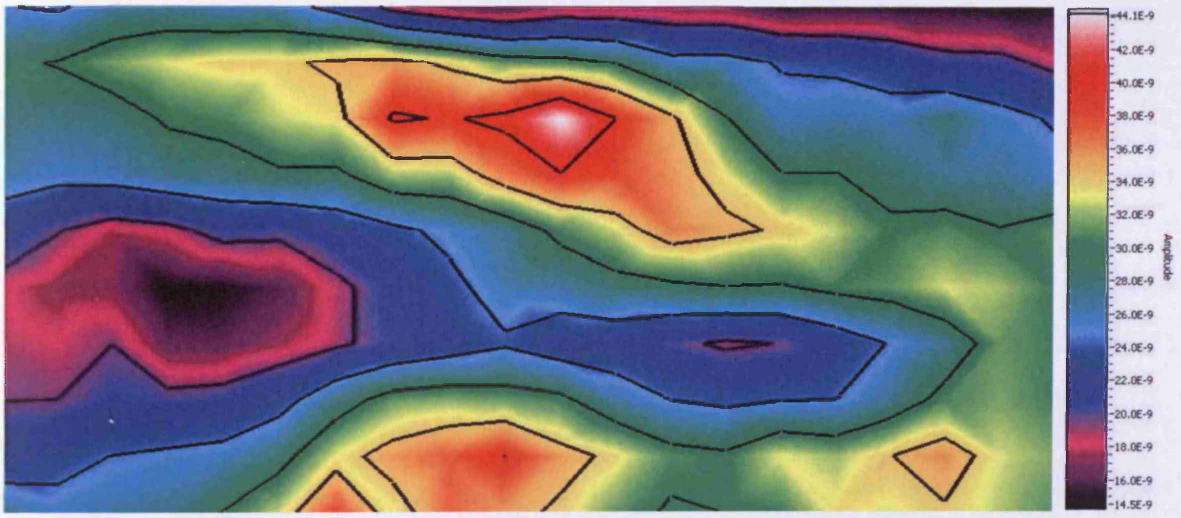

Figure 6.54. Surface scan of power spectrum of Barkhausen noise, area scanned 40 mm × 20 mm, at 0.5 T magnetic flux density, at 50 Hz magnetising frequency, for coated 3%Si sample, measured with the ferrite sensor, with step scan of 2 mm

When the magnetising frequency is reduced, it was expected that the rms Barkhausen noise would reduce but the same regions would be noticeable. Therefore, the magnetising frequency was reduced to 25 Hz at 1.0 T magnetic flux density (the results can be seen on figures 6.55 to 6.58).

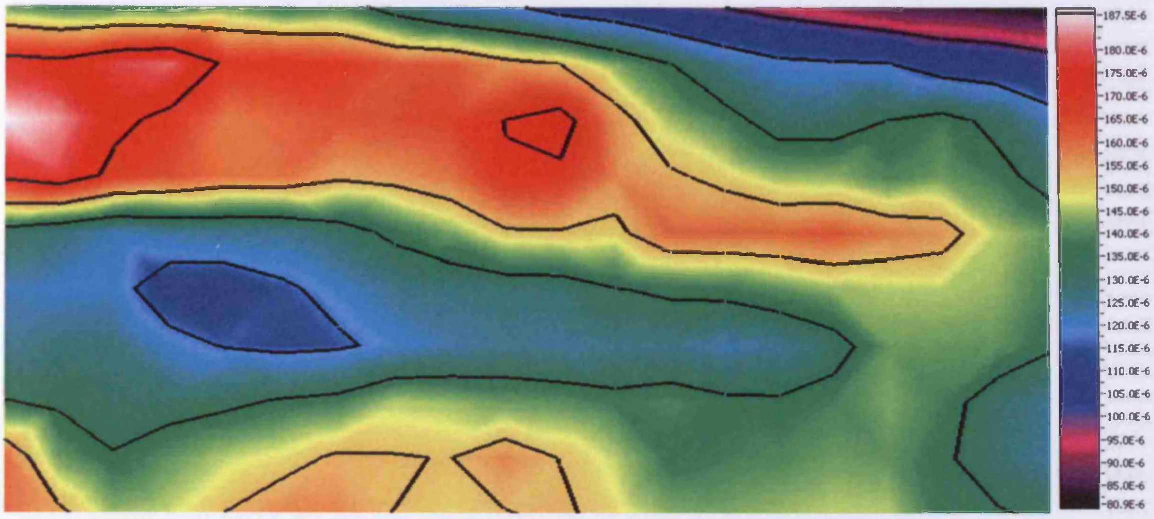

Figure 6.55. Surface scan of rms Barkhausen noise, area scanned 40 mm × 20 mm, at 1.0 T magnetic flux density, at 25 Hz magnetising frequency, for coated 3%Si sample, measured with the ferrite sensor, with step scan of 2 mm

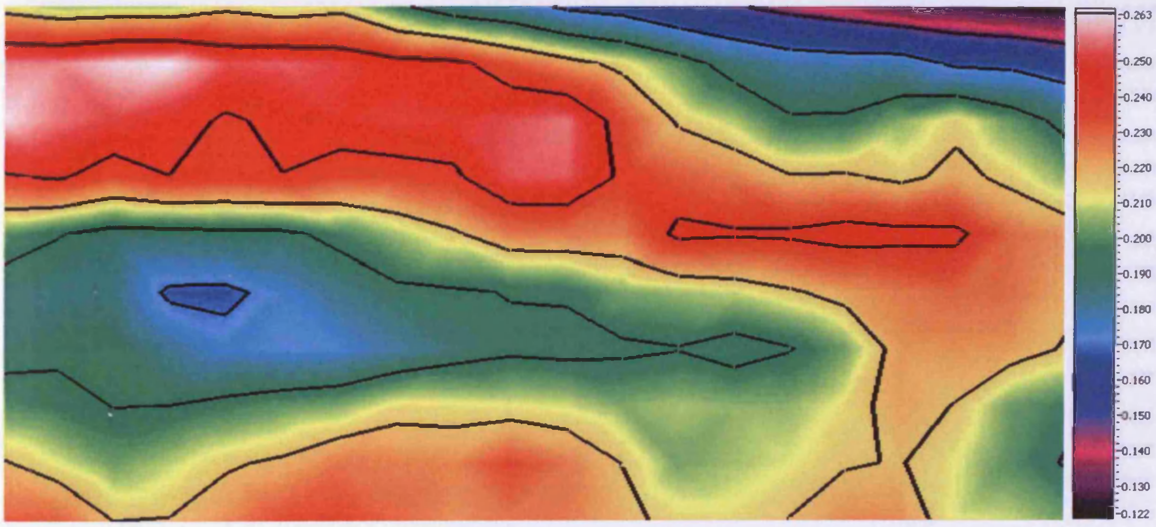

Figure 6.56. Surface scan of total sum of amplitudes of Barkhausen noise, area scanned 40 mm × 20 mm, at 1.0 T magnetic flux density, at 25 Hz magnetising frequency, for coated 3%Si sample, measured with the ferrite sensor, with step scan of 2 mm

Figure 6.57. Surface scan of kurtosis Barkhausen noise, area scanned 40 mm × 20 mm, at 1.0 T magnetic flux density, at 25 Hz magnetising frequency, for coated 3%Si sample, measured with the ferrite sensor, with step scan of 2 mm

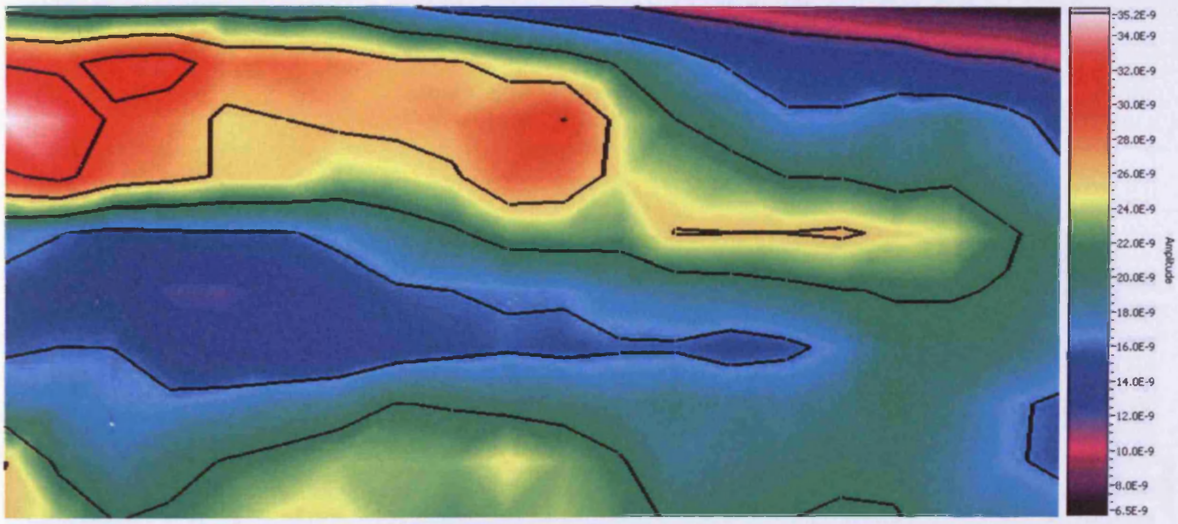

Figure 6.58. Surface scan of power spectrum of Barkhausen noise, area scanned 40 mm × 20 mm, at 1.0 T magnetic flux density, at 25 Hz magnetising frequency, for coated 3%Si sample, measured with the ferrite sensor, with step scan of 2 mm

The same regions can be observed, but the regions are less intense as expected, which mean the Barkhausen noise activity over the whole area has reduced, due to magnetising frequency. However, the interesting result here is that the kurtosis analysis does not show the distinct pattern as before but it shows a uniform distribution of the area measured.

The magnetic flux density was reduced to 0.5 T at 25 Hz magnetising frequency (figures 6.59 to 6.62), and here again a distinct pattern can be seen in all analysis methods other than the kurtosis analysis at 25 Hz at 1.0 T.

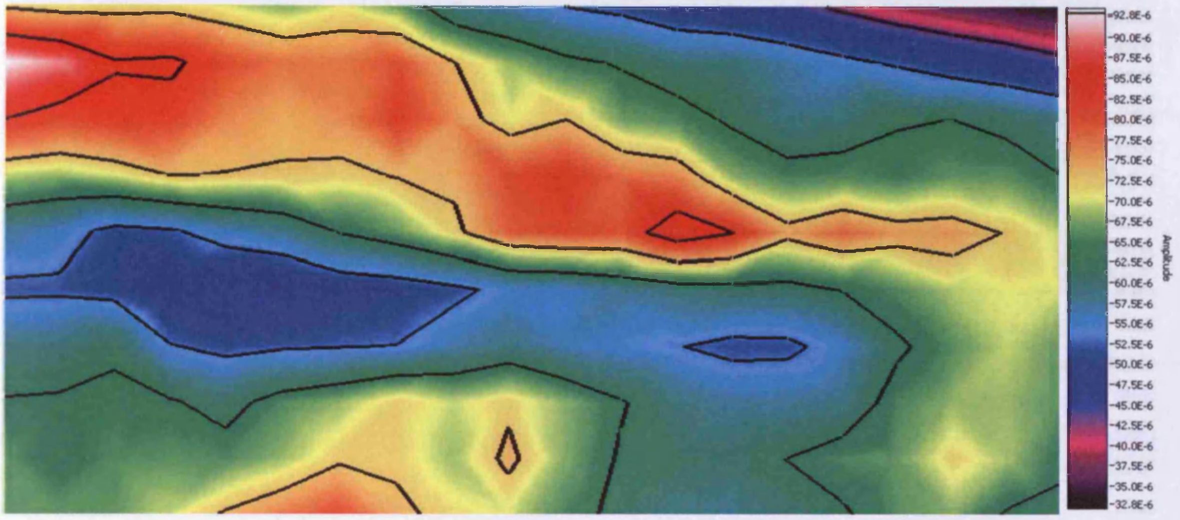

Figure 6.59. Surface scan of rms Barkhausen noise, area scanned 40 mm × 20 mm, at 0.5 T magnetic flux density, at 25 Hz magnetising frequency, for coated 3%Si sample, measured with the ferrite sensor, with step scan of 2 mm

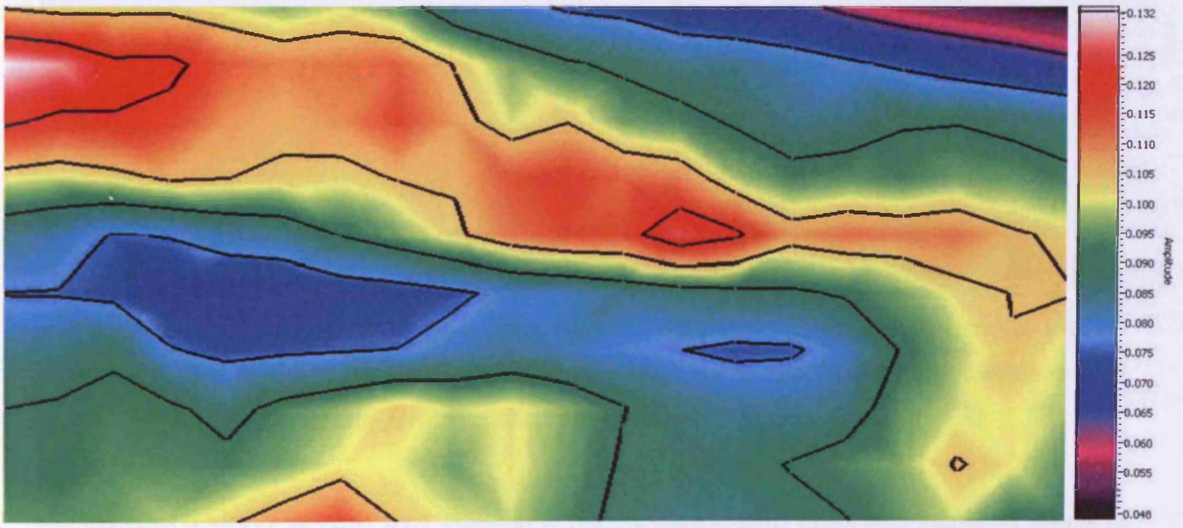

Figure 6.60. Surface scan of total sum of amplitudes of Barkhausen noise, area scanned 40 mm × 20 mm, at 0.5 T magnetic flux density, at 25 Hz magnetising frequency, for coated 3%Si sample, measured with the ferrite sensor, with step scan of 2 mm

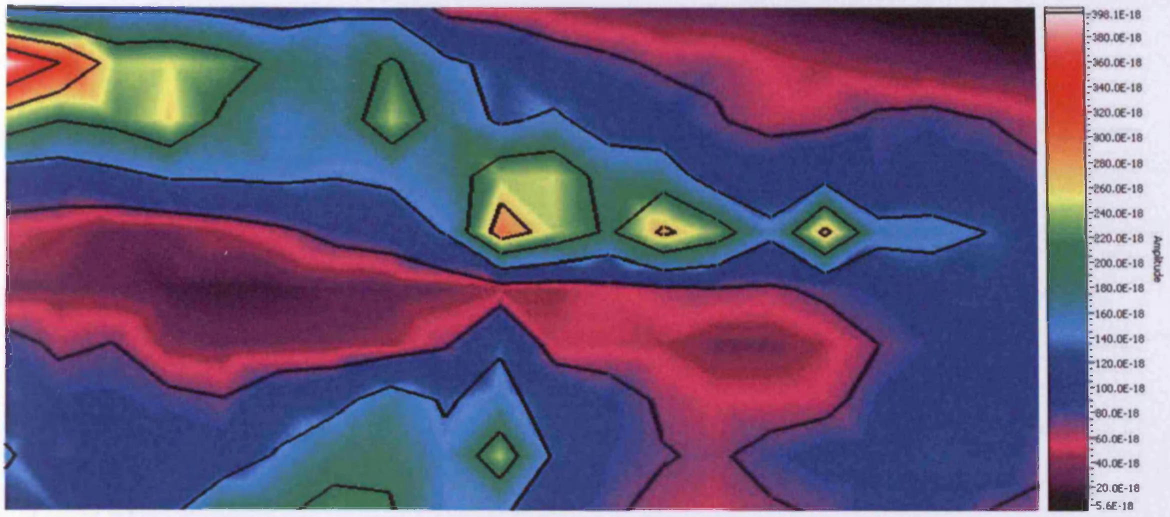

Figure 6.61. Surface scan of kurtosis Barkhausen noise, area scanned 40 mm × 20 mm, at 0.5 T magnetic flux density, at 25 Hz magnetising frequency, for coated 3%Si sample, measured with the ferrite sensor, with step scan of 2 mm

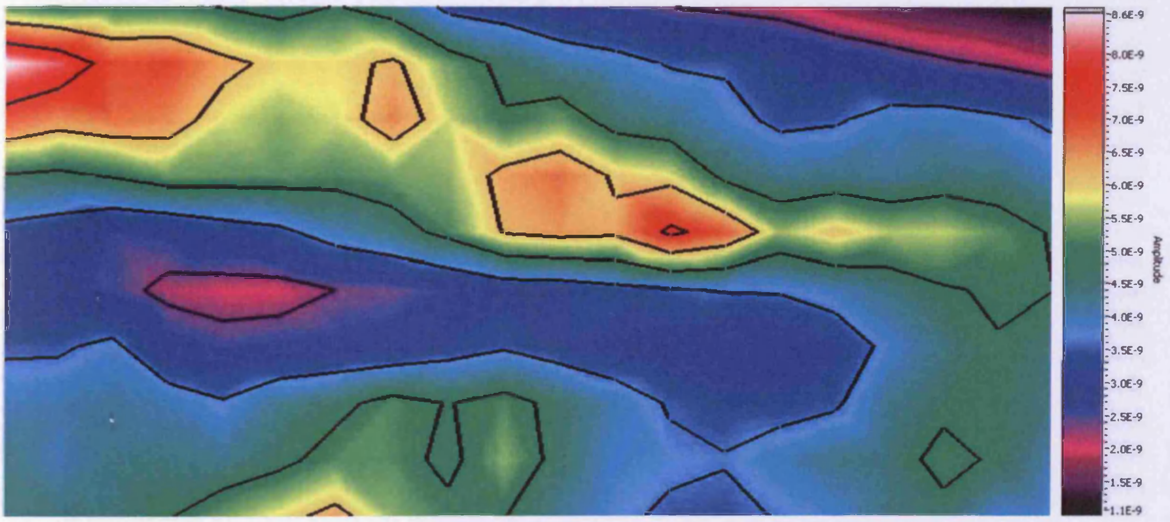

Figure 6.62. Surface scan of power spectrum of Barkhausen noise, area scanned 40 mm × 20 mm, at 0.5 T magnetic flux density, at 25 Hz magnetising frequency, for coated 3%Si sample, measured with the ferrite sensor, with step scan of 2 mm

The step size was decreased to 1 mm, and the measurement area was scanned again at 1.0 T magnetic flux density, at 50 Hz magnetising frequency (figures 6.63 to 6.66).

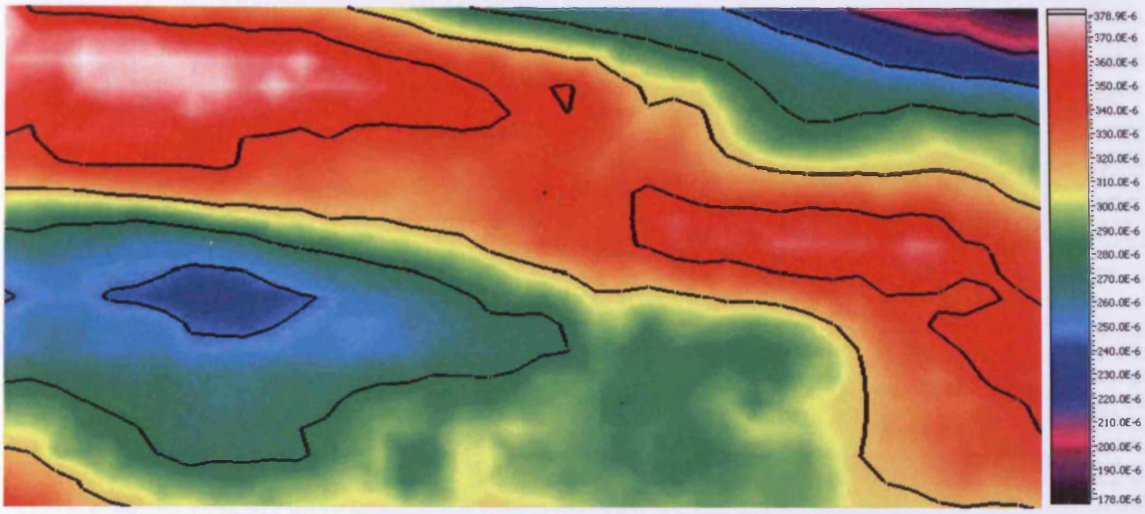

Figure 6.63. Surface scan of rms Barkhausen noise, area scanned 40 mm × 20 mm, at 1.0 T magnetic flux density, at 50 Hz magnetising frequency, for coated 3%Si sample, measured with the ferrite sensor, with step scan of 1 mm

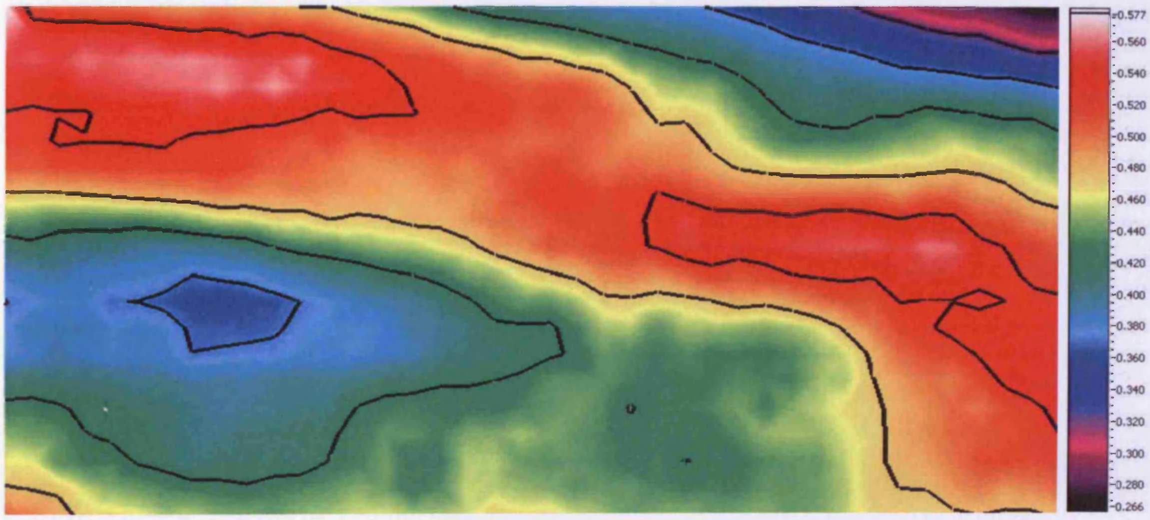

Figure 6.64. Surface scan of total sum of amplitudes of Barkhausen noise, area scanned 40 mm × 20 mm, at 1.0 T magnetic flux density, at 50 Hz magnetising frequency, for coated 3%Si sample, measured with the ferrite sensor, with step scan of 1 mm

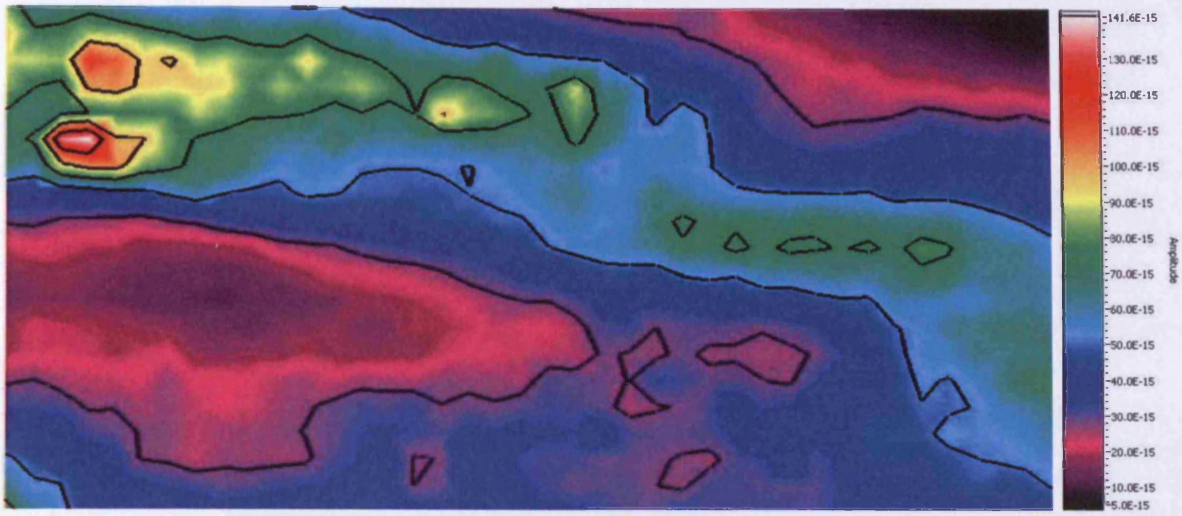

Figure 6.65. Surface scan of kurtosis Barkhausen noise, area scanned 40 mm × 20 mm, at 1.0 T magnetic flux density, at 50 Hz magnetising frequency, for coated 3%Si sample, measured with the ferrite sensor, with step scan of 1 mm

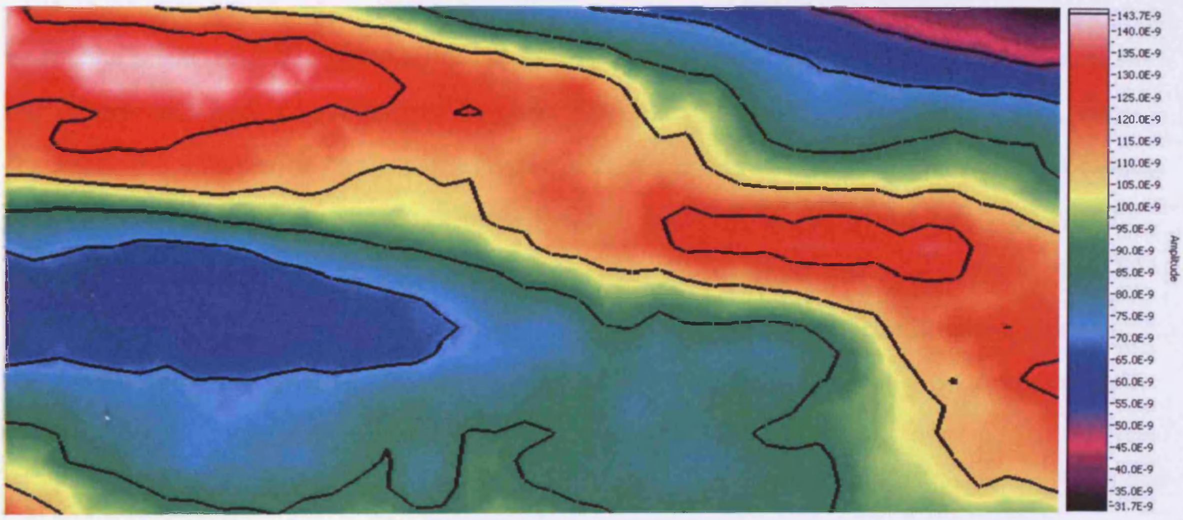

Figure 6.66. Surface scan of power spectrum of Barkhausen noise, area scanned 40 mm × 20 mm, at 1.0 T magnetic flux density, at 50 Hz magnetising frequency, for coated 3%Si sample, measured with the ferrite sensor, with step scan of 1 mm

With a lowered step size there are some common features with the 2 mm step size, there are some small differences between the two different step sizes. This would be due to the sample positioning errors and measurement uncertainty. However, the main areas of high and low Barkhausen noise activity are visible in both step sizes, therefore it is was concluded that a 2 mm step size is valid step size for Barkhausen noise measurement, allowing measurements can be conducted faster.

Once measurements were conducted, the coating of the grain-oriented sample was removed, to reveal the actual grain structure under the area scanned. Figure 6.67 shows the area of the sample scanned.

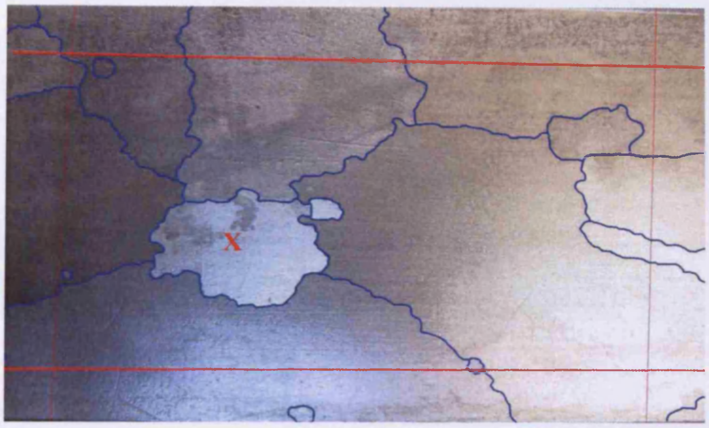

Figure 6.67. Picture of the area scanned on the grain-oriented 3%SiFe electrical steel sample (red lines indicate the area scanned, and the blue lines outline the grains)

From the photo and Barkhausen noise scanning images, it can be seen that the grain in the centre (marked X) produces the least Barkhausen noise activity. However, from the scanning images, it cannot be clearly seen where grain boundaries lie, but a clear pattern can be seen where Barkhausen noise activity is high and low. It can be concluded, that with the Barkhausen noise scanning method, the grain size and grain structure cannot be detected. However, regions of high and low Barkhausen noise can be detected which in turn shows regions of high and low loss due to domain wall pinning.

Further analysis was carried out on figure 6.63, and lines across the image were examined. Figure 6.68, shows figure 6.63 with paths A-A', B-B', C-C' and D-D'. These paths intercept the grains where regions of high and low Barkhausen noise activity occur. Figure 6.69, shows the variation of Barkhausen noise along paths A-A' and B-B'. Figure 6.70 shows the variation of Barkhausen noise along paths C-C' and D-D'.

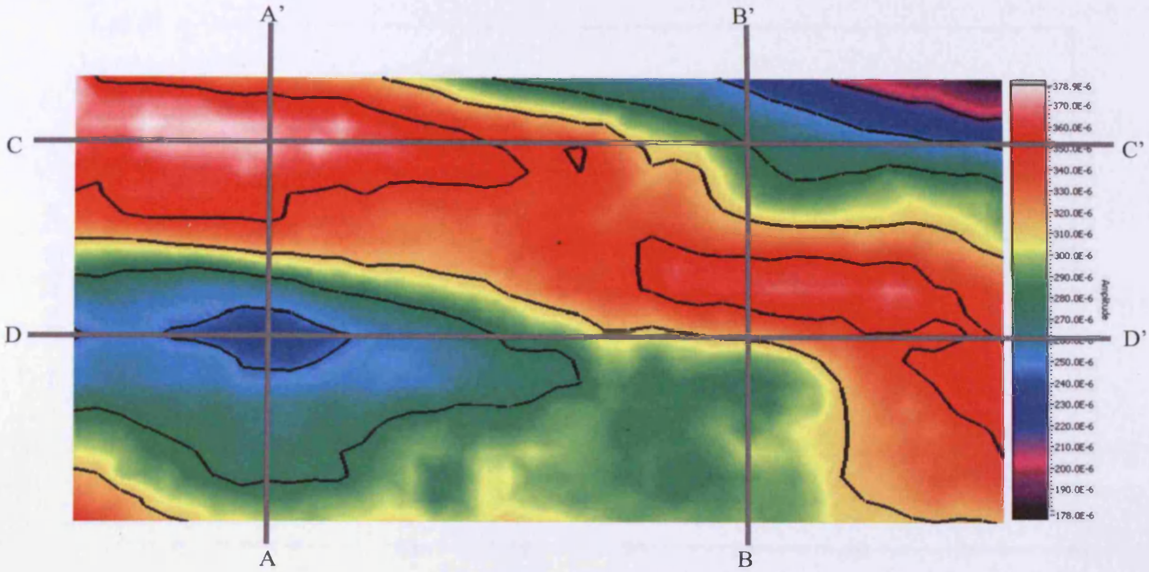

Figure 6.68. Surface scan of rms Barkhausen noise, area scanned 40 mm × 20 mm, at 1.0 T magnetic flux density, at 50 Hz magnetising frequency, for coated 3%Si sample, measured with the ferrite sensor, with step scan of 1 mm, indicating paths A-A', B-B', C-C' and D-D'

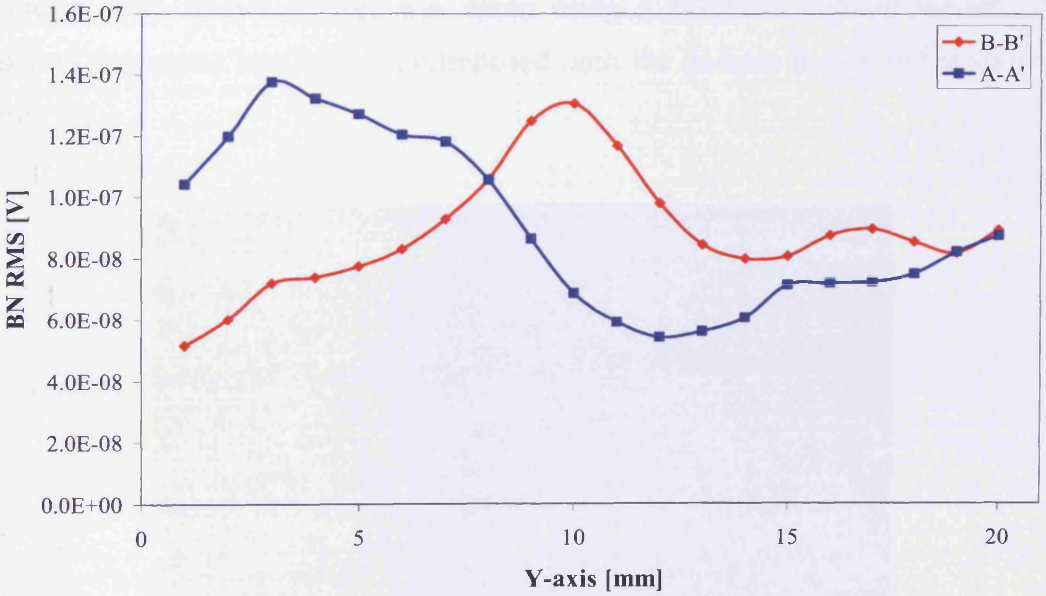

Figure 6.69. Variation of rms Barkhausen noise over paths A-A' and B-B' from figure 6.68

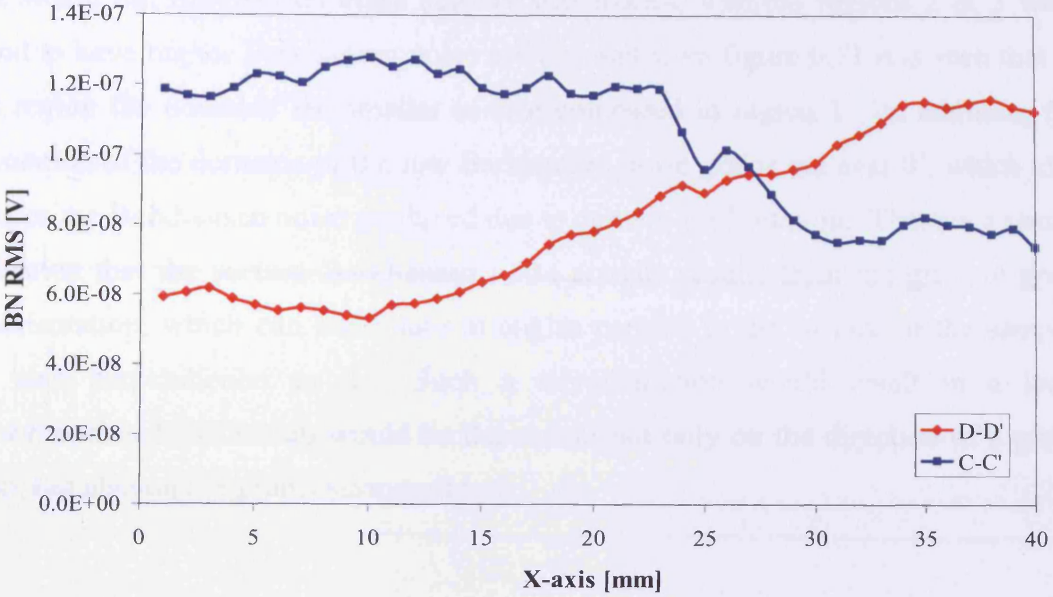

Figure 6.70. Variation of rms Barkhausen noise over paths C-C' and D-D' from figure 6.68

Figures 6.69 and 6.70 show that the Barkhausen noise at some regions increases by up to 60%, from region to region. Further more, before removing the coating off the sample, a static domain image was taken using a magnetic domain viewer. The outline of the grains has been superimposed onto the domain image and is shown in figure 6.71.

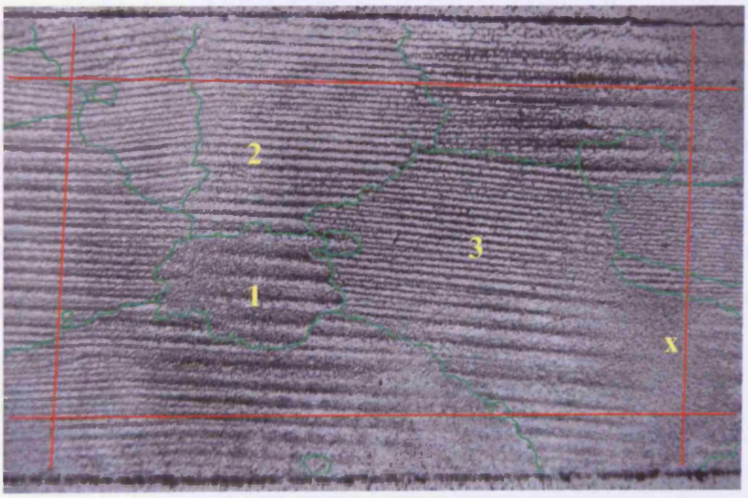

Figure 6.71. Magnetic domain viewer image of the area scanned with an outline of the grains superimposed on the image

With the above image, it could be concluded that Barkhausen noise activity increases with decrease in domain size. Region marked 1, has larger grain size and this is the area where the Barkhausen noise activity was lowest, whereas regions 2 & 3 were found to have higher Barkhausen noise activity and from figure 6.71 it is seen that in this region the domains are smaller in size compared to region 1. In addition, the orientation of the domains of the low Barkhausen noise grains are near 0^o, which also reduces the Barkhausen noise produced due to domain wall rotation. There is a strong indication that the surface Barkhausen noise activity results from the grain-to-grain misorientation, which can take place at angles parallel to the surface of the sample, but also perpendicular to it. Such a misorientation would result in a local demagnetising field, which would be dependent not only on the direction of a given grain, but also on the grains surrounding it.

The same sample that was used for scanning Barkhausen noise (grain-oriented electrical steel) was sent to Warsaw University of Technology, to scan the same area for the tangential component of surface field, H_S. This is because small misoriented grains are known to contribute to elevated local losses and a tangential component of surface field [6.26]. Warsaw University of Technology used the Magnetivision system [6.26], which comprised of a permalloy magnetoresistive sensor. The surface of the sample was scanned with the sensor with steps of 0.25 mm. The H_S was measured at various values of peak flux density, B_{peak}, which was measured by means of a search coil wrapped around the sample.

Figure 6.72 shows the distribution of peak values of H_S acquired with the Magnetivision system at 50 Hz and three levels of sinusoidal B_{peak} = 0.5 T, 1.0 T and 1.5 T. The measured area is 140 mm × 30 mm and the values for each flux density shown in figure 6,72, H_S values are normalised to an arbitrary scale. The white rectangle shows the area at which the Barkhausen noise was scanned.

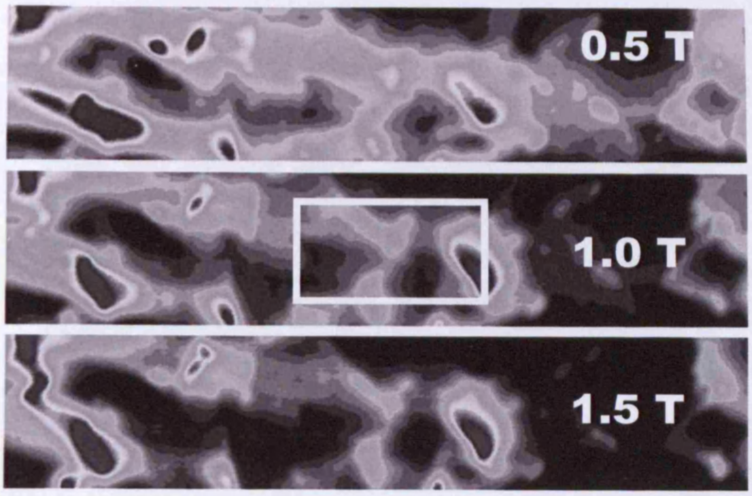

Figure 6.72. Typical H_S patterns at flux densities of 0.5 T, 1.0 T and 1.5 T, at 50 Hz magnetising frequency, on a grain-oriented electrical steel sample (arbitrary scale was used for each pattern)

It can be seen from figure 6.72, the distribution of H_S changes with flux density, as expected. It can also be seen that the overall topography remains similar at any flux density. However, this surface field activity is not directly connected to the grain structure, which is seen in figure 6.67 and 6.71. The comparison of results scanned for rms Barkhausen noise and H_S from the two systems is shown in figure 6.73.

Paths A-A' and D-D' intercept at a grain over which there is very little activity for both Barkhausen noise and H_S. On the right end of the D-D' path there is elevated activity (light grey or white) visible again in both cases.

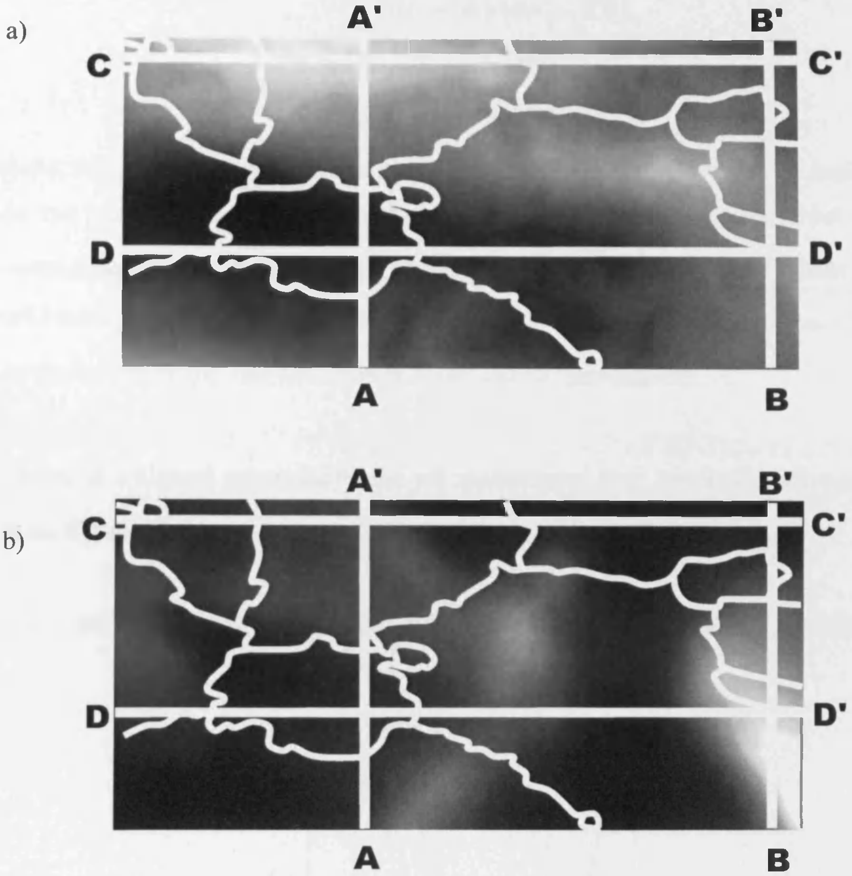

Figure 6.73. Distribution of a) rms Barkhausen noise and b) H_S measured at 1.5 T, 50 Hz, on a grain-oriented electrical steel sample

The central area 40 mm × 20 mm (shown with the white rectangle in figure 6.72) of the same sample was scanned with the Magnetivision system. The resultant Barkhausen noise (rms value of the noise over one cycle) distribution measured at 1.0 T and 50 Hz is shown in figure 6.73a. Some correlations can see seen in the scanned Barkhausen noise (figure 6.73a) and scanned surface field (figure 6.73b). These similarities become more evident when a correlation factor is calculated for each path in the image (figure 6.73). The data was separated into vertical and horizontal paths (with resolution of 1 mm, this is due to the Barkhausen noise step size being 1 mm) and the Pearson correlation coefficient (*PCC*) was calculated for each set of the data, by using the following expression:

$$PCC = \frac{\sum_i \left(Hs_i - \overline{Hs}\right)\cdot\left(BN_i - \overline{BN}\right)}{(n-1)\cdot s_{H_s}\cdot s_{BN}} \tag{6.2}$$

where: Hs_i and BN_i - are consecutive values along a given vertical or horizontal paths of surface field and rms Barkhausen noise, respectively; i - is consecutive points (from 0 to 19 mm for vertical or from 0 to 39 mm for horizontal paths); $\overline{Hs}$ and $\overline{BN}$ - the average values of surface field and rms Barkhausen noise, respectively; n - is total number of points; s_{H_s} and s_{BN} - are the standard deviations of surface field and rms Barkhausen noise values, respectively.

The PCC was calculated separately for all horizontal and vertical paths and the results are shown in figure 6.74.

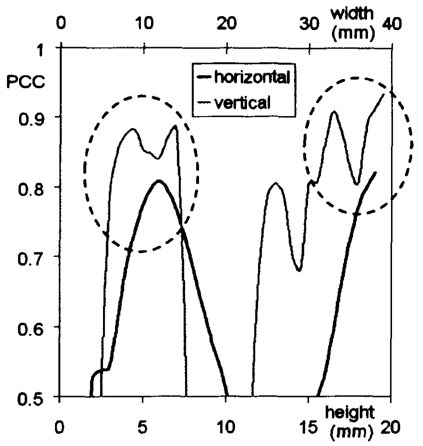

Figure 6.74. Correlation between H_S and rms Barkhausen noise values (dashed areas show regions with high correlation)

The statistical analysis (figure 6.74) shows that there are two areas of very strong correlation for both horizontal and vertical data. Path A-A' is positioned at 14 mm horizontally and path D-D' at 7 mm vertically. The correlation coefficient for each of these paths is around 0.8 (see figure 6.75).

A similar situation occurs for the crossing of paths B-B' (38 mm horizontally) and D-D' (18 mm vertically). Again, they both have correlation coefficient 0.8 and above, and from figure 6.75 it is evident that they have very similar characteristics.

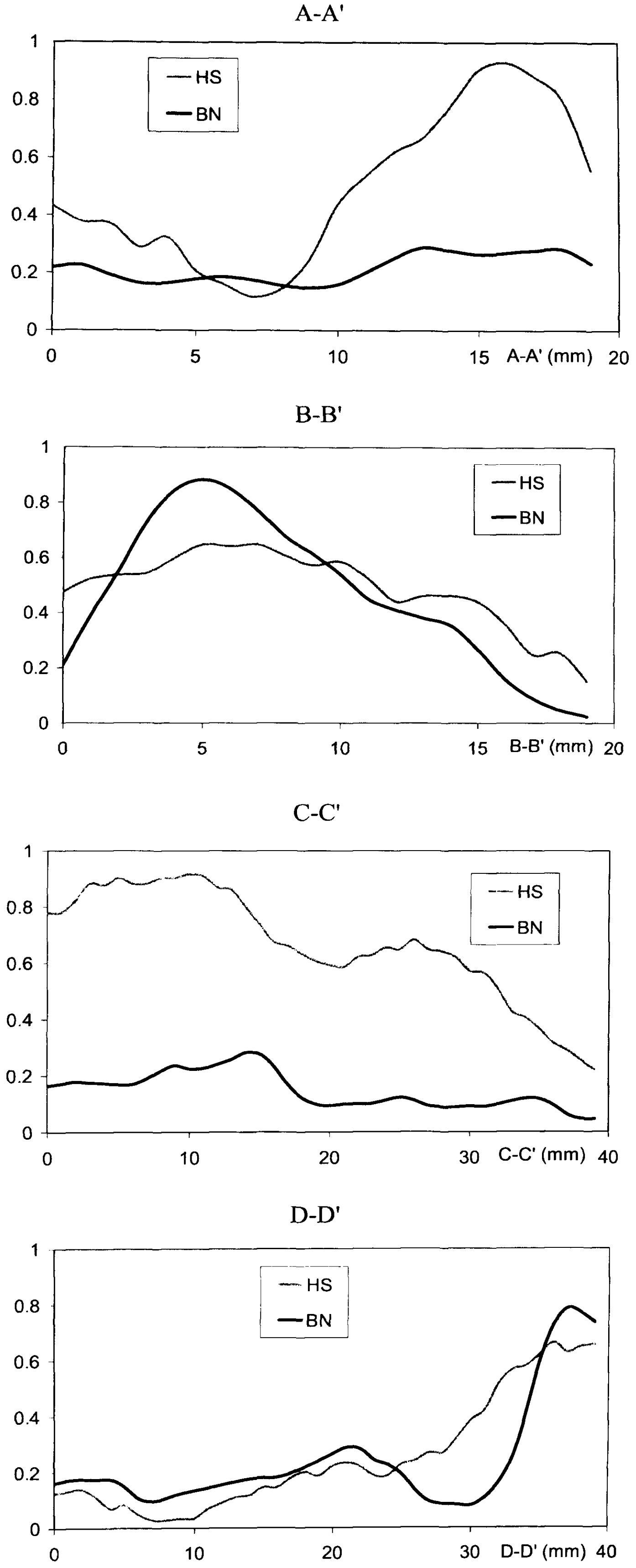

Figure 6.75. Distribution of H_S and rms Barkhausen noise, BN, along paths A-A', B-B', C-C' and D-D' (data normalised to arbitrary scale from 0 to 1)

There is further evidence of coincidence between the H_S and rms Barkhausen noise activity. For instance, values along a vertical path positioned at 34 mm (i.e. parallel to D-D') are of striking similarity, as shown in figure 6.76. These characteristics, together with the area of elevated activity close to the crossing of paths B-B' and D-D' seem to be related with a grain visible in figure 6.71 (marked x) and figure 6.73.

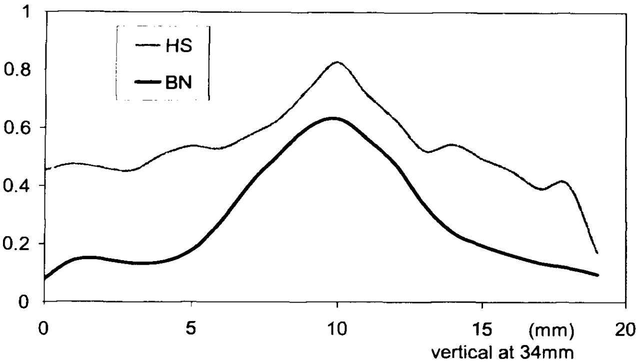

Figure 6.76. Distribution of H_S and rms Barkhausen noise over a vertical path positioned at 34 mm

There is a correlation between H_S and rms Barkhausen noise along another horizontal path parallel to and 2 mm below D-D', that indicates further correlation between the H_S and rms Barkhausen noise, as shown in figure 6.77.

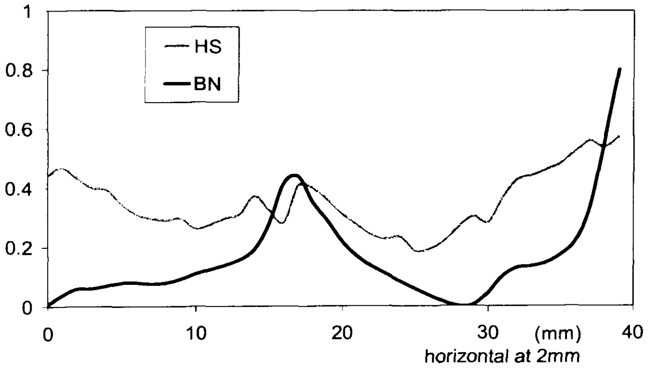

Figure 6.77. Distribution of H_S and rms Barkhausen noise over a horizontal path positioned at 2 mm

The intensity of H_S and rms Barkhausen noise activities is clearly linked over around 50% of the tested surface area (see figure 6.74). However, this does not seem to be related to the position of the grain boundaries. It is therefore possible that the presented surface activity results from the grain-to-grain misorientation, which can take place at angles parallel to the surface of the sample, but also perpendicular to it. Such a misorientation would result in local demagnetising field, which would be dependent not only on the direction of a given grain, but also on the grains surrounding it [6.27].

Elevated H_S and rms Barkhausen noise values are recorded in the vicinity of certain grains, whilst within other grains there is very little activity. This probably relates to the anticipated variation of domain wall mobility from grain to grain. Similar behaviour was observed at flux density levels from 0.5 T to 1.5 T and magnetising frequencies of 25 Hz and 50 Hz.

References to chapter 6

[6.1] D. C. Jiles, "Introduction to magnetism and magnetic materials", Chapman & Hall, 1991

[6.2] A. J. Moses, F. J. G. Landgraf, K. Hartmann, T. Yonamine, "Correlation between angular dependence of AC Barkhausen noise and hysteresis loss in non-orientated electrical steel", Stahleisin Dusseldorf, 215-219, 2004

[6.3] D. Spasojevic, S. Bukvic, S. Milosevic, H. E. Stanley, "Barkhausen noise: Elementary signals, power laws, and scaling relations", Physical Review E, Vol 54, No 3, 2531-2546, 1996

[6.4] G. Durin, Home webpage, http://www.ien.it/~durin/index.html

[6.5] P. Robert, "Electrical and magnetic properties of materials", Artech house, 1998

[6.6] P. Beckley, "Some aspects of the relationship between loss, domain wall motion and ageing in grain-oriented silicon iron", PhD Thesis, Cardiff University, 1969

[6.7] F. Bohn, A. Gündel, F. J. G. Landgraf, A. M. Severino and R. L. Sommer, "Magnetostriction in non-oriented electrical steels", Physica B: Condensed Matter, Vol 384, Issues 1-2, 294-296, 2006

[6.8] L. B. Sipahi, D. C. Jiles, D. Chandler, "Comprehensive analysis of Barkhausen emission spectra using pulse height analysis, frequency spectrum, and pulse wave form analysis", Journal of Applied Physics, Vol 73, 5623, 1993

[6.9] G. L. Houze, "Domain-wall motion in grain-oriented silicon steel in cyclic magnetic fields", Journal of Applied Physics, Vol 38, No 3, 1089-1096, 1967

[6.10] T. R. Haller, J. J. Kramer, "Observation of dynamic domain size variation in a silicon-iron alloy", Journal of Applied Physics, Vol 41, No 3, 1034-1035, 1970

[6.11] T. R. Haller, J. J. Kramer, "Model for reverse-domain nucleation in ferromagnetic conductors", Journal of Applied Physics, Vol 41, No 3, 1036-1037, 1970

[6.12] G. Rankis, V. Nikitin, V. Yurshevich, J. Jankovskis, "Noise in physical systems and $1/f$ fluctuations", World Scientific Publishing, ISBN 981-02-3141-5, 1997

[6.13] A. Dhar, D. L. Atherton, "Influence of magnetising parameters on the magnetic Barkhausen noise", IEEE Transactions on Magnetics, Vol 28, No 6, 3363, 1992

[6.14] M. Komatsubara, J. L. Porteseil, "Influence of the magnetising frequency on the Barkhausen noise power of non-oriented Si-steel sheets", Journal de Physique, Vol 46, C6-173, 1985

[6.15] M. Komatsubara, J. L. Porteseil, "Barkhausen noise behaviour in grain oriented 3%Si-Fe and the effect of local strain", IEEE Transactions on Magnetics, Vol 22, 496-498, 1986

[6.16] M. Emura, M. F. Campos, F. J. G. Landgraf, J. C. Teixerira, "Angular dependence of magnetic properties of 2% silicon electrical steel", Journal of Magnetism and Magnetic Materials, Vol 226-230, 1524-1526, 2001

[6.17] M. A. Cunha, N. C. S. B. Zwirmann, V. W. Volgien, R. S. Germano, F. J. G. Landgraf, T. Yanimine, R. Takanohashi, N. B. de Lima, "The angular dependence of magnetic properties of electrical steels", In:21st Annual Conference on properties and applications of magnetic materials Illinois institute of technology, USA, 2002

[6.18] A. J. Moses, F. J. G. Landgraf, K. Hartmann, T. Yonamine, "Correlation between angular dependence of A.C. Barkhausen noise and hysteresis loss in non-orientated electrical steel", Stahleisin Dusseldorf, 215-219, 2004

[6.19] G. Bertotti, "General properties of power losses in soft ferromagnetic materials", IEEE Transactions on Magnetics, Vol 24, No 1, 621-630, 1988

[6.20] J. Sievert, H. Ahlers, M. Birkfeld, B. Cornut, F. Fiorillo, K. A. Hempel, T. Kochmann, A. Kedous-Lebouc, T. Meydan, A. J. Moses, A. M. Rietto, "European intercomparison of measurements of rotational power loss in electrical sheet steel", Journal of Magnetism and Magnetic Materials, Vol 160, 115-118, 1996

[6.21] R. Gozdur, "Wyznaczanie quasi-statycznej petli histerezy blach elektrotechnicznych, (Determining quasi-static hysteresis loop of electrical steel, in Polish)", Przeglad elektrotechniczny (Electrotechnical review), R. 80, Nr 2/2004, Poland, 147-149, 2004

[6.22] Y. G. Kayhanian, "Novel concepts in transformer core design and minimisation of power loss", PhD Thesis, Cardiff University, 1999

[6.23] A. J. Moses, "Electrical steels: past, present and future developments", IEE proceedings A, Vol 137, 233-245, 1990

[6.24] V. Kavečanský, J. Gajdušek, L. Potocký, S. Uličiansky, V. Wiglasz, "Influence of grain orientation on local losses in oriented transformer sheets", Journal of Magnetism and Magnetic Materials, Vol 19, 1-3, 374-376, 1980

[6.25] S. Yamaura, Y. Furuya, T. Watanabe, "The effect of grain boundary microstructure on Barkhausen noise in ferromagnetic materials", Acta Materialia, Vol 49, 3019-3027, 2001

[6.26] S. Tumanski, M. Stabrowski, "The magnetovision method as a tool to investigate the quality of electrical steel", Measurement Science and Technology, 9, 488-495, 1998

[6.27] B. B. Mohd Ali, A. J. Moses, "A detection system for grain-oriented electrical steels", IEEE Transactions on Magnetics, Vol 25, No 6, 4421-4426, 1989

CHAPTER 7

DISCUSSION OF RESULTS ON ANCILLARY STUDY

7.1. Introduction

The NDE and Science Research Centre of Iwate University provided two types of samples, which are to be used from steam pipes in nuclear power generation. The first was cold rolled low carbon steel with three different shapes (charpy, picture frame, and plate shape) with various rolling reductions; the second was Fe 1%Cu alloy with two shapes (charpy, ring) and with a rolling reduction of 0% and 10%, the samples were also thermally aged. The total power loss and Barkhausen measurements were conducted on these samples.

7.2. Cold rolled low carbon steel

Low carbon steels were the original materials used in transformers, motors and generators but have long been superseded by silicon-iron [7.1]. Low carbon steel is still used for dc applications such as laboratory electromagnets for which it remains the best material [7.1]. Iron with low levels of impurities such as carbon, once annealed can give a maximum relative permeability of 100,000 [7.1]. Higher permeabilities can be achieved from soft iron however, it is commercially too expensive to manufacture. In order to provide longer service life with higher performance of steel components, quality control is essential. There is a growing need for non-destructive characterisation of steel components and Barkhausen noise measurement provides a good alternative to the traditional methods in terms of speed and accuracy.

Five slabs with different thicknesses (12.0, 12.6, 13.3, 15.0, 20.0 mm) were prepared by cutting from the same cylindrical ingot. Then they were annealed at 1173 K in air and then air cooled to room temperature. Each slab was cold rolled with a series of rollers so that the thickness becomes 12.0 mm, as indicated in table 7.1.

0% reduction	12.0 → 12.0 mm
5% reduction	12.6 → 12.0 mm
10% reduction	13.3 → 12.0 mm
20% reduction	15.0 → 12.0 mm
40% reduction	20.0 → 12.0 mm

Table 7.1. The thickness decrease in the cold rolled low carbon steel samples

The surface layers (1 mm) either side of the slabs were removed by milling and thickness was reduced to 10 mm. Then the samples were cut to the desired charpy and plate shapes. The picture frame samples were cut from the charpy test pieces by electric discharge machine. It must be noted that the samples were not annealed after these production processes.

The Barkhausen noise signal was measured using the double B-coil method for the charpy and plate samples for the picture frame sample a single coil was used. Due to time constraints, an H-coil for measuring the magnetic field could not be constructed. Therefore, the current flowing to the magnetising coils was measured and the magnetic field was calculated using equation 4.4.

The assumption made for equation 4.4 was that the magnetising path length was set to the length of the sample. This is due to the flux density of the yoke being considerably lower than the flux density of the sample. This assumption is valid if the cross sectional area of the yoke is much larger than the cross sectional area of the sample. For the charpy sample, the cross sectional area of the yoke is 40 times larger and for the plate samples the cross sectional area is 10 times larger. In addition, if the permeability is taken in to account the yoke is constructed from grain-oriented electrical steel laminations, which has a very large permeability compared with the cold rolled low carbon steel sample. This means that the flux density in the yoke would be lower still, so 40 times and 10 times is the worse case for the charpy and plate samples, respectively.

Hardness tests and Transmission Electron Microscopy (TEM) images were provided with the samples, which can be seen in appendix I. The grain size was observed by the manufacturer to be about 20 micron for the 0% rolling reduction sample, non of the other samples were analysed. It can be seen that the mechanical hardness of the material increases with increasing rolling reduction. The TEM images show that the dislocation density increases as the rolling reduction is increased. (The dislocation density is the number of dislocation lines that intersect a unit area in the crystal [7.2].) Also, an elongation direction can be seen which indicates the rolling direction of the material.

The total power loss and rms Barkhausen noise variation with 0%, 5%, 10%, 20% and 40% rolling reduction in cold rolled low carbon steel of charpy shape, at 0.06 T and 0.1 T magnetic flux density, was measured. Figure 7.1 and 7.2 shows the variation of total power loss and rms Barkhausen noise, respectively, with rolling reduction.

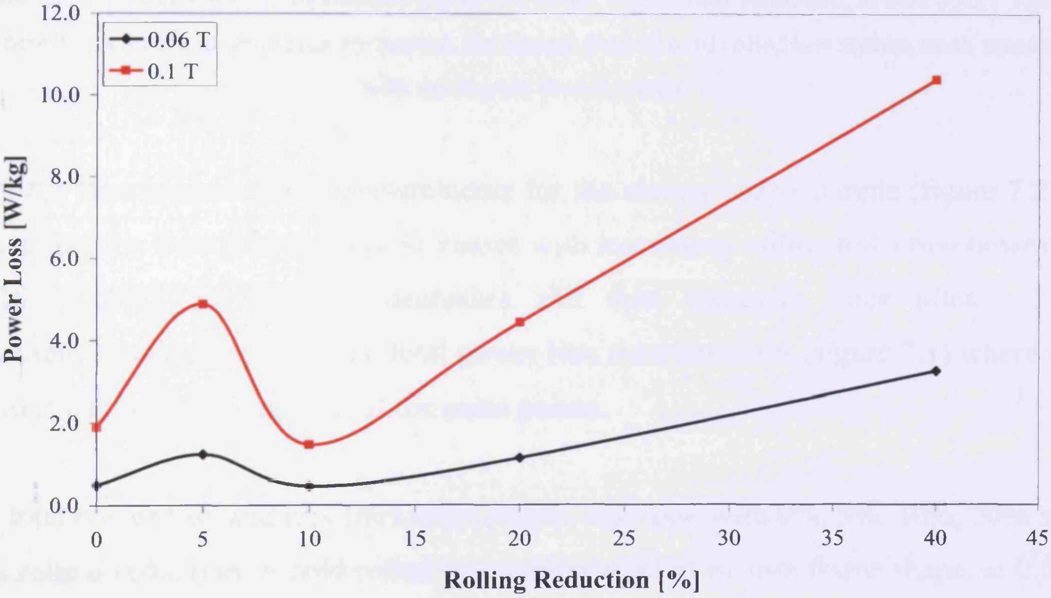

Figure 7.1. Variation of total power loss (W/kg), with rolling reduction, at 0.06 T, 0.1 T peak flux density, at 50 Hz magnetising frequency, for charpy shaped cold rolled low carbon steel, measured with the double B-coil sensor

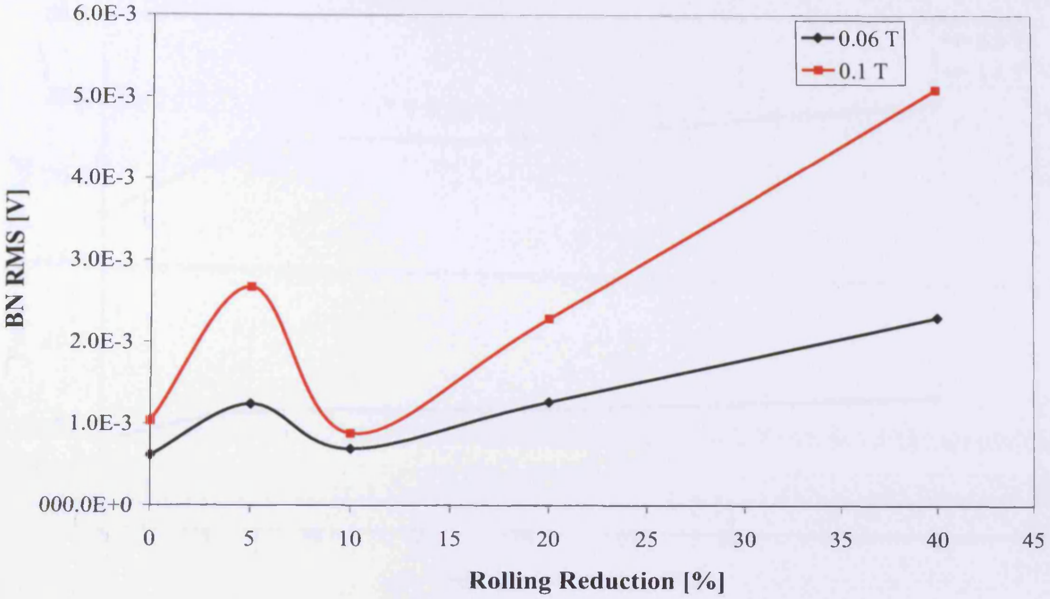

Figure 7.2. Variation of rms Barkhausen noise, BN RMS, with rolling reduction, at 0.06 T, 0.1 T peak flux density, at 50 Hz magnetising frequency, for charpy shaped cold rolled low carbon steel, measured with the double B-coil sensor

With the Barkhausen noise measurements for the charpy shape sample (figure 7.2) it is seen that the Barkhausen noise increases with increasing rolling reduction however, at 10% rolling reduction it decreases and then increases there after. This measurement correlates with the total power loss measurements (figure 7.1) where the increase and decrease happens at the same points.

The total power loss and rms Barkhausen noise variation with 0%, 5%, 10%, 20% and 40% rolling reduction in cold rolled low carbon steel of picture frame shape, at 0.6 T and 1.0 T magnetic flux density, was measured. Figure 7.3 and 7.4 shows the variation of total power loss and rms Barkhausen noise, respectively, with rolling reduction.

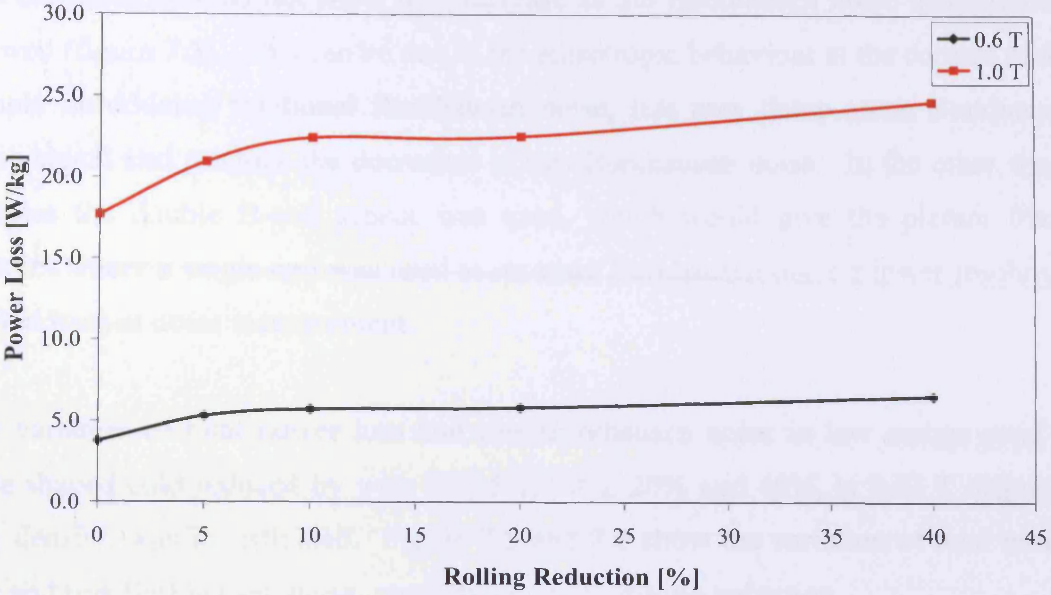

Figure 7.3. Variation of total power loss (W/kg), with rolling reduction, at 0.6 T, 1.0 T peak flux density, at 50 Hz magnetising frequency, for picture frame shaped cold rolled low carbon steel, measured with the double B-coil sensor

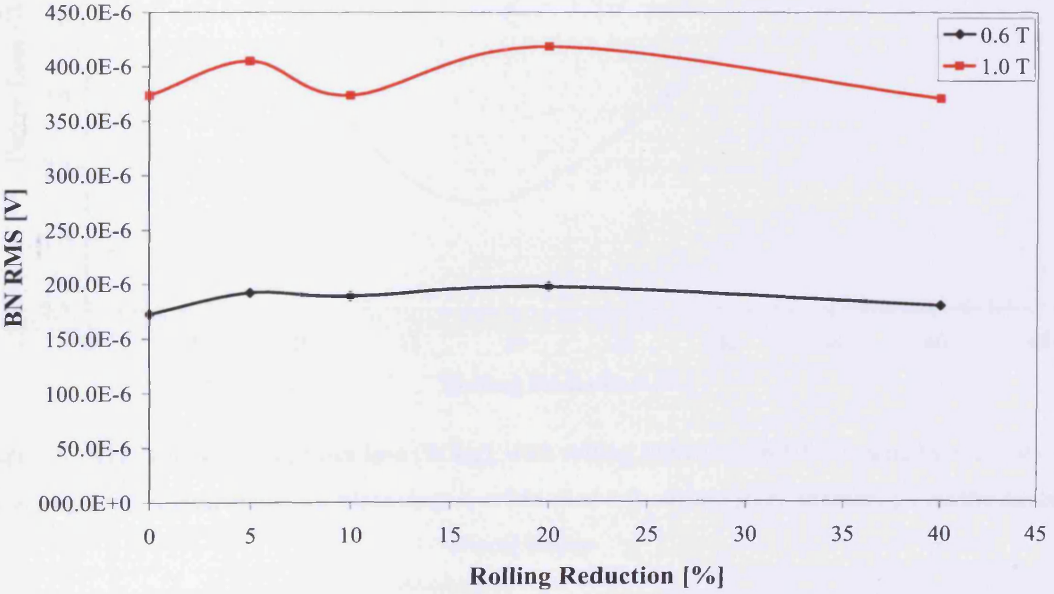

Figure 7.4. Variation of rms Barkhausen noise, BN RMS, with rolling reduction, at 0.6 T, 1.0 T peak flux density, at 50 Hz magnetising frequency, for picture frame shaped cold rolled low carbon steel, measured with the double B-coil sensor

For the picture frame sample (figure 7.4) a similar decrease can be seen at 10% rolling reduction, however a significant increase afterwards was not seen. Also, the power loss measurements do not show this decrease as the Barkhausen noise measurement showed (figure 7.3). This can be due to the anisotropic behaviour at the corners of the sample introducing rotational Barkhausen noise, this may damp some Barkhausen noise signal and produce the decreases in rms Barkhausen noise. In the other shape samples the double B-coil sensor was used, which would give the picture frame samples where a single coil was used to measure Barkhausen noise a lower resolution of Barkhausen noise measurement.

The variation of total power loss and rms Barkhausen noise in low carbon steel of plate shaped cold reduced by with 0%, 5%, 10%, 20% and 40%, at 0.03 T magnetic flux density, was investigated. Figure 7.5 and 7.6 show the variation of total power loss and rms Barkhausen noise, respectively, with rolling reduction.

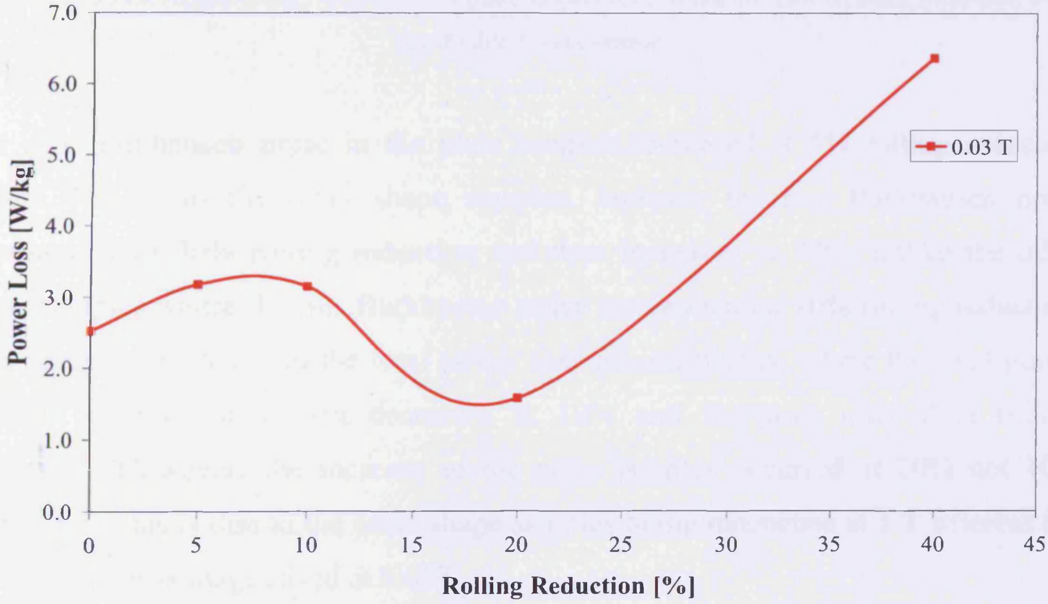

Figure 7.5. Variation of total power loss (W/kg), with rolling reduction, at 0.03 T peak flux density, at 50 Hz magnetising frequency, for plate shaped cold rolled low carbon steel, measured with the double B-coil sensor

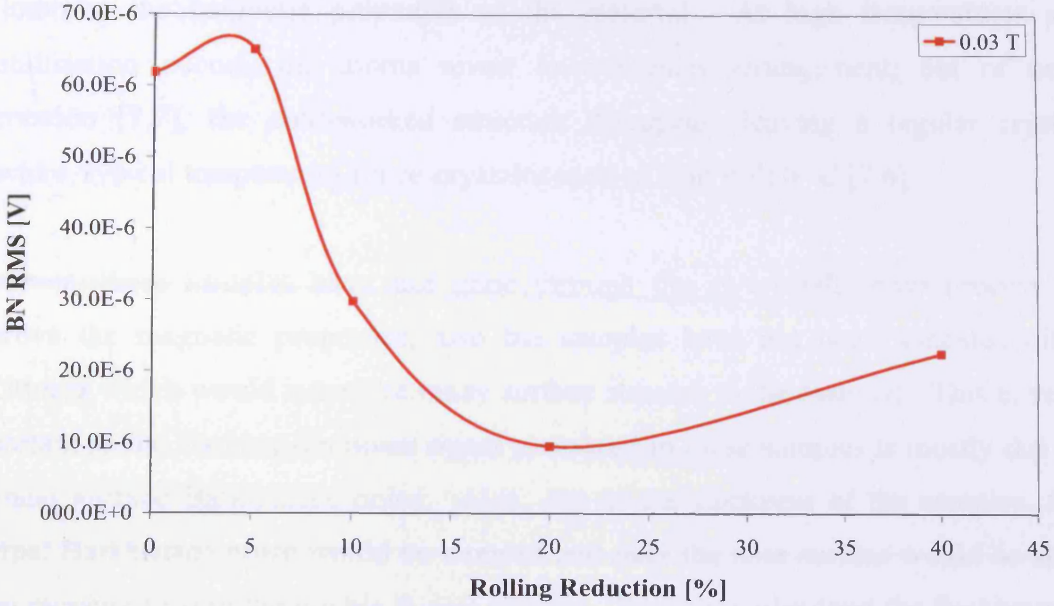

Figure 7.6. Variation of rms Barkhausen noise, BN RMS, with rolling reduction, at 0.03 T peak flux density, at 50 Hz magnetising frequency, for plate shaped cold rolled low carbon steel, measured with the double B-coil sensor

The rms Barkhausen noise in the plate samples increased at 5% rolling reduction (figure 7.6) as in the other shape samples, however the rms Barkhausen noise decreased until 20% rolling reduction and then increased at 40%, unlike the other shape samples where the rms Barkhausen noise increases after 10% rolling reduction. This again correlates with the total power loss measurements, where the total power initially increases and then decreases at 10% and increases after 20% rolling reduction. However, the increase in the plate samples occurred at 20% not 10% (figure 7.5), this is due to the other shape samples being magnetise at 1 T whereas the plate sample was magnetised at 0.03T.

The results show that magnetic Barkhausen noise is influenced by the tempering which, as a function of the temperature, causes changes in dislocation density, lattice straining (i.e., micro residual stresses) and the morphology and size of cementite, and corresponding variations in hardness. However, the results are not in agreement with previous studies [7.3, 7.4, 7.5].

Under cold working conditions, metals break ultimately across the grains [7.6] when under high stress conditions. That is when re-crystallisation and annealing is required to improve the magnetic properties of the material. At high temperatures re-crystallisation occurs, the atoms revert to a regular arrangement, but of new orientation [7.7], the cold-worked structure disappears leaving a regular crystal structure, typical temperature for re-crystallisation of iron is 450 °C [7.6].

However, these samples have not gone through the re-crystallisation process to improve the magnetic properties, also the samples have not been annealed after machining which would introduce many surface stresses to the material. This is very important as the Barkhausen noise signal measured in these samples is mostly due to the near surface Barkhausen noise. Also, due to the thickness of the samples, the internal Barkhausen noise would be damped and only the near surface would be able to be measured using the double B-coil method. To fully understand the Barkhausen noise measurements conducted on these samples the metallurgy of the material needs to be fully investigated also there are many variables in these samples which would affect the Barkhausen noise which is out of the scope of this study.

7.3. Thermally aged Fe 1wt%Cu alloy

Slabs of hot rolled FeCu alloys, which were obtained from the same ingot, were solution treated at 1123K for 5 hours, followed by water quenching. Then one of the slabs was cold rolled with a series of rolling by 10%. All samples were then milled and cut to shape. Then they were isothermally aged at 773K for 0-5000 minutes. The grain size after solution treatment was 125 micron.

Hardness tests results were provided with these samples, which can be seen in appendix II. It is seen that the mechanical hardness of the material increases with increasing thermal ageing however, at 5000 min the hardness decreases.

It must be noted that once the samples were machined to shape they were not annealed and therefore surface stresses would be high and influence the Barkhausen noise measurements.

A final anneal takes residual carbon into solution and some of this may precipitate over a period of years leading to increases in coercive forces as domain wall motion becomes impeded by carbon precipitates [7.8]. Ageing maybe minimised by keeping the carbon content low and by use of special stabilising additions (e.g. silicon) to the steel.

The variation of total power loss and rms Barkhausen noise with aging time in iron copper samples of Charpy and bar (not notched) shape, of 0% rolling reduction, at 0.6 T and 1.0 T peak magnetic flux density, was investigated. Figure 7.7 and 7.8 shows the variation of total power loss and rms Barkhausen noise, respectively, with ageing time.

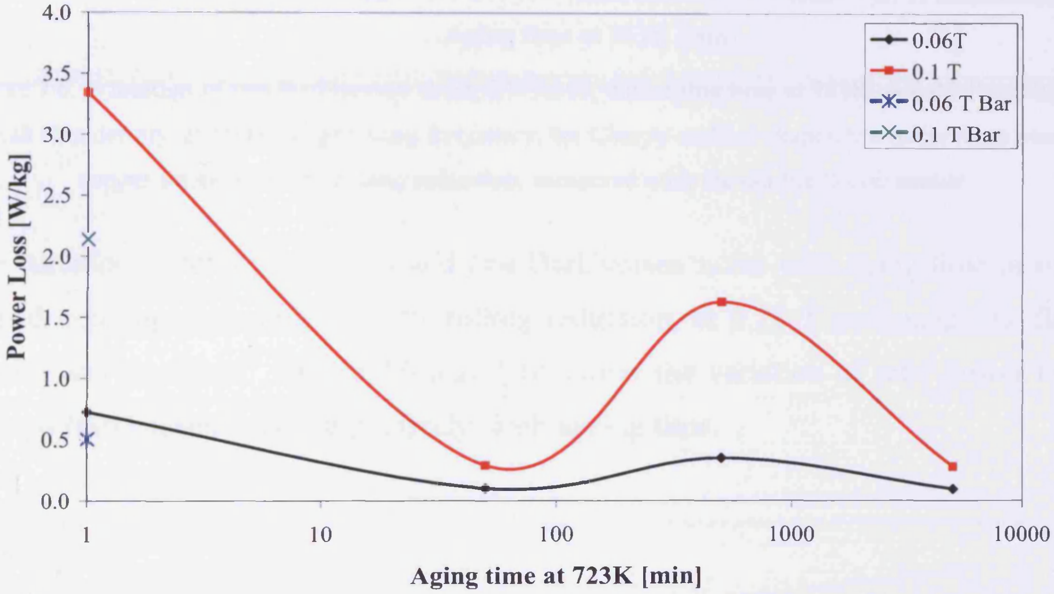

Figure 7.7. Variation of total power loss (W/kg), with aging time at 723K, at 0.06 T and 0.1T peak flux density, at 50 Hz magnetising frequency, for Charpy and bar shaped thermally aged iron copper samples, of 0% rolling reduction, measured with the double B-coil sensor

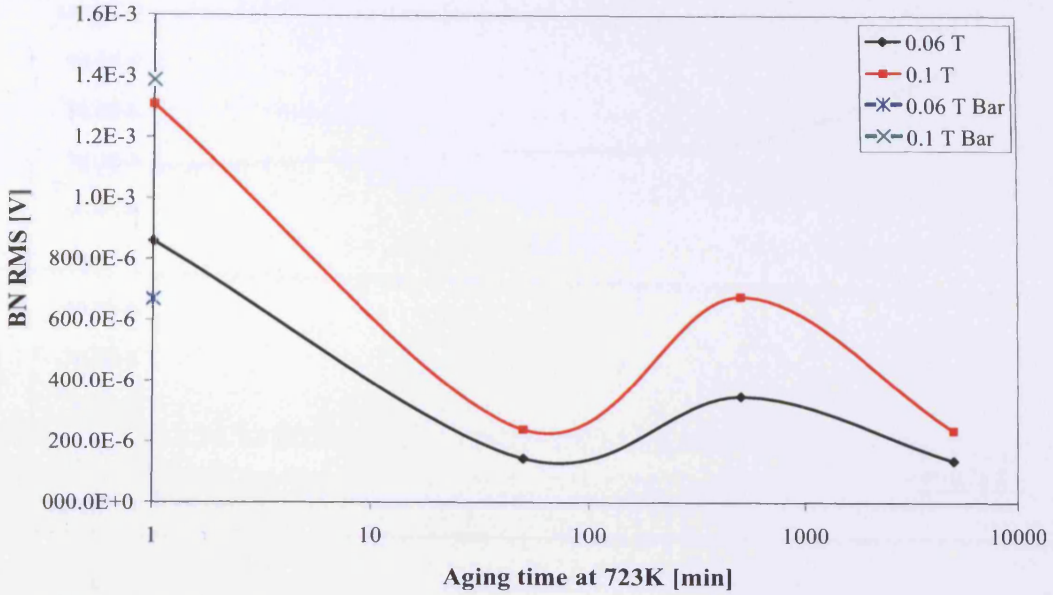

Figure 7.8. Variation of rms Barkhausen noise, BN RMS, with aging time at 723K, at 0.06 T and 0.1T peak flux density, at 50 Hz magnetising frequency, for Charpy and bar shaped thermally aged iron copper samples, of 0% rolling reduction, measured with the double B-coil sensor

The variation of total power loss and rms Barkhausen noise with aging time in ring shaped iron copper samples, of 0% rolling reduction, at 0.75 T peak magnetic flux density was measured. Figure 7.9 and 7.10 shows the variation of total power loss and rms Barkhausen noise, respectively, with ageing time.

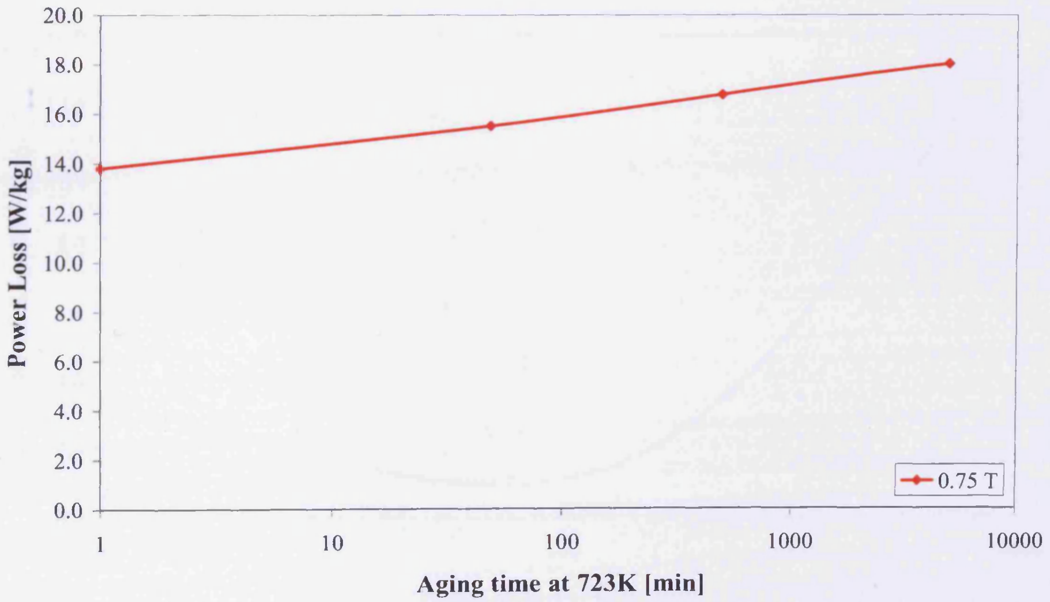

Figure 7.9. Variation of total power loss (W/kg), with aging time at 723K, at 0.75 T peak flux density, at 50 Hz magnetising frequency, for ring shaped thermally aged iron copper samples, of 0% rolling reduction, measured with the double B-coil sensor

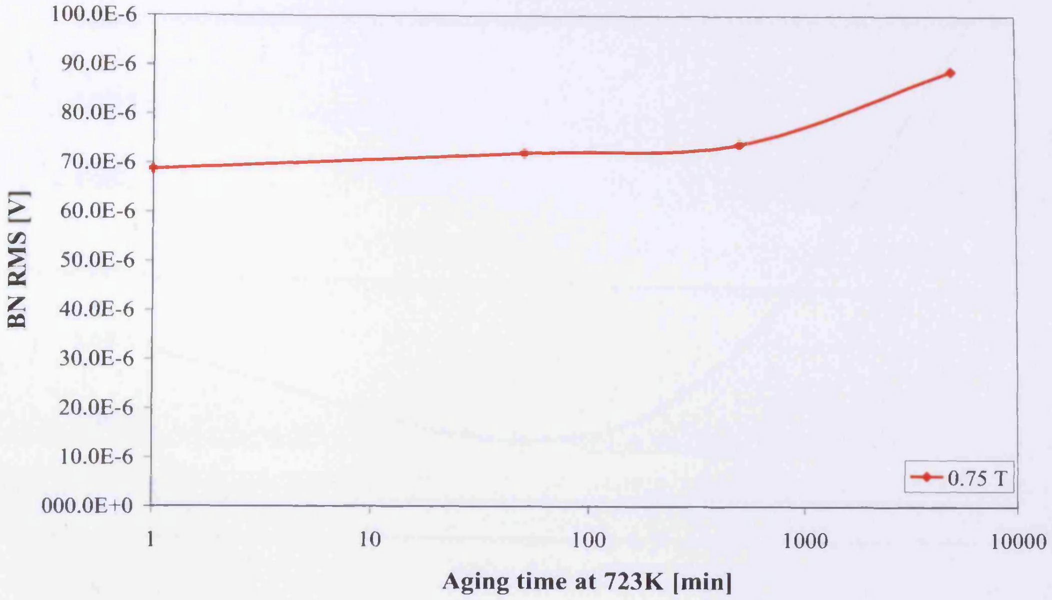

Figure 7.10. Variation of rms Barkhausen noise, BN RMS, with aging time at 723K, at 0.75 T peak flux density, at 50 Hz magnetising frequency, for ring shaped thermally aged iron copper samples, of 0% rolling reduction, measured with the double B-coil sensor

The variation of total power loss and rms Barkhausen noise with aging time iron copper samples of Charpy shape, of 10% rolling reduction, at 0.1 T peak magnetic flux density, was measured. Figure 7.11 and 7.12 show the variation of total power loss and rms Barkhausen noise, respectively, with ageing time.

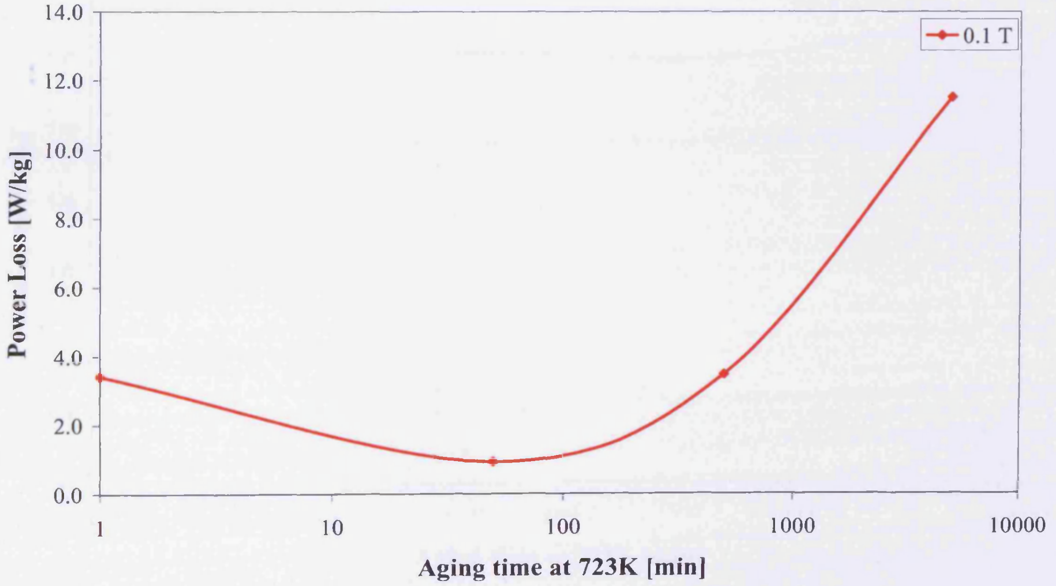

Figure 7.11. Variation of total power loss (W/kg), with aging time at 723K, at 0.1 T peak flux density, at 50 Hz magnetising frequency, for Charpy shaped thermally aged iron copper samples, of 10% rolling reduction, measured with the double B-coil sensor

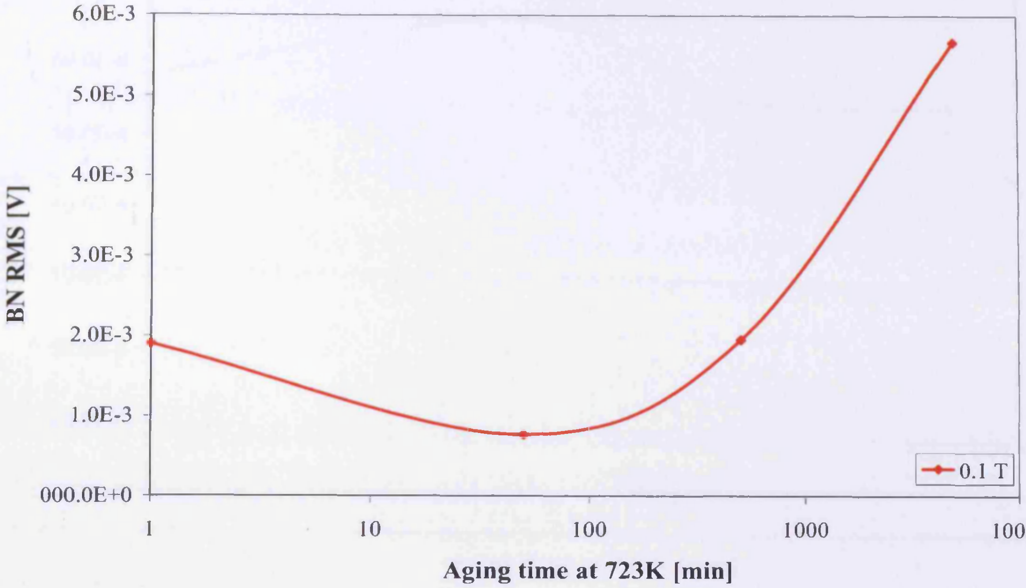

Figure 7.12. Variation of rms Barkhausen noise, BN RMS, with aging time at 723K, at 0.1 T peak flux density, at 50 Hz magnetising frequency, for Charpy shaped thermally aged iron copper samples, of 10% rolling reduction, measured with the double B-coil sensor

The variation of total power loss and rms Barkhausen noise with aging time in ring shaped iron copper samples, of 10% rolling reduction, at 0.5 T peak magnetic flux density, was measured. Figure 7.13 and 7.14 shows the variation of total power loss and rms Barkhausen noise, respectively, with ageing time.

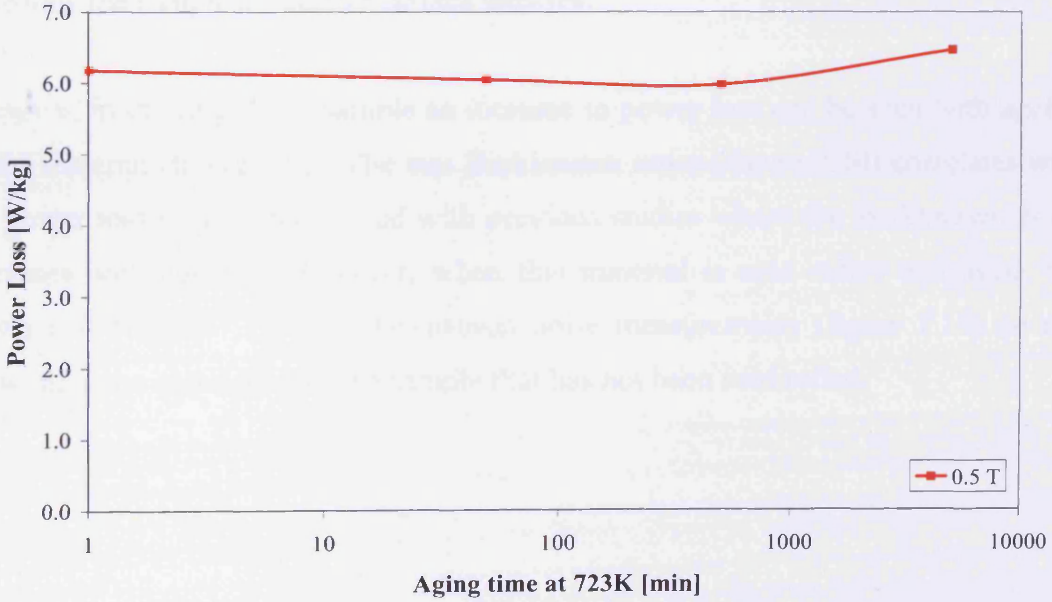

Figure 7.13. Variation of total power loss (W/kg), with aging time at 723K, at 0.8 T peak flux density, at 50 Hz magnetising frequency, for ring shaped thermally aged iron copper samples, of 10% rolling reduction, measured with the double B-coil sensor

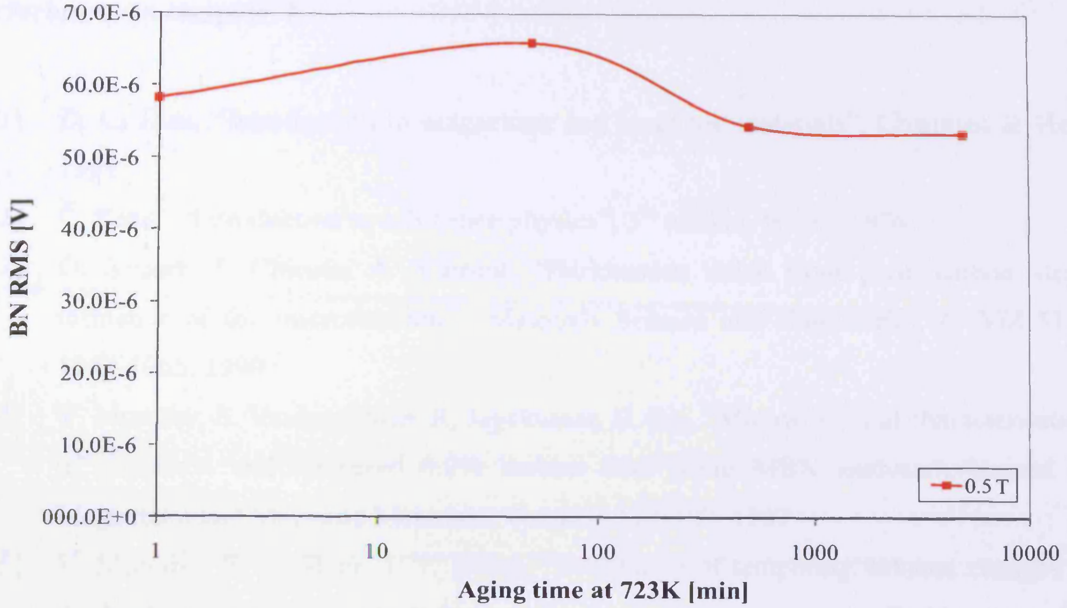

Figure 7.14. Variation of rms Barkhausen noise, BN RMS, with aging time at 723K, at 0.8 T peak flux density, at 50 Hz magnetising frequency, for ring shaped thermally aged iron copper samples, of 10% rolling reduction, measured with the double B-coil sensor

In previous studies, it is seen that the rms Barkhausen noise increases with increasing ageing time [7.9]. However again the current measurements do not correlate well to the measurements taken for the charpy shape samples (figure 7.7, 7.8, 7.11, 7.12). Again, this is due to the surface stress caused by milling the sample and then not annealing the sample to remove surface stresses.

However, in the ring shape sample an increase in power loss can be seen with ageing of the material (figure 7.9). The rms Barkhausen noise (figure 7.10) correlates with the power loss measurements and with previous studies where the Barkhausen noise increases with ageing. However, when this material is cold rolled and aged, the power loss (figure 7.13) and Barkhausen noise measurements (figure 7.14) do not show the same correlation as the sample that has not been cold rolled.

References to chapter 7

[7.1] D. C. Jiles, "Introduction to magnetism and magnetic materials", Chapman & Hall, 1991

[7.2] C. Kittel, "Introduction to solid state physics", 5th edition, Wiley, 1976

[7.3] O. Saquet, J. Chicois, A. Vincent, "Barkhausen noise from plain carbon steel: influence of the microstructure", Materials Science and Engineering A, Vol 31A, 1053-1065, 1999

[7.4] V. Moorthy, S. Vaidyanathan, R. Jayakumar, B. Raj, "Microstructural characterisation of quenched and tempered 0.2% carbon steel using MBN analysis", Journal of Magnetism and Magnetic Materials, Vol 171, 179-189, 1997

[7.5] V. Moorthy, B. A. Shaw, J. T. Evans, "Evaluation of tempering induced changes in the hardness profile of case-carburised En-36 steel using magnetic Barkhausen noise analysis", NDT&E International, Vol 36, 43-49, 2003

[7.6] A. R. Bailey, "A textbook of metallurgy", 2nd edition, St Martin's press inc, New York, 1960

[7.7] R. A. Higgins, "Engineering metallurgy: Part 1 - applied physical metallurgy", 6th edition, Arnold, 1993

[7.8] P. Beckley, "Some aspects of the relationship between loss, domain wall motion and ageing in grain oriented silicon iron", PhD thesis, Cardiff University, 1969

[7.9] J. W. Byeon, S. I. Kwun, "Effect of thermal exposure of 2.25Cr-1Mo steel on magnetic Barkhausen noise", Journal of the Korean Physical Society, Vol 45, No. 3, 733-737, 2004

CHAPTER 8

CONCLUSIONS

In all the materials tested the rms Barkhausen noise at 50 Hz rises with static hysteresis confirming the general trend found previously. The results indicate that a close relationship between Barkhausen noise and hysteresis under ac magnetisation does exist.

The rms Barkhausen noise also showed a similar trend to the total power loss with a peaked increase at 45°. This verifies that there is a correlation between the hysteresis component of loss and the rms Barkhausen noise.

Both the non-oriented electrical steel samples cut at various angles with different material textures show similar trends with both power loss and Barkhausen noise increasing with cutting angle and peaking at 45°. This further verifies the correlation between Barkhausen noise and hysteresis in other materials. This helps provide an understanding of the effects of texture on loss, which would help in the development of new grades of low loss motor steels.

When varying the silicon content in non-oriented electrical steel the hysteresis loss decreases with increasing silicon content. This trend was also observed in rms Barkhausen noise; thus adding further evidence to there being a close relationship between Barkhausen noise and hysteresis loss under ac magnetisation.

Removing the coating from a grain-oriented electrical steel sample caused the domains to widen over the whole sample, thus causing the overall power loss to increase by 25.2% (at 1.4 T, 50 Hz magnetising frequency). The same increase of 25% was observed with the rms Barkhausen noise, thus further indicating a strong correlation between power loss and Barkhausen noise.

Barkhausen noise shows good correlation with power loss, this would help predict power loss throughout the magnetisation process. Absolute values of power loss cannot be derived from Barkhausen noise measurements, except some reference measurement or trend information can be made available.

Measurements conclude that rms Barkhausen noise is made of two components, one that is frequency independent and relates to the static hysteresis component, and a second component that is frequency dependent.

Barkhausen mapping of the surface of grain-oriented electrical steel shows definite localised variation in Barkhausen noise. However contrary to previous research, this investigation has shown (at least on a scale of mm's) that Barkhausen noise amplitudes cannot be correlated with grain boundary positions.

Measurements indicate that Barkhausen noise activity increases with a decrease in domain size. There is a strong indication that the surface Barkhausen noise activity results from the grain-to-grain misorientation.

The measurements of the surface field and Barkhausen noise on the surface of grain-oriented electrical steel sample show strong correlation. However, there is a lack of clear influence of grain boundaries, although the surface activity, which seems to be more affected by certain grains. If Barkhausen noise is closely associated with hysteresis loss, the results infer that this component varies spatially possibly independent of grain structure.

The adaptive automated feedback system for Barkhausen noise measurement was capable of fully controlling flux density waveforms. The system is capable of controlling the flux density waveforms under sinusoidal conditions at flux densities of up to 1.8 T, at magnetising frequencies of 5 to 100 Hz. Special care must be taken when controlling the magnetising waveform to ensure that a sinusoidal form factor within ±1% is achieved. It was also found essential in this investigation to minimise the THD down to ±2% for improved waveform shape.

A Barkhausen noise signal is stochastic in nature but RMS, total sum of amplitudes, power spectrum and kurtosis, all showed consistent trends and repeatability. These methods can be used to analyse Barkhausen noise signals. Also, the rms Barkhausen noise, total sum of amplitudes of all the peaks, and the power spectrum of the signal, all obey a power distribution law.

It has been demonstrated that the enwrapping coils and the ferrite cored surface sensor methods, although oriented perpendicular to each other, produce very similar trends.

It has been demonstrated that Barkhausen noise can be measured at power frequencies in electrical steels. At higher magnetising frequencies, Barkhausen jumps coalesce to form a continuous fluctuating signal and individual Barkhausen peaks cannot be distinguished, therefore sampling at a higher frequency would not add more benefit to Barkhausen noise analysis. Thus, no more Barkhausen information is obtained using a value of sampling frequency higher than 102.4 kHz for grain-oriented 3%SiFe steel at 50 Hz magnetisation.

The optimum spacing for the double B-coil sensor in Epstein electrical steel samples is 5 mm. This gave the optimum Barkhausen contribution whilst minimising stray field pickup in the sensor.

CHAPTER 9

FURTHER RESEARCH

In this investigation, it was found that Barkhausen noise and static hysteresis loss follow a linear relationship in non-oriented electrical steel samples. Future work would be to investigate this relationship in other materials, such as grain-oriented electrical steel. In addition, the relationship between silicon content in electrical steel and Barkhausen noise was investigated, an understanding of other material characteristics with Barkhausen noise would be informative.

Scanning the surface of the grain-oriented electrical steel sample indicates that the sample had regions of high and low Barkhausen noise, thus high and low regions of total loss. This could be further investigated, to find the cause of such regions (rolling reduction, pickling, various production parameters) and possible research can be conducted to reduce regions of high Barkhausen noise, thus reducing hysteresis loss i.e. reducing total power loss.

The surface field and Barkhausen noise measurement indicate that the hysteresis component of loss varies spatially possibly independent of grain structure. More experimental work is required in order to understand and confirm the practical implications of these phenomena.

In this research, a ferrite core of 3 mm diameter was used for scanning measurements. However, for a sensor of such diameter, a sample with grains larger than 3 mm is desired for scanning measurements. It would be very useful to have a sensor head with a smaller diameter so that more localised measurements can be conducted. With a smaller size sensor, it would be possible to measure Barkhausen noise near grain boundaries. Also, samples with smaller grain sizes can be observed for Barkhausen noise studies, such as non-oriented electrical steel.

An extension of the magnetising frequency range of the measurement system would be useful. Measurements were carried out in the frequency range of 5 Hz to 100 Hz in this study. It would be interesting to observe if a similar relationship of Barkhausen noise with magnetising frequency seen in this study still exist at higher magnetising frequencies. With the development of next generation DAQ cards it would be possible to carry out further research of this frequency relationship.

Future work would be to design a surface detection system incorporating an integrated surface sensor and magnetising yoke. This system would make measurements more flexible with samples of different shapes and sizes. The advanced system should also allow the user to conduct measurements without changing the magnetic circuit and changing the LabVIEW code.

Also with the ancillary study samples, future work could be carried out to understand the metallurgy of the material to have a greater understanding of the results seen in this study.

APPENDIX I – MECHANICAL PROPERTIES OF COLD-ROLLED LOW CARBON STEEL SAMPLES

Vickers hardness

The Vickers hardness was measured with the standard Vickers's indentation technique. The applied load was 300 gf. All five samples with each rolling reduction were tested and 10 indents were taken for each sample. In figure 1, it is seen that the Vickers' hardness test reveals that the sample increases in hardness with increase in rolling reduction.

Reduction (%)	AVERAGE	STDEV
0	139.6	4.2
5	164.3	7.1
10	177.3	7.2
20	187.5	8.4
40	205.8	10.1

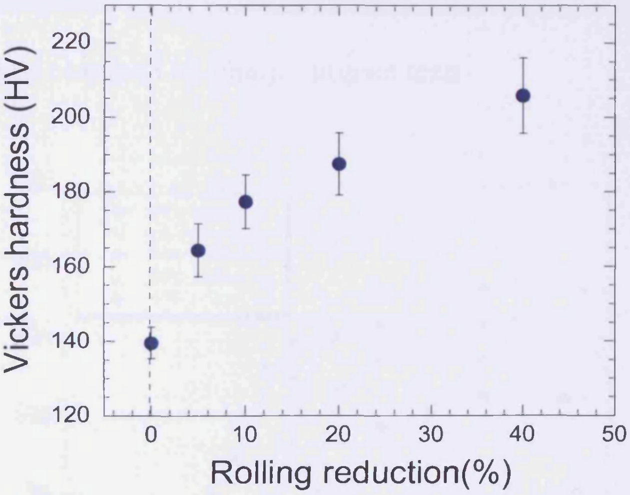

The results from the Vickers' hardness test. The table shows the results measured with the error in measurements and the graph shows these results plotted.

Ductile-Brittle transition temperature (DBTT)

Charpy impact test were preformed with a pendulum of 27.6 kg and lift angle of 138.5° in the temperature range of 201 – 363 K. Five V-notched charpy samples were tested at each temperature and both the largest and smallest values of absorption energy were eliminated when averaging the data. DBTT was defined as a midpoint between low toughness brittle and high toughness ductile fracture regimes.

Reduction (%)	DBTT(K)
0	245.9
5	259.3
10	261.5
20	272.1
40	280.1

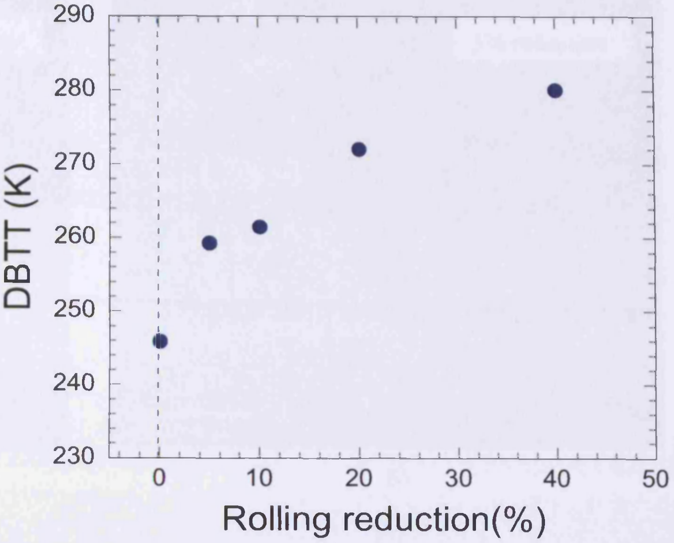

The results from the DBTT test. The table shows the results measured and the graph shows these results plotted

Absorption energy at various temperatures obtained by charpy impact tests.

T (K)	0%	5%	10%	20%	40%
363					111.6
333	183.1	175.7	160.5	137.3	112.2
313					100.9
295	180.8	177.7	159.3	138.5	92.9
288		178.5			
283					44.8
278		154.9	152.2	119.6	
273	180.0	149.2		52.3	37.9
263	147.2	132.5	125.6	39.1	36.1
253	130.4	46.1	13.0	20.3	19.8
243	73.0	9.5	10.4	7.6	13.3
233	49.3				
223	17.1				
201	4.5	3.6	4.5	4.9	4.7

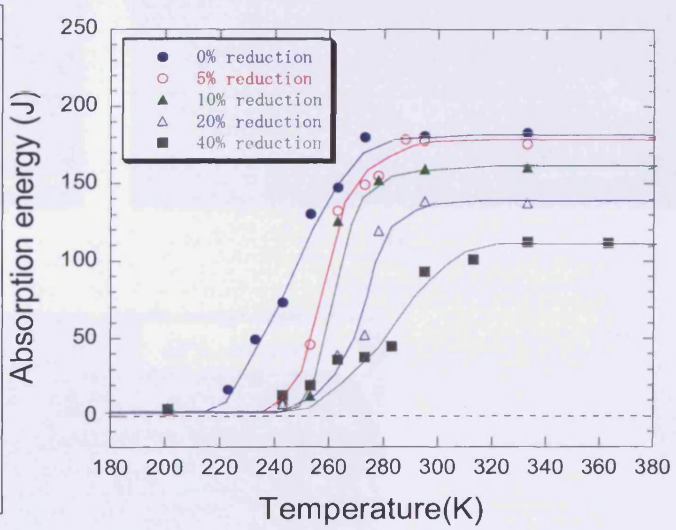

The table shows the absorption energy at 201 - 363 K with the results plotted on a graph besides it

TEM Micrographs

Transmission electron microscopy (TEM) is an imaging technique whereby a beam of electrons is transmitted through a specimen, then an image is formed, magnified and directed to appear either on a fluorescent screen or on layer of photographic film, or to be detected by a sensor such as a CCD camera. The images seen using the above technique are seen below, showing a pattern of grain size and formation.

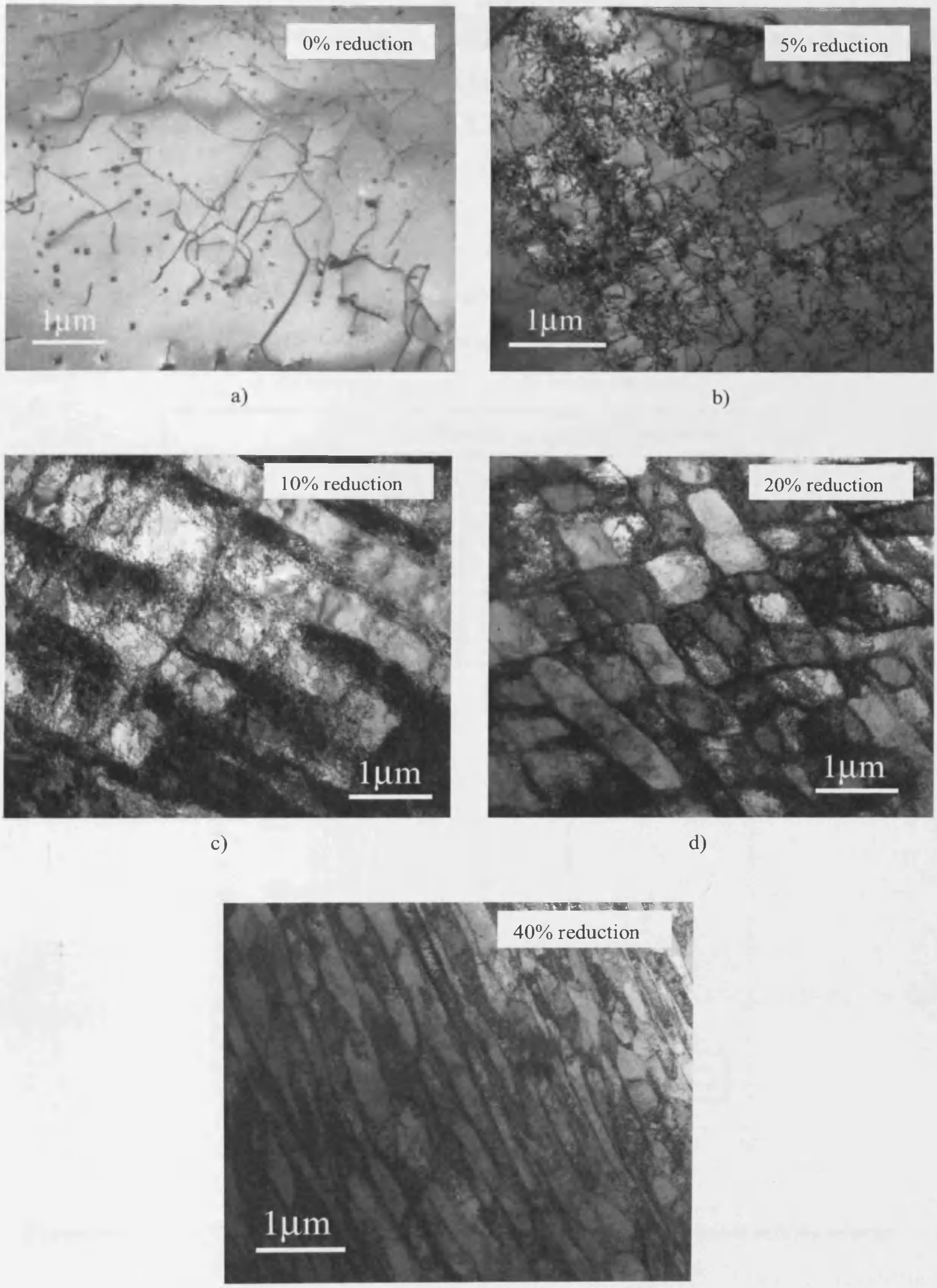

a) b) c) d) e)

TEM micrograph images of the cold rolled low carbon steel samples with a rolling reduction of a) 0%, b) 5%, c) 10%, d) 20%, e) 40%

APPENDIX II – MECHANICAL PROPERTIES OF THERMALLY AGED FE 1WT%CU ALLOY SAMPLES

Vickers hardness

The Vickers hardness was measured with the standard Vickers' indentation technique. The applied load was 300 gf and 15 indents were taken for each aging condition.

	0% reduction		10% reduction	
Aging time (min)	AVERAGE	STDEV	AVERAGE	STDEV
0	113.9	2.8	151.5	5.9
50	160.4	3.8	180.9	7.4
500	188.0	5.4	192.0	7.6
5000	169.5	5.5	173.1	4.5

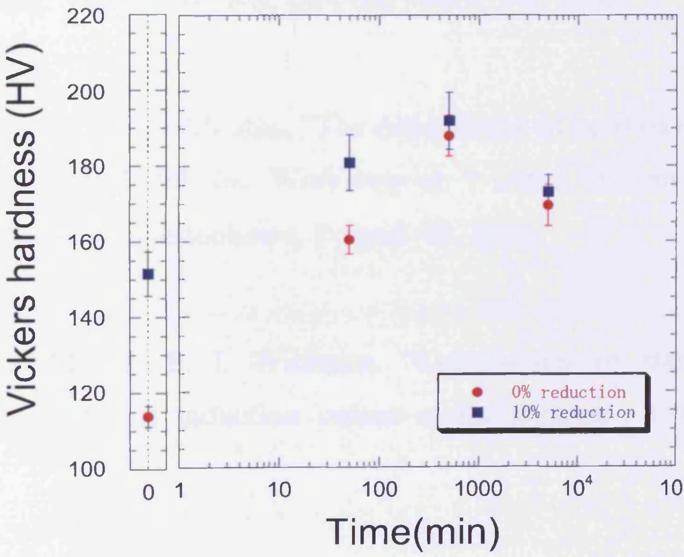

The results from the Vickers' hardness test. The table shows the results measured with the error in measurements and the graph shows these results plotted.

APPENDIX III – PUBLISHED WORK

S. Zurek, P. Marketos, S. Tumanski, **H. V. Patel**, A. J. Moses, "Correlation between surface magnetic field and Barkhausen noise in grain-oriented electrical steel", Abstract submitted for poster contribution to IEEE International Magnetics Conference, Spain, May 2008

A. J. Moses, **H. V. Patel**, P. I. Williams, "Challenges in quantifying Barkhausen noise in electrical steels", Electromagnetic Non-Destructive Evaluation, Vol 28, Studies in Applied Electromagnetics and Mechanics, 300, 2007

A. J. Moses, **H. V. Patel**, P. I. Williams, "AC Barkhausen noise in electrical steels: Influence of sensing technique on interpretation of measurements", Journal of Electrical Engineering, Vol 57, No. 8/S, (Special Issue), 3-8, 2006

H. V. Patel, A. J. Moses, P. I. Williams, "The dependence of ac Barkhausen noise on data acquisition parameters", 9th Int. Workshop on 1 and 2 Dimensional Magnetic Measurements and Testing, Czestochowa, Poland, 68, 2006

H. V. Patel, A. J. Moses, P. I. Williams, "Comparison of Barkhausen noise measurements using different induction sensor methodologies", UNMNE Prague, 2006

H. V. Patel, S. Zurek, T. Meydan, D. C. Jiles, L. Li, "A new adaptive automated feedback system for Barkhausen signal measurement", Journal of Sensors and Actuators A: Physical, Vol 129, Issues 1-2, 112-117, 2006